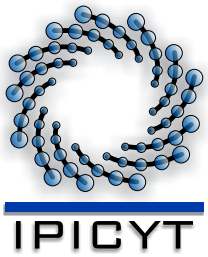

Instituto Potosino de Investigación
Científica y Tecnológica, A.C.

Posgrado en Ciencias Aplicadas

Attachment of transition metal nanoparticles on nitrogen doped carbon nanotubes (MWNTs-CN_x) and their further reactions

Tesis que presenta

Xavier Norberto Lepró Chávez

Para obtener el grado de

Maestro en Ciencias Aplicadas

En la opción de

Nanociencias y Nanotecnología

Realizada bajo la codirección de:

Dr. Mauricio Terrones Maldonado
Dra. Yadira Itzel Vega Cantú

San Luis Potosí, S.L.P., México, Septiembre de 2006

Attachment of transition metal nanoparticles on nitrogen doped carbon nanotubes (MWNTs-CN_X) and their further reactions

I.Q. Xavier Norberto Lepró Chávez

Thesis presented for the degree of

Master in Applied Sciences,
option in Nanosciences and Nanotechnology

Co-supervised by:

Dr. Mauricio Terrones Maldonado
Dra. Yadira Itzel Vega Cantú

Advanced Materials Division
Potosian Institute of Technology (IPICYT)
San Luis Potosí, S.L.P., México

September 2006

IPICYT

Certificate of Thesis Approval

The thesis "**Attachment of transition metal nanoparticles on nitrogen doped carbon nanotubes (MWNTs-CN_x) and their further reactions**" submitted for the degree of Master in Applied Sciences in the option of Nanosciences and Nanotechnology was developed by **Xavier Norberto Lepró Chávez** and approved on **September 29th of 2006** by the signatories, designated by the Professors Committee of the Advanced Materials Division in the Instituto Potosino de Investigación Científica y Tecnológica, A.C.

Dr. Mauricio Terrones Maldonado
Thesis co-supervisor

Dra. Yadira Itzel Vega Cantú
Thesis co-supervisor

Dr. Fernando Jaime Rodríguez Macías
Committee member

IPICYT

Instituto Potosino de Investigación Científica y Tecnológica, A.C.

Acta de Examen de Grado

COPIA CERTIFICADA

El Secretario Académico del Instituto Potosino de Investigación Científica y Tecnológica, A.C., certifica que en el Acta 018 del Libro Primero de Actas de Exámenes de Grado del Programa de Maestría en Ciencias Aplicadas en la opción de Nanociencias y Nanotecnología está asentado lo siguiente:

En la ciudad de San Luis Potosí a los 29 días del mes de septiembre del año 2006, se reunió a las 17:00 horas en las instalaciones del Instituto Potosino de Investigación Científica y Tecnológica, A.C., el Jurado integrado por:

Dr. Mauricio Terrones Maldonado	**Presidente**	**IPICYT**
Dra. Yadira Itzel Vega Cantú	**Secretaria**	**IPICYT**
Dr. Eduardo Sánchez Cervantes	**Sinodal externo**	**UANL**
Dr. Fernando Jaime Rodríguez Macías	**Sinodal**	**IPICYT**

a fin de efectuar el examen, que para obtener el Grado de:

MAESTRO EN CIENCIAS APLICADAS
EN LA OPCIÓN DE NANOCIENCIAS Y NANOTECNOLOGÍA

sustentó el C.

Xavier Norberto Lepró Chávez

sobre la Tesis intitulada:

Attachment of Transition Metal Nanoparticles on Nitrogen Doped Carbon Nanotubes (MWNTs-CNx) and their Further Reactions

que se desarrolló bajo la dirección de

Dra. Yadira Itzel Vega Cantú
Dr. Mauricio Terrones Maldonado

El Jurado, después de deliberar, determinó

APROBARLO

Dándose por terminado el acto a las 18:50 horas, procediendo a la firma del Acta los integrantes del Jurado. Dando fé el Secretario Académico del Instituto.

A petición del interesado y para los fines que al mismo convengan, se extiende el presente documento en la ciudad de San Luis Potosí, S.L.P., México, a los 29 días del mes septiembre de 2006.

Dr. Marcial Bonilla Marín
Secretario Académico

L.C.C. Ivonne Lizette Cuevas Velez
Jefa del Departamento de Asuntos Escolares

INSTITUTO POTOSINO DE INVESTIGACIÓN CIENTÍFICA Y TECNOLÓGICA, A.C.
IPICYT
SECRETARIA ACADEMICA

Institutional Credits

This thesis was elaborated in the Nanostructures Laboratory of the Advanced Materials Division at the Instituto Potosino de Investigación Científica y Tecnológica, A.C. under the co-supervision of Dr. Mauricio Terrones Maldonado and Dra. Yadira Itzel Vega Cantú.

During the performance of this work, the author had a scholarship from the Consejo Nacional de Ciencia y Tecnología (Register number 183133) and from the Instituto Potosino de Investigación Científica y Tecnológica, A.C.

The graduate program of Applied Sciences with specialization in Nanosciences and Nanotechnology of the Instituto Potosino de Investigación Científica y Tecnológica, A.C. is appointed in the Padrón Nacional de Posgrado of CONACYT.

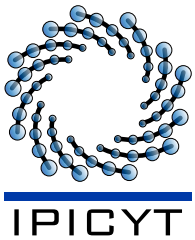

Dedicated to

My family who have been always supporting me.

Attachment of transition metal nanoparticles on nitrogen doped carbon nanotubes (MWNTs-CN_x) and their further reactions

Xavier Norberto Lepró Chávez

Submitted for the degree of Master in Applied Sciences
September 2006

Abstract

The MWNTs-CN_x exhibit important electronic and mechanical properties, that together with its small diameter, make them attractive for sensors production, substances specific filters and as field electrodes. Due to their structure, the MWNTs-CN_x could also play an important role as substrates for the deposition of transition metal nanoparticles that allow to develop new catalysts. Thereby, the possibility of depositing some of this metals on MWNTs-CN_x by a simple method, that does not involve oxidizing treatments in the nitrogen-doped carbon nanotubes, would enable to take advantages of their other properties.

The results obtained from the use of the MWNTs-CN_x as substrates for the transition metal nanoparticles deposits are presented in this work. At first stage, it was achieved an iron (Fe) deposit on the MWNTs-CN_x, that by subsequent treatments produced a new type of hybrid structure composed by N-doped and undoped carbon nanotubes. Furthermore, are discussed the platinum (Pt) nanoparticles deposits that were also obtained in surface of MWNTs-CN_x. Later, the morphological changes observed in the MWNTs-CN_x by their electrochemical treatment or by the adding of titanium (Ti) during their synthesis by chemical vapor deposition (CVD) are explained. Finally, the feasibility of achieving silicon (Si) nanoparticles deposits on the surface of MWNTs-CN_x by potentiometric techniques is also depicted.

KEYWORDS: MWNTs-CN_x | N-doped MWNTs | metal cluster deposition | chemical reactions of MWNTs-CN_x | reactive N-site | platinum (Pt) | iron (Fe) | titanium (Ti) | nylon | silicon (Si) | coaxial hetero-nanocables | junctions | hetero-junctions | CN_x@CNT | coaxial hetero-nanotube | sharp tip-end | branching | voltammetric studies | MWNTs-CN_x as working electrodes (WE) | composites

PALABRAS CLAVE: MWNTs-CN_x | MWNTs dopados con nitrógeno | depósito de cúmulos metálicos | reacciones químicas de MWNTs-CN_x | sitio N reactivo | platino (Pt) | hierro (Fe) | titanio (Ti) | nailon, nilón (nylon) | silicio (Si) | hetero-nanocables coaxiales | uniones | hetero-uniones | CN_x@CNT | hetero-nanotubos coaxiales | extremo terminado en punta | ramificaciones | estudios voltamperométricos | MWNTs-CN_x como electrodos de trabajo (WE) | compositos, materiales compuestos

Acknowledgements

First of all, I would like to thank my advisors, Dr. Mauricio Terrones and Dra. Yadira I. Vega Cantú for their guidance and help during the development of this thesis. In the same way, I am grateful to Dr. Fernando Jaime Rodríguez Macías for his comments and helpful suggestions along this thesis work.

I also would like to acknowledge M.Sc. Grisel Ramírez Manzanares and Ing. Daniel Ramírez González for their valuable help during sample's characterization. Similarly, I want to thank Dr. Fernando Hernández Ramírez for his valuable comments about the electrochemical part of this work. I also appreciated the access to specialized facilities provided by Dr. Norberto Casillas (UdeG), Dr. Maximiliano Bárcena (UdeG), Dr. Francisco Medellín (UASLP), CHREM (in ASU) and NIMS (Japan), where some experiments using diverse techniques could be performed and characterization as well.

I am thankful to all my laboratory colleagues but, in particular, to my friends Adalberto Zamudio, David Meneses, Ana Laura Elías and Eduardo Cruz for their support, advices and confidence in both scopes, academic and otherwise. I thank to Aurora Espinoza, Jaime Pérez, Pily Monsiváis, Pedro Palomares, Vianney Bojórquez, Leonardo Chávez, José M. Romo and Julio Rodríguez who helped me in diverse ways during my stay here.

To my friends known along my graduate studies, such as Raymundo Torres, Sandrita Chávez, Pablo Treviño, Alejandro Juárez, Sandra Pérez, Josefat, Candy Ramírez, Yadira Díaz, Mayte Cervantes and Víctor Mata.

To my parents and old friends who, in some way have been close to me during this last two years.

Finally, I want to thank to CONACYT for the master's scholarship (183133) that allowed me to successfully finish this stage of my life.

Xavier N. Lepró

Contents

List of Figures

List of Tables

Chapter 1

Carbon Nanostructures: An Overview

Carbon is one of the most abundant elements in nature. Its chemical symbol is C and its atomic number 6. Due to its electronic configuration, $1s^2 2s^2 2p^2$, carbon can exhibit a divalent and tetravalent behavior. It is a remarkable element for many reasons. For instance, it has a great affinity for bonding with other carbon and small non-metal atoms. Because of these properties, carbon is known to form nearly ten million different compounds that constitute the basis of all living organisms on Earth.

Before 1985, only three allotropic forms of carbon were known: *amorphous carbon, graphite* and *diamond* (see fig. 1.1), where the latter is a fully tetra-coordinated material that makes it the hardest natural mineral. However, in that year, a new form of carbon was discovered by H. Kroto *et al.* [1], the *fullerene*, C_{60}, (fig. 1.1*d*) which is a molecule belonging to a vast family of *C cages* that were later synthesized in bulk amounts. This discovery motived other scientist to search for new structures and a novel branch of carbon science emerged: *carbon nanoscience.*

1.1 Carbon Nanotubes

Graphite is composed of hexagonal layers (fig. 1.1*b*), and each layer (graphene) could be curled and curved so as to form tubules and fibers. These fibers can

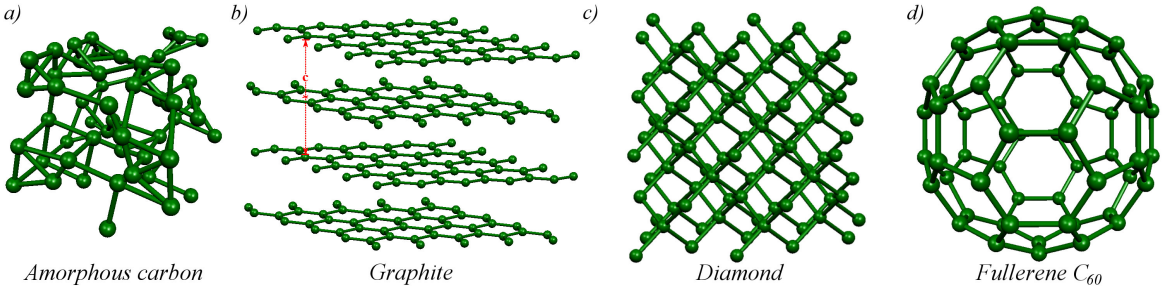

Figure 1.1: Carbon allotropes. Molecular models of different carbon allotropes. Amorphous carbon (**a**) does not present a characteristic crystalline structure. Graphite (**b**) consists of parallel sheets of carbon atoms, each containing hexagonal arrays of atoms. Each atom has three nearest neighbors (within the sheets) joined by sp^2 hybridized covalent bonds of 1.415 Å. The sheets are held together by Van der Waals forces (in an "ABAB..." stack) and are separated from each other by a distance of 3.35 Å. Diamond (**c**) is a a very rigid structure due its fully tetra-coordinated bonding. Each carbon atom in this structure has four nearest neighbors separated by a covalent bond of 1.5445 Å with an angle of 109.5° among them. Fullerene C_{60} (**d**) is a discrete structure of carbon formed by 60 carbon atoms and is the smallest fullerene in which two pentagons are not next to each other. The structure of C_{60} is a truncated icosahedron, which resembles a round soccer ball. The C_{60} molecule possess two bond lengths. The 6:6 ring bonds (between two hexagons) can be considered "double bonds" and are shorter than the 6:5 bonds (between a hexagon and a pentagon). Other fullerenes are formed by closed cage molecules of C_{2n} with n = 12,13,14...; C_{70}, C_{78} and C_{540} are some examples of them. [2] Structural data of some allotropes were obtained from [3].

exhibit diverse structures and diameters as a function of the specific arrangement of the graphene sheets. If their diameter is small enough to fit in the nanometer scale (1 nm = 10^{-9} m), a nanofiber is produced. Carbon nanofibers could be categorized by the angle in which the graphene layers arrange with respect to the filament axis, such as *stacked* (array of parallel sheets normal to the filament axis), *cup-stacked* (wedge shaped structures or cones along the filament axis) and *nanotubular* carbon fibers (coaxial cylinders) (see fig. 1.2). When the tubular graphene walls are parallel to the filament axis, the fibers are commonly called *carbon nanotubes*, whereas the first two cases are known under the generic name of *nanofibers*. [4] Some researchers consider that carbon nanotubes and fullerenes constitute another allotropic form of carbon.

Even carbon nanotubes (CNTs) were first reported in 1976 by Oberlin and Endo [5], was until their subsequent structural identification in 1991 by Ijima [6] when they began to be extensively studied from both theoretical and experimental approaches. The latter author reported that highly graphitized carbon nanotubes

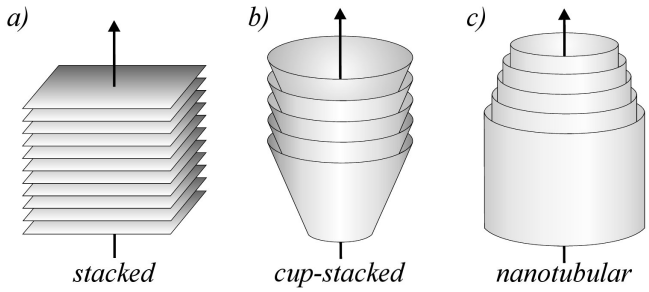

Figure 1.2: Different types of carbon fibers. Carbon fibers can be classified according to the arrangement of graphene sheets with respect to the principal axis. Nanotubular carbon nanofibers are named *carbon nanotubes*. Adapted from [4].

formed by an arc discharge between two graphite electrodes, contained multi-coaxial tubes (now known as multiwalled carbon nanotubes). [6] These tubular structures exhibit mechanical, chemical, electronic, magnetic and transport properties that can be considered unique making CNTs a technologically important material for fabricating various electronic and mechanical devices. [4] Their small diameter (1 – 70 nm) and length in the order of micrometers, centimeters [7] and recently meters of yarns of them [8], allows to consider these systems as one-dimensional [9] and highly anisotropic structures. CNTs exhibit high mechanical strength and thermal conductivity along their axis and can also possess high electrical conductivity in the same direction. [4] The small amount of dangling bonds in their structure, and the presence of few open edges makes them chemically inert. For this reason, chemical species tend to be only physically absorbed on a perfect nanotube surface. So, in order to establish covalent bonds between molecules and the nanotube surface, defect sites need to be introduced. [4]

1.1.1 Single-walled Carbon Nanotubes (SWCNTs)

Carbon nanotubes are classified in two types: single-walled (SWCNTs) and multi-walled (MWCNTs); according to the number of coaxial graphene layers involved in the structure. A SWCNT can be visualized as a graphene sheet rolled around a principal axis thus forming a cylinder. The direction in which this graphene layer is rolled, known as *chirality*, is represented by a *chiral vector*, $\mathbf{C}_h$ composed by a linear combination of integer multiples, n and m, of the unit vectors $\mathbf{a_1}$ and $\mathbf{a_2}$ defining the hexagonal network (see fig. 1.3). Each integer pair (n, m) represents the

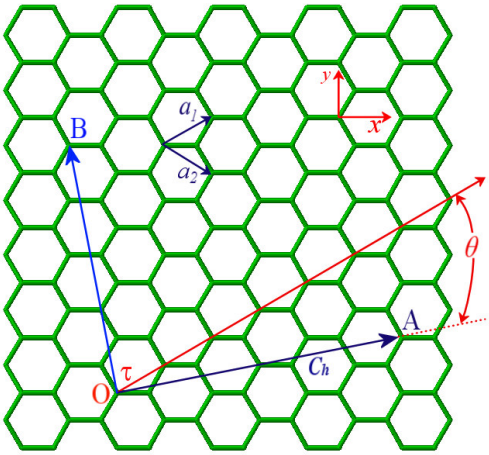

Figure 1.3: Rolling a graphene sheet. 2D graphene sheet that shows the vector which specifies the chirality of a nanotube. The chiral vector **OA** or $\mathbf{C}_h = n\mathbf{a_1} + m\mathbf{a_2}$ is defined on the honeycomb lattice by unit vectors $\mathbf{a_1}$ and $\mathbf{a_2}$ and the chiral angle θ measured respect to zigzag axis ($\theta = 0°$). The lattice vector **OB** perpendicular to $\mathbf{C}_h$ and indicates the direction of the length of nanotube. This diagram is constructed for a (n,m)=(4,2) chiral nanotube. Adapted from [12].

length of the unitary cell that defines a particular nanotube structure. The length L of the chiral vector is directly proportional to the tubule diameter (d_L) by the relation: [10]

$$d_L = \frac{L}{\pi} = \frac{\sqrt{n^2 + nm + m^2}}{\pi} a \tag{1.1}$$

where a is the length of the unit vector $\mathbf{a_i}$, that is, the lattice parameter. In the case of graphene $|\mathbf{a_1}| = |\mathbf{a_2}|$ and their magnitude a takes the value of 2.46 Å. The narrowest diameter for a nanotube found experimentally corresponds to 3.3 Å. [11] Despite theoretical predictions stating that the smallest possible SWCNT should be capped with a C_{60} hemisphere in order to avoid dangling bonds, and therefore, the narrowest and most stable tube must have a diameter of the order of 7 Å. [10]

The angle between $\mathbf{C}_h$ and the zigzag direction of the honeycomb lattice (n,0) is called *chiral angle*, θ, and it is also important for specifying particular kinds of SWCNTs.

This chiral angle θ, can be calculated by the relationship: [10]

$$\tan\theta = \frac{\sqrt{3} \cdot m}{2n + m} \tag{1.2}$$

Three types of carbon nanotubes can be defined according to their chirality: **zigzag** ($\theta = 0°$, $m = 0$), **armchair** ($\theta = 30°$, $m = n$) and **chiral** ($0° < |\theta| < 30°$, $m \neq n$) (shown in fig. 1.4). While the first two possess mirror symmetry, the chiral

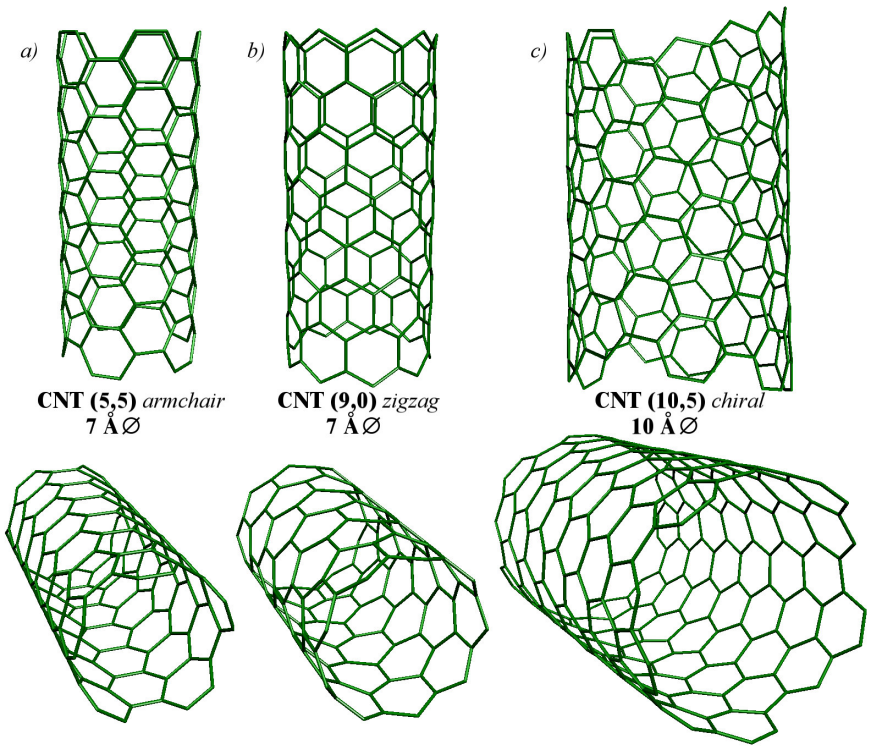

Figure 1.4: Different chiralities in CNTs. Examples of carbon nanotubes of different chirality. The Structures were obtained from the implementation and adaptation to Fortran 90 of the code made by R. Saito in Fortran 77 (October 16th, 1995), published in [12].

does not. The chirality modifies the density, the lattice structure and the *electronic density of states (DOS)* in carbon nanotubes, thus giving them different electronic properties. Consequently, a zigzag SWCNT is a semiconductor (with a bandgap typically in the order of 0.4 – 0.7 eV), whereas all armchair tubes are metallic. Theoretical studies show that a SWCNT is metallic if the value $|n - m|$ is divisible by 3, otherwise a carbon nanotube is semiconductor. Therefore, when nanotubes are formed with random values of n and m, we would expect that two-thirds of them would be semiconducting, whereas the remaining third would be metallic. [10; 13; 14] Furthermore, the bandgap in semiconducting tubes is predicted to scale inversely with the diameter [14].

Upon cooling, the electrical resistance of a metallic nanotube decreases. This can be attributed to the reduced scattering of electrons by lattice vibrations. Due to a reduced number of carriers that are able to overcome the bandgap, semiconducting

Table 1.1: Physicochemical properties of carbon nanotubes, taken from [4].

Mechanical Properties	
Young's modulus (MWCNTs)	∼1 – 1.2 TPa
Young's modulus (SWCNTs ropes)	∼1 TPa
Tensile strength (SWCNTs ropes)	∼60 GPa
Electrical Properties	
Typical Resistivity of MWCNTs	10^{-6} Ω m
Maximum current density	$10^7 - 10^9$ A/cm^2
Quantized conductance, theoretical\measured	$(6.5\ \text{k}\Omega)^{-1}$\$(12.9\ \text{k}\Omega)^{-1}$
Thermal properties at room temperature	
MWCNTs Thermal conductivity	>3000 W/m·K
SWCNTs Thermal conductivity	1750-5800 W/m·K
Electronic Properties	
SWCNTs band gap:	
$\frac{\lvert n-m\rvert}{3} = integer$	0 eV
$\frac{\lvert n-m\rvert}{3} \neq integer$	0.4 – 0.7 eV
MWCNT bandgap	∼ 0 eV

nanotubes exhibit the opposite behavior; that is, with decreasing temperature their resistance increases. [14]

1.1.2 Multiwalled Carbon Nanotubes (MWCNTs)

Multiwalled carbon nanotubes (MWCNTs) contain several concentric graphene cylinders with interlayer spacings in the range of 0.34 and 0.39 nm. The intershell spacing in a MWCNT decreases as we move away from its principal axis, that is, as we increase the diameter of the coaxial graphene cylinder, the graphene layers tends to be closer (becoming closer to graphite which has an interlayer spacing of 0.335 nm). Geometrical constraints in forming seamless graphene cylinders cause the layers to be uncorrelated with respect to one another. This contrasts to crystalline graphite, which exhibits perfect "ABAB..." layer stacking. Thus, MWCNTs tend to exhibit properties of turbostratic graphite, in which the layers are essentially uncorrelated and separated by distances larger than 0.335 nm. Therefore, every single carbon nanotube within a MWCNT is expected to have a different chirality. [4]

Table 1.2: Properties of SWCNTs compared with other materials. Taken from [15].

Property	SWCNTs	By comparison
Size	0.6 – 1.8 nm in diameter.	Electron beam lithography can make lines of 50 nm of width.
Density	1.33 – 1.40 g/cm^3.	Aluminum exhibits a density of 2.7 g/cm^3.
Tensile strength	On the order of 45 thousand millions of Pa.	Steel iron alloys break around 2 thousand millions of pascals.
Resilience	Can be bended in high angles and returns to their original state without damage.	Metals and carbon fibers break under similar efforts.
Current-carrying capacity	Estimated in 1000 millions of A/cm^2.	Cu wires burn when conducting 1 million of A/cm^2.
Field emission	Can activate phosphor with 1 – 3 V if both electrodes have a separation of 1 μm.	Molybdenum tips require fields of 50 – 100 V/m and have a very limited half-life.
Thermal conductivity	It is predicted that is as high as 6,000 V/m $\cdot$ K at 298 K.	Almost pristine diamond conducts 3,320 V/m $\cdot$ K.
Thermal stability	Stable up to 2,800°C at vacuum and 750°C in air.	Metallic wires in microchips melt between 600 – 1000°C.

Although every cylinder could exhibit a distinctive chirality in MWCTNs, the electric current is transported through the outermost shell only. For large diameter tubes, the band gap approaches 0 eV. Therefore, this outer nanotube is essentially, a non-semiconductor type. [4]

Some of the properties of CNTs measured so far are shown in table 1.1, and comparisons with those of common materials used at present are in table 1.2.

1.1.3 Synthesis of carbon nanotubes

Other synthesis methods have been described apart from the arc-discharge method used for bulk production of carbon nanotubes reported by Ebbesen and Ajayan in 1992. [16] This technique is similar to that used for producing fullerenes —which consist in generating an arc-discharge between two graphite electrodes within inert atmosphere—. At present, carbon nanotubes can also be produced by hydrocarbon thermolysis over catalysts —also called chemical vapor deposition (CVD)—, gas-phase chemical-vapor deposition process in high pressure carbon monoxide (∼30 – 50 atm), (HiPco), laser vaporization of graphite, and by electrolysis

of graphite electrodes in molten ionic salts. Characteristics of these synthesis methods have been described in the literature. [4; 14; 16–26]

In general, highly crystalline SWCNTs can be produced by high temperature methods (such as arc-discharge and laser ablation) and MWCNTs by medium and high temperature methods (mainly CVD and, in low yield rates, by electrolysis). Despite these wide range of possibilities, it is still necessary to scale up the methods in order to achieve industrial production (ton/day). Medium temperature methods seem to have economical advantages for this purpose.

1.2 Nitrogen-doped multiwalled carbon nanotubes (MWNTs-CN_x)

The idea of doping carbon nanotubes is attractive because it is possible to control their electronic and chemical properties by the addition of electron donors or acceptors. Doping can be achieved by replacing some of the carbon atoms in the graphitic network of the nanotubes with other elements. In this case, the doping is called *substitutional*. It is also possible to introduce different elements by chemical functionalization of the nanotube surfaces. [9] Exohedral doping is used in SWCNT bundles that intercalate alkali metals such as Li, K, Rb and Cs. Metals of the p block such as Al and Co, halides (Br, I and F) and non-metals like B and N, have also been tested for doping CNTs. [9] In this thesis, only nitrogen-doped carbon nanotubes and their possible applications will be discussed in detail.

Small amounts of nitrogen, less than 15%, have been introduced into carbon nanotubes successsfully. The use of triaminotriazine (melamine, $C_3H_6N_6$) as MWNT-CN_x precursor in a CVD setup has produced arrays of "corrugated" carbon tubular structures (see fig. 1.5) with less than 7% of nitrogen content. It is important to note that the degree of perfection within the tubes decreases as a result of the incorporation of nitrogen in the carbon lattice. [16]

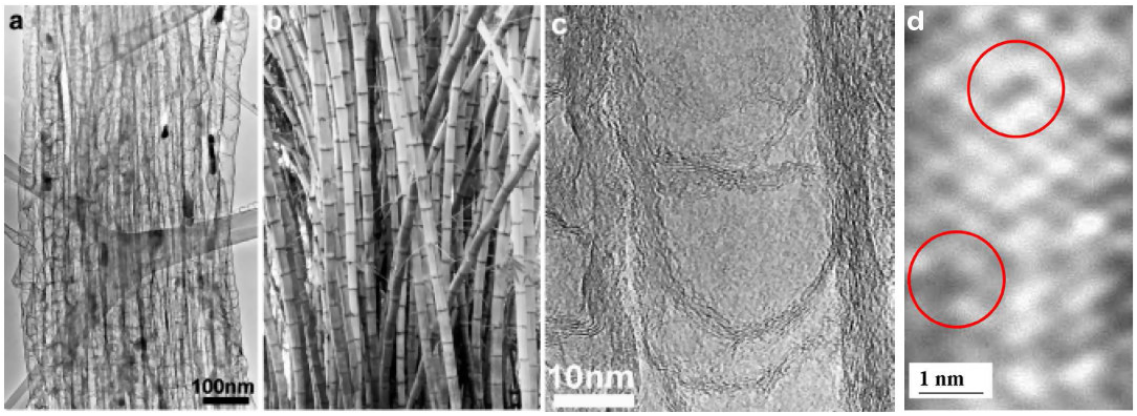

Figure 1.5: Images of MWNTs-CN_x. a) TEM image of a region that shows high density packed and aligned MWNTs-CN_x. **b)** Morphologically they have a "bamboo-like" structure due to their compartment structure. **c)** HRTEM image of an MWNT-CNx exhibiting corrugation, interlinkage and compartments. **d)** Atomic resolution STM image of an area in a nanotube with diameter of 20 nm exhibiting vacancies as holes (inside red circles) which indicates existence of pyridine-like bond. Taken from [16; 27].

Nitrogen-doped multiwalled carbon nanotubes (MWNTs-CN_x) are of interest because nitrogen atoms inject electrons into the nanotube lattice, resulting in an enhancement of their conducting properties. For pure carbon nanotubes, the valence and conduction band features appear to be symmetrical around the Fermi level (E_f), while for the N-doped nanotube, a sharp peak in the conduction band occurs at ca. 0.18 eV experimentally (see fig. 1.6). The presence of these electronic states close to the E_f indicates that MWNTs-CN_x may be metallic, and exhibit donor states. [16] Lim *et al.* by ultraviolet photoemission spectroscopy (UPS) on MWNTs-CN_x observed that nitrogen doping resulted in enhancement of the leading edge of the valence band in a large binding energy region (up to 3 eV) associated to the N lone pair. This therefore would include a donor level near the bottom of the conduction band, raising the Fermi level. X-ray photoelectron spectroscopy (XPS) performed on MWNTs-CN_x and MWCNTs allowed these researchers to also find a 0.5 eV reduction in the work function of MWNTs-CN_x when compared with that of the MWCNTs. [28] One implication of this effect is, for example, that the field emission of aligned MWNTs-CN_x with high concentration of N, shows better performance when compared to undoped carbon nanotubes. [9]

Terrones M. *et al.* found by electron energy loss spectroscopy (EELS) analysis

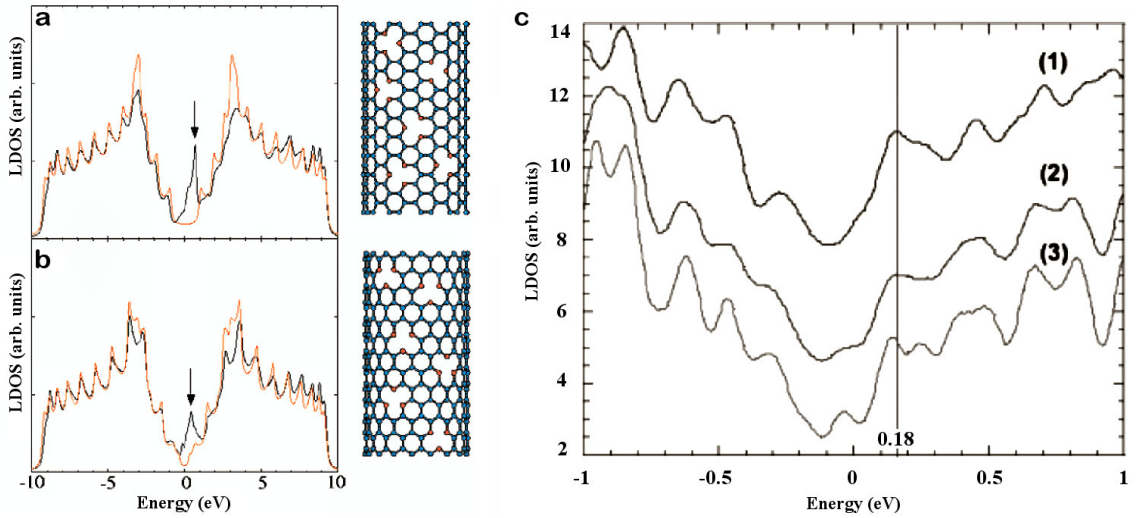

Figure 1.6: Theoretical and experimental LDOS CN_x and CNT The *local density of states* (LDOS) of N-doped (black curve) and undoped (red curve) carbon nanotubes are compared. In CN_x theoretical LDOS are associated with a pyridine like structure of N-doping in (**a**) armchair (10,10) and (**b**) zigzag (17,0) nanotubes. A random but homogeneous doping (N, red spheres; C, blue spheres) is adopted in both cases, as illustrated on the right-hand side of the figures. According with the calculations of the authors, the pyridine-like structure of N-doping is responsible for the prominent donor-like features close-above the Fermi energy. Note that the semiconducting (zigzag) nanotube becomes metallic after introducing N in the carbon lattice. **c)** Tunneling spectra acquired on a straight and clean section of an N-doped carbon nanotube. Spectra (1)-(3) were taken at different locations along the surface but close to a "hole" as shown in fig. 1.5*d*. Note the peak at 0.18 eV in all spectra. Images taken from [16; 27].

on MWNTs-CN_x a splitting in the π^*-type peak of the nitrogen K-edge, suggesting two types of bonding between N and C within the hexagonal network. Using XPS and atomic resolution of scanning tunneling microscopy (STM), these authors were able to determine that N is bonded in two ways: pyridine-like bond (N bonded to two C atoms) or substitutional doping (N bonded to three carbon atoms). When the overall N content increases within these structures, the number of graphitic walls of the MWNTs-CN_x decreases and the proportional amount of pyridine-like N also increases, keeping the number of substitutional N doping almost constant. Pyridine-like N promotes cavities and rugosity on the graphitic framework. This was observed by atomic resolution STM analysis (see *d* in fig. 1.5 and fig. 1.7) and high resolution transmission electron microscopy (HRTEM) studies. [16]

Similarly, Czerw *et al.* found that N-doping in pyridine-like sites within the carbon nanotube lattice, resulted in the introduction of electronic states in the

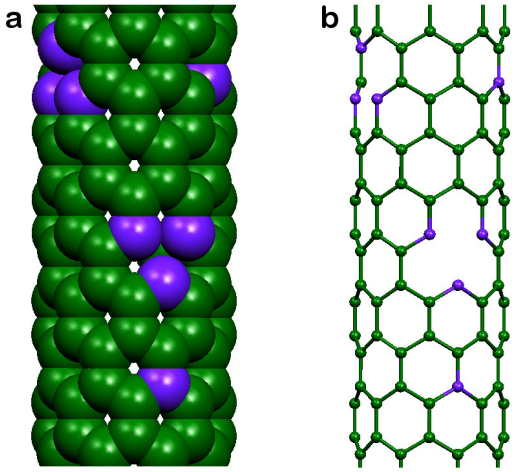

Figure 1.7: Structure of a CN_x nanotube. Representations of N defects on CNTs. Nitrogen atoms are in purple, carbon atoms in green. Structure **b** is displayed for clarity. Substitutional and pyridine-like doping are shown. It is remarkable how the pyridine-like doping causes a vacancy of one carbon atom in graphene lattice. Note the similarity between **a** and the experimental STM image **d**, shown in fig. 1.5.

conduction band, including a large electron donor state (n-type) lying approximately 0.2 eV above the Fermi level [27]. Their findings are in a good agreement with the experimental data obtained using STS (scanning tunneling spectroscopy) reported by Terrones *et al.* [16] and subsequently XPS and UPS analysis performed by Lim *et al.* [28].

Kaun *et al.* reported *ab initio* studies of current-voltage characteristics of carbon nanotubes with substitutional nitrogen doping. They found that for zigzag semiconducting tubes, doping with a single N atom increases the current flow, and for small radius tubes, it narrows the current gap. These researchers pointed out that one N-doping impurity per nanotube unit cell would generate a metallic transport behavior. However, for armchair metallic nanotubes with substitutional doping, a reduction occurred because of the elastic backscattering caused by the N impurity. [9] A similar calculation was reported by Terrones *et al.* with ca. 5.5% N content in nanotube lattice and they showed that, although N was the responsible for an increase in the Fermi level, and for the presence of electronic states in the conduction band, this kind of substitution by itself, was unable to explain the strong donor signal observed experimentally. [16; 27]

Low nitrogen doping does not significantly modify the mechanical properties of carbon nanotubes. Several research groups are currently studying the use of nitrogen sites as anchoring links for covalent bonds (e.g. peptidic bonds) through different chemical reactions. Research on the direct attachment of metallic clusters to nitrogen in MWNTs-CN_x has not been reported yet and all approaches until now, have been attempted via the covalent functionalization of MWNTs-CN_x.

1.3 Attachment of metallic clusters on MWCNTs

The morphology and size of carbon nanotubes suggest that they can be used as substrates for heterogeneous catalysis and as templates for the creation of thin wires or tubular structures by coating them with metals. The simplest way of doing this would be melting a metal on the surface of the nanotubes. However, MWCNTs are not wet by liquids with a surface tension larger than 100-200 mN/m, [29] which excludes most of the metals (see table 1.3). Therefore, one of the most viable approaches to metal coat carbon nanotubes is through chemical reactions on both the inner and outer surfaces. [29] Nevertheless, the chemical stability of carbon nanotubes imposes a severe hurdle for the methods allowing its selective and covalent functionalization. [14] This low chemical reactivity in the sidewalls is mainly because of the large diameter of the nanotubes which makes them very similar to inert graphite.

Table 1.3: Surface tension of some metals of *d* block. Source [30].

Surface tension of metals	
Metal	γ, 10^{-3}J/m^2
Ag (silver)	126
Au (gold)	132
Cu (copper)	177
Mn (manganese)	206
Ni (nickel)	255
Fe (iron)	204
Pd (palladium)	209
Pt (platinum)	240

Among the physical techniques used for obtaining a metal coating on SWCNTs are sputtering and electron-beam deposition. Deposits of Ti, Ni, Pd, Au, Al and Fe have been reported by the use of this last technique. [31]

1.3.1 Chemical functionalization of carbon nanotubes

Narrow carbon nanotubes are highly polarizable and smooth-sided molecules with attractive interactions of 0.5 eV per nanometer of tube-to-tube contact. Because of these extreme cohesive forces, SWCNTs exist as bundled structures, often called ropes. This causes pristine carbon nanotubes to agglomerate and exhibit limited solubility. Covalent functionalization provides researches with the ability to manipulate these entities in typical organic solvents or even in solvent-free conditions. [32] At present, functionalization methods are the most used techniques for attaching metallic clusters on carbon nanotubes.

Although covalent functionalization schemes for MWCNTs have been proposed, most of the methods developed until now have considered only SWCNTs. These functionalization methods can be classified according to Balasubramanian and Marko [14] in: *thermally activated chemistry, electrochemical modification, photochemical functionalization, free-radicals reactions, by using diazonium salts reagents and other typical organic routines for graphite functionalization.* All these methods have one thing in common: a highly reactive intermediate is necessary to attack the carbon nanotubes [32] and to introduce defects in their structure, so that covalent bonding can be promoted.

Before describing the functionalization methods for carbon nanotubes, it could be of interest to point out some details about their chemical reactivity and its relation with their ideal structure. The caps of ideal SWCNTs possess higher reactivity than the sidewalls because of their high curvature (presence of pentagons) and the transition of the hybridization of C atoms from sp^2 to sp^3-like. The curvature on the sidewalls of narrow SWCNTs makes them more reactive when compared to planar graphene sheets, and correspondingly, the binding energy of atoms or functional

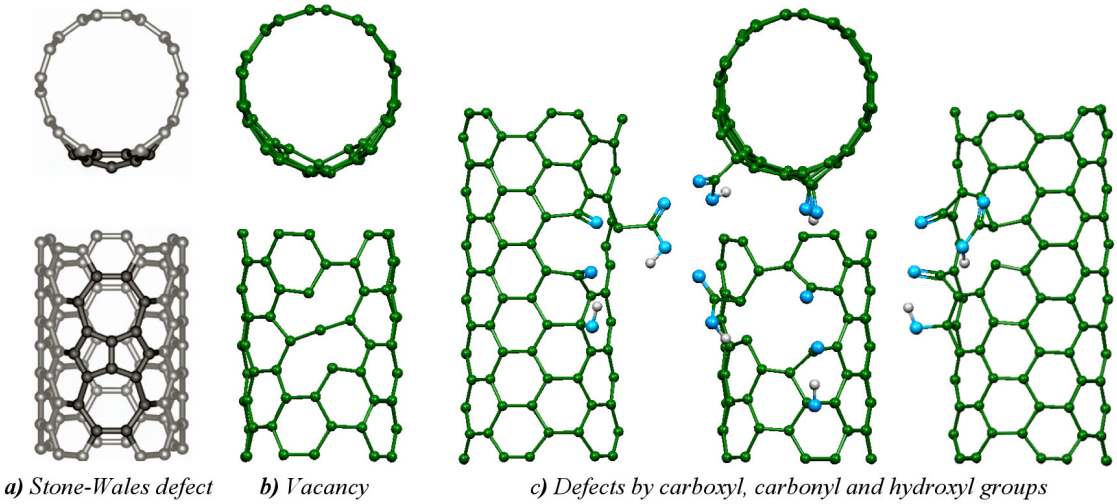

Figure 1.8: Kinds of defects in CNT. a) Illustration of the *Stone-Wales or 7-5-5-7 type defect*, showing also its effect on the sidewall of a SWCNT. This is a proposed mechanism for the releasing of stress in strained SWCNTs. These defects act as nucleus of relaxation for both plastic and brittle cleavage of nanotubes [11], however they are less common than vacancies or carboxyl group generation (in an highly oxidizing medium). Image taken from [14]. **b)** *Vacancy* in a SWCNT. This image shows the change of morphology in the nanotube and the creation of more reactive sites for chemical reactions. **c)** *Carboxyl, carbonyl and hydroxyl groups* generated from the sidewall of nanotube. Oxygen atoms are in slight blue, hydrogen in white and carbon in green color. These kind of functional groups are expected to appear after a wet acid treatment of the carbon nanotubes (H_2SO_4/HNO_3). It is notable the amount of defect generation in the sidewall of nanotubes consequently increasing the chemical reactivity in those regions. Images *b* and *c* were obtained after *Ab-initio* geometry optimization performed by the software code *Siesta*. [34–36]

groups on the sidewall should increase with decreasing the tube diameter. This tendency is supported by theoretical studies related to the bonding of alkyl radicals to sidewall of SWCNTs. [14; 33] Contrarily, the concave curvature of the inner surface of nanotube, besides its inaccessibility, results in a very low reactivity towards addition reactions. However we must stress that carbon nanotubes are not perfect structures; typically, around 1 - 3% of carbon atoms are located in a defect site, of which the most common are vacancies and *Stone-Wales type defects* consisting of two pairs of pentagons and heptagons joined. This is the reason for being referred as 7-5-5-7 defect. Stone-Wales type defects leads to a local deformation of curvature (see fig. 1.8) that induces a more favorable behavior to addition reactions. [14]

The first functionalization method dealing with *thermally activated chemistry* was developed for the oxidation of SWCNTs using extensive ultrasonic treatments

in a mixture of nitric (HNO_3) and sulphuric acids (H_2SO_4). Such drastic conditions led to the opening of tube caps and to the shortening of nanotubes with open edges highly functionalized with carboxyl groups. Under less extreme conditions, such as refluxing in HNO_3, shortening of tubes can be minimized, and functionalization is limited to defect sites and caps. Nanotubes functionalized in this way tend to retain their electronic and mechanical properties. [14]

In addition, *electrochemical modification of carbon nanotubes* is based on applying a constant potential (potentiostatic methods) or current (galvanostatic methods) to CNT electrodes in order to obtain, depending on the reagents in solution, covalent or non-covalent bonded species to the sidewalls of CNTs. [14]

Just one case of *photochemical functionalization* of SWCNTs has been reported to date. This is the sidewall osmylation, that in dry conditions can be done reversibly. In this reaction scheme, OsO_4 is put in contact with CNTs and then the mixture is irradiated with UV-light in order to cycloadduct the metallic oxide on CNTs. [14].

Free-radical methods are based in stabilizing electrons onto carbon nanotubes to confer them a negative charge and making them more reactive. This technique allows, among a variety of possibilities, the use of carbon nanotubes as anions than can react with alkali metals forming compounds similar to salts. [37]

There have also been reports of SWCNTs sidewall functionalization by fluorination [38; 39] followed by subsequent interactions with alkyl/lithium and Grignard reagents or diamines, and the direct reactions on SWCNTs with aryl diazononium salts [40], azomethine ylides, nitrenes and organic radicals. [41–43]

Other methods used in organic chemistry and graphite functionalization can be found in specialized chemical literature and adapted for carbon nanotubes. Other common methodologies for sidewall functionalization that can be classified within these methodologies are resumed in [32; 42; 43] and references therein.

Spectroscopic techniques such as absortion and resonance Raman spectroscopy are employed to verify that the functionalization is covalent and occurs on the

sidewalls. Subsequently, thermogavimetric analysis (TGA) and X-ray electron spectroscopy (XPS) are used to determine the degree of functionalization. Imaging techniques such as atomic force microscopy (AFM), scanning electron microscopy (SEM) and transmission electron microscopy (TEM) are also used to analyze the nanotube diameters, lengths and morphologies. [32]

1.3.2 Attachment of metallic clusters on SWCTNs and MWCNTs

Metal coatings on the surface of carbon nanotubes have been obtained by diverse methods. A first attempt was reported in 1994 by Planeix *et al.*, using ruthenium 2,5-pentanedionate ($Ru(C_5H_7O)_3$) to decorate raw SWCNTs suspended in dry toluene. After vacuum evaporation, the resulting solid was treated for 3h under nitrogen (523K) and then the metal was reduced for 1h in dilute hydrogen (H_2/N_2 = 10/90 mol). A homogeneous distribution of metallic clusters on the nanotubes was achieved. [44]

Wet oxidation with nitric acid (HNO_3) is one of the most used techniques for functionalizing carbon nanotubes. In this method, the carbon nanotube surface is oxidized, thus promoting the formation of hydroxyl (–OH), carboxyl (–COOH), and carbonyl (>C=O) groups. [45] These species are capable of ion exchange in the system CNT–COOH where the proton (H^+) is replaced by a metallic ion M^+ according to the reaction R 1.1.

$$\mathrm{CNT{-}COOH + M^+X^- \rightleftharpoons CNT{-}COOH^-M^+} \qquad \text{(R 1.1)}$$

Applications of this procedure are wide ranging, Ebbesen *et al.* (1996), decorated SWCNTs with yttrium putting a solution of tris(cyclopentadienyl)yttrium(III), $I(C_5H_5)_3$, in contact with carboxylated nanotubes previously dispersed in dry toluene. [29]. In the same year, Satishkumar *et al.* reported small clusters (1 nm $\leq$ $\varnothing$ $\leq$ 7 nm) of gold (Au), platinum (Pt) (of diameters less than 3 nm)

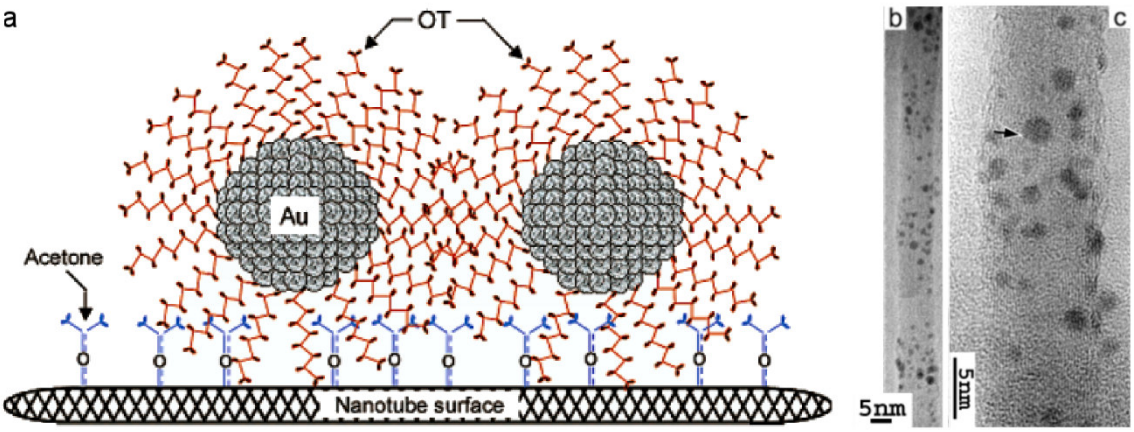

Figure 1.9: Anchoring of capped Au nanoparticles to acetone activated MWCNTs nanotubes. **a)** Schemmatic sketch illustrating the proposed mechanism of attachment of octanethiol (OT)-capped Au nanoparticles to acetone activated MWCNTs. Dashed lines in acetone molecules illustrate that acetone is not attached to nanotubes by C=O type bonds. Its believed acetone is adsorbed to nanotube walls via C–O–C type bonds or resonance structures, in configurations where the terminal methyl groups point away from the nanotube surfaces. **b)** and **c)** HRTEM images of deposited Au clusters on SWCNTs. Taken from [45].

and silver (Ag) deposited on carboxy-SWCNTs (obtained from wet acid treatment) when reacting with $H[AuCl_4]$, $H_2[PtCl_6]$ and $Ag[NO_3]$ respectively. Their results suggested that the metal nanoparticles were deposited on the acidic sites (shown in reaction R 1.1) homogeneously dispersed all over the surface of nanotubes. This method differs from those used for metallic decoration on oriented graphite crystals where, the metal clusters were preferentially deposited along dislocations and grain boundaries. [46]

In the same way, Lordi *et al.* (2001) made an *in situ* reduction of $K_2[PtCl_4]$ followed by an ion exchange in order to add Pt clusters to SWCNTs via an attachment through carboxyl groups. The same year, Azamian *et al.* anchored nanoclusters of Au on SWCNTs using thiamides obtained from a chemical transformation of the carboxylic groups present in nanotube surface. [45] Meanwhile, Haremza *et al.* (2002) attached aminade CdSe nanocrystals to SWCNTs with acyl chloride groups in their sidewalls (this by the reaction of $SOCl_2$ on carboxylated SWCNTs). [47]

Subsequently, in 2003, Ellis *et al.* anchored Au nanoclusters of 1 – 3 nm in diameter on outer walls of highly crystalline multiwalled-carbon nanotubes by

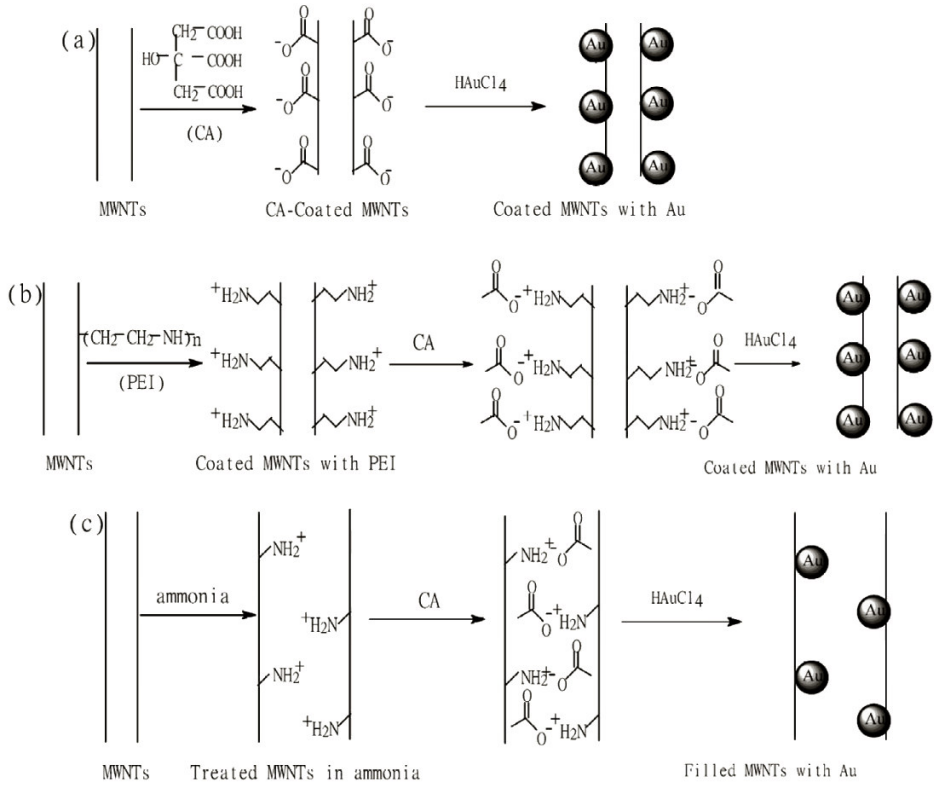

Figure 1.10: Selective coating of Au nanoparticles. Schematic view of the process for selective attachment of Au nanoparticles on the inner or outer side wall of MWCNTs. Method suggested by Linqin Jiang *et al.* Taken from [48].

hydrophobic interactions between octanethiols capping the metallic clusters and the acetone activated sites in MWCNTs (see fig. 1.9). [45] The same year, L. Jiang *et al.* achieved an effective and selective deposit of Au nanoclusters with 10 nm in diameter on inner or outer surfaces of MWCNTs —using NH_3 as a crucial step in the reaction procedure— towards an interaction between carboxylic groups and gold particles formed from $H[AuCl_4]$. A scheme of their proposed method is depicted in fig. 1.10. [48]

Soon after, Liu *et al.* reported another kind of attachment of gold nanoparticles on surfaces of non-oxidized multiwalled carbon nanotubes using bridge molecules, in particular, a bifunctional molecule, PHT (17-(1-pyrenil)-13-oxy-heptadecanethiol). In this case, $\pi - \pi$ interactions between π electrons of the pyrenil group in one end and the walls of carbon nanotubes are responsible for the non-covalent binding with MWCNTs. Meanwhile, the thiol end of PHT binds to the gold nanoclusters. [49]

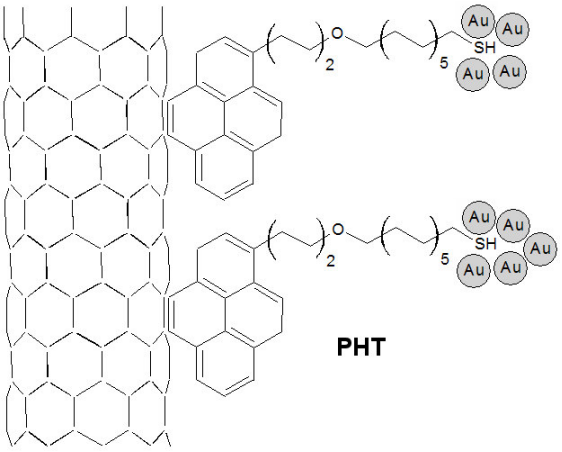

Figure 1.11: Chemical Structure of PHT for assembling of Au on MWCNTs. Schematic attachment of Au nanoparticles on MWCNTs by self assembling process through PHT proposed by Liu *et al.* Adapted of [49].

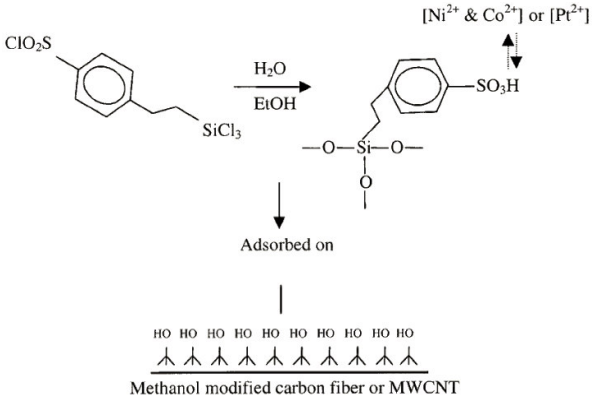

Figure 1.12: Ionic interchange reaction for silane derivative in MWCNTs. Shematic reaction of hydrolization of silane derivative that polymerizes becoming a sulfonic acid-silicate layer onto MWCNTs. This layer is able to exchange protons (H^+) with of Ni^{+2}, Co^{+2}, and Pt^{+2} ions. Taken from [50].

The reader could refer to fig. 1.11 for more clarity.

In 2003, X. Sun *et al.* attached Pt nanoparticles of 1.2 ± 0.3 nm in diameter to MWCNTs synthesized from Co-Ni deposited on carbon paper. This was achieved by pre-treating MWCNTs with methanol followed by their immersion in a solution containing 0.04 M $PtCl_2$ in $6\%^{v}/_{v}$ ethanol/water and $1\%^{v}/_{v}$ of a silane derivative, 2(4-chloro-sulfonyl-phenyl)-ethyl-tricholorosylane. This last compound allows the interchange of the sulphonic group H^+ by Co^{+2} and Ni^{+2} (see fig. 1.12). [50]

A year later, Xu *et al.* deposited Cu clusters of 10 nm in diameter on carboxylated MWCNTs by *electroless plating* (autocatalytic or chemical reduction that does not requires electric currents) from $CuSO_4$, using HCOH as reducing agent in distilled water by controlling the temperature and pH value. [51]

Metal oxide particles have also been obtained following functionalization methods for carboxy-SWCNTs. As an example, Han and Zettl (2003) coated cleaned SWCNTs (in HNO_3 $40\%^{v}/_{v}$ at 120°C) with SnO_2 from the chemical reaction of these carbon nanotubes with $SnCl_4/HCl_{(dil)}$. [52]

J. Sun *et al.* (2004) attached SWCNTs to amine-TiO_2 nanoparticles synthesized from $TiCl_4$. [53] More recently, Shirashi *et al.* (2005) made nanocomposites of

MWCNTs and TiN nanoparticles by laser ablation of a TiN disk in a N_2(g) atmosphere with carbon nanotubes close to the disk ablated. Nanoparticles with a diameter between 20 – 70 nm deposited on untreated-MWCNTs previously ultrasonicated were obtained. [54]

Different methods to incorporate metal nanoparticles during the synthesis of carbon nanotubes are being developed. In this context, Bera *et al.* (2004) encapsulated Pd nanoparticles (diameter ~ 3 nm) inside CNTs during the nanotube synthesis by an arc-discharge in a solution of $PdCl_2$/HCl. [55]

1.4 Attachment of metallic clusters on MWNTs-CN_x

The efforts to coat MWNTs-CN_x with metal clusters have followed the same directions used for MWCNTs. [56–58] However, new methods taking advantage of the chemical differences between MWNTs-CN_x and MWCNTs are just starting to be developed. Jiang K. *et al.* (2003) have selectively anchored Au colloidal nanoparticles in carboxylated sites (by wet oxidation in H_2SO_4/HNO_3) using a cationic polyelectrolyte as a bridge between the nanoparticles and the carboxylated N-doped carbon nanotubes. Well-dispersed gold nanoparticles uniformly deposited on the walls and ends of the nanotubes were obtained (see fig. 1.13). [56]

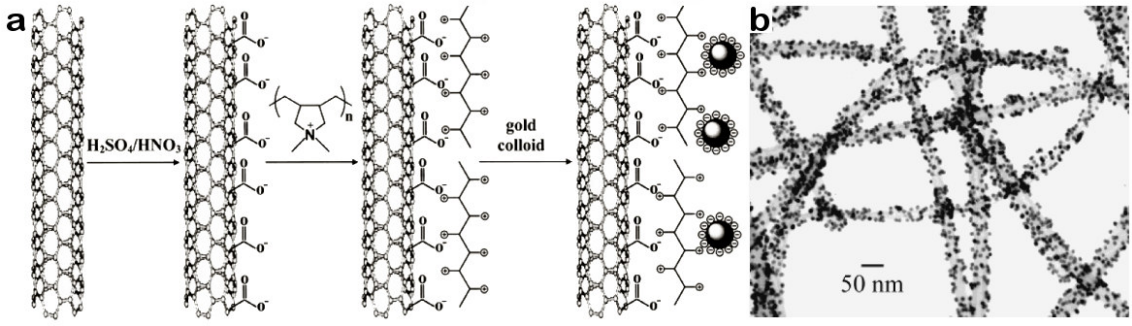

Figure 1.13: Anchoring of Au nanoparticles to MWNTs$-CN_x$ **nanotubes. a)** Schematic view of the process for anchoring gold nanoparticles to MWNTs$-CN_x$ particles. **b)** TEM photograph for hybrid structures. Taken from [56].

Biomolecules have also been attached to MWNTs-CN_x. Nitrogen doping produces more defect sites on the graphene walls when compared to undoped-carbon nanotubes, and also provides a more biocompatible surface (by the C–N bond). [57] K. Jiang *et al.* (2004) reacted carboxylated MWNTs-CN_x with the amine groups of ferritine proteins by a two-step process of active amidation of di-imide. The covalent attachment between the nanotube and proteins was achieved through a peptidic-like bond (see fig. 1.14). [58] Subsequently, Jia *et al.* (2005) covalently bonded hemoglobin to oxidized MWNTs-CN_x in an acid medium. Electrocatalytic reduction studies of H_2O_2 by cyclic voltammetry showed that iron in hemoglobin kept its catalytic activity after the protein attachment on MWNT-CN_x. [57]

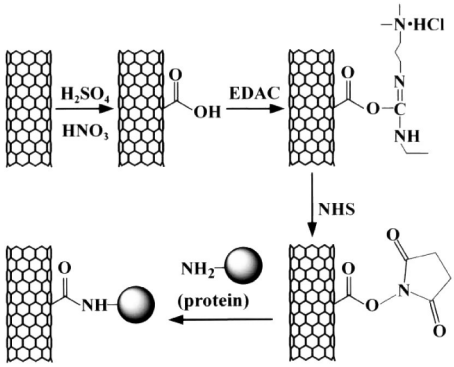

Figure 1.14: Protein immobilization on MWNTs-CN_x. Schematic view of attachment of proteins to MWNTs-CN_x *via* a to step–process of diimide amidation. Details of process at reference. Taken from [58].

Endo M. *et al.* (2003) obtained an efficient and homogeneous dispersion in a narrow size distribution (medium diameter about 3 nm) of Pt nanoclusters on cup-stacked carbon nanofibers. They suggested that the edges of these fibers behave as active sites because Pt appeared to be deposited on them (see *b* in fig. 1.15). [59]

Endo *et al.* used the edges of cup-stacked carbon nanofibers as reactive sites for a homogeneous dispersion of metallic nanoparticles. Then, our aim is the use of the nitrogen reactive site of MWNTs-CN_x in order to achieve similar results.

In this work, the reactions proposed for the deposit of metallic nanoparticles on MWNTs-CN_x arise from the hypothesis that nitrogen doped carbon nanotubes exhibit similar chemical properties to amines (–C=$\ddot{N}$-C–, $R_3\ddot{N}$) or pyridinic (–C-$\ddot{N}$=C–) compounds. This consideration is justified by the experimental

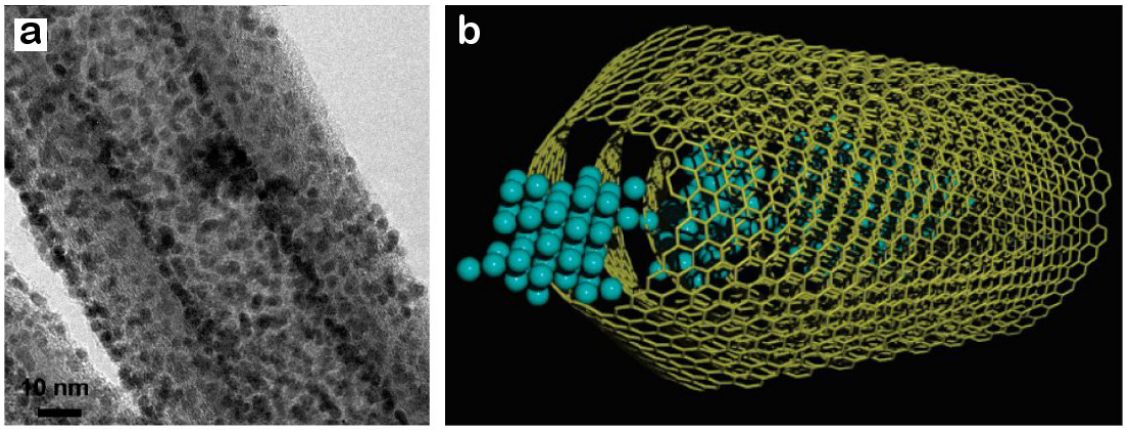

Figure 1.15: Pt clusters deposited on cup-stacked carbon nanofibers. **a)** HRTEM image of highly dispersed nanoparticles on both inner and outer surface. **b)** Schematic model of cup-stacked carbon fibers decorated with Pt clusters due to strong interaction between the metal salt and the edges planes. Taken from [59].

observations on MWNTs-CN_x previously mentioned.

In this thesis, we develop a novel method for anchoring metal nanoclusters to MWNTs-CN_x, assisted by the nitrogen sites present in this kind of nanotubes. Our proposal is the use of the chemical properties of nitrogen, which is more reactive than the rest of the C atoms that forms the graphitic network, so as to anchor efficiently metallic clusters on the surface of MWNTs-CN_x. This could be a new and easy method that will not modify the pristine properties of MWNTs-CN_x by the functionalization of sidewalls with carboxylic groups.

Transition metals ($d-$block) such as iron (Fe), platinum (Pt), and titanium (Ti) have been selected to prove several deposit techniques not previously applied on MWNTs-CN_x. The catalytic effect of Fe is shown by the subsequent growth of nanotubes on these materials forming nanotube junctions and networks. Pt was selected due to their known catalytic properties. Ti, on the other hand, was selected due to its biocompatibility, which could then increase MWNTs-CN_x affinity for living organisms, making them useful for cellular growth, replacing bony tissue or as support for microorganisms in bio-reactors. Our aim is to find alternative methods for the incorporation of Ti clusters on MWNTs-CN_x using different approaches.

1.5 Applications of Carbon Nanotubes

Some of the potential applications of chemically modified carbon nanotubes are summarized in table 1.4.

Table 1.4: Potential applications of chemically modified carbon nanotubes. Taken from [14].

(Potential) Application	Function of the covalently bonded moiety
Nanostructured electronic devices, e.g. nanodiodes	Local modification of the electronic band structure.
(Bio-) chemical sensors	Selective recognition of analyte molecules.
Catalyst supports	Anchoring of molecules or metal nanoparticles. Surface area of SWCNTs measured by N_2 physisorption at 77 K is about 27 m^2/g. [29]
Mechanically reinforced composites	Chemical coupling with a matrix.
Chemically sensitive tips for scanning probe microscopy	Selective chemical interaction with surfaces.
Field emission	Reduction of the work function for electrons at the tube ends.
Nanofiltration	Control of the passage of molecules or ions through steric effects or Coulomb interactions.
Artificial muscles	Mechanical stabilization of nanotube films through covalent cross-linking.
Controlled drug release	Biocompatibility, recognition of biological fingerprints.
Pharmacology	Enzyme inhibition of blocking of ionic channels in the cell membrane.
Direct cell growth on surfaces	Specific interactions with cell surfaces.

Because of the nearly one-dimensional electronic structure, electronic transport in metallic SWNTs and MWNTs occurs ballistically (*i.e.* without scattering), enabling them to carry high currents with essentially no heating. The high thermal conductivity of MWCNTs (> 3000 W/m·K, see table 1.1) indicates that phonons also propagate easily along the nanotubes at room temperature. [60]

One of the most promising applications of carbon nanotubes is the creation of modern electronics devices. Achieving an economical large-scale method, will allows us to overcome the actual technological limitations on building smaller circuits for a new generation of molecular-scale devices. While metallic nanotubes are desirable for nanoscale electrical interconnections in some applications, fabrication of nanotransistor devices requires nanotubes of the semiconductor type. [14] The

development of technologies for patterned deposition of nanotubes on the micro- to nanometer scale are also important for electronic devices, displays and nanoscale actuators. [60]

Up to date, there is no synthesis method that allows control the chirality of SWCNTs (*i.e.* and their electronic properties). [14] However, selective reactions can now be made with SWCNTs based on their type (n, m value). This functionalization reaction then, allows manipulation and separation in a highly chiral enriched SWCNTs fractions, achieved since metallic SWCNTs react faster than the semiconductor counterparts. [32] Electrical heating can be also used to destroy the metallic SWCNTs allowing to survive only the semiconducting ones. [60] As a MWCNT is built of concentric SWCNTs, each exhibiting different chirality, it would be meaningless to talk about a separation method for MWCNTs.

Approaches using doped carbon nanotubes could be more promising for reaching an efficient synthesis of nanoelectronic devices. For instance, the studies performed by Czerw *et al.* suggested a way to achieve full p-n junctions, which are necessary to develop novel nanoelectronic devices, by using N- and B-doped carbon nanotubes. These junctions result in a potential barrier of about 0.5 V. [9]

Adsorption of molecules on nanotubes is associated with a partial charge transfer, from either electron acceptors (e.g. NO_2) or donors (like NH_3), that can cause an alteration in the charge-carrier concentration or may affect the potential barriers presented at the tube-electrode contacts. [14] This phenomenon may make feasible the use of carbon nanotubes as chemical sensors. The successful use of arrays of aligned MWNTs-CN_x in sensing relatively low concentrations of gases (acetone, ethanol, gasoline, chloroform, pyridine and ammonia) has been reported, showing a reversible electric response of MWNTs-CN_x in the majority of the tested cases. The chemical reactivity of MWNTs-CN_x appears to be higher than those of pure MWCNTs. This effect can be attributed to the presence of pyridine-like sites located on the surface of the nanotubes, that bind strongly to ammonia, acetone and –OH groups. [61].

Carbon nanotubes also exhibit high electron transfer rates for different redox couples in various media. Their high aspect ratio and their diameter in the nanometer range make them well suited for a direct electrochemical communication with the redox site of a protein, without requiring any mediator. [14] Studies of electrochemical behavior of hemoglobin proteins covalently bonded to MWNTs-CN_x have been performed, thus demonstrating that they keep their catalytic activity. [57]

Transition metal deposits on MWCNTs have been analyzed in order to probe their catalytic properties. For example, work on rhutenium clusters coating MWCNTs, revealed that Ru keeps its catalytic effect in the liquid-phase cinnamaldehyde hydrogenation reaction. [44]

Alkali metal intercalation in carbon nanotubes and tube bundles has been extensively studied due to its potential application in the fabrication of batteries. The charge capacity of a SWCNT is 495 – 677 mAh/g, but can be improved by chemical etching or ball milling of the nanotube material to 900 – 1037 mAh/g. These values surpass the capacity of actual commercial graphite (375 mAh/g). Although MWCNTs are below the SWCNTs in charge capacity, with ∼250 mAh/g for raw material, their value can be improved up to 440 mAh/g by the same treatments mentioned for SWCNTs. [9]

Because of the high area of porous nanotube arrays, capacitors with giant capacitances can be built. These capacitances are typically between ∼15 and ∼200 F/g (values of 180 and 102 F/g have been observed for SWCNTs and MWCNTs electrodes, respectively), depending on the surface area of the nanotube array, and result in a large amounts of charge injection when a few volts are applied. This energy storage can provide electrode expansions and contractions that can do mechanical work in electromechanical actuators required for technological applications such as robots. [60]

The high tensile strength of carbon nanotubes (see table 1.1 in page 6) surpasses that of steel (0.40 GPa for structural steel, 0.69 GPa for high strength alloy and 1.65 GPa for high tensile steel) by one order of magnitude, making them a valuable

component for mechanically reinforced composite materials. However, a critical issue in composite preparation is to achieve good adhesion between the matrix and the individual tubes, which is required for an effective transfer of the mechanical load onto the nanotubes. Therefore, covalent coupling between the matrix and nanotubes is currently under extensive investigation. Optimizing the density of covalently bonded groups on the nanotube surfaces would ensure forming enough bonds to achieve load transfer to the matrix without significant alteration of the mechanical stability of the nanotubes. [14] For MWCNTs, the possibility that the concentric graphene cylinders slide from each other cannot be neglected. So, the actual strength attainable from aggregates of nanotubes could be much lower than that expected from the ideal structure of isolated tubes. [62]

A monotonic increase of resistance to indentation up to 3.5 times with loading up to 2% SWCNTs and a doubling of thermal conductivity with 1% have been observed in polystyrene. A 1% load of MWCNTs in the same polymer can also increase the modulus and breaking stress up to 42% and 25% respectively. [60]

Advances in producing polymer composites with SWCNTs by melt spinning and aligning the nanotubes by drawing have been achieved. The use of MWCNTs as electrically conducting components in polymer composites is the first actual major commercial application. Depending on the polymer matrix, conductivities of 0.01 to 0.1 S/cm can be obtained for 5% loading; much lower conductivity levels are enough to dissipate electrostatic charge. For instance, in automotive gas lines and filters, the nanotube filler dissipates charge buildup that can lead to explosions and maintains barrier properties against fuel diffusion better than plastics filled with carbon black. The shielding of electromagnetic radiation from cell phones and computers by using molded SWCNTs and MWCNTs composites is also a potentially lucrative application. [60]

Carbon nanotubes are light-weight, capable of reversibly storing and releasing hydrogen in a modest range of near-ambient temperature and pressure. Since pure carbon nanotubes do not present sufficient storage capacity for commercial

use, researchers have looked into Li- and K-doped carbon nanotubes in order to achieve a much better storage system. [9] Electron emitters and nanoprobes are more alternatives of the vast areas of applications of both doped- and undoped-carbon nanotubes. [62]

Carbon nanotubes can be considered as fascinating macromolecules, and even if their possible applications could not be generalized, big efforts to achieve a major control when producing structures at the atomic level are underway. This thesis attempts to explore several unexplored aspects of the reactivity of MWNTs-CN_x. Their use as blocks that could interact with other macromolecules forming supramolecular structures could be achieved using the processes presented in this account, among other relevant results.

In chapter 2, we will show the interaction of MWNTs-CN_x with Fe particles and their use in synthesizing various coaxial hetero-tubes and cables from two types of carbon nanotubes: undoped and nitrogen doped ones. Also, some different kinds of 3D hetero-junctions between MWCNTs and MWNTs-CN_x will be described.

In chapter 3, we will focus on an efficient and homogeneous deposition of metallic nanoclusters of platinum on MWNTs-CN_x. It was obtained by an easy method that does not involve chemical functionalization of carbon nanotubes. This is desirable in order to get a fine size distribution of metallic clusters; because, the existence of functional groups –COOH and –OH has been shown to spread the size scattering of nanoparticles on them. [59] The possibilities of their subsequent use for heterogeneous catalysis in chemical reactions are important.

The attachment of titanium clusters on carbon nanotubes will be explained in chapter 4. One method involves the addition of a Ti precursor during the pyrolytic synthesis of CNTs. Here we noted that Ti tends to sharpen the nanotube tips giving them ends like truncated cones. An alternative electrochemical method for an effective metal anchoring on MWNTs-CN_x is also described and discussed in

chapter 4.

Finally, chapter 5 describes the main conclusions of our work and the future work that needs to be carried out.

References

[1] Kroto, H.W.; Heath, J.R.; S. C. O'Brien, R.F.C. and Smalley, R.E. *C_{60}: Buckminsterfullerene*. Nature **318**:162–163, 1985.

[2] *"Fullerene"*. Wikipedia the free encyclopedia, `http://en.wikipedia.org/wiki/Fullerene`, 2006.

[3] *Library of 3-D molecular structures: Carbon section*. `http://www.nyu.edu/pages/mathmol/library/carbon/`, 2006.

[4] Teo, K.B.K.; Singh, C.; Chhowalla, M. and Milne, W.I. *Encyclopedia of Nanoscience and Nanotechnology*, volume 10, chapter Catalytic Synthesis of Carbon Nanotubes and Nanofibers, pages 1–22. Nalwa, H. S., 2003.

[5] Oberlin, A. and Endo, M. *Filamentous growth of carbon through benzene decomposition*. Journal of Crystal Growth **32**(3):335–349, 1976.

[6] Ijima, S. *Helical microtubules of graphitic carbon*. Nature **354**:56–58, 1991.

[7] Zhu, H.; Xu, C.; Wu, D.; Wei, B.; Vajtai, R. and Ajayan, P. *Direct synthesis of long single-walled carbon nanotube strands*. Science **296**:884–886, 2002.

[8] Zhang, M.; Fang, S.; Zakhidov, A.A.; Lee, S.B.; Aliev, A.E.; Williams, C.D.; Atkinson, K.R. and Baughman, R.H. *Strong, transparent, multifunctional carbon nanotube sheets*. Science **309**:1215–1219, 2005.

[9] Xie, R.H.; Zhao, J. and Rao, Q. *Encyclopedia of Nanoscience and Nanotechnology*, volume 10, chapter Doped Carbon Nanotubes, pages 1–31. Nalwa, H. S.: www.aspbs.com/enn, 2004.

[10] Dresselhaus, M.S.; Dresselhaus, G. and Saito, R. *Physics of carbon nanotubes*. Carbon **33**(7):883–891, 1995.

[11] Troiani, H.; Miki-Yoshida, M.; Camacho-Bragado, G.; Marques, M.; Rubio, A.; Ascencio, J. and José-Yacaman, M. *Direct observation of the mechanical*

properties of single-walled carbon nanotubes and their junctions at the atomic level. Nano Letters **3**(6):751–755, 2003.

[12] Saito, R.; Dresselhaus, G. and Dresselhaus, M. *Physical Properties of Carbon Nanotubes*. Imperial College Press: London, United Kingdom, 1998.

[13] Wildöer, J.W.; Venema, L.C.; Rinzler, A.G.; Smalley, R.E. and Dekker, C. *Electronic structure of atomically resolved carbon nanotubes*. Nature **391**:59–62, 1998.

[14] Balasubramanian, K. and Marko, B. *Chemically functionalized carbon nanotubes*. Small **1**(2):180–192, 2005.

[15] Garritz Ruiz, A. *Nanotecnología II: Nanotubos de carbono*. Educación Química **2**:67–68, 2001.

[16] Terrones, M.; Ajayan, P.; X., B.; Carroll, D.; Czerw, R.; Foley, B.; Grobert, N.; Kamalakaran, R.; Kohler-Redlinch, P.; Rühle, M. and Terrones, H. *N-doping and coalescence of carbon nanotubes: Synthesis and electronic properties*. Applied Physics A: Materials Science and Processing **74**:355–361, 2002.

[17] Kamalakaran, R.; Terrones, M.; Seeger, T.; Kohler-Redlich, P.; Rühle, M.; Kim, Y.; Hayashi, T. and Endo, M. *Synthesis of thick and crystalline nanotube arrays by spray pyrolysis*. Applied Physics Letters **77**(21):3385–3387, 2000.

[18] Mayne, M.; Grobert, N.; M., T.; Kamalakaran, R.; Rühle, M.; Kroto, H. and Walton, D. *Pyrolytic production of aligned carbon nanotubes from homogeneously dispersed benzene-based aerosols*. Chemical Physics Letters **338**:101–107, 2001.

[19] Glerup, M.; Kanzow, H.; Almairac, R.; Castignolles, M. and Bernier, P. *Synthesis of multi-walled carbon nanotubes and nano-fibers using the aerosol method with metal-ions as the catalyst precursors*. Chemical Physics Letters **377**:293–298, 2003.

[20] Pinault, M.; Mayne-L'Hermite, M.; Reynaud, C.; Pichot, V.; Launois, P. and Ballutaud, D. *Growth of multiwalled carbon nanotubes during the initial stages of aerosol-assisted CCVD.* Carbon **43**:2968–2976, 2005.

[21] Terrones, M.; Grobert, N. and Terrones, H. *Synthetic routes to nanoscale $B_xC_yN_z$ architectures.* Carbon **40**:1665–1684, 2002.

[22] Terrones, M.; Terrones, H.; Grobert, N.; Hsu, W.; Zhu, Y.; Hare, J.; Kroto, H.; Walton, D.; Kohler-Redlich, P.; Rühle; Zhang, J. and A.K., C. *Efficient route to large arrays of CN_x nanofibers by pyrolysis of ferrocene/melamine mixtures.* Applied Physics Letters **75**(25):3932–3934, 1999.

[23] Wen-Kuang-Hsu. *Carbon Nanotubes: Production, Growth and Characterization.* Ph.D. thesis, University of Sussex, 1997.

[24] Chen, G.Z.; Kinloch, I.; Shaffer, M.S.; Fray, D. and Windle, A.H. *Electrochemical investigation of the formation of carbon nanotubes in molten salts.* High Temperature Material Processes **2**(4):459–469, 1998.

[25] Kinloch, I.A.; Chen, G.Z.; Howes, J.; Boothroyd, C.; Singh, C.; Fray, D.J. and Windle, A.H. *Electrolytic, TEM and Raman studies on the production of carbon nanotubes in molten NaCl.* Carbon **41**:1127–1141, 2003.

[26] Bronikowski, M.J.; Willis, P.A.; Colbert, D.T.; Smith, K.A. and Smalley, R.E. *Gas-phase production of carbon single-walled nanotubes from carbon monoxide via the HiPco process: A parametric study.* Journal of Vacuum Science Technology A **19**(4):1800–1805, 2001.

[27] Czerw, R.; Terrones, M.; Charlier, J.; Blase, X.; Foley, B.; Kamalakaran, R.; Grobert, N.; Terrones, H.; Tekleab, D.; Ajayan, P.; Blau, W.; Rühle, M. and Carroll, D. *Identification of electron donor states in N-doped carbon nanotubes.* Nano Letters **1**(9):457–460, 2001.

[28] Lim, S.H.; Elim, H.I.; Gao, X.Y.; Wee, A.T.S.; Ji, W.; Lee, J.Y. and Lin,

J. *Electronical and optical properties of nitrogen-doped multiwalled carbon nanotubes*. Physical Review B **73**:045402, 2006.

[29] Ebbesen, T.W.; Hiura, H.; Bisher, M.E.; Treacy, M.M.J. and Shreeve-Keyer, J.L. *Decoration of carbon nanotubes*. Advanced Materials **8**(2):155–157, 1996.

[30] Turnbull, D. *Correlation of liquid-solid interfacial energies calculated from supercooling of small droplets*. Journal of Chemical Physics **18**(5):769, 1950.

[31] Zhang, Y.; Franklin, N.W.; Chen, R.J. and Dai, H. *Metal coating on suspended carbon nanotubes and its implication to metal-tube interaction*. Chemical Physics Letters **331**:35–41, 2000.

[32] Dyke, C.A. and Tour, J.M. *Covalent functionalization of single-walled carbon nanotubes for materials applications*. Journal of Physical Chemistry A **108**(51):11151–11159, 2004.

[33] Mylvaganam, K. and Zhang, L.C. *Chemical bonding in polyethylene-nanotube composites: A quantum mechanics prediction*. Journal of Physical Chemistry B **108**(17):5217–5220, 2004.

[34] For structural relaxation the DFT method with LDA and LCAO approximations using a double-zeta basis was used. r_{cut}=100 Ry, E_{cut}=50 Hartree were the parameters used.

[35] Soler, J.M.; Artacho, E.; Gale, J.D.; García, A.; Junquera, J.; Ordejón, P. and Sánchez-Portal, D. *The SIESTA method for ab initio order-N materials simulation*. Journal of Physics: Condensed Matter **14**:2745–2779, 2002.

[36] Ordejón, P.; Artacho, E. and Soler, J.M. *Self-consistent order-n density-functional calculations for very large systems*. Physical Review B **53**(16):10441–10444, 1996.

[37] Liang, F.; Sadana, A.K.; Peera, A.; Chattopadhyay, J.; Gu, Z.; Hauge, R.H.

and Billups, W.E. *A convenient route to functionalized carbon nanotubes.* Nano Letters **4**(7):1257–1260, 2004.

[38] Mickelson, E.; Huffman, C.; Rinzler, A.; Smalley, R.; Hauge, R. and Margrave, J. *Fluorination of single-wall carbon nanotubes.* Chemical Physics Letters **296**:188–194, 1998.

[39] Kelly, K.; Chiang, I.; Mickelson, E.; Hauge, R.; Margrave, J.; Wang, X.; Scuseria, G.; Radloff, C. and Halas, N. *Insight into the mechanism of sidewall functionalization of single-walled nanotubes: a STM study.* Chemical Physics Letters **313**:445–450, 1999.

[40] Bahr, J.L. and Tour, J.M. *Highly functionalized carbon nanotubes using in situ generated diazonium compounds.* Chemical Materials **13**:3823–3824, 2001.

[41] Peng, H.; Alemany, L.B.; Margrave, J.L. and Khabashesku, V.N. *Sidewall carboxylic acid functionalization of single-walled carbon nanotubes.* Journal of American Chemical Society **125**:15174–15182, 2003.

[42] Bahr, J.L. and Tour, J.M. *Covalent chemistry of single-wall carbon nanotubes.* Journal of Materials Chemistry **12**:1952–1958, 2002.

[43] Sinnott, S.B. *Chemical functionalization of carbon nanotubes.* Journal of Nanoscience and Nanotechnology **2**(2):113–123, 2002.

[44] Planeix, J.M.; Coustel, N.; Coq, B.; Brotons, V.; Kumbhar, P.S.; Dutartre, R.; Geneste, P.; Bernier, P. and Ajayan, P.M. *Application of carbon nanotubes as supports in heterogeneous catalysis.* Journal of American Chemical Society **116**:7935–7936, 1994.

[45] Ellis, A.V.; Vijayamohanan, K.; Goswami, R.; Chakrapani, N. and Ramanathan, L.S. *Hydrophobic anchoring of monolayer-protected gold clusters to carbon nanotubes.* Nano Letters **3**:279–282, 2003.

[46] Satishkumar, B.C.; Vogl, E.M.; Govindaraj, A. and Rao, C.N.R. *The decoration of carbon nanotubes by metal nanoparticles.* Journal Physics D: Applied Physics **29**(2):3173–3176, 1996.

[47] Haremza, J.M.; Hahn, M.A.; Krauss, T.D. and Chen, S. *Attachment of single CdSe nanocrystals to individual single-walled carbon nanotubes.* Nano Letters **2**(11):1253–1258, 2002.

[48] Jiang, L. and Gao, L. *Modified carbon nanotubes: an effective way to selective attachment of gold nanoparticles.* Carbon **41**:2923–2929, 2003.

[49] Liu, L.; Wang, T.; Li, J.; Guo, Z.X.; Dai, L.; Zhang, D. and Zhu, D. *Self-assembly of gold nanoparticles to carbon nanotubes using a thiol-terminated pyrene as interlinker.* Chemical Physics Letters **367**:747–452, 2003.

[50] Sun, X.; Li, R.; Villers, D.; Dodelet, J.P. and Désilets, S. *Attachment of single CdSe nanocrystals to individual single-walled carbon nanotubes.* Chemical Physics Letters **379**:99–104, 2003.

[51] Xu, C.; Wu, G.; Liu, Z.; Wu, D.; Meek, T.T. and Han, Q. *Preparation of copper nanoparticles on carbon nanotubes by electroless plating method.* Materials Research Bulletin **39**:1499–1505, 2004.

[52] Han, W.Q. and Zettl, A. *Coating single-walled carbon nanotubes with tin oxide.* Nano Letters **3**(5):681–683, 2003.

[53] Sun, J.; Iwasa, M.; Gao, L. and Zhang, Q. *Coating single-walled carbon nanotubes with tin oxide.* Carbon **42**(5):885–901, 2004.

[54] Shiraishi, M.; Koshio, A.; Deno, H. and Kokai, F. *Nanocomposites formed by deposition of tin nanoparticles on carbon nanotubes.* New Diamond and Frontier Carbon Technology **15**:91–97, 2005.

[55] Bera, D.; Kuiry, S.C.; McCutchen, M.; Kruize, A. and Heinrich, H. *In-situ*

synthesis of palladium nanoparticles-filled carbon nanotubes using arc-discharge in solution. Chemical Physics Letters **386**:364–368, 2004.

[56] Jiang, K.; Eitan, A.; Schadler, L.S.; Ajayan, P.M.; Siegel, Richard, W.; Grobert, N.; Mayne, M.; Reyes Reyes, M.; Terrones, H. and Terrones, M. *Selective attachment of gold nanoparticles to nitrogen-doped carbon nanotubes.* Nano Letters **3**(3):275–277, 2003.

[57] Jia, N.; Wang, L.; Liu, L. and Zhou, Q. *Bamboo-like CN_x nanotubes for the inmobilization of hemoglobin and its bioelectrochemistry.* Electrochemistry Communications **7**:349–354, 2005.

[58] Jiang, K.; Schadler, L.S.; Siegel, Richard, W.; Zhang, X.; Zhang, H. and Terrones, M. *Protein immobilization on carbon nanotubes via two-step process of diimide-activated amidation.* Journal of Materials Chemistry **14**:37–39, 2004.

[59] Endo, M.; Ahm Kim, Y.; Ezaka, M.; Osada, K.; Yanagisawa, T.; Hayashi, T.; Terrones, M. and Dresselhaus, M.S. *Selective and efficient impregnation of metal nanoparticles on cup-stacked-type carbon nanofibers.* Nano Letters **2**(6):723–726, 2003.

[60] Baughman, R.H.; Zakhidov, A.A. and de Heer, W.A. *Carbon nanotubes–the route toward applications.* Science **297**:787–792, 2002.

[61] Villalpando-Páez, F.; Romero, A.; Muñoz-Sandoval, E.; Martínez, L.; Terrones, H. and Terrones, M. *Fabrication of vapor and gas sensors using films of aligned CN_x nanotubes.* Chemical Physics Letters **386**:137–143, 2004.

[62] Ajayan, P. *Handbook of Nanostructured Materials and Nanotechnology*, volume 5, chapter Carbon Nanotubes, pages 375–406. Ed. Academic Press, 2000.

Chapter 2

Iron cluster deposition on MWNTs-CN_x

In this chapter we describe the results obtained of the different methods tested to achieve the deposition of iron clusters on MWNTs-CN_x.

Reactivity of MWNTs-CN_x is expected to be higher when compared to undoped carbon nanotubes (sections 1.1 and 1.2). This is mainly because of the introduction of more reactive nitrogen atoms within the hexagonal carbon network. It is reasonable to expect that these compounds would exhibit similar chemical properties to amino compounds by the two fashions in which the nitrogen atom is covalently linked to the carbon network in MWNTs-CN_x (substitutional and pyridine-like). Therefore, it could be possible to treat the nitrogen in the tubes with some of the characteristic reactions for this functional group, in order to take advantage of their existence within carbon nanotubes. This behavior could be used, for instance, for depositing metallic clusters on the surface of MWNTs-CN_x without the requirement of previous acid functionalization which significantly changes the electronic and mechanical properties of the nanotubes.

2.1 Introduction

2.1.1 General Properties of Amines

Amines are important organic compounds that exhibit considerably basicity. Their general formula could be $R\ddot{N}H_2$, $R_2\ddot{N}H$ or $R_3\ddot{N}$, where R is any alkyl or aryl group. Three kinds of amines exist: primaries, secondaries and tertiaries. These differ by the number of groups attached to the nitrogen atom. Independent of their type, the nitrogen of the amines exhibit an unshared pair of electrons. Therefore, the entire chemical behavior of amines relies in the tendency of nitrogen to share this pair of electrons. One of their fundamental properties tied to its basicity is the associated nucleophilicity. All amines are polar compounds, except for the tertiaries. These compounds form hydrogen bonds with water and show a solubility limit at 6 °C. [1]

Aromatic amines are generally very toxic and are readily absorbed through the skin. Among their general chemical properties, we can mention that they are easily oxidized in air, and the aqueous mineral acids or carboxylic acids readily convert amines into their salts. On the other hand, the aqueous hydroxide ion readily converts these salts into free amines again. [1]

Amine reactions are of the classic acid-base type, that is $R\ddot{N}H_2 \underset{OH^-}{\overset{H^+}{\rightleftarrows}} RNH_3^+$:

$$\underset{\text{Stronger Base}}{R\ddot{N}H_2} + H_3O^+ \rightarrow RNH_3^+ + \underset{\text{Weaker Base}}{H_2O} \qquad \text{(R 2.1)}$$

$$RNH_3^+ + \underset{\text{Stronger Base}}{OH^-} \rightarrow \underset{\text{Weaker Base}}{R\ddot{N}H_2} + H_2O \qquad \text{(R 2.2)}$$

The basicity constant, K_b, is defined from the reaction $R\ddot{N}H_2 + H_2O \rightleftharpoons RNH_3^+ + OH^-$, where

$$K_b = K_{EQ}[H_2O] = \frac{[RNH_3^+][OH^-]}{R\ddot{N}H_2}$$

in general, the larger K_b, the stronger is the base. Basicity constants for aliphatic amines are in the range of $10^{-3} \leq K_b \leq 10^{-4}$, making them stronger than ammonia, ($K_{b_{\ddot{N}H_3}} = 1.8 \times 10^{-5}$) and also stronger than aromatic amines ($K_b \leq 10^{-9}$). [1]

Thus, the substitutional N-doping in the MWNTs-CN_x (see section 1.2) can be approximated to ternary amines. Meanwhile, the other kind of N-doping in the graphitic network could resemble a secondary amine, since they seem to be more related to pyridines, whose properties are described in the following section.

2.1.2 General Properties of Pyridines

Pyridine is a 6 member heterocycle compound formed by 5 carbon atoms and one nitrogen atom. It is classified as an aromatic compound according with the Hückel's rule. This rule establishes that a cyclic ring molecule is aromatic when the number of π electrons equals $4n+2$, where n is zero or any positive integer. Pyridine is a planar compound with bonding angles of 120°. Inside the ring, the nitrogen, and each carbon atom, are linked one another using sp^2 orbitals, and supply a π electron to the electronic cloud. The third sp^2 orbital of each carbon atom is used for bonding while nitrogen has a free pair of electrons available for sharing with Lewis acids.

However, this electron pair occupying an sp^2 orbital, responsible for the basicity of pyridine (pK_a of their conjugated acid is 5.30 [2]), is held tightly and is less available for sharing with acids than the free pair of electrons of an aliphatic amine, which occupies the outer sp^3 orbital. Due to the presence of a lone pair of localized electrons at the N atom within the aromatic π-system (see fig. 2.1*a*), pyridine exhibits chemical properties similar to tertiary amines. Pyridine is protonated by reaction with acids and forms a positively charged aromatic polyatomic ion called pyridinium cation. The bond lengths and bond angles in pyridine and the pyridinium ion are almost identical because protonation does not affect the aromatic π system. [2]

Among the characteristic chemical behavior of pyridines, we could emphasize their great reactivity towards nucleophilic substitution. This effect is very strong and is able to displace the basic hydride ion, $\ddot{H}^-$. Consequently, pyridine is not reactive in electrophilic substitution but is highly reactive in nucleophilic substitution. In

addition, it also reacts with alkyl halides to produce quaternary ammonium salts (R_4N^+). A typical reaction of this kind is shown in fig. 2.1*b*. [3]

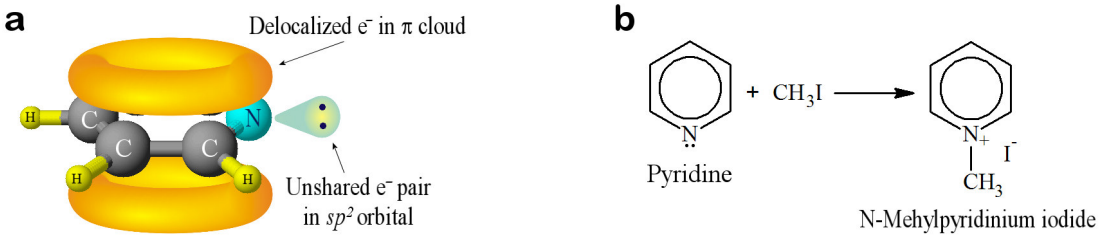

Figure 2.1: Pyridine structure and quaternary ammonium salt reaction. a) Schematic representation of a pyridine molecule. The *p* orbitals overlap to form π clouds above and below the plane ring; two unshared electrons are still in a sp^2 orbital of nitrogen. **b)** Reaction between the pyridine and an alkyl halide, the methyl iodide. The unshared electron pair of nitrogen attacks the partially polarized positive methyl group and forms a quaternary ammonium salt. Images were adapted from [3].

2.1.3 Coordination Salts

Coordination compounds were first described when studying complex compounds of cobalt(III) with ammonia by Alfred Werner at the end of the XIX century. Since then, diverse theories have been developed in order to describe the bonding in coordination compounds. [4]

In the coordination compounds, the metal atom exhibits a constant coordination number (being 6 the most common) and the elements attached to it behave as covalent bonded. Therefore, for describing the chemistry of the complex compounds it is necessary to consider not only the oxidation state of the metal, but also its coordination number. [4] The elements that bind to metals, via "lone pairs" contributing to electronic density, are called *ligands*. The number of sigma bonds between ligands and the central atom is called coordination number. Ligands surrounding the metal inside a structure (known as *internal coordination sphere*) could behave as anions or cations, according to the overall charge of the system. When cations constitute an external sphere enclosing the internal one by electrostatic forces they neutralize charges and form salts. Elements in the internal coordination sphere are usually written between square brackets, whereas those

belonging to the external sphere are positioned outside the brackets. Therefore, in the compound $A_y[ML_x]$, the inner sphere is formed by the metal, **M** attached to the ligands, **L**; and A is the cation (that is not necessarily of only one specie) that is found forming the outer coordination sphere. It is noteworthy that the reactions of the internal sphere are more complicated than those for external one because, in the first case they require, besides electron transfer, the generation and breaking of bonds. [4]

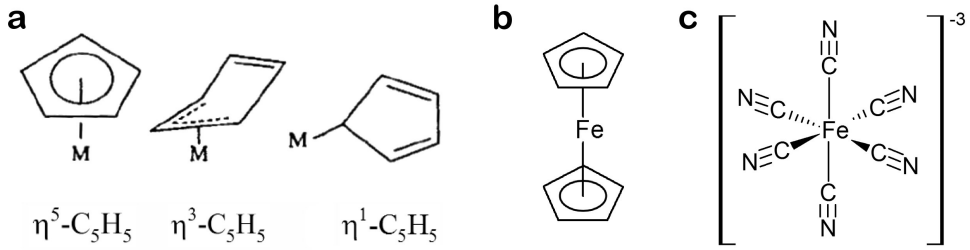

Figure 2.2: Hapticity and coordination compounds. a) Illustration of the three hapticities that can exhibit the cyclopentadienyl as ligand in different compounds. **b)** Representation of the ferrocene molecule, that is a coordination compound known as organometallic. Each cyclopentadienyl ligands exhibit hapticity 5 when are coordinated with iron. **c)** The hexacyanoferrate(III) is an inorganic coordination anion of octahedric (O_h) symmetry. In this complex the iron in oxidation state of +3 is surrounded by six cyano groups, C≡N, so the whole charge exhibited by the coordination sphere is −3. Adapted from [4].

Ferrocene (pentahaptyl biscyclopentadienyl iron, $Fe(\eta^5 - C_5H_5)_2$) and potassium hexacianoferrate(III) ($K_3[Fe(CN)_6]$) are examples of coordination salts (see fig. 2.2*b* and *c*). In the first case, the compound is also known as an organometallic because carbon atoms are directly linked to transition-metal atom. The greek letter η^x refers to the term *hapticity* used to denote the number of atoms in the ligand that are simultaneously bonded to the metallic center. This term is important, because in some cases, the same ligand can bond a different number of atoms to a metal when a coordinate bonding is formed. The broader the π system in a ligand is, the larger the number of possibilities to bond to a central metal. The cyclopendanienyl ($C_5H_5^-$), for instance, can bond one (η^1), three (η^3) and five (η^5) carbon atoms to a metallic center (see fig. 2.2*a*). [4]

2.2 Proposed Reactions between MWNTs-CN_x and Coordination Salts

An easy method to obtain a homogeneous Pt cluster deposit on cup-stacked carbon nanofibers (see fig. 1.15 in page 22) was proposed by Endo *et al.* in 2003. This procedure included dispersion of fibers in a solution of $H_2[PtCl_6]$ followed by an annealing at low temperatures [5], following the procedure described below.

First of all, carbon nanofibers were dispersed in distilled water by an ultrasonic process. Subsequently, an adequate concentration of hexachloroplatinate acid, $H_2[PtCl_6]$, (5–50% wt) was added to this suspension. Then, the mixture was annealed at 90°C on a hotplate with continuous stirring. Soon after, the Pt nanoparticles were stabilized at 300°C under a nitrogen atmosphere (100 cm^3) during 3 h (see also page 16). [6]

These authors pointed that in their experiment, the Pt deposit on carbon nanofibers was probably due to strong interactions between the salt of metal precursor and the open edges (dangling bonds) of cup-stacked fibers. [5]

The process developed by Endo *et al.* involves the use of a coordinated compound, the dihydrogen hexachloroplatinate(IV), $H_2[PtCl_6]$, which has a metal Pt^{+4} immersed in a coordination sphere that exhibits an overall negative charge of -2. Therefore, if one considers MWNTs-CN_x as macromolecules that can exhibit a local behavior to amino compounds, it is possible to use coordination salts for depositing metals on doped carbon nanotubes surface without any prior functionalization of their surface. Avoiding then the creation of functional –COOH and –OH groups. [5]

In order to achieve a reaction between MWNTs-CN_x and coordination salts, a protic solvent[1] medium is necessary for the dissolution of the coordination salt. Highly polar solvents are required to overcome the powerful forces that hold together

[1] *Protic solvents* are solvents containing hydrogen that is attached to oxygen or nitrogen and hence is acidic enough to form hydrogen bonds. [7]

an ionic lattice. In addition, a high dielectric constant is needed to decrease the attraction between opposite charged ions once they are solvated, meaning that the solvent must be also a good insulator. [7]

Because of their structure, the MWNTs-CN_x and MWCNTs can be dispersed in organic solvents such as toluene, benzene and acetone, among others. On the other hand, it is well known that MWCNTs are insoluble in protic solvents since they do not possess any ionic group that can be solvated by species like water or highly polar solvents. As was mentioned earlier, our aim is to avoid the chemical functionalization of the nanotubes in order to prevent a decrease in their mechanical and electronic properties.

By selecting MWNTs-CN_x over MWCNTs we take advantage of the chemical properties of the N-doped tubes (possible formation of amino groups on the tube surface). Therefore, in this work, we propose that a protonation of nitrogen in an acidic medium, could make the MWNTs-CN_x "soluble" in protic solvents, in a similar way to the amine reaction shown in R 2.1. Additionally, the medium will also dissolve the coordination compound, providing a confined metal inside of a negative coordination sphere that we expect will be attracted by the protonated nitrogen located on the surface of MWNTs-CN_x. We could achieve a metal deposit inside coordinated spheres by evaporating the solvent. These complexs can be broken by a thermal treatment in an inert atmosphere for preventing the oxidization of the metallic particles after their release.

2.2.1 Experimental methodology

2.2.1.1 MWNTs-CN_x dispersions in different media

The selected media for a first proof of solubility of MWNTs-CN_x were suspensions of hydrochloric acid (HCl) and acetic acid (CH_3COOH) at different pH values. A sample in distilled water was also used as a control. Aqueous solution of hydrochloric acid was used in order to have another protic medium with a small counter-ion which

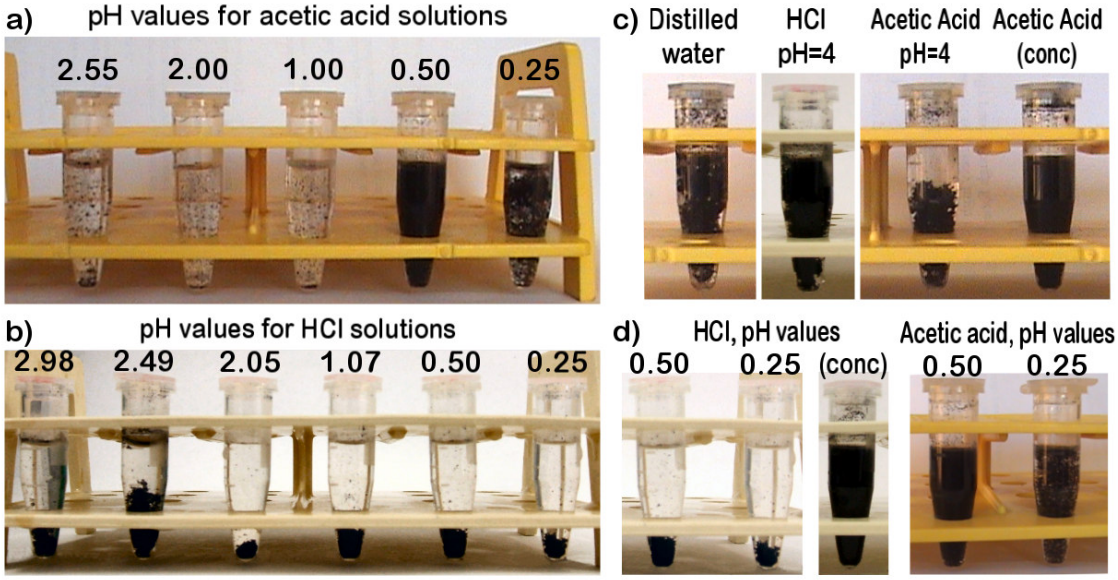

Figure 2.3: MWNTs-CN_x dispersion test in different acidic media. a) Results obtained from dispersion proofs of MWNTs-CN_x in aqueous acetic acid solutions adjusted at different pH values. **b)** Different dispersion of MWNTs-CN_x obtained in aqueous HCl adjusted at several pH values. **c)** Comparative studies between various dispersion media, and the distilled water used as control. **d)** Dispersion at low pH values in the different media. In the right-hand section one can observe how the dispersion in an aqueous suspension of acetic acid is better than in HCl.

can be used as comparison. Acidity was adjusted at values of $0 < \text{pH} \leq 4$.

Systems composed of MWNTs-CN_x and acidic solution were dispersed in an ultrasonic bath (Cole-Parmer model 8891, 42 kHz) for 30 minutes. Soon after, a visual inspection was carried out.

The best dispersed systems were found at pH values of 0.5 and 0.25 in concentrated acetic acid. However, by visual inspection, it seemed that MWNTs-CN_x in concentrated acetic acid and pH value of 0.5 exhibited a better dispersion than those at pH values of 0.25. MWNTs-CN_x dispersion in HCl at pH 4 tends to agglomerate; and this dispersion is similar to the obtained using distilled water (see fig. 2.3*c*). These suspensions placed in Eppendorf vials were stables in the range of months (3-4 months).

It is noteworthy how the MWNTs-CN_x dispersed in HCl solutions, shown in fig. 2.3*b*, with similar pHs to those of acetic acid (fig. 2.3*a*) exhibit a different behavior. The MWNTs-CN_x at pHs of 0.50 and 0.25 precipitate in the aqueous HCl

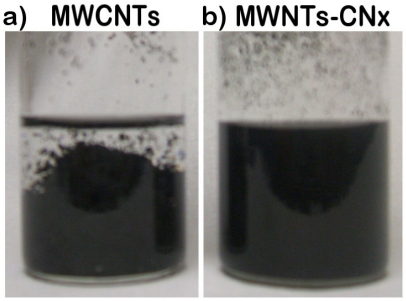

Figure 2.4: Solubility of MWNTs-CN_x *vs* MWCNTs in an aqueous acetic acid (67 v %). A similar quantity of nitrogen-doped multiwalled carbon nanotubes (**b**) and undoped ones (**a**) in an aqueous CH_3COOH solution (67 v %) were sonicated for 1 h in an ultrasonic bath. After 5 minutes (of repose), the picture was taken. It is noteworthy how MWCNTs tend to agglomerate in the medium showing a lack of miscibility. However, MWNTs-CN_x disperse homogeneously in the same medium, showing more stable dispersions than those with MWCNTs.

solutions (see fig. 2.3*d*) meanwhile they remain fully dispersed in the acetic acid solutions of similar pHs. One of the possibilities is the production of quaternary ammonium salts between the protonated-MWNTs-CN_x and the small chloride counterion in the hydrochloric acid. Thus, chloride would attach to the protonated sites and decrease the amount of available positive sites for the solvation of MWNTs-CN_x by the aqueous medium.

The effect of the different solvents was also tested with MWCNTs as a reference. Dispersions of MWCNTs in these acidic media did not work better to that of MWNTs-CN_x in distilled water (see fig. 2.4). They usually precipitate just after sonication.

According to the results obtained from these experiments, the acetic acid was selected as dispersive medium in order to protonate nitrogen sites within MWNTs-CN_x, as stated previously.

The systems composed of MWCNTs and MWNTs-CN_x in 10 mL of aqueous acetic acid solution (67 v %) were dispersed ultrasonically for 1 h and pH measurements were performed. After sonication, a dispersion of 11.9 mg MWNTs-CN_x in that medium exhibits a pH of 0.84, meanwhile for an equivalent quantity (in weight) of MWCNTs this value corresponded to 0.59. The mean pH value found, for MWNTs-CN_x system, was of about $7.23\text{x}10^{-2}\frac{\text{pH units}}{\text{mg MWNTs-CNx}}$, whereas for MWNCTs, it was $6.14\text{x}10^{-2}\frac{\text{pH units}}{\text{mg MWCNTs}}$. The pH values for the measurements obtained for MWCNTs-CN_x/(CH_3COOH, H_2O) was never lower than $7.06\text{x}10^{-2}\frac{\text{pH units}}{\text{mg MWNTs-CNx}}$.

In general, the dispersions of MWCNTs tend to exhibit a minor pH value than

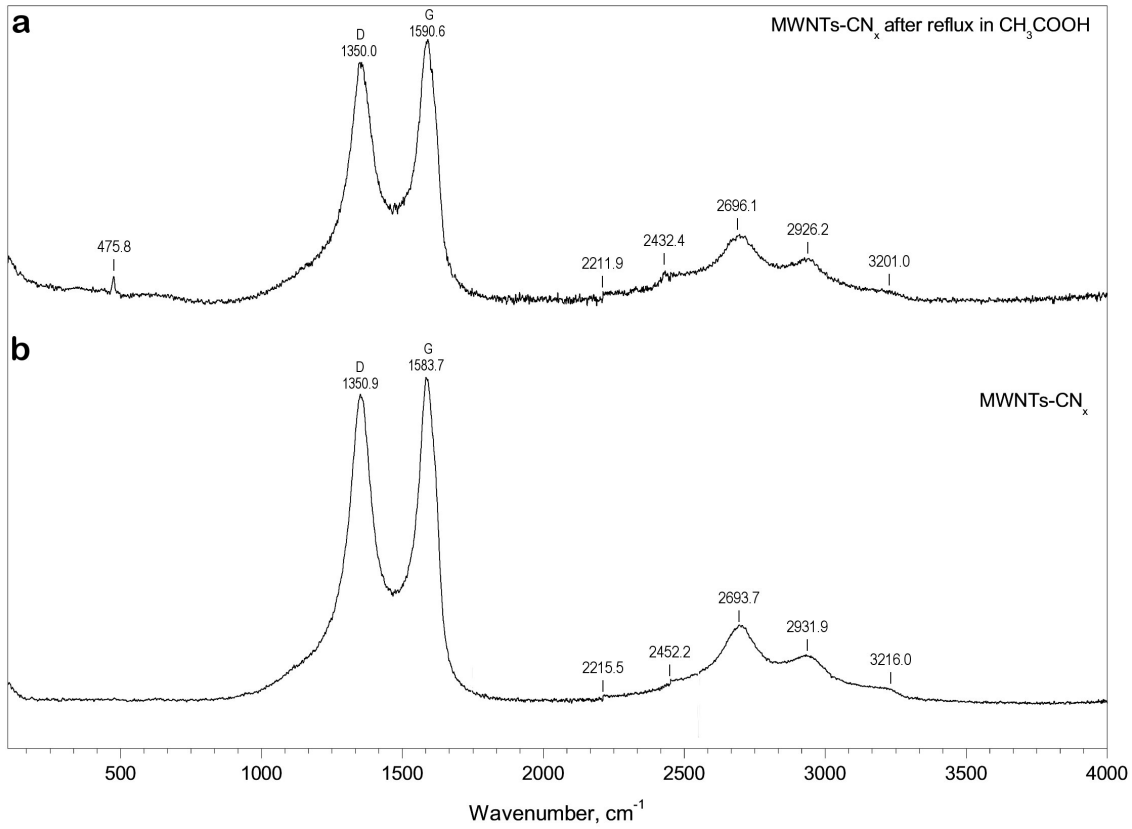

Figure 2.5: Raman spectra of MWNTs-CN_x before and after acidic treatment. **a)** Raman spectrum for MWNTs-CN_x after their reflux in an aqueous acetic acid solution (2:1 v water to CH_3COOH). **b)** Raman spectrum for as-produced MWNTs-CN_x.

those of MWNTs-CN_x. This indicates that additional free $[H^+]$ are found in the dispersion of MWCNTs when compared to MWNTs-CN_x. The reduced quantity of free $[H^+]$ in MWNTs-CN_x suspensions could imply that their nitrogenated sites are able to catch protons that help increasing the solubility of MWNTs-CN_x in protic media (fig. 2.4). These observations support our hypothesis stating that MWNTs-CN_x could behave chemically as amino compounds.

The dispersion efficiency of MWNTs-CN_x in similar pH values varies as a function of the proton source. Then, it could be possible that functionalization could explain this fact. However, this event is considered unlikely because, the aqueous CH_3COOH in inert atmosphere is not known as an oxidative medium.

Raman spectra performed in a Kraiser Holo Lab 5000 system (2.33 eV at $\lambda = 533$ nm; located at Shinshu University, Japan) of MWNTs-CN_x before and

after the acidic treatment are displayed in fig. 2.5. For carbon, two main peaks are clearly identified, the so called D (ca. 1350 cm^{-1}) and G (ca. 1585 cm^{-1}) bands. The intensity of the D signal is related with the quantity of "disorder" in the sample, that is the sp^3 fashion bonding in carbon or other types of defects that break the hexagonal symmetry of graphite. The G intensity is related to the degree of crystallinity in the graphite system, namely the sp^2 hybridized C-bonding. In other words, the G band represents the tangential vibrational mode of carbon atoms in graphene sheets. Shifts in this band are interpreted in terms of C–C expansion (or contraction) an their changes in the electronic structure, whereas shifts in the D band are attributed to the occurrence of new types of defects. [8] Thus, the ratio between the intensities of the peaks D and G (I_D/I_G) provides information related to the crystallinity within the tubes.

In the Raman spectra shown in fig. 2.5, the ratios I_D/I_G correspond to 0.953 for as produced MWNTs-CN_x, and 0.933 after their acid processing. The first quantity agrees with the I_D/I_G value of 0.95 for MWNTs-CN_x reported by Lim *et al.* [9].

It is noteworthy that for MWNTs-CN_x treated with acetic acid, the mean I_D/I_G was of 0.908 ± 0.025, a value which is lower than that observed for as produced MWNTs-CN_x (0.953). This reduction in the ratio of I_D/I_G indicates that the D signal intensity is decreasing. However, another possibility for the decrement of this value could be related to an increase in the G signal during the reflux process but it seems unlikely because of the low temperature used in the experiment. Then, a reduction in the D-band intensity is indicative of a decrease in the amount of "defects" in the tubes, i.e. less sp^3 bonding. This result is contrary to expectations for a oxidization of MWNTs-CN_x after the acidic treatment. During this process sp^3 bonding is formed between C and O atoms. The change in the I_D/I_G ratio together with the knowledge that the acetic acid (CH_3COOH) is not a strong oxidizer medium, lead us to conclude that a soft functionalization probably did not occur.

Raman measurements performed on MWCNTs after and before their treatment in acetic acid are plotted in fig. 2.6. Note that both spectra look similar, their

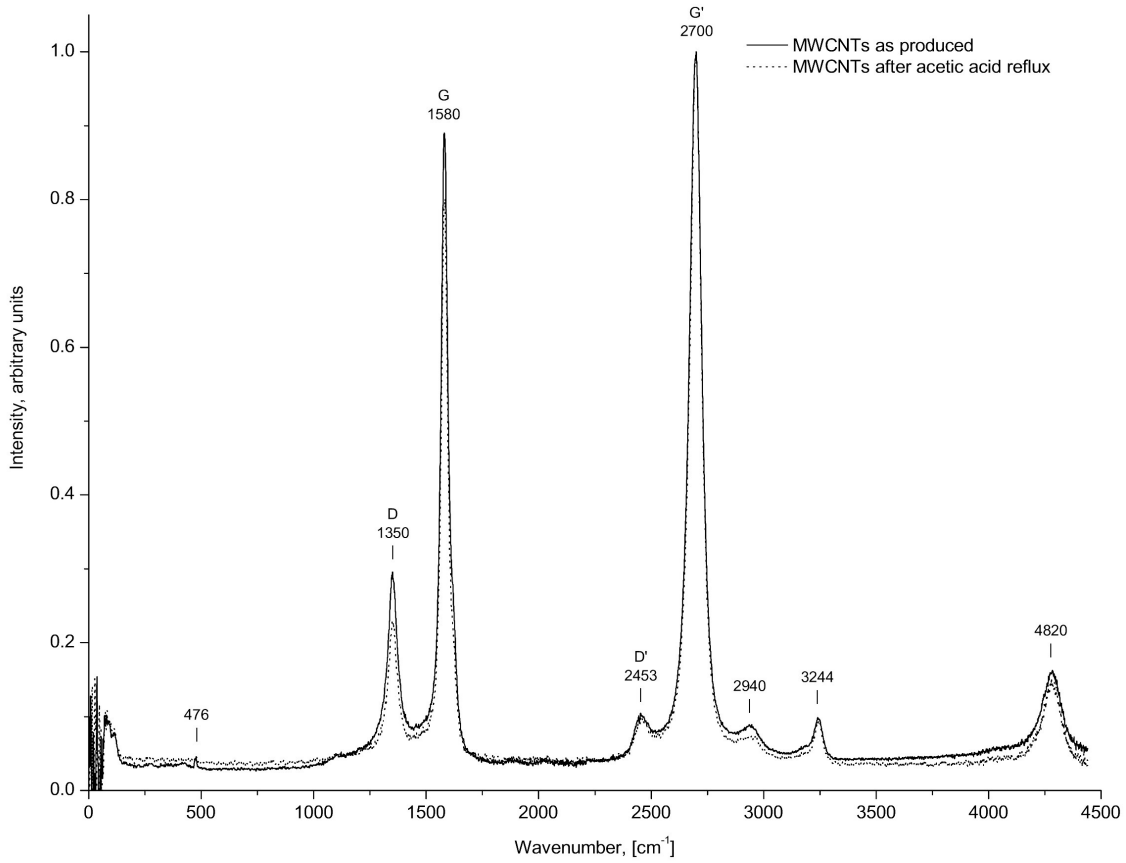

Figure 2.6: Raman spectrums of MWCNTs before and after their acidic treatment. It is shown how the D-band diminished in the MWCNTs after their reflux in an aqueous solution of CH_3COOH (67% v).

I_D/I_G ratio also decreases, from 0.32 ± 0.1 to 0.29 ± 0.01. Probably this treatment is "cleaning" the tubes from possible amorphous carbon deposited on them during their synthesis, which could also explain the reduction of I_D/I_G.

2.2.1.2 Methodology for depositing metallic clusters on MWNTs-CN_x using coordination salts

Once dispersion of MWNTs-CN_x was achieved, a procedure for attaching metallic clusters on the N-doped carbon nanotubes using coordination salts was developed.

Although one of the best dispersions of MWNTs-CN_x was obtained in a concentrated acetic acid, these conditions were not selected because it was difficult to dissolve completely the coordination salt employed in the process. This is due to the

high ionic charge of the medium that prevents the dissolution of more electrolytes. Therefore, an acetic acid of ca. 50 v % in distilled water, was used for dispersing MWNTs-CN_x ultrasonically in order to enhance the dissolution of electrolytes in the medium.

Several attempts on adding directly the coordination salt and its dissolution in water to the dispersed MWNTs-CN_x were carried out. The addition of an aqueous solution of the $K_3[Fe(CN)_6]$ into the MWNTs-CN_x dispersion was preferred for establishing the final standard procedure, because it does not require an additional sonication process for ensuring an efficient dispersion of the salt in the media with MWNTs-CN_x.

In order to achieve metallic cluster deposition on MWNTs-CN_x, three steps are required: (*i*) the protonation of N sites in MWNTs-CN_x, (*ii*) the coordination salt interaction with MWNTs-CN_x and, (*iii*) the breaking of the inner coordination sphere of the salt. Therefore we proposed different experimental procedure stages that allowed us to achieve these requirements. In fig. 2.7; these stages are depicted for potassium hexacyanoferrate(III), $K_3[Fe(CN)_6]$, a coordination salt selected for iron deposition on MWNTs-CN_x.

The experimental procedure developed for attaching Fe clusters on MWNTs-CN_x consists of the following steps:

1. An acidic solution (CH_3COOH/H_2O with a 2:1 ratio in volume) was prepared. Optionally, this solution was bubbled with N_2(g) for displacing dissolved O_2.

2. Subsequently, 10 mL of this solution were added to previously weighted MWNTs-CN_x (about 10 mg in a typical experiment). This mixture then was sonicated by 1 h to ensure a complete dispersion and detachment of the arrays of MWNTs-CN_x.

3. A known quantity of coordination salt dissolved in 2.5 mL of water was added to the MWNTs-CN_x acidic dispersion drop by drop under continuous stirring. This volume of added water was selected in order to obtain a concentration of

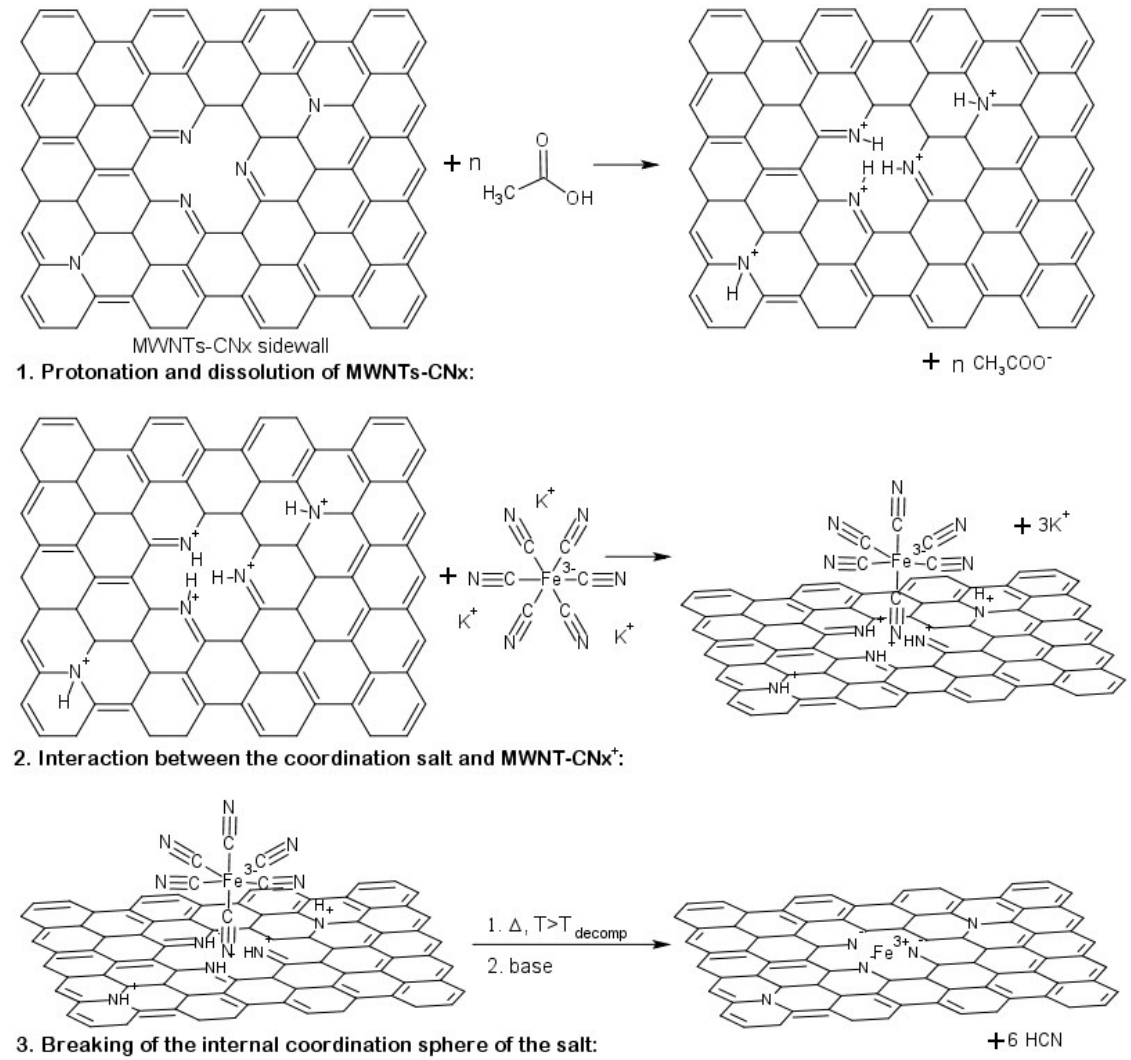

Figure 2.7: Proposed reaction scheme between MWNTs-CN$_x$ and coordination salts. Schematic representation of the reactions proposed for attaching metallic clusters to MWNTs-CN$_x$. **1)** In the *first step* we expect that the acidic medium promotes the protonation of nitrogen sites in the nanotubes, that besides of promoting a positive charge on them, this aids the efficient dispersion of the MWNTs-CN$_x$ in the protic medium. **2)** The coordination salt is added expecting some kind of interaction between the negative inner coordination sphere and the protonated sites in MWNTs-CN$_x$. **3)** The last step consists of the decomposition of the coordination sphere, leaving the metal in the hexagonal lattice. In the special case of the potassium hexacyanoferrate(III), the decomposition of its inner sphere produces HCN that is a gaseous compound.

$\sim$50% in acetic acid in the dispersion.

4. The system was refluxed under continuous stirring in an open system (see fig. 2.8) at a set temperature under an Ar flow until the sample dried. The Ar flow was kept low just to ensure an inert atmosphere inside the refluxing

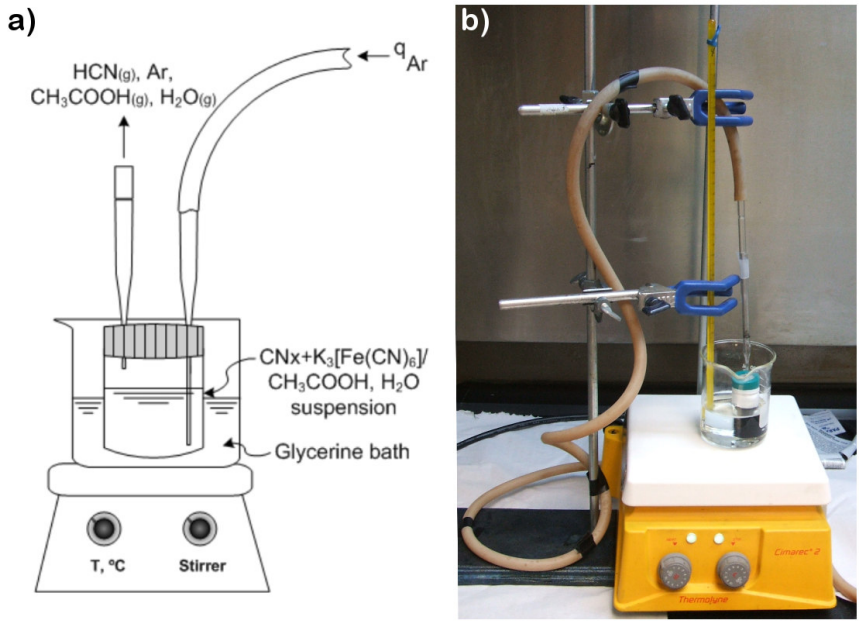

Figure 2.8: Experimental open reflux setup system for MWNTs-CN_x reaction with coordination salts. **a)** Scheme of the system used for the open reflux of MWNTs-CN_x and the coordination salt within an acidic medium. **b)** Picture of the experimental setup used in the laboratory.

system. The target temperature was varied with the coordination salt used. Usually this temperature was chosen, when possible, to be higher than the decomposition temperature of the coordination compound but lower than the boiling point of the aqueous acidic solution (ca. 118°C).

5. The final product was recuperated by scraping the base of the vessel used for the refluxing treatment.

A refluxing system was selected since it was found a better interaction between the MWNTs-CN_x and the coordination salt than when the system was only heated in an oven. This could probably be because during the refluxing process, there is more contact between both species due to an increment in the convective mass transport.

MWNTs-CN_x used through this thesis work were synthesized by a conventional *chemical vapor deposition (CVD)* procedure described elsewhere [10–12]. Specifically, for synthesizing MWNTs-CN_x, a solution of ferrocene, $Fe(\eta^5 - C_5H_5)_2$ (Aldrich,

98%), (5% wt) in benzylamine, $C_6H_6CH_2NH_2$ (Aldrich, 99%) was sprayed inside a quartz tube contained in a two stage furnace at 800 °C in the presence of flowing Ar. MWCNTs, used as control in some stages of this research, were also produced by a CVD process. Their synthesis was achieved by pyrolysis of a ferrocene (10 wt %) in toluene, C_7H_8 (Fermont 99.9%), solution in a two stage furnance at 800 °C in an Ar atmosphere.

The MWNTs-CN_x, as produced, were treated with the procedures described in page 48. As an approximation, the weight of MWCNTs and MWNTs-CN_x was converted to carbon moles, and then this quantity was correlated with the iron supplied by the coordinated salt (1 mol Fe/mol $K_3[Fe(CN)_6]$) for maintaining a constant ratio of 0.23 mol Fe (from potassium hexacyanoferrate(III))/mol C (supplied from MWNTs-CN_x) during all the experiments. Other atomic Fe/C ratios such as 0.06 and 0.46 were also tested for finding optimal reactive conditions.

The products were characterized by scanning electron microscopy (SEM) using a FEI FEG-XL30, field emission operating at acceleration voltages below 23 keV and equipped with an EDS detector, used to perform elemental microanalysis of the products.

2.2.2 Results and Discussion: Iron Deposits on MWNTs-CN_x using $K_3[Fe(CN)_6]$

The results for the deposition of iron on MWNTs-CN_x using potassium hexacyanoferrate(III) are shown in fig. 2.9, and the control experiments on MWCNTs are depicted in fig. 2.10.

Figure 2.9*a* shows a SEM image of as-produced MWNTs-CN_x and its corresponding EDX spectrum in 2.9*b*; the atomic percentage measurements in the EDX are reported for reference (90.80% C, 1.39% Fe and 7.86% O). Due to the low nitrogen-doping percentage in the MWNTs-CN_x used, estimated to be of 4 at % [13], and the possible existence of an overlaying between the C and N peaks, the signal

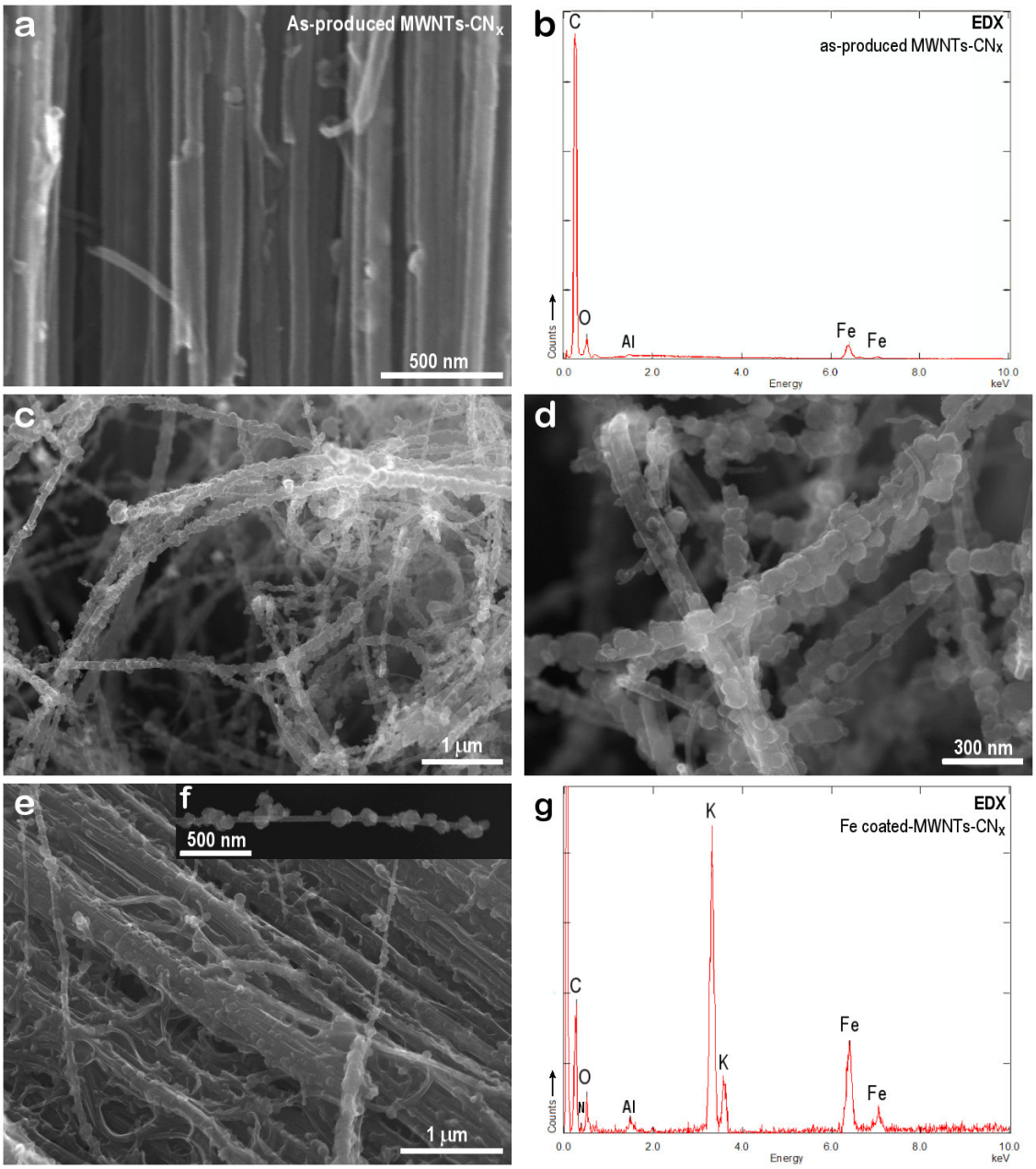

Figure 2.9: SEM images of MWNTs-CN_x before and after their treatment with $K_3[Fe(CN)_6]$. a) SEM image of MWNTs-CN_x before any treatment. **b)** EDX spectrum of the MWNTs-CN_x used, shown in *a.* Atomic quantifications gave 90.80% C, 1.39% Fe and 7.86% O. **c)** MWNTs-CN_x after treatment with $K_3[Fe(CN)_6]$ in acidic medium. **d)** Close-up of *c.* An important interaction can be noted. **e)** Zone where tubes are agglomerated appearing wet. **f)** Approach to a carbon nanotube showing the deposit of particles on it. **g)** EDX spectrum of the final product obtained. Atomic percentages for the product indicate 57.76% C, 13.47% K, 10.42% O, 9.40% N and 8.97% Fe.

of nitrogen can not be detected during the EDX analysis.

The products obtained after the treatment proposed in section 2.2.1.2 can be

visualized in figs. 2.9*b* to *f*. An interaction between the particles and the MWNTs-CN_x is observed in these images. Metal particles tend to deposit on the surface of nanotubes. Figure 2.9*f* shows a magnification of a MWNT-CN_x with particles deposited on the surface. Some parts of the sample seemed to be wet by a layer that kept together bundles of MWNTs-CN_x (see fig. 2.9*e*). The EDX analysis of this "wet" product (fig. 2.9*g*) exhibit an increasing in the relative signal of Fe, and the emergence of those for K and N. The nitrogen signal recorded is mainly due to the coordination salt (in a ratio 1:1, respect to C). Values of the atomic percentages in 2.9*g* are 57.76% C, 13.47% K, 10.42% O, 9.40% N and 8.97% Fe. These data confirmed that the quantity of Fe increased after the acidic treatment of MWNTs-CN_x in presence of the $K_3[Fe(CN)_6]$.

The results of the control with MWCNTs using similar experimental conditions (see fig. 2.10) reveal that, the salt compound does not exhibit a high interaction with the MWCNTs. A typical image of the MWCNTs before treatment is shown in fig. 2.10*a*. Its corresponding EDX spectrum is shown in fig. 2.10*b*. EDAX analysis displays a composition of 92.87 at % C, 6.20% at Fe and 0.92% at O in the sample. Since the sample mount is made of Al its signal appears in the EDX spectrum just like in the case of MWNTs-CN_x EDX. In fig. 2.10*c*, cubic particles can be easily identified, and it can also be emphasized that they do not have a strong interaction with the carbon nanotubes. These cubic structures are probably formed during the slow cooling of the sample after the drying process, when the refluxing finished. However, as observed in figs. 2.10*c*-*e*, the crystals are mixed with the nanotubes but are not really interacting with them. In order to ensure the nature of these particles, an EDX spectrum of the final product was recorded (fig. 2.10*f*). The characteristic signals for C, N, K, O and Fe (in both transitions K (at 6.403 keV) and L (0.705 keV)) are present, and the atomic percentages measured corresponded to 62.23% C, 19.21% N, 7.59% O, 5.99% K and 4.99% Fe.

An EDX analysis of the potassium hexacyanoferrate(III) was carried out for comparison. This spectrum is depicted in fig. 2.11. Atomic percentage

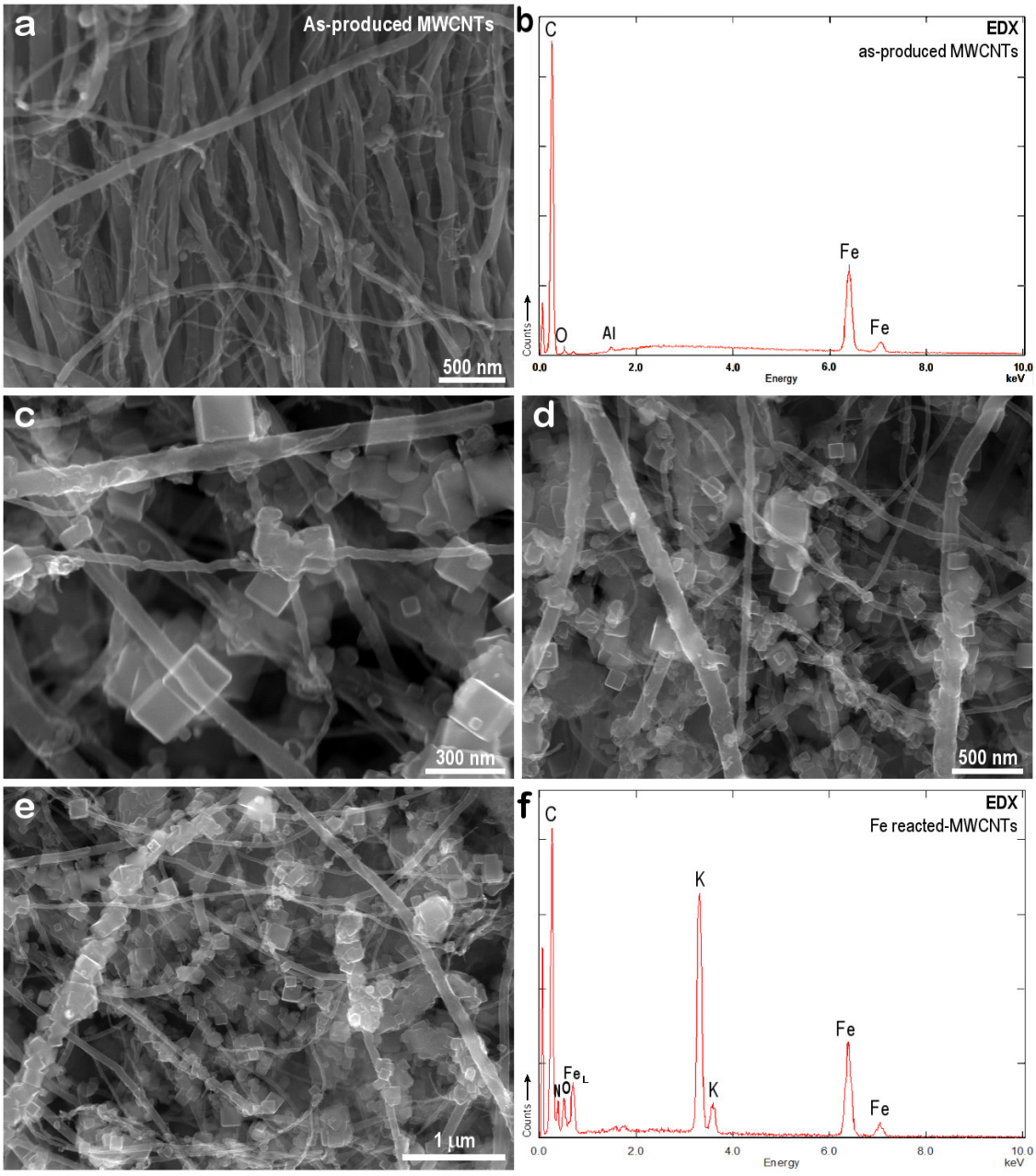

Figure 2.10: SEM images of MWCNTs before and after their treatment with $K_3[Fe(CN)_6]$**. a)** SEM image of as-produced MWCNTs. **b)** EDX spectrum of as-produced MWCNTs used shown in *a*. Atomic quantifications revealed 92.87% C, 6.20% Fe and 0.92% O. Al signal comes from the specimen holder used during the analysis. **c)** MWCNTs after treatment with $K_3[Fe(CN)_6]$ in acidic medium. Cubic structures are presumably $K_3[Fe(CN)_6]$ crystals. **d)** and **e)** Different magnifications that show the carbon nanotubes and the coordination salt crystals. **g)** EDX spectrum of the mixed products (*i.e.* MWCNTs and potassium ferricyanide crystals). Atomic percentages for the product indicate 62.23% C, 19.21% N, 7.59% O, 5.99% K and 4.99% Fe.

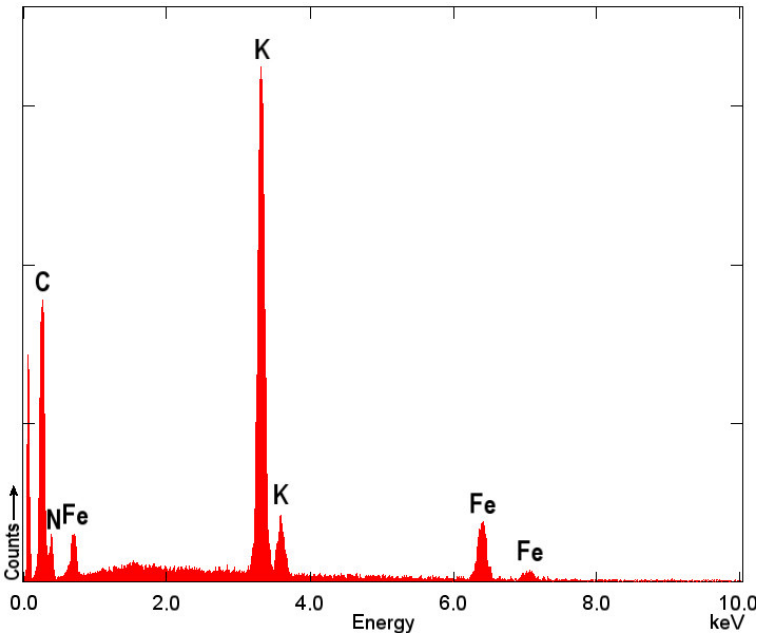

Figure 2.11: EDX spectrum of $K_3[Fe(CN)_6]$. EDAX atomic quantification for this salt exhibits 48.35% C, 20.35% N, 22.93% K and 8.37% Fe. Acoording with these data, the ratios C/Fe, K/Fe and C/N correspond to 5.78, 2.74 and 2.38 respectively, meanwhile the theoretical expectations indicate that they should be of 6, 3 and 1.

measurements corresponding to this case are 48.35% C, 20.35% N, 22.93% K and 8.37% Fe. For the coordination salt used, $K_3[Fe(CN)_6]$, the ratio expected between their elements, is 3:1 for K:Fe and 6:1 in the case of C:Fe and N:Fe. The experimental ratios found in our case were 5.78 for C/Fe, and 2.74 for K/Fe; similar to the theoretical values. However, the experimental C/N ratio is only 2.38, which significantly differs of the expected value of 1. These results indicates that the nitrogen could be underestimated during the analysis. We note a similarity between the EDX of $K_3[Fe(CN)_6]$ and that obtained in fig. 2.10*f* for the crystals mixed with MWCNTs.

The refluxing temperature in these experiments was maintained at 110 °C. This value is below the boiling point of the acidic solution used. The decomposition temperature for the coordination sphere of the hexacyanoferrate(III) ion, $[Fe(CN)_6]^{\equiv}$, is around 310 °C, therefore, the coordination sphere was not fully broken during the refluxing process. In order to achieve the complete dissociation of the coordination sphere, a subsequent annealing of this product up to 400 °C within

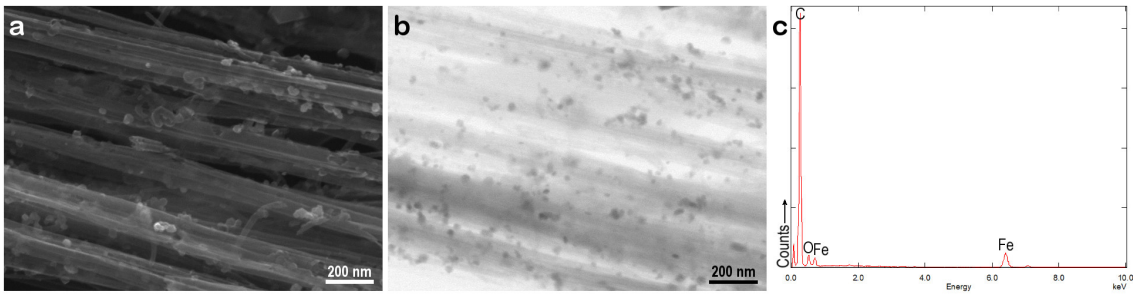

Figure 2.12: STEM image of the MWNTs-CN_x reacted with $K_3[Fe(CN)_6]$ after annealing at 400 °C in Ar atmosphere. a) SEM image of MWNTs-CN_x covered by iron particles. **b)** Bright field STEM image of MWNTs-CN_x covered by iron particles (from image *a*). **c)** EDX of the sample obtained. Quantifications gave 92.78% at C, 4.86% at O and 2.36% at Fe. No potassium signal present.

and Ar atmosphere was required. The subproduct generated when the coordination sphere breaks is the hydrocyanic acid, HCN; a gaseous compound.

Following the statement mentioned earlier, we took a sample of iron already deposited on MWNTs-CN_x (with molar ratio of 0.23 mol $Fe_{K_3[Fe(CN)_6]}$/mol C_{CN_x}) and subjected to an annealing treatment in an Ar flow (0.33 L/min) at 400 °C for 10 min. When the temperature reached 400 °C, an overshooting up to 480 °C was noted, but the temperature was fastened lowered, in about 3 min to the target one. Before this thermal treatment, the product exhibited a "bluish" color, but, after treatment, this color changed into black.

After recovering, the product was washed in distilled water aided by mechanical stirring and subsequent centrifugation (4,000 rpm). This process was repeated three times. Finally, the product was dried in air inside a convective oven at 60 °C. The aim of this washing process was to remove the remaining potassium in the sample by its dissolution in water. If iron is released during the annealing and remains deposited on the sample, it is expected to be insoluble in water because it would be exhibiting an oxidization state of 0, which does not allow the dissolution of the metal in this solvent.

STEM imaging was carried out on the sample (see fig. 2.12). The SEM image, fig. 2.12*a*, clearly shows the presence of particles on the surface of the MWNTs-CN_x. Bright field STEM image of the same zone, indicates that they possess a higher

atomic mass than carbon. EDX analysis (fig. 2.12*c*) confirms that we "cleaned" the potassium from the iron deposits on MWNTs-CN_x.

It was also observed that during the cleaning process, the particles of iron were oxidized (a molar ratio of 2.06 mol O/mol Fe is obtained from EDX quantifications), or at least its surface, by the air and dissolved oxygen in water. In addition, the SEM observations seem to indicate that a percentage of the deposited iron was lost during the distilled water washings, probably because a not reducing medium (*i.e.* Ar/H_2 mixture) was used during annealing, and not all the Fe was able to go to an oxidization state of zero. However this was selected to make further comparisons with the deposits of other metals.

With the last result we only specify the possibility of obtaining iron deposits on MWNTs-CN_x without potassium. This element comes from the coordination salt used for the deposition process.

EDX line scans analysis for the deposit experiments as obtained (without annealing and washing) were performed in a TEM/SEM Phillips CM200-FEG at 200 kV (located in the John M. Cowley Center for High Resolution Electron Microscopy (CHREM) at Arizona State University, ASU). The results obtained are shown in fig. 2.13. Dark field Scanning Transmission Electron Microscopy (STEM) performed on the sample can be seen in fig. 2.13*a*. In this technique the electrons dispersed are detected, so the brighter zones corresponds to the elements of higher atomic numbers.

EDX line scans in direction of the arrow were recorded (see fig. 2.13*b*). It is easily observed how the elemental composition across the nanotube changes. Signals of iron (1.72% at) and oxygen (3.20% at) appear as the probe comes near to the particle located on the nanotube, identified by a spot in bright color crossed in path (*i*). Meanwhile, outside of this region, only carbon (94.35% at) potassium (0.184% at) are detected. The percentages reported are measured along the vertical line in the EDX spectrum (2.13*b*); which corresponds to the marked position in the STEM images. This location was selected because of the high signal of iron detected. The

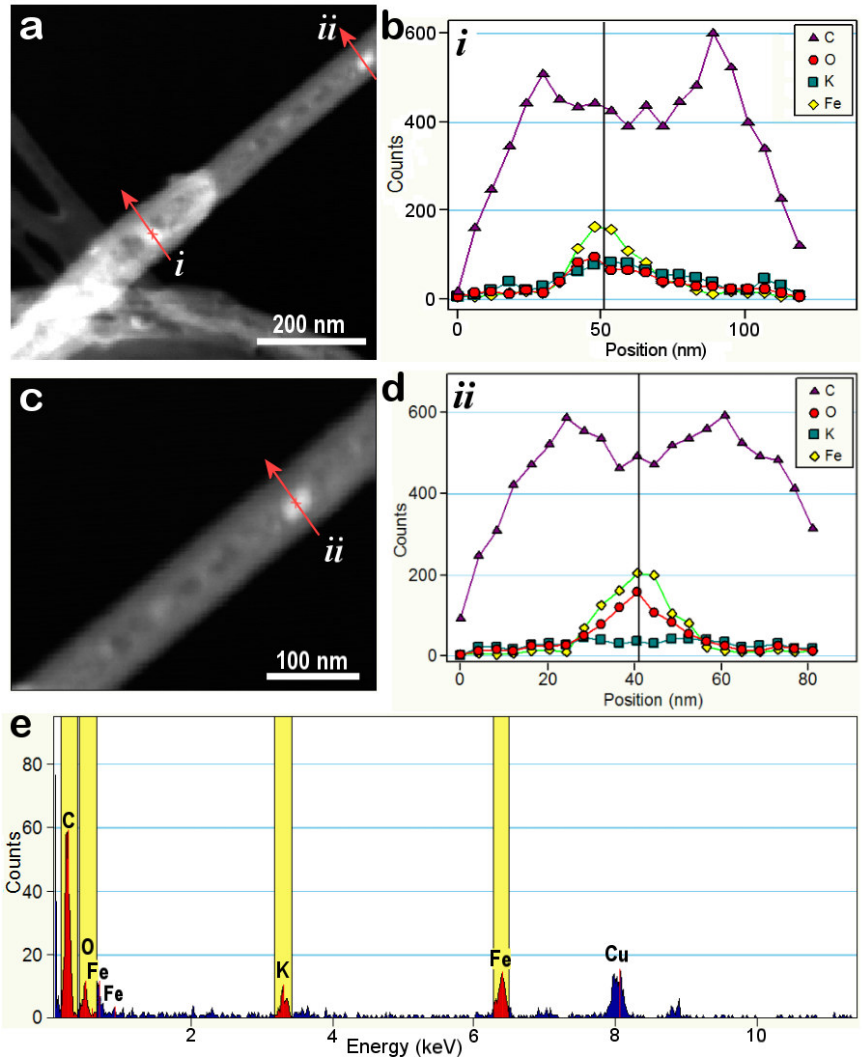

Figure 2.13: EDX line scans of the MWNTs-CN_x reacted with $K_3[Fe(CN)_6]$. **a)** STEM image where two paths for the EDX line analysis are pointed; **b)** EDX line scan of (i) in *a*. Quantifications at the cross mark for the elements detected, in atomic percentage, are 94.35% C, 3.20% O, 1.72% Fe and 0.727% K. **c)** STEM image of a close up of (ii) path in *a*. **d)** EDX line scan of (ii) shown in *a* and *c*. Atomic quantifications give the values of 92.21% C, 5.72% O, 1.88% Fe and 0.190% K. **e)** EDX spectrum at the cross marked point in (i). Cu signal comes from the TEM grid used for mounting the sample.

corresponding EDX local spectrum is shown in fig. 2.13*e*, in which the Cu signal comes from the TEM grid used during the analysis.

The particle crossed in the path (ii) (fig. 2.13*c*) exhibits a similar elemental (fig. 2.13*d*) composition (1.88% at Fe and 5.72% at O). The ratios between the percentages of O to Fe detected were 1.86 and 3.04 in (i) and (ii) respectively.

These results imply that the particles detected on the nanotubes are composed by a kind of iron oxide, probably Fe_2O_3 (with O/Fe ratio of 1.5). This oxide was most probably formed during the storage (in air) of the product. It is very well known that iron in contact with air readily forms Fe_2O_3. Since the experimental ratios are higher of the expected, a presence of additional oxygen of those forming the iron(III) oxide is denoted. This presence could be probably due to adsorption of O on the particle surface. It is noteworthy that almost not oxygen signal was detected on the carbon nanotube surface, since this was concentrated only on the surface of the particles.

High Resolution Transmission Microscopy (HRTEM) was also carried out to this sample using a JEOL JEM 4000EX (TEM) at 400 kV (at CHREM in ASU). The focus of this characterization was the observation of nanotubes' surface and their final morphology.

The general morphology of MWNTs-CN_x after their treatment with coordination salts can be appreciated in fig. 2.14*a* and *b*. Here a layer on the whole external surface of the MWNT-CN_x can be clearly observed, meanwhile their internal surface seems to be clean. A MWNT-CN_x is in fig. 2.14*c* shows the apparent wetting of its external surface. Close-ups of this surface are displayed in figs. 2.14*d* and *e*. Some atomic planes of the deposit performed can be observed in 2.14*d* besides the graphitic planes that form the external shell of the MWNT-CN_x. Fast Fourier Transforms (FFT) were performed on the areas delimited by the dashed rectangles marked as (*i*), (*ii*) and (*iii*) in order to obtain their inter-atomic plane distance. The graphene (002) planes in (*iii*) were used as a reference and was considered to be separated by 3.4 Å. Interplanar spaces measured in (*i*) are ca. 2.9 Å (at 136.4° with respect the surface of MWNT-CN_x) for one direction in body cubic center structure (*bcc*); and 3.1 Å for the another direction (at 20.6° respect to surface of MWNT-CN_x). These planes correspond only to (110), ($\bar{1}$10), (1$\bar{1}$0) and ($\overline{11}$0); and are obtained when electrons or X-rays fall on the (001) face of a *bcc* structure and diffract in a pattern.

For (*ii*), these distances correspond to 3.1 Å (at 76° respect to MWNT-CN_x

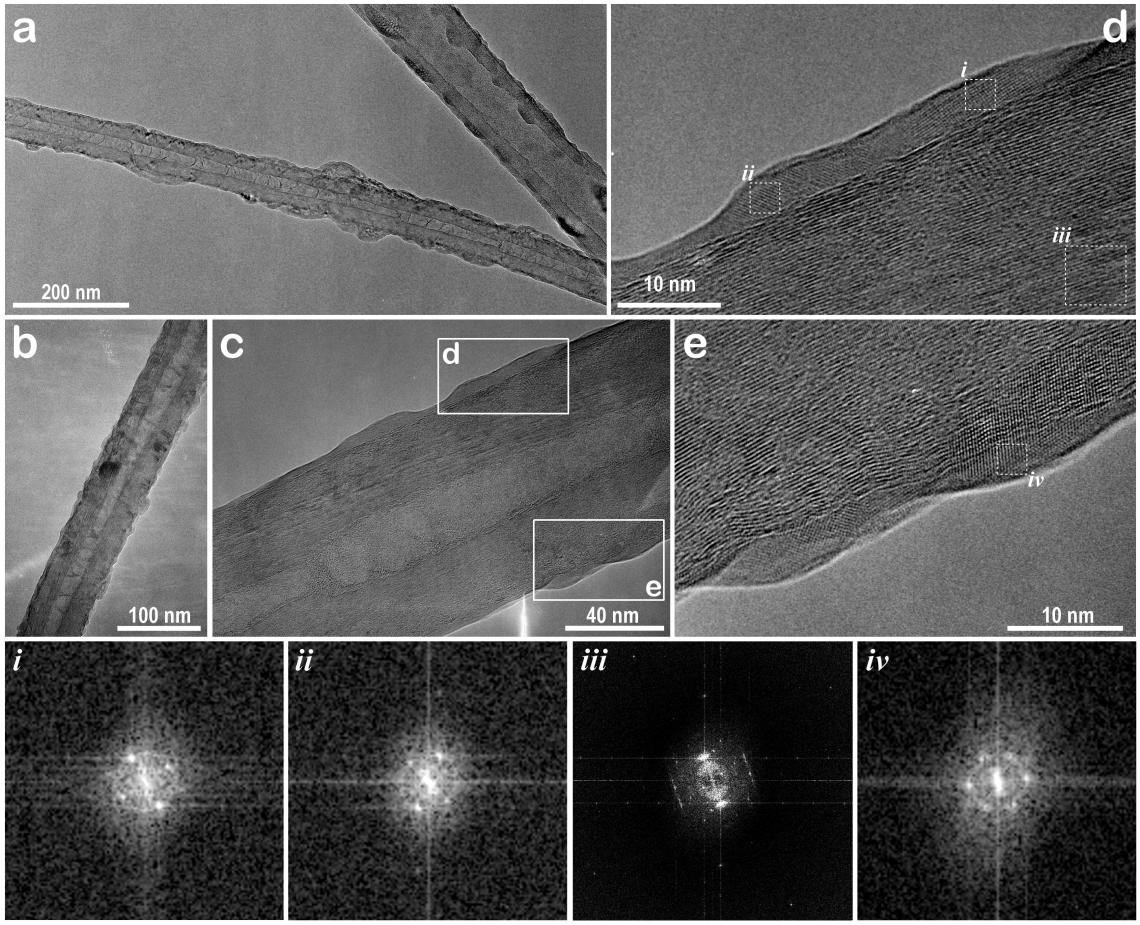

Figure 2.14: HRTEM images of the MWNTs-CN_x reacted with $K_3[Fe(CN)_6]$. **a)** HRTEM image of MWNTs-CN_x reacted with $K_3[Fe(CN)_6]$ shown in SEM images at fig. 2.9. The surface of MWNTs-CN_x seem to be wet and rugous which is indicative of the existence of some kind of coating layer on the nanotube surface. **b)** HRTEM image of a MWNTs-CN_x where the high rugousity of the surface is easily appreciated. **c)** A MWNTs-CN_x HRTEM image where the graphene sheets that form the walls of the nanotube can be observed. **d)** Close-up of the region marked as *d* in *c*. Fast Fourier Transforms (FFT) of diverse zones of the deposit on the surface of MWNTs-CN_x are shown in the insets (*i*) and (*ii*). (*iii*) shows the FFT of the graphene planes that form the walls of nanotube. **e)** Close-up of the region identified as *e* in *c*. Planes of particles wetting the outer surface of MWNTs-CN_x are shown. FFT of the zone inside the dash rectangle (*iv*) is shown in the inset.

surface) and 3.0 Å (at 8° respect to MWNT-CN_x). Other crystalline planes of the particles were found in fig. 2.14*e* and their respective measurements were done on its FFT shown in (*iv*). The mean interlayer spacing found (3.07 Å) is close to that exhibited by the plane (111) of K *bcc* (3.02 Å). The presence of this metal, which exhibit low surface tension of ca. 110 m/N [14], could explain the wet appearance on the MWNT-CN_x surface.

Interlayer spacing in other particles have given interplanar distances of 2.01 Å, 2.64 Å and 2.89 Å. These distances are in agreement with the planes (110) of Fe *bcc* (2.01 Å), (200) of K *bcc* (2.61 Å) and (210) of K_2O *fcc* (2.88 Å). Distances reported inside parenthesis were calculated from the simulation in software Cerius[2] of the crystallographic data obtained from [15].

With these values and the EDX line scans, it is reasonable to establish that one of the present phases in the particles belong to K *bcc*, while K_2O *fcc* and Fe *bcc* in some others are observed. It is possible to think that the oxygen detected by EDX is related only to the external surface of these particles, and not to the clusters. Therefore, we believe that the oxidization occurred on the surface of the final product and not during the synthesis. This is in agreement with the expected results from our experimental setup which maintained inert atmosphere during the iron deposition for avoiding its oxidization.

2.3 Reactions between MWNTs-CN_x and Simple Iron Salts

In this section we take advantage of the possible local nucleophilic properties of the N pyridinic doping site in MWNTs-CN_x. As depicted in section 2.1, the pyridines also exhibit nucleophilic properties and react with alkyl halides to form quaternary ammonium salts by sharing its electronic pair. [3]

In order to promote the nucleophilic behavior of the MWNTs-CN_x, an aprotic solvent was selected for carrying out this reaction. Dimethylformamide (DMF), $HCON(CH_3)_2$, is a widely used solvent for promoting S_N2 reactions, of the kind:

$$R{-}W \xrightarrow{:Z} [Z{\cdots}R{\cdots}W] \longrightarrow Z{-}R + :W \qquad (R\,2.3)$$

This reaction is favored by solvents that stabilize (and thus deactivate) the anionic nucleophile *least*, that is aprotic solvents or solvents of low polarity, as with phase-

transfer catalysis. [7]

2.3.1 Experimental Methodology

As DMF is an organic solvent it was expected a homogeneous dispersion of MWNTs-CN_x. The iron promoter selected in this case, is a simple salt of the metal, iron(III) chloride, $FeCl_3$. An isolation of the metallic cation was performed in order to avoid interferences of the chloride counter-ions. This method was achieved by the following procedure:

1. 106 mL of NH_4OH (conc) were added to 25 mL of an aqueous solution 1 F of $FeCl_3$ in order to promote the precipitation of Fe as $Fe(OH)_3$ according the reaction:

$$FeCl_3 + 3\,NH_4OH \longrightarrow Fe(OH)_3\downarrow + 3\,NH_4^+ + 3\,Cl^- \qquad (R\,2.4)$$

2. This solution was centrifugated at a relative centrifugal force (rfc) of $2500\times g$ (g is the gravity constant, 9.8066 m/s^2 at sea level), and washed with distilled water three times.

3. The precipitate was dissolved by an aqueous solution of CH_3COOH (2 v of water: 1 v of acetic acid), pH=3. In this case, the molar ratio between acetic acid and $Fe(OH)_3$ was selected to be 3 in order to accomplish the reaction R 2.5.

$$Fe(OH)_3 + 3\,CH_3OOH \longrightarrow Fe^{+3} + \tfrac{3}{2}H_2O + 3\,CH_3COO^- \qquad (R\,2.5)$$

4. This final solution, exhibiting a $[Fe^{+3}]$=0.10 M and $[CH_3COOH]$=2.82 F, was stored and used as a mother solution for posterior dissolution preparation.

Once the metallic cation was isolated, a procedure for achieving an interaction between the Fe^{+3} and MWNTs-CN_x was performed as follows:

1. Several solutions of Fe^{+3} ranged from 5 at % to 15 at % (mol Fe respect to mol C from MWNTs-CN_x) were obtained from dissolution in distilled water

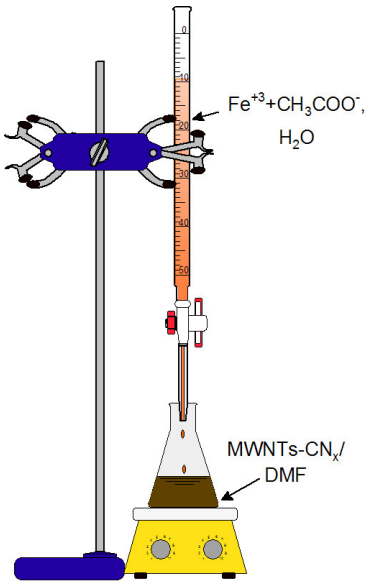

Figure 2.15: Experimental setup for the reaction between MWNTs-CN_x and Fe^{+3} in acidic medium. Scheme of the experimental setup arranged to use simple salts.

of an aliquot of the mother solution described above. The final volume of ferric solution used was always calculated to be ca. 5 mL. This solution was identified as *solution I*.

2. Separately, 10-16 mg of MWNTs-CN_x were dispersed in 15 mL of DMF (Sigma-Aldrich, 99%) by their immersion in an ultrasonic bath (Cole-Parmer model 8891, 42 kHz) along 1 h (*Solution II*).

3. The acidic solution of iron (solution I) was added by slow dropping onto the dispersed MWNTs-CN_x (solution II) under continuous stirring at room temperature (see fig. 2.15).

4. Once the dropping finished, this system was then dried in a hot plate at ca. 80 °C under continuous stirring. The final product was recovered by scrapping.

2.3.1.1 Characterization Parameters

The results obtained by these experiments were characterized by SEM and STEM imaging performed in a FEI FEG-XL30, field emission operating at acceleration voltages below 30 keV, and equipped with an EDAX EDS detector.

2.3.2 Results and Discussion: Iron Deposits on MWNTs-CN_x using acidic solution of Fe^{+3}

Dispersion in DMF worked satisfactorily for our objectives aiming to disperse the nanotubes before the treatment with the metallic iron cation. This procedure proved to be faster than the one that incorporates the use of coordination salts. The product obtained by this last method is also easier to scrape.

In this procedure, we are trying to react the MWNTs-CN_x with the iron cation alone; thus avoiding a posterior annealing for breaking a coordination sphere.

As it can be observed in fig. 2.16*a*, the N-doped carbon nanotubes seem to be more rugous when compared to pristine MWNTs-CN_x (see fig. 2.9*a*). It is remarkable how these tubes, despite of the fact that they seem rough, they are actually different from those reacted with $K_3[Fe(CN)_6]$. This difference could be due to a fine dispersion of the iron particles obtained by this procedure.

The EDX spectrum shown in fig. 2.16*b* displays a relative increment in the quantity of iron with respect to pristine MWNTs-CN_x (see fig. 2.9*b*). In the case of as-produced MWNTs-CN_x, the relative percentage of iron detected by EDX analysis was only 1.39 at % whereas; in the case of treated tubes with an acidic ferric medium, this value increased up to 12.49 at % Fe. These results confirm that there exists an interaction between the MWNTs-CN_x and the metallic cation added during the reaction.

In order to confirm these results, the sample was put on a copper support film to perform STEM imaging searching for iron particles deposited on MWNTs-CN_x. Bright field STEM image (fig. 2.16*c*) reveals small clusters formed by elements of higher atomic weight than carbon deposited on the surface of the nanotubes. Close-up images of the MWNTs-CN_x in the bright field mode can be observed in fig. 2.16*d*. In this image, the particles are clearly observed. The inset shows the dark field image of this picture. From the EDX analysis made, only the signal of iron was detected; therefore, we could deduce, that these are iron clusters. As the ratio between Fe

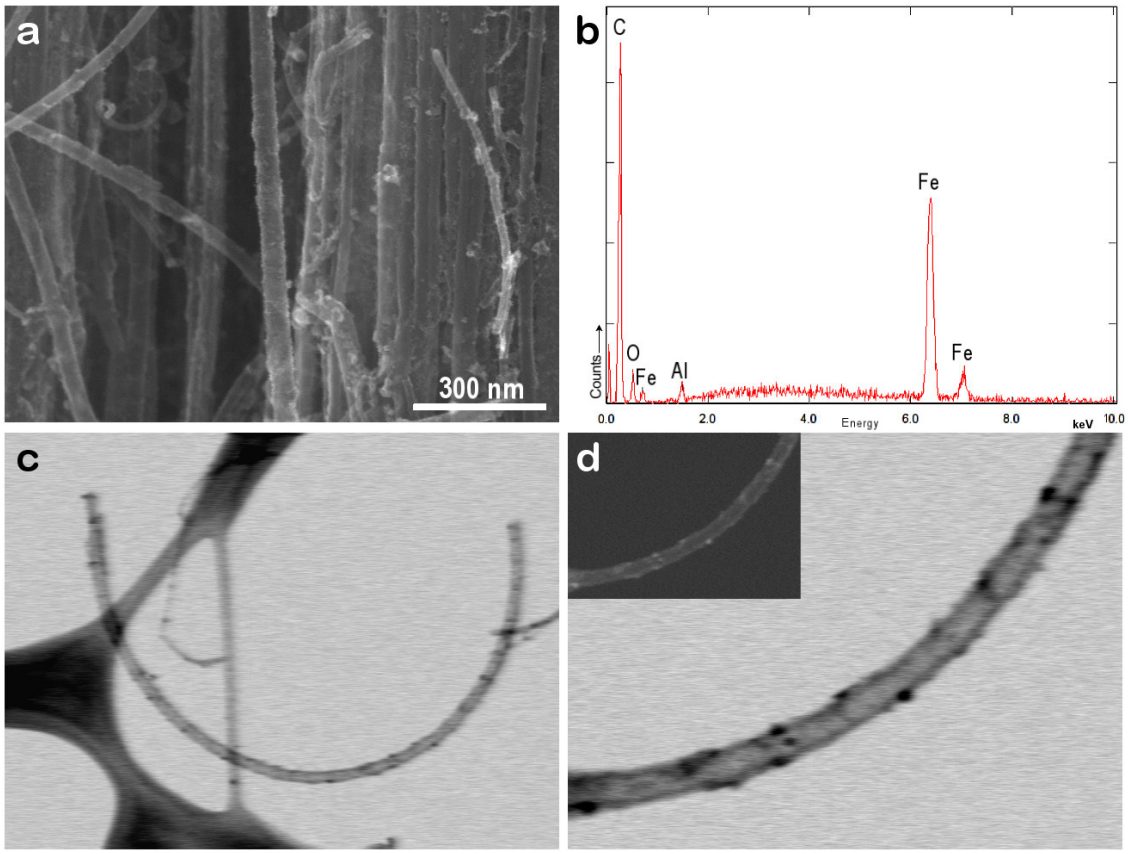

Figure 2.16: SEM and STEM images of MWNTs-CN_x reacted with Fe^{+3} in acidic medium. a) SEM image of the MWNTs-CN_x after their treatment with Fe^{+3} in acidic medium. **b)** EDX spectrum of the product. Elemental atomic quantifications are 83.81% C, 12.49% Fe and 3.71% O. Support mount for SEM specimens is made of Al. **c)** Bright field STEM image of a MWNTs-CN_x covered by small particles of iron. **d)** Close-up of the nanotube shown in *c*. Diverse particles can be deposited on the surface of the tubes. Dark field image is shown in the inset.

and O are about 3.37 $\frac{\text{mol Fe}}{\text{mol O}}$, the quantity of possible iron oxide is low like in the case of the iron deposited from $K_3[Fe(CN)_6]$.

2.4 Summary

We have presented results related to the deposition of iron particles on MWNTs-CN_x using two different approaches. These deposits have been characterized and studied using different techniques.

The methods developed for depositing iron nanoparticles in the sections 2.2.1.2

and 2.3.1 are exclusively for MWNTs-CN_x. The application of these procedures on MWCNTs resulted in poor interactions between the iron particles and the pure carbon nanotubes. Our results demonstrate that N-doped carbon nanotubes have indeed different surface properties to those of MWCNTs.

It is well known that the growth of carbon nanotubes by the CVD method requires catalyst nanoparticles of transition metals, usually elements located in the fourth period of the VIIIB group. That is, this procedure requires Fe, Co and Ni; a carbon feedstock, which is usually a hydrocarbon or CO at high temperatures. [16] On the other hand, metals such as Ag, Au, Pt and Pd are not appropriate for growing good quality CNTs from pyrolysis. [17] The peculiar ability of the first enumerated transition metals to form graphitic carbon is thought to be related to a combination of factors that include their catalytic activity for the decomposition of volatile carbon compounds, the formation of metastable carbides, and the diffusion of carbon through the metal particles. [16]

Therefore, it is possible that once having MWNTs-CN_x with Fe clusters deposited, the latter particles could catalyze the growing of new MWCNTs on the surface of MWNTs-CN_x. The results obtained of applying this idea are described in the following section.

2.5 Growth of Heterojunctions and New Carbon Nanotube Structures from MWNTs-CN_x coated with Iron Particles

Due to their high mechanical strength (see table 1.1 in page 6), CNTs are considered as ideal blocks for building new robust materials [18]. In addition, different nanoscale electronic devices could be generated by joining covalently carbon nanotubes exhibiting different chiralities or electronic properties. [19] It is

noteworthy that N-doped carbon nanotubes could also be used in the fabrication of composite or electronic devices. Theoretical studies indicate that these kind of doped carbon nanotubes act as electron donors [20] due to the fact that nitrogen has one electron more than carbon and tends to share it. Therefore, the fabrication of junctions using undoped and doped carbon nanotubes could be important in the production of Schottky diodes.

Interlinked two-dimensional (2D) and three-dimensional (3D) carbon nanotube networks are necessary in order to develop novel carbon-carbon composite materials with unique properties. [21–24]

However, it is still necessary to develop more efficient techniques for interconnecting carbon nanotubes. In this context, several successful studies in producing branched carbon nanotubes have been reported by different research groups. [25–31]

Some approaches used to interconnect nanotubes include the use of a high intensity electron beam that is able to weld carbon nanotubes. [27] Other methods such as CVD have been successful in creating Y-branching in MWCNTs and MWNTs-CN_x by pyrolysis of nickelocene ($Ni(\eta^5 - C_5H_5)_2$) in a thiophene (C_4H_4S) enriched Ar/H_2 flow; [25] hot-filament CVD of acetone/H_2 gas mixture in presence of cooper vapor; [32] and by titanium doped catalysts using a flow of ethene (C_2H_4), carried by N_2/H_2 in presence of Ti and B_2O_3 powders, [28] or by a co-injection of tetrakis(diethylamino)titanium ($C_{16}H_{40}N_4Ti$) with a mixture of ferrocene and xylene (C_8H_{10}) during the CVD process. [29] Direct current plasma-enhanced chemical vapor deposition (PECVD) on Ni films have also produced branched structures; [33] and conventional pyrolysis methods of ethyne (C_2H_2) have been used in pre-synthesized nanostructured channel templates for the growth of branched CNTs. [34]

In addition, heterojunctions and branches linking nitrogen-doped and non-doped carbon nanotubes have been synthesized by diverse methods such as microwave plasma-assisted CVD in N_2 or H_2/CH_4 [26]; pyrolysis of ferrocene and melamine powders in a sequential two-stage heating process; [30] and variations in the inlet

gas composition and flux during the CVD growth (with H_2 as carrier gas). [31]

Recently, Xi *et al.* [35] reported nanocable structures and branched-nanobelts formed by pyrolysis of ethylene glycol monoethyl ether ($CH_3CH_2O(CH_2)_2OH$) using Fe as catalyst in a stainless autoclave heated in an electric stove. High resolution TEM images of these cables reveal that the inner tubes present a lower crystallinity than the outer tubes.

In this section, we demonstrate that iron particles deposited in MWNTs-CN_x (in sections 2.2.2 and 2.3.2) can act as catalyst for growing carbon nanotubes, thus growing nanotube networks.

2.5.1 Experimental Methodology

We used Fe deposited on MWNTs-CN_x obtained from the approaches mentioned above. The treated MWNTs-CN_x were introduced in a CVD system to grow multiwalled-carbon nanotubes (MWCNTs). They were placed inside open alumina capsules in a typical CVD system for growing MWCNTs (fig. 2.17). [11; 36] The capsules were located in the middle part of the second furnace, under an Ar flow. Once the temperature in the furnace reached the target temperature (800 °C, 825 °C and 850 °C were tested), toluene, (Fermont 99.9%), without any ferrocene, was sprayed for different time steps (5-15 min) using an Ar flow of 0.3-0.5 L/min.

After this treatment, the MWNTs-CN_x used as a precursor changed from a "bluish" tone into a black color. A control experiment using MWNTs-CN_x without any previous deposition Fe treatment was also performed and their final products where compared with the rest of the samples produced.

The products obtained were analyzed using the following techniques: SEM (FEI SFEG-XL30) operating at 10-15 keV and equipped with an EDAX EDS detector, for elemental microanalysis. HRTEM (Field emission JEOL-JEM-3000F) with a 300 keV acceleration voltage and equipped with a Gatan 766 2D-DigiPEELS. Powder X-Ray Diffraction (XRD) in a Brucker D8, equipped with a Cu anode ($\lambda = 1.5406$ Å)

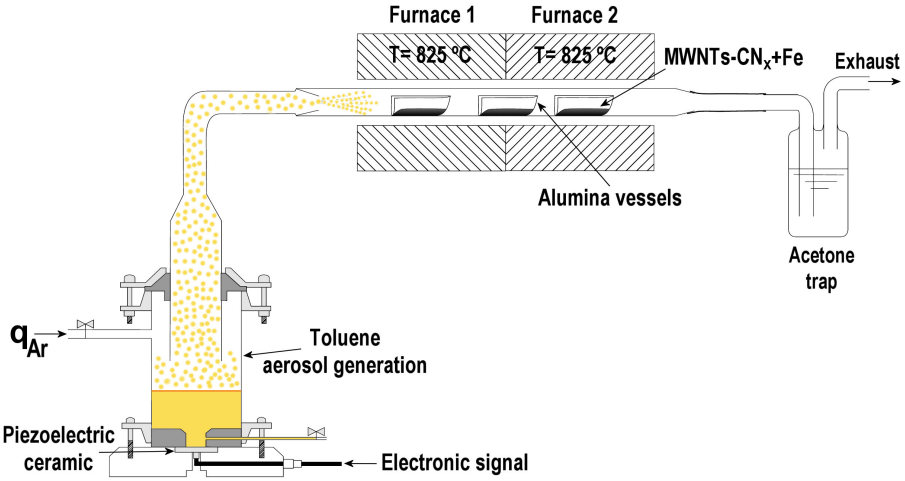

Figure 2.17: Experimental setup for producing nanotube heterojunctions and novel CNT structures. Pristine toluene was sprayed over MWNTs-CN_x coated with Fe under an Ar flow at 825° C.

operated at 35 kV, 25 mA and 293 K (angles 2θ varied from 10° to 110°).

Thermogravimetric analysis (TGA) were also performed in a Thermo Haake, Cahn VersaTherm HS in air using the following parameters:

1. A ramp of 10 °C/min from room temperature to 100 °C.
2. An isotherm of 10 min when temperature reaches 100 °C for ensuring the ambient humidity evaporation from the sample.
3. A ramp of 5 °C/min was set from 100 °C to 800 °C.
4. A last isotherm of 20 min at 800 °C was applied before cooling to room temperature.

2.5.2 Results and Discussion: CVD treatment of Iron deposited MWNTs-CN_x

Fig. 2.18*a* shows the result of the toluene CVD treatment over MWNTs-CN_x without any previous iron deposit. It is noteworthy, how its surface seems to be rough and covered by an amorphous carbon layer. It is clear that these tubes

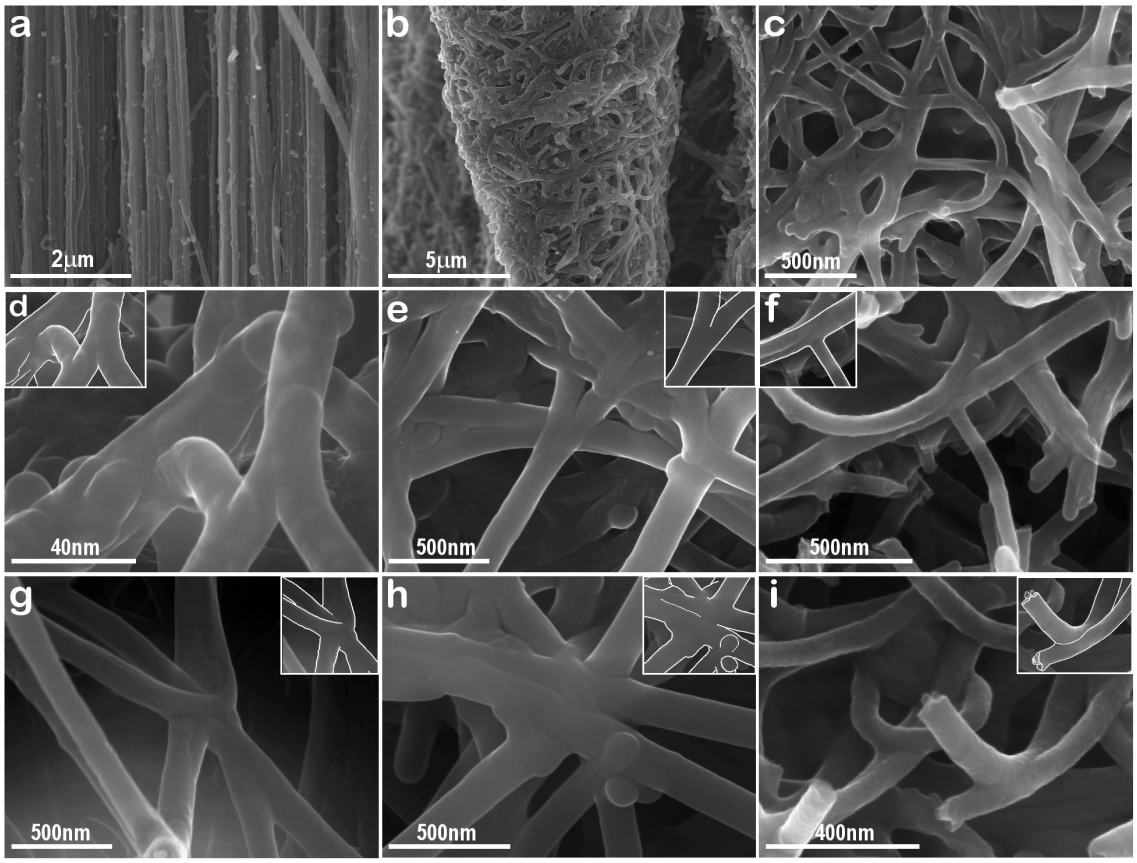

Figure 2.18: SEM images of MWNTs-CN_x treated with Fe after the CVD treatment. **a)** Pristine and alligned MWNTs-CN_x, used as control, after the CVD treatment. **b)** Product obtained after toluene CVD treatment on MWNTs-CN_x . **c)** Close-up of the obtained product in *b* showing the interconnections. **d)** and **e)** are images of Y-junctions. **f)** A T-junction. **g)** and **h)** are images of multijunction structures. **i)** An "on-junction" where a carbon nanotube seems to be joined on the other one.

are very different from the structures obtained after passing toluene over MWNTs-CN_x treated with iron. Figures 2.18*b*-*i* show different nanotube interconnections and branched nanotubes. Fig. 2.18*c* shows a close-up of the general compacted morphology found in the sample after the toluene CVD treatment. Different kind of junctions were identified by SEM in these products. Figures 2.18*d* and *e* show Y-junctions established between carbon nanotubes. Meanwhile T-type junctions can be also observed in fig. 2.18*f* (see inset) and multi-junction structures in figs. 2.18*g* and *h*.

The results presented above (in figs. 2.18 and 2.19), show that both iron deposition procedures were effective for creating catalyst particles over the MWNTs-

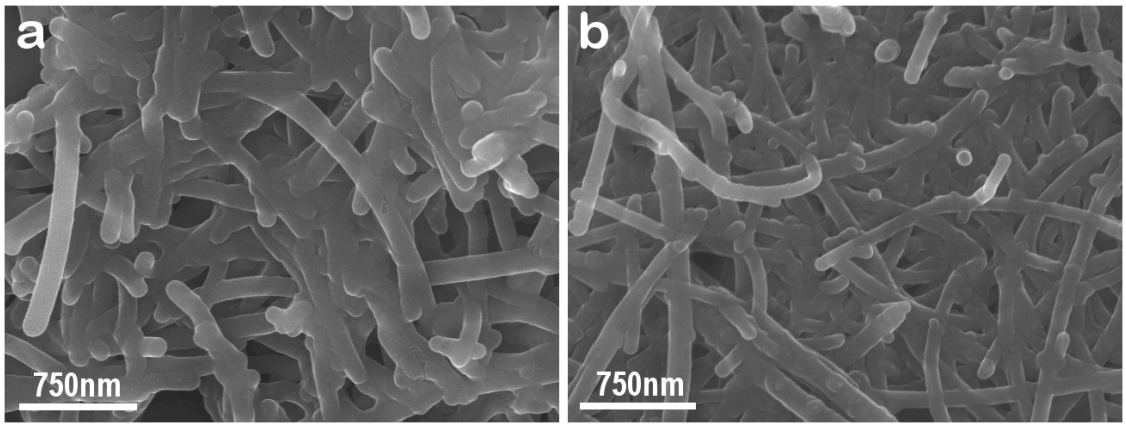

Figure 2.19: SEM images of samples obtained after toluene CVD on MWNTs-CN_x treated with different iron precursors. **a)** MWNTs-CN_x treated with $K_3[Fe(CN)_6]$ (method depicted in section 2.2.1.2) after CVD treatment with pristine toluene, and **b)** MWNTs-CN_x previously dispersed in DMF reacted with Fe^{+3} in acidic medium (method explained in section 2.3.1) followed a CVD treatment with pristine toluene.

CN_x surface.

When these interconnected structures where compared with the original N-doped carbon nanotubes used as templates, we denote that their outer diameter increased from 35 nm (measured for the pristine MWNTs-CN_x used, shown in 2.9a) to ca. 100 nm after the toluene CVD treatment. This indicates that growth of new nanostructured carbon was achieved over MWNTs-CN_x. It was observed that the general morphology of the final product, where the junction structures were found, appeared to be more compact than in the cases where junctions formation were not observed.

X-Ray diffraction (XRD) analysis of these junction-like structures were performed (fig. 2.20). The XRD pattern for the pristine MWNTs-CN_x used in the experiments without any previous treatment is also shown (fig. 2.20d). Signals of the (002) plane of graphite, which corresponds to the graphene layers are significant in the pattern. Other signals of possible iron oxides coming from the oxidization of nanoparticles exposed to air are also present.

XRD patterns for MWNTs-CN_x after their Fe anchoring treatments were also performed. For the method depicted in section 2.2.1.2 (fig. 2.20c), we observed that signals for the graphite (002) plane decreased, meanwhile other diffraction peaks

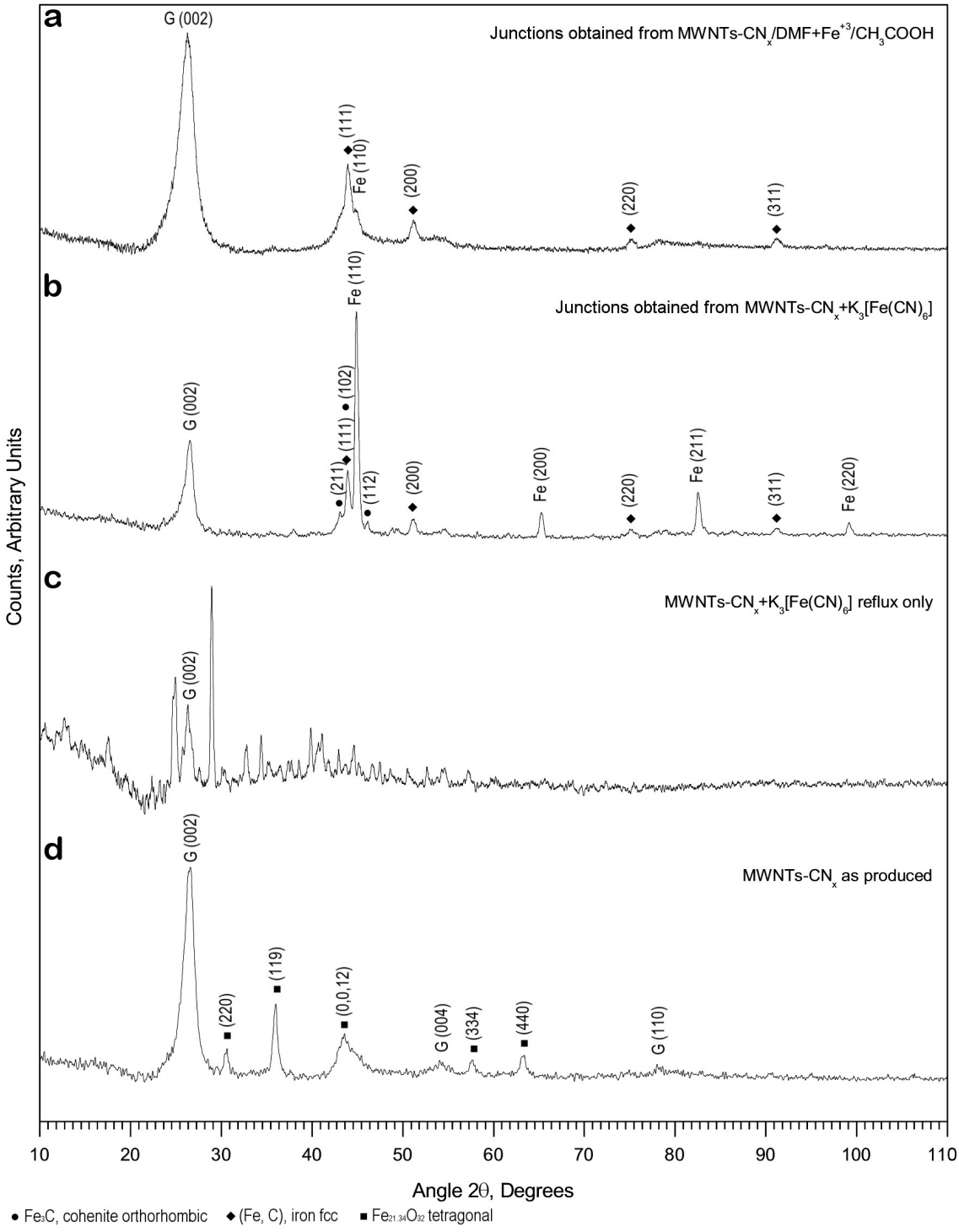

Figure 2.20: Comparative XRD pattern of the branched structures and their precursors. Signals marked as G correspond to graphite ($P6_3/mmc$, $a = 2.4560$ Å, $c = 6.6960$ Å) and those with Fe to a *bcc* structure ($Im\bar{3}m$, $a = 2.8607$ Å). Other compounds such as cohenite (•), Fe_3C (Pnma, $a = 5.0910$ Å, $b = 6.7434$ Å, $c = 4.5260$ Å), Fe *fcc* (⧫) ($Fm\bar{3}m$, $a = 3.600$ Å) and iron oxide (■), $Fe_{21.34}O_{32}$ (P41212, $a = 8.3474$ Å, $c = 25.0422$ Å) were also detected.

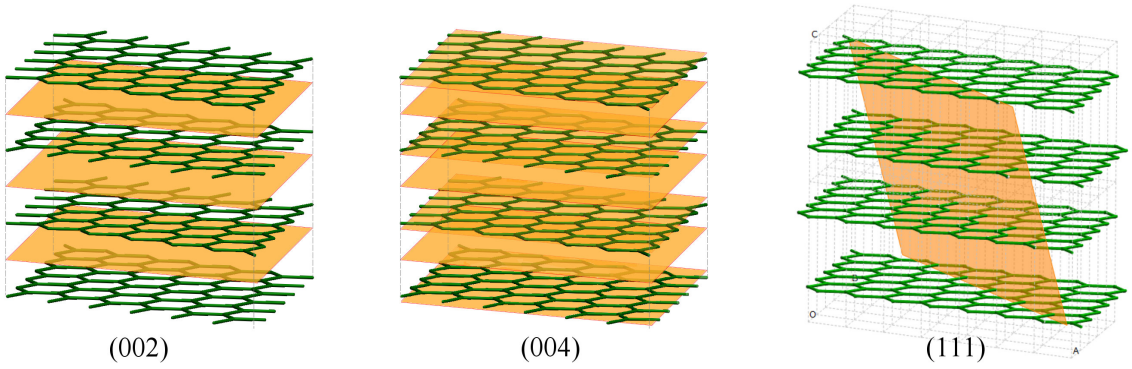

Figure 2.21: Crystallographic planes of graphite identified in the XRD patterns. Family of planes (002) and (004) of graphite. Only one (111) plane is shown for clarity. These planes can also be observed for MWNTs-CN_x, as shown in the XRD patterns depicted in fig. 2.20.

that could not be clearly identified appear. It is remarkable that those signals do not correspond to the *Prussian* ($K_3[Fe(CN)_6]$) or to *Turnbull's blue* ($Fe_4[Fe(CN)_6]$) and if they were the responsible of the coloration in the product, probably they were decomposed during the acid refluxing treatment (most likely because of the temperature).

After the CVD treatment (fig. 2.20*b*), both, the signals of Fe *bcc* phase and Fe *fcc* appear with higher and lower intensities respectively. Peaks corresponding to cohenite (Fe_3C) indicate that this phase is also formed. The phase diagram for the C-Fe system (fig. 2.22) indicates that cohenite (also known as cementite) is stable for the range of concentrations and temperature where our samples were treated during the CVD process.

The XRD pattern for the junctions obtained from the treatment described in section 2.3.1 (MWNTs-CN_x dispersed in DMF reacted with Fe^{+3} in acidic solution) is shown (fig. 2.20*a*). Peaks corresponding to the (002) graphite plane, Fe *bcc* and Fe *fcc* phases are observed. These signals confirm that the catalytic cluster obtained by this deposition method are mainly composed of iron and not from its oxides. This is an important evidence that could not be determined fully using HRTEM.

When the XRD patterns for the junctions obtained using the iron deposited MWNTs-CN_x from their treatment with $K_3[Fe(CN)_6]$ are compared with those obtained using the acidic iron solution Fe^{+3} (figs. 2.20*a* and *b*), clear differences

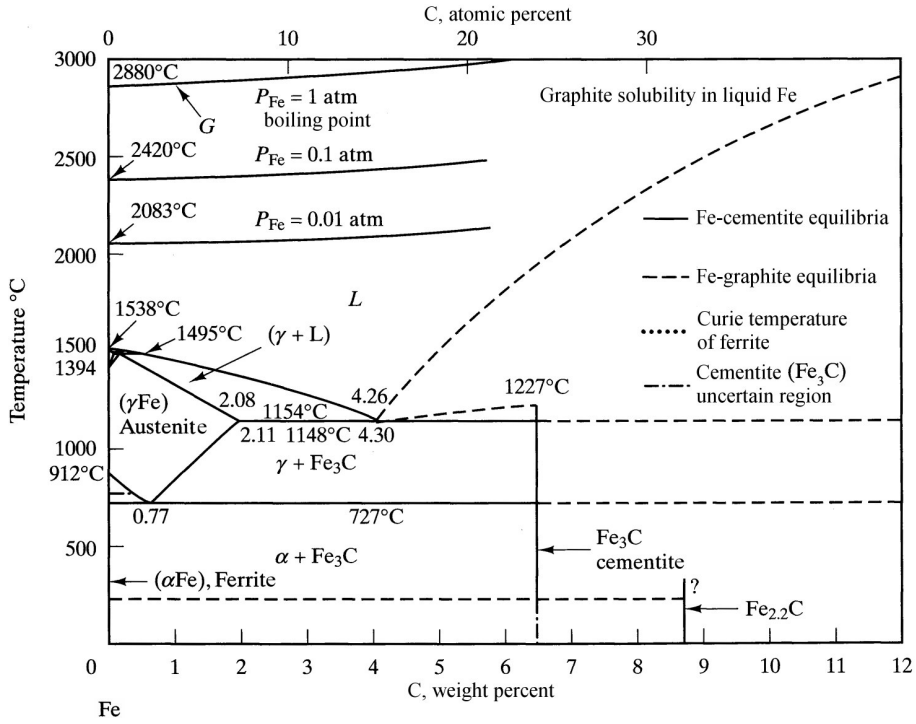

Figure 2.22: Phase equilibrium for C-Fe system. αFe is another way to name the Fe *bcc* phase, the γFe, on the other hand, is the common name for the Fe *fcc* system. The iron carbide (Fe_3C) here named cementite is also known as cohenite. Taken from [37].

can be noticed. The most notorious is the high relative intensity of the signal corresponding to the (002) graphite plane in fig. 2.20*a*.

The explanation of why the intensity of the (002) graphite signal is different in the Fe-coated tubes by different procedures could be due to the amount of this crystallite[2] in the sample. The molar ratio between the iron introduced in the system with respect to the carbon (that is from the MWNTs-CN_x) corresponds to 6.29×10^{-2} $\frac{\text{mol Fe}}{\text{mol C}}$ for the tubes shown in fig. 2.20*a*. This ratio is as high as 0.228 for the MWNTs-CN_x treated with $K_3[Fe(CN)_6]$ (2.20*b*), and because of that, the crystallite size of the graphitic plane (002) is decreased when compared with the Fe *bcc*.

Even when both XRD patterns look different for the junctions obtained by using distinct iron deposition methods on MWNTs-CN_x, they mainly differ in the amount

[2] *Crystallite* is the degree of crystallinity of a specimen in a particular direction

of crystalline phases present. Therefore, we believe that both iron phases (in different percentages) were obtained by the different deposition methods used.

It is noteworthy how these results agree with the HRTEM observations carried out in clusters obtained using the coordination salt deposition method on MWNTs-CN_x (fig. 2.14). For this sample, the XRD pattern indicates that the iron phase encountered in higher quantity was Fe *bcc*, a fact previously observed from the FFT analyses performed on the iron clusters (fig. 2.14*iv*). XRD analysis also confirm that the clusters deposited on MWNTs-CN_x consisted mainly of iron instead of iron oxide particles.

Further studies were required in order to understand the detailed structure of the junctions structures obtained. Therefore, HRTEM studies of nanotube junctions were carried out. Figure 2.23*a* shows a Y-junction, in which the MWNTs-CN_x can be clearly identified in the core of the tubular structure of the "Y"-junction by observing their characteristic bamboo-like structure, being wrapped with carbon. Higher magnification images of these regions (figures 2.23*b* and *c*) show the crystalline planes of the bamboo-like MWNT-CN_x covered by less crystalline graphene layers composed of pure carbon.

FFT analysis of these images were performed in order to obtain interlayer spacings among different graphitic planes in the structure. These measurements considered the interlayer spacing in MWNTs-CN_x to be exactly 3.40 Å. The corresponding mean interlayer spacing measured for the outer graphitic sheets, less crystalline, was ca. 3.48 Å.

Therefore, it is clear that we have obtained MWNTs-CN_x wrapped with pure carbon MWCNTs (fig. 2.23).

An on-junction, shown in fig. 2.23*d*, also presents an internal core of MWNTs-CN_x surrounded by graphene layers which kept the MWNT-CN_x joined in this morphology. Graphitic planes in a T-junction (fig 2.23*f*) can be seen in fig. 2.23*e*, clearly indicating the growth of a pure carbon nanotube on a N-doped tube.

Several graphitic planes separate the MWNTs-CN_x in the junctions but, at the

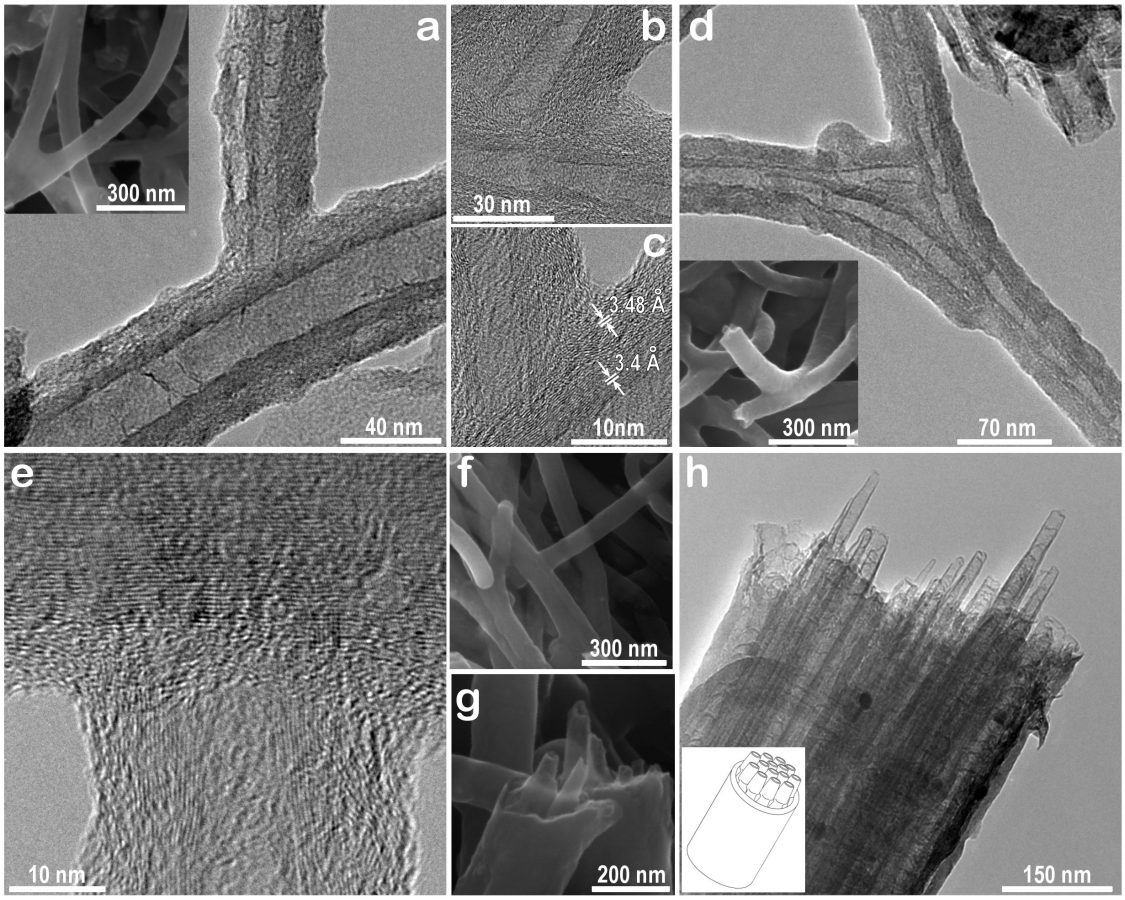

Figure 2.23: HRTEM images of different types of junctions and hetero-nanocables produced in this work. a) SEM and HRTEM images of a Y-junction; **b)** Close-up of a Y-junction similar to the shown in *a*. **c)** Graphitic planes and different interplanar distances values shown for the internal graphitic planes and the outer shells. **d)** SEM and HRTEM images of On-junction. **e)** HRTEM image of a T-junction. **f)** SEM image of another T-junction. **g)** SEM image of a broken cable showing several MWNTs-CN_x inside. **h)** HRTEM image showing a bundle of MWNTs-CN_x wrapped by a graphene sheets (CNx@CNT). *Inset.* Scheme of the structures displayed in *h*.

same time, they are maintained held together by outer graphene layers that appear to be forming a continuous wrap over all the structure. The poorer crystallinity of these external graphene layers is also easily noted in 2.23*e*.

We clearly observe two families of graphitic planes: *a)* the inner N-doped layers and *b)* the pure carbon layers exhibiting less degree of crystallinity. The poor crystallinity of the pure carbon sheets may be due to the pyrolytic deposition of carbon without the aid of a posterior annealing process.

2.5.2.1 New coaxial CNT structures: Hetero-nanocables (CN_x@CNT)

The image of a bundle of MWNTs-CNx immersed in a carbon nanotube of larger diameter shown in fig. 2.23*h* is one of the main representative images that supports our discovery. This is also observed in SEM images (fig. 2.23*g*). The arrangement proposed for this heteronanocables is depicted in the low inset of fig. 2.23*h*. These structures are similar to coaxial cables composed by two kinds of carbon nanotubes: N-doped ones in the internal tubular part and undoped (pure carbon) tubes constituting the outer shell.

The best of our knowledge, this kind of hetero-nanocables have not been reported hitherto and are very different from the "carbon nanotube bags" described by Schneider J. *et al.* [38] (2001), composed only by helicoidal MWCNTs wrapped in a large CNT. Their method involves the reduction of $Fe(NO)_3$ impregnating a membrane disk support at 500 °C under a H_2/N_2 atmosphere followed by the pyrolysis of propene (C_3H_6) in N_2 flow at 650–800°C and a subsequently laser-assisted parallel patterning. This contrasts with our method which does not require H_2 and the membrane support used for the CNTs growth.

Figure 2.24*a* exhibits a broken coaxial-cable showing the bamboo-like structure (of MWNTs-CN_x) in the inner core and the pure carbon MWCNT on the outside. Two kinds of breaking mechanisms are observed in this coaxial cable. The MWNT-CN_x inside breaks by an apparent sliding of the cup-stacked graphene layers, whereas the outer MWCNTs seems to crack by breaking the defective graphitic planes (similar to a brittle fracture). A molecular representation of this type of tubes is depicted in fig. 2.24*c*, where the N atoms are represented in a light color whereas C atoms are in dark. Only one shell of each type of carbon nanotube is used in the model for clarity.

As mentioned earlier, we expected that the iron particles deposited on MWNTs-CN_x could act as catalysts for the formation of new MWCNTs after pyrolyzing toluene. The image presented in fig. 2.25*a* clearly shows that during the experiment, the deposited iron nanoparticles agglomerate into larger particles that could form

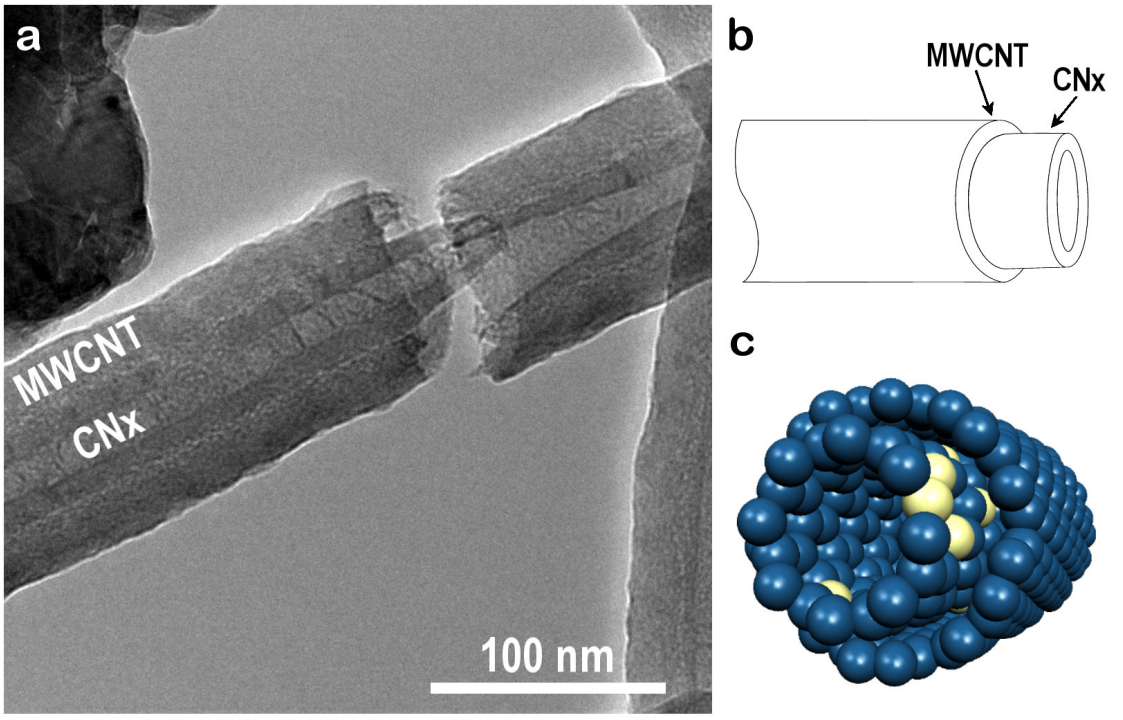

Figure 2.24: HRTEM image of a coaxial hetero-nanocable. a) A HRTEM image of a broken coaxial tube CNx@CNT showing different kinds of fracture for the inner and the outer shells. **b)** Schematic representation of the coaxial hetero-nanotubes. **c)** Molecular representation of a CNx inside a CNT (only a layer of each type of carbon nanotube is shown for clarity). Bright atoms are N, darker ones are C.

iron rods (180 nm length by 30 nm width in the example shown), which we believe act as catalytic centers for the growth of new carbon nanotubes. This is the result of an annealing process promoting the coalescence of Fe particles directly above the MWNT-CN_x surface when the temperature of the system is increased (fig. 2.25*b*). During this growing process, pure carbon fragments deposit on the MWNTs-CN_x and the newly formed Fe nanorod. Close-up of the interface between the metal and the surface is shown in fig. 2.25*c*. Electron energy loss spectroscopy (EELS) mapping confirms that these bars are composed only of iron (see figs. 2.25*d* and *e*), without any oxide, since oxygen was not detected by this technique. This is in agreement with previous XRD studies performed in the sample and the HRTEM analysis.

Thermogravimetric analysis (TGA) curves obtained for the two junction samples are shown in fig. 2.26*a*; labeled as CN_x@CNT (1) and (2). Both junction systems

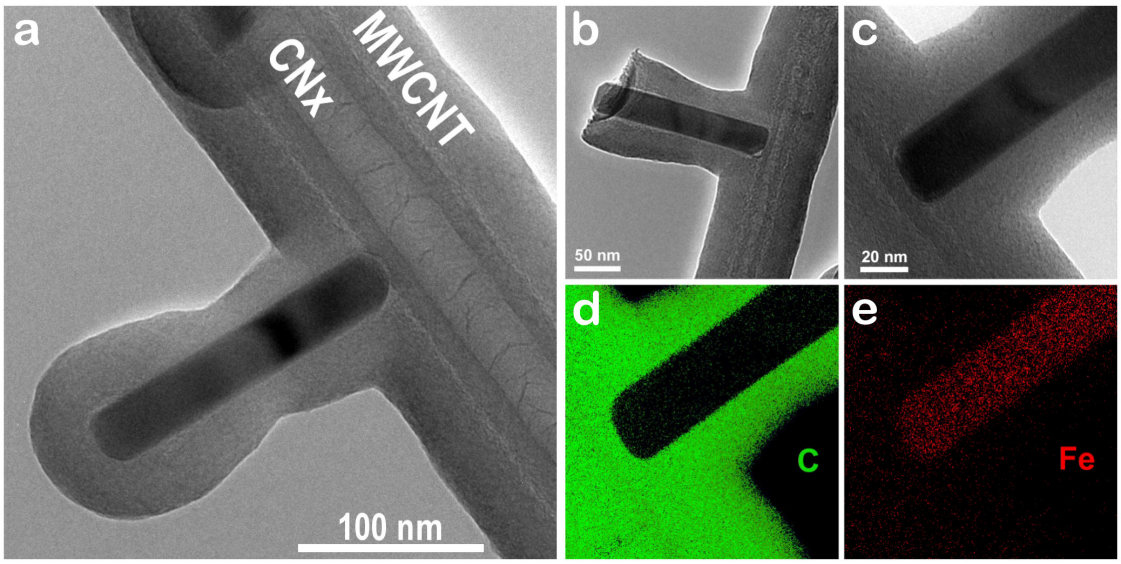

Figure 2.25: HRTEM images showing a base growth mechanism and their corresponding EELS mapping. **a)** HRTEM image exhibiting a MWCNT attached in a T junction on a MWNT-CN_x. **b)** A similar structure in detail and a close-up of the interface between the metal and the surface of the MWNT-CN_x. **c)** Close-up on the MWNT-CNx at the zone where the iron bar is placed. **d)** Carbon EELS mapping of the image shown in *c*. **e)** Iron EELS mapping of the image shown in *c*.

were synthesized by CVD using toluene on MWNTs-CN_x reacted with $K_3[Fe(CN)_6]$. Similar runs were performed for the MWCNTs and MWNTs-CN_x used in previous experiments for reference. Their decomposition curves are plotted in the same graph. Air was selected as atmosphere for performing the TGA experiments in order to burn the carbon nanotubes and form CO_2, thus oxidizing the remainder iron used as catalyst to Fe_2O_3. The weight fraction corresponding to the residues of each run are displayed in the low part of the curves where the final weight is stationary, that is where the slopes of curves are zero. This fraction corresponds to the non-volatile products, that we related with the quantity of iron(III) oxide (Fe_2O_3) formed from the iron present in the sample.

The iron(III) oxide fractions found for the samples were: 0.269, 0.330 for CN_x@CNT (1) and (2) respectively, which corresponds to 18.81 wt % 23.08 wt % of Fe. For MWCNTs, the remaining iron was 8.67 wt % (0.124 of Fe_2O_3) and 6.75 wt % (9.66×10^{-2} of Fe_2O_3) in MWNTs-CN_x. From these results we could observe an increment of 12.06 wt % and 16.33 wt % in the MWNTs-CN_x after their

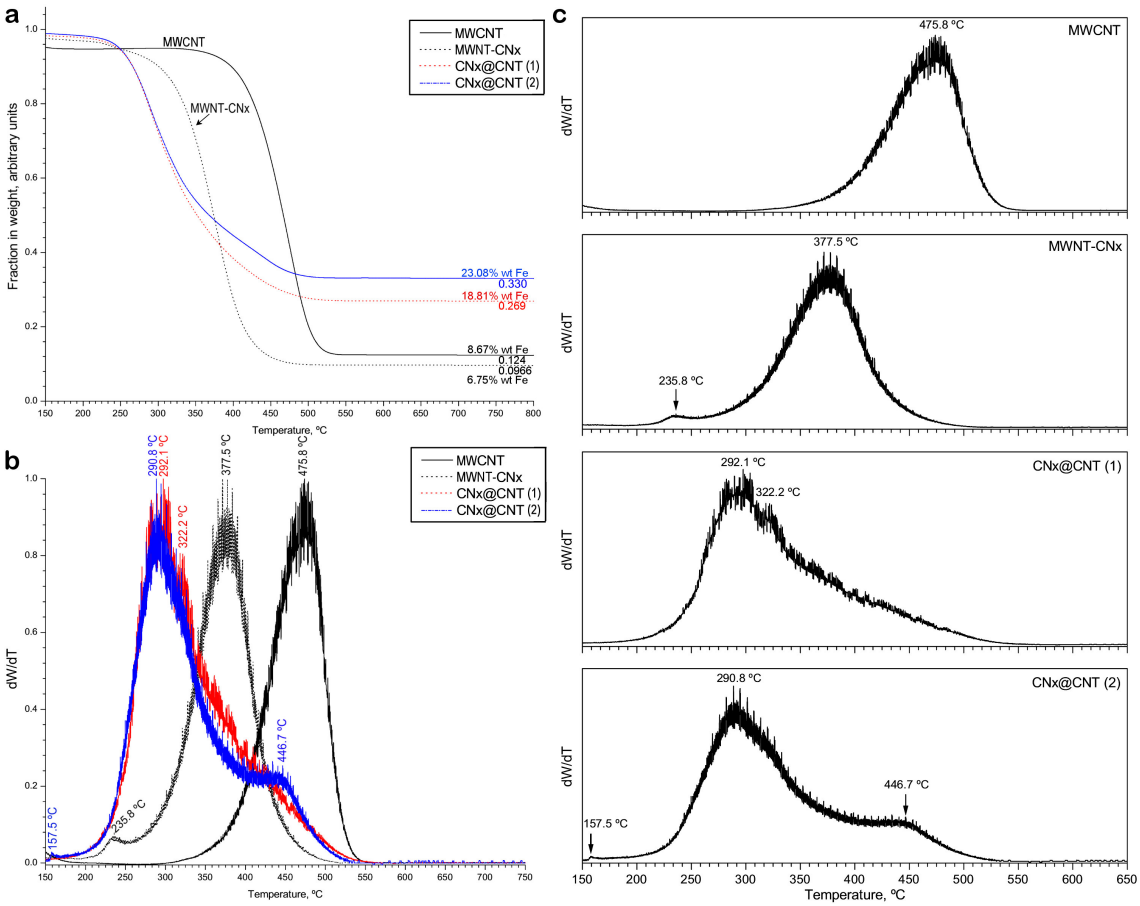

Figure 2.26: Comparative TGA studies of MWCNTs, MWNTs-CN_x and junctions/hetero-nanocables. a) TGA curves obtained for MWCNTs, MWNTs-CN_x and the product that exhibit hetero-nanocables and junctions (CN_x@CNT). **b)** Superposed first derivative curves of the weight with respect to the temperature (dW/dT) of the TGA curves shown in *a*. **c)** First derivative of the 4 samples shown in a vertical stacked arrangement for clarity. (*Top to bottom:* MWCNTs, MWNTs-CN_x and junctions).

reaction with the iron precursor.

First derivative of the graph shown in fig. 2.26*a* was calculated and plotted together in fig. 2.26*b* for obtaining the characteristic decomposition temperature for each material (fig. 2.26*c*). The decomposition temperature for typical MWCNTs in air was found to be around 476 °C, meanwhile the corresponding for the MWNTs-CN_x is ca. 378 °C. The low burning temperature for the MWNTs-CN_x is expected because its cup-stacked like structure, result of the nitrogen presence. It propitiates more defects in the graphitic network that are highly reactive and decrease the resistance to oxygen of the nanotubes at high temperatures.

For CN_x@CNT structures, we found the occurrence of two different decomposition temperatures (see fig. 2.26 CN_x@CNT (1) and (2)), displaced by -86 °C and by +69 °C respect to the characteristic decomposition temperature of MWNTs-CN_x (T_{dec}=378 °C). Both temperatures are lower respect to the decomposition temperature of MWCNTs (T_{dec}=476 °C). For CN_x@CNT (1), two local minimal corresponding to a couple of nearby thermal degradation temperatures, 292 °C and 322 °C, were identified together with a large tail that decreases faster once 450 °C is reached. In the case for the hetero-nanostructures marked as CN_x@CNT (2), the curve follows a similar behavior to that observed in (1). The temperature of 291 °C is easy recognized, a hump appears at the right of this temperature, which could correspond to the 322 °C found in curve (1). A temperature preceding a fast decay in the quantity of the product (or, an increment in the decomposition rate) was found at 447 °C.

The presence of a couple of different decomposition temperatures in the CN_x@CNT compounds synthesized would be consistent with SEM and HRTEM observations (figs. 2.23 and 2.24) as an assembled of two materials, MWNTs-CN_x and MWCNTs, which exhibit different resistance to thermal degradation.

At that moment, we believed that the low crystallinity of the external MWCNTs and the possible defects incorporation in the MWNTs-CN_x during the acid treatment could be responsible of these oxidation temperature differences.

Since the temperatures at which the structure seems to decompose are different to the characteristic for MWNTs-CN_x and MWCNTs, a CN_x@CNT sample was mounted in the TGA system and heated up to 300 °C in order to identify the less stable structure in oxygen. This target temperature was selected because, at this value, the first weight drop was observed. The procedure, parameters and ramps used in this experiment were the same of the complete TGA runs before mentioned. As final step, the sample was subjected to an isothermal annealing at this maximum temperature (300 °C) for 5 min. After cooling down to room temperature, the residues were analyzed by SEM and STEM for the purpose of

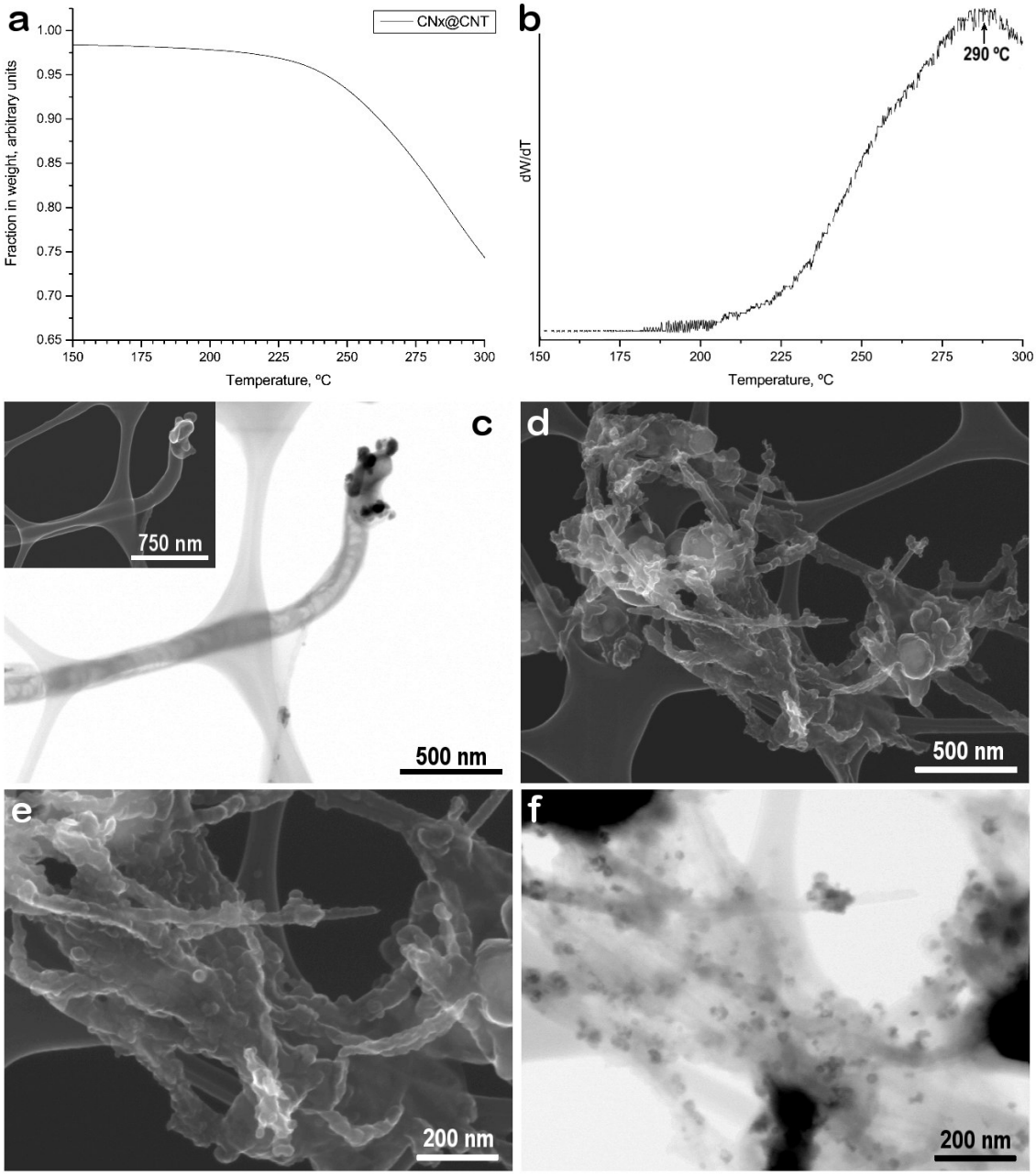

Figure 2.27: Burned CN_x@CNTs at 300 °C in air. a) TGA curve for CN_x@CNT heated up to 300 °C in air. **b)** First derivative of the weight with respect to the temperature (dW/dT) of the TGA curve shown in *a*. **c)** Bright field STEM image of the remainder after the oxidization of CN_x@CNT at 300 °C. *Inset:* SEM image of the MWNTs-CN_x shown in *c*. **d)** SEM image of the residue after the oxidization of a possible bundle in the CN_x@CNT; **e)** Close-up of *d*. **d)** Bright field STEM image of *e*.

classifying the remaining structures.

The TGA curve recorded during this experiment is shown in fig. 2.27*a*. The calculated first derivative, displayed in 2.27*b*, shows that at this temperature

(300 °C), we had achieved a first decomposition temperature (290 °C) and we expect that the part of the sample exhibiting low thermal stability had been already degraded.

From SEM, we were able to recognize carbon nanotubes (see inset in fig. 2.27*c*), in the after-burning remaining product. Here, we could identify MWNTs-CN_x by its typical bamboo-like structure (fig. 2.27*c*). We also found structures that seemed to be the remainders of CN_x@CNT bundles. Figure 2.27*d* shows several MWNTs-CN_x still a little aggregated by amorphous carbon. A close-up of this picture is displayed in fig. 2.27*e* and their corresponding bright field image in *f*. MWNTs-CN_x covered by iron particles can be identified in this last STEM image. After a detailed analysis on these images, we concluded that the amorphous carbon that appears wrapping the MWNTs-CN_x is product of the incomplete burning of the previously external MWCNTs.

The outer MWCNTs covering the core structure decomposes first, ca. 322 °C (found for CN_x@CNT (1) in fig. 2.26). Meanwhile, the last thermal break down temperature found (∼447 °C) which also appears in other TGA studies, corresponds to the decomposition of MWNTs-CN_x. This temperature is higher than those of pristine MWNTs-CN_x by ca. 69 °C which indicates that the carbon coating prevents MWNTs-CN_x to oxidize faster. But also, we consider the possibility that the thermal annealing at which the MWNTs-CN_x were subject increased its crystallinity (at 825 °C) when the temperature of the CVD system for the toluene spray was raised; thus, making them more resistant to the oxidization by the relaxing of strains and reducing the defects on their structure.

The thermal break down temperature exhibited by the carbon graphitic layers wrapping the MWNTs-CN_x is lower than the usual exhibited by MWCNTs (in this case, ∼378 °C). This effect was anticipated in some way before, and we believe it to occur because of the low crystallinity exhibited by these layers.

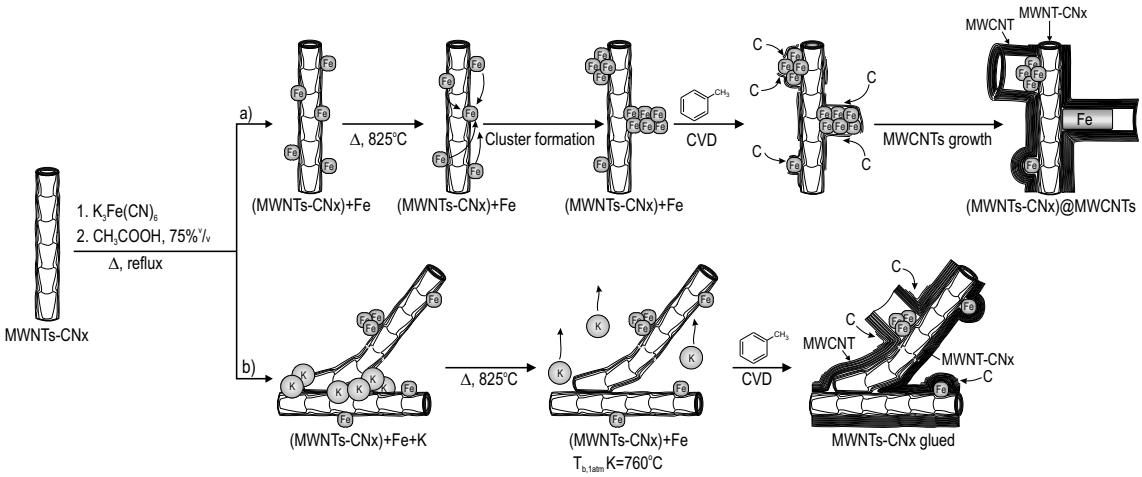

Figure 2.28: Schematic diagram depicting the growth mechanism for producing coaxial CN_x@CNT structures. The starting material (*left*) is MWNTs-CN_x reacted with $K_3[Fe(CN)_6]$, contain a higher amount of iron than the starting material, and potassium, as shown in the EDX spectra (see fig. 2.9*g*). **a)** *Growth of branches and coaxial structures:* Iron nanoparticles migrate and coalesce into larger clusters during heating to 825 °C. At that temperature toluene is introduced and the iron clusters catalyze the formation of MWCNT branches, additionally graphene sheets form a continuous wrapping around MWNT-CN_x. **b)** *Growth of on-junctions and coaxial nanocables:* The potassium present in the samples could help binding nanotube bundles, keeping them together for the formation of on-junctions (T_{bK}: 760 °C, 1 atm). At the same time, iron cluster formation occurs and catalyzes the growth of subsequent MWCNTs. Given how close the MWNTs-CN_x are, the carbon sheets wrap more than one nanotube, forming either on-junctions or nanocables when bundles of parallel nanotubes are present.

2.5.2.2 Growth mechanism for generating CN_x@CNT coaxial structures

The results presented above suggest that iron remains at the base, *i.e.* deposited on MWNTs-CN_x surface, and acts as catalyst for subsequent MWCNT growth. During this process carbon deposits and forms a concentric carbon nanotube which covers the entire MWNT-CN_x. Therefore, the structures increase their diameter after the CVD process.

The proposed growth mechanism is depicted in fig. 2.28. We start from MWNTs-CN_x reacted with $K_3[Fe(CN)_6]$. From EDX spectra (shown in fig. 2.9*g*, page 53), we found potassium and a higher iron concentration in them when compared to pristine MWNTs-CN_x (fig. 2.9*b*). During heating in an Ar atmosphere, a breaking of the remaining coordination spheres of $K_3[Fe(CN)_6]$ deposited on MWNTs-CN_x generates gaseous hydrogen cyanide (HCN) before temperature reaches 400 °C. Meanwhile,

migration of Fe nanoparticles also takes place, coalescing to form clusters and eventually elongated bars. This coalesce occurs below the melting point of bulk Fe which is 1538 °C at 1 atm. These iron bars act as catalyst sites for MWCNTs formation when toluene is sprayed over the sample at 825 °C. At this point, it is expected that all the potassium had been evaporated, because its boiling point is 760 °C at 1 atm. As the iron particles are distributed along the MWNTs-CN_x, they can also act as a binder for the carbon nanotube coating. Because of the proximity between the MWNTs-CN_x acting as templates, the formation of additional graphene sheets start joining and interconnecting tubes, thus forming networks of coaxial MWNTs-CN_x inside CNTs (CN_x@CNT).

It is believed that further thermal annealing of these structures would increase the crystallinity of the outer MWCNTs wrapping the MWNTs-CN_x, and, therefore also increase the mechanical strength of these hetero-structures.

2.5.3 Summary

In this section, we illustrated how two different methods for depositing iron clusters on carbon nanotubes were successful in creating new interlinked nanotube structures. Four different types of junctions were produced ("Y" and "T" like, multibranching and "On-junctions") and characterized by SEM, HRTEM, XRD and TGA.

We have shown the feasibility of fabricating coaxial hetero-nanotubes using doped and undoped carbon nanotubes consisting of an internal core of MWNTs-CN_x and an external shell of pure carbon layers (MWCNTs). This result could be optimized further in order to produce three-dimensional interlinked CNT structures in large scale. This cylindrical assembly of two different kinds of carbon nanotubes with different electronic properties could be of interest in the elaboration of new nanoelectronic devices.

It is expected that the internal core of MWNTs-CN_x would exhibit higher electric conductance when compared to the outer shell of MWCNTs.

Additional studies would be necessary to explore the properties and applications of these materials. However, theoretical calculations and experimental conductivity tests need to be carried out in order to find important applications.

The procedure that we presented is useful to produce coaxial structures. Further experiments are planed in order to optimize the process. As mentioned earlier, the limiting process during the production of coaxial nanocables and heterostructures, is the diffusion of the carbon precursor through the Fe coated-MWNTs-CN_x during the CVD treatment. We propose that one way to overcome this problem is by changing our experimental setup to one that includes a fluidized bed reactor, where the MWNTs-CN_x coated with Fe could be the floating substrate, through which the toluene vapor will be sprayed at high temperature.

2.6 Conclusions

The objective of the work described in this chapter was to achieve an efficient anchoring of iron clusters on MWNTs-CN_x using several methods, avoiding the use of strong acid treatments that significantly change their properties. Two approaches were successfully developed taking the advantage of the structure and chemical reactivity of MWNTs-CN_x; different from pure MWCNTs.

First of all, we demonstrated that MWNTs-CN_x can be suspended in an acidic solution whereas the MWCNTs cannot. We stated that the reason of this behavior is probably the protonation of the nitrogen site present in MWNTs-CN_x enabling the suspension of these macromolecules in a protic medium. The MWCNTs do not exhibit this behavior due to the absence of nitrogen sites in their structure.

Subsequently, we used these uniform MWNTs-CN_x suspensions for depositing Fe clusters using coordination iron salts, like the potassium hexacyanoferrate(III), $K_3[Fe(CN)_6]$. A possible interaction between the positive charged protonated nitrogen sites and the internal coordination sphere where the metal is immersed was proposed in this chapter.

We found an efficient anchoring of Fe clusters composed on the surface of MWNTs-CN_x in the absence of strong acid (e.g. HNO_3, H_2SO_4, etc.) previous oxidizing treatments. The products were characterized by diverse techniques including SEM, HRTEM, EDX and XRD.

The second method tested for iron deposition on MWNTs-CN_x, developed in this chapter, required a dispersion of MWNTs-CN_x in an organic solvent (dimethylformamide, DMF) and their reaction with an aqueous acidic solution of the Fe^{+3} cation. This method showed similar results to those obtained with the coordination salts. Both methods were simple, but the second one was faster.

We can conclude that MWNTs-CN_x exhibit novel chemical properties which can be exploited making use of common techniques of organic and colloidal chemistry. This would allow us to synthesize new MWNTs-CN_x-composite compounds in a

more efficient way.

We then proceed to use these Fe-coated MWNTs-CN_x as a catalytic support for growing nanotubes radially to the existing tubes. Therefore, we pyrolyzed pure toluene over Fe coated MWNTs-CN_x and found the formation of coaxial CN_x-C nanotube junctions and networks. These coaxial cables are formed by an inner core of MWNTs-CN_x wrapped by carbon layers similar to MWCNTs. These cables can also interconnect covalently among them, producing amazing branched structures.

We were able to reproduce these structures in a reproducible way and also found the experimental conditions for improving their yield.

Diverse analysis were performed on the product, such as SEM, HRTEM, EDX, XRD and TGA. HRTEM allowed to visualize the graphene layers, the arrangement and the differences between structures, meanwhile the TGA curves revealed their stability in an oxygen atmosphere at high temperatures.

We named these discovered structures **CN_x@CNT**. It is remarkable that these structures were not reported in the literature previously, so we are the first research group in reporting them.

The interest of producing such structures composed of doped and undoped carbon nanotubes may find use in new technological applications in the near future. New alternative methods for producing composites could be realized from this approach. However further experimental and theoretical work should be carried out for understanding the electronic properties of our CN_x@CNT.

References

[1] Morrison, R. and Boyd, R.N. *Organic Chemistry*, chapter 22–23. Amines, pages 821–879. Prentice Hall: Englewood Cliffs, New Jersey, 6th edition, 1992.

[2] *"pyridine"*. Wikipedia the free encyclopedia, `http://en.wikipedia.org/wiki/Pyridine`, 2006.

[3] Morrison, R. and Boyd, R.N. *Organic Chemistry*, chapter 30. Heterocyclic Compounds, pages 1057–1072. Prentice Hall: Englewood Cliffs, New Jersey, 6th edition, 1992.

[4] Huheey, J.E.; Keiter, E.A. and Keiter, R.L. *Química Inorgánica*, chapter 11–13. Química de los compuestos de coordinación, pages 411–450,500–612. Harla-Oxford University Press: México, D.F., 4th edition, 1997.

[5] Endo, M.; Ahm Kim, Y.; Ezaka, M.; Osada, K.; Yanagisawa, T.; Hayashi, T.; Terrones, M. and Dresselhaus, M.S. *Selective and efficient impregnation of metal nanoparticles on cup-stacked-type carbon nanofibers.* Nano Letters **2**(6):723–726, 2003.

[6] Planeix, J.M.; Coustel, N.; Coq, B.; Brotons, V.; Kumbhar, P.S.; Dutartre, R.; Geneste, P.; Bernier, P. and Ajayan, P.M. *Application of carbon nanotubes as supports in heterogeneous catalysis.* Journal of American Chemical Society **116**:7935–7936, 1994.

[7] Morrison, R. and Boyd, R.N. *Organic Chemistry*, chapter 7. Solubility, pages 252–270. Prentice Hall: Englewood Cliffs, New Jersey, 6th edition, 1992.

[8] Yang, Q.H.; Hou, P.X.; Unno, M.; Yamauchi, S.; Saito, R. and Kyotani, T. *Dual Raman features of double coaxial carbon nanotubes with N-doped and B-doped multiwalls.* Nano Letters **5**(12):2465–2469, 2005.

[9] Lim, S.H.; Elim, H.I.; Gao, X.Y.; Wee, A.T.S.; Ji, W.; Lee, J.Y. and Lin,

J. *Electronical and optical properties of nitrogen-doped multiwalled carbon nanotubes*. Physical Review B **73**:045402, 2006.

[10] Kamalakaran, R.; Terrones, M.; Seeger, T.; Kohler-Redlich, P.; Rühle, M.; Kim, Y.A.; Hayashi, T. and Endo, M. *Synthesis of thick and crystalline nanotube arrays by spray pyrolysis*. Applied Physics Letters **77**(21):3385–3387, 2000.

[11] Mayne, M.; Grobert, N.; Terrones, M.; Kamalakaran, R.; Rühle, M.; Kroto, H.W. and Walton, D.R.M. *Pyrolytic production of aligned carbon nanotubes from homogeneously dispersed benzene-based aerosols*. Chemical Physics Letters **338**:101–107, 2001.

[12] Terrones, M. *Science and technology of the twenty-first century: Synthesis, properties, and applications of carbon nanotubes*. Annual Review Material Research **33**:419–501, 2003.

[13] Carrero-Sánchez, J.C.; Elías, A.L.; Mancilla, R.; Arrellín, G.; Terrones, H.; Laclette, J.P. and Terrones, M. *Biocompatibility and toxicological studies of carbon nanotubes doped with nitrogen*. Nano Letters **6**(8):1609–1616, 2006.

[14] Lide, D.R., ed. *CRC Handbook of Chemistry and Physics*. Taylor and Francis: Boca Raton, FL, 86th edition, 2005.

[15] Villars, P. and Calvert, L.D. *Pearson's Handbook of crystallographic data for intermetallic phases*. ASM International, Materials Park, OH, 2nd edition, 1991.

[16] Teo, K.B.K.; Singh, C.; Chhowalla, M. and Milne, W.I. *Encyclopedia of Nanoscience and Nanotechnology*, volume 10, chapter Catalytic Synthesis of Carbon Nanotubes and Nanofibers, pages 1–22. Nalwa, H. S., 2003.

[17] Huang, S.M. *Controllable 3D architectures of aligned carbon nanotube arrays by multi-step processes*. Chemical Physics Letters **374**:157–163, 2003.

[18] Troiani, H.; Miki-Yoshida, M.; Camacho-Bragado, G.; Marques, M.; Rubio, A.; Ascencio, J. and José-Yacaman, M. *Direct observation of the mechanical properties of single-walled carbon nanotubes and their junctions at the atomic level*. Nano Letters **3**(6):751–755, 2003.

[19] Xie, R.H.; Zhao, J. and Rao, Q. *Encyclopedia of Nanoscience and Nanotechnology*, volume 10, chapter Doped Carbon Nanotubes, pages 1–31. Nalwa, H. S.: www.aspbs.com/enn, 2004.

[20] Czerw, R.; Terrones, M.; Charlier, J.; Blase, X.; Foley, B.; Kamalakaran, R.; Grobert, N.; Terrones, H.; Tekleab, D.; Ajayan, P.; Blau, W.; Rühle, M. and Carroll, D. *Identification of electron donor states in N-doped carbon nanotubes*. Nano Letters **1**(9):457–460, 2001.

[21] Sun, X.; Li, R.; Stansfield, B.; Dodelet, J.P. and Dsilets, S. *3D carbon nanotube network based on a hierarchical structure grown on carbon paper backing*. Chemical Physics Letters **394**:266–270, 2004.

[22] Ting, J.M.; Li, T.P. and Chang, C.C. *Carbon nanotubes with 2D and 3D multiple junctions*. Carbon **42**:2997–3002, 2004.

[23] Collins, P.G.; Zettl, A.; Bando, H.; Thess, A. and Smalley, R.E. *Nanotube device*. Science **278**:100–103, 1997.

[24] Baughman, R.H.; Zakhidov, A.A. and de Heer, W.A. *Carbon nanotubes–the route toward applications*. Science **297**:787–792, 2002.

[25] Satishkumar, B.C.; John Thomas, P.; Govindaraj, A. and Rao, N.R. *Y-junction carbon nanotubes*. Applied Physics Letters **77**(16):2530–2532, 2000.

[26] Ma, X. and Wang, E.G. *CN_x/carbon nanotube junctions synthesized by microwave chemical vapor deposition*. Applied Physics Letters **285**:978–980, 2001.

[27] Terrones, M.; Banhart, F.; Grobert, N.; Charlier, J.C.; Terrones, H. and Ajayan, P.M. *Molecular junctions by joining single-walled carbon nanotubes.* Physical Review Letters **89**(7):075505, 2002.

[28] Gu, P.; Zhao, J.H. and Li, G.H. *Synthesis of Y-branching multiwalled carbon nanotubes with a bamboolike structure.* Journal of Materials Research **17**(11):2768–2770, 2002.

[29] Gothard, N.; Daraio, C.; Gaillard, J.; Zidan, R.; Jin, S. and Rao, A. *Controlled growth of Y-junction nanotubes using Ti-doped vapor catalyst.* Nano Letters **4**(2):213–217, 2004.

[30] Chai, Y.; Zhang, Q.F. and Wu, J.L. *A simple way to CN_x/carbon nanotube intramolecular junctions and branches.* Carbon **44**:687–691, 2006.

[31] Wei, D.; Liu, Y.; Cao, L.; Fu, L.; Li, X.; Wang, Y.; Yu, G. and Zhu, D. *A new method to synthetize complicated multibranched carbon nanotubes with controlled architecture and composition.* Nano Letters **6**(2):186–192, 2006.

[32] Gan, B.; Ahn, J.; Zhang, Q.; Rusli; Yoon, S.F.; Huang, Q.-F.and Chew, K.; Ligatchev, V.A.; Zhang, X.B. and Li, W.Z. *Y-junction carbon nanotubes grown by in situ evaporated copper catalyst.* Chemical Physics Letters **333**:23–28, 2001.

[33] AuBuchon, J.F.; Chen, L.H.; Daraio, C. and Jin, S. *Multibranching carbon nanotubes via self-seeded catalysts.* Nano Letters **6**(2):324–328, 2006.

[34] Li, J.; Papadopoulos, C. and Xu, J. *Growing Y-junction carbon nanotubes.* Science **402**:253–254, 1999.

[35] Xi, G.; Zhang, M.; Ma, D.; Zhu, Y.; Zhang, H. and Qian, Y. *Controlled synthesis of carbon nanocables and branched-nanobelts.* Carbon **44**:734–741, 2006.

[36] Pinault, M.; Mayne-L'Hermite, M.; Reynaud, C.; Pichot, V.; Launois, P. and

Ballutaud, D. *Growth of multiwalled carbon nanotubes during the initial stages of aerosol-assisted CVD.* Carbon **43**:2968–2976, 2005.

[37] Mangonon, P.L. *Ciencia de Materiales: Selección y Diseño.* Prentice Hall: Mexico, 2001.

[38] Schneider, J.J.; Engstler, J.; Franzka, S.; Hofmann, K.; Albert, B.; Ensling, J.; Gütlich, P.; Hildebrandt, P.; Döpner, S.; Pfleging, W.; Günther, B. and Müller, G. *Carbon nanotube bags: Catalytic formation, physical properties, two-dimensional alignment and geometric structuring of densely filled carbon tubes.* Chemistry-A European Journal **7**(13):2888–2895, 2001.

Chapter 3

Platinum cluster deposits on MWNTs-CN_x

Small clusters have attracted great attention in recent years due to their large surface to volume ratio and different electronic properties with respect to their bulk counterparts because of the finite spacing of their energy levels. [1] Nanoparticles exhibit high reactivity as a consequence of their large number of surface atoms. [2] It has been long recognized that regarding catalytic applications the size of the particle becomes an important issue. However the catalytic behavior of nanoparticles and its association with their size and structure is not fully understood at the present. [1]

Supported metallic clusters are widely used to catalyze chemical reactions, such as methanation, hydroformylation, reforming and partial oxidation. [2; 3] The size of these clusters strongly influence the turnover rates and selectivities of catalytic reactions. [3] As the catalytic activity depends on the size of the crystallites, it has been shown that it decreases with increasing the crystallite size because of a very strong interaction on low coordination sites. In addition, it has been observed a complex interaction between the porous of the surface support materials and the outer-shell of noble metal precursors, such as platinum, palladium, rhodium and ruthenium. [2]

The high reactivity of nanoparticles makes them good candidates for improving

automobile exhausts to further achieve the reduction of volatile organic compounds (VOCs) as well as their use as catalyst in fuel cells. [2]

Pt surfaces, for example, show higher reactivity for the activation of C–H bonds in CH_4 than other noble metals (e.g. Rh, Ru, Ir) for a given cluster size. [3] Platinum is also an important component of catalytic converters in automobiles used to reduce the emission toxic pollutants, such as CO, NO_x and hydrocarbons, and besides, it is a valuable heterogeneous catalyst for hydrogenation reactions. [1]

Compared to thin Pt films, platinum nanoparticles exhibit large surface available areas per Pt atom. Then, the use of CNTs as supports for keeping Pt particles well dispersed is convenient. The main advantage of using carbon nanotubes instead of carbon black as Pt supports is because the metallic particles usually are trapped in deep cracks of the carbon black particles, preventing them from working as catalysts or electrodes, while in CNTs most of the Pt particles are expected to be exposed for their use as effective catalysts. [4] This difference lies in the mass transfer resistance involved in the passage of the chemical species from the bulk of the solution to the available catalytic surface. At most unaccessible will be the catalyst, more difficult for the particle to reach and to react with it will be.

Recently, Matsumoto *et al.* [4] (2004) deposited Pt nanoparticles on MWCNTs treated with an aqueous mixture of $HNO_3/H_2[PtCl_6] \cdot 6H_2O$, and on carboxylated-MWCNTs' surface by their interaction with $[K_2PtCl_4]$. They reported that these coated MWCNTs show a higher performance than a commercial Pt-deposited on carbon black while reducing 60% Pt load (0.06–0.2 mg/cm^2 in Pt-CNT compared with the value of 0.5 mg/cm^2 for 0.5 mg/cm^2) per electrode area in polymer electrolyte fuel cells (PEFCs) in order to achieve currents below the 500 mA/cm^2.

This efficient loading is thus an important reason for the development of PEFC applying CNTs as support for Pt catalysts. [4] A network constructed by CNTs, similar to the one described in section 2.5, is expected to enhance the yield of the catalyst turnover. The possible micropores or gas lines throughout the CNT network will result in high performance anode. [4]

We studied the feasibility of producing platinum deposits on MWNTs-CN_x due to the possible catalytic properties of Pt clusters. The advantage of using MWNTs-CN_x is that they are chemically more reactive than MWCNTs and, therefore, they do not require previous acidic treatment to create an efficient deposition of Pt nanoparticles on their surface. In this chapter, we discuss the results obtained for platinum cluster deposition on MWNTs-CN_x.

3.1 Experimental methodology: Anchorage of Pt clusters on MWNTs-CN_x

The method used to deposit Fe clusters involving an open reflux in aqueous acetic acid medium (described in section 2.2.1.2), was extended to Pt-coordination salts. Detailed experimental procedure was explained in chapter (see page 49).

The selected Pt precursor was sodium hexachloroplatinate(IV) hexahydrate, $Na_2[PtCl_6]\cdot 6H_2O$, (Aldrich 98%). This compound decomposes at 110 °C and 1 atm of pressure. [5] Since this temperature is below the estimated boiling point of the aqueous acidic solution (ca. 118 °C), a reflux temperature slightly higher was selected in order to promote the complete breaking of the platinum coordination salt.

The experiments were set up in order to have obtain constant concentrations of 0.05 mol Pt/mol $C_{MWNTs-CN_x}$ in the system. The temperature values ranging from 108 °C to 112 °C and an Ar flow of $\leq$ 0.70 L/min were found to be suitable for achieving an efficient Pt deposition.

The products were characterized by SEM (Philips FEG-XL30 equipped with an EDAX EDS detector) operating at acceleration voltages below 10 keV; HRTEM (Field emission JEOL-JEM-3000F) with 400 keV for acceleration voltages; powder XRD (Brucker D8) equipped with a Cu anode (λ = 1.5406 Å) operated at 35 kV, 25 mA and 293 K from 10° to 100° in 2θ angle; and, by Raman in a Kraiser Holo Lab 5000 system (2.33 eV) at λ = 533 nm (located at Shinshu University, Japan).

3.2 Results and Discussion: Pt clusters deposition on MWNTs-CN_x

The parameters identified as critical in order to control the Pt size and their interaction and distribution on the MWNTs-CN_x were the temperature profile and the Ar flow during the open reflux. In general, the mean crystallite size increased by raising the mean temperature of the deposition process. This observation agrees with those reported by Gorišek P. *et al.* [2]

Characteristics of the Pt deposit are highly related with the temperature profile used in the reflux during the experiment. The temperature varied between 108–112 °C and remained constant until all acidic solution became evaporated. Nevertheless, during the final cooling process at about the 56th hour, the temperature increased rapidly up to 118 °C because the sample was completely dried to that moment and, the hot plate was heating at the same rate that when the system was not dried. Minutes after recording this overheating, the hot plate was completely turned off and the temperature finally cooled down to room temperature. This situation is normal and was observed in all the experiments performed.

SEM images of the product obtained after refluxing the MWNTs-CN_x in acidic medium with $Na_2[PtCl_6]$ under the conditions explained above are shown in fig. 3.1.

Figure 3.1*a* shows the pristine MWNTs-CN_x used in this study. It can be observed that the nanotubes are highly aligned in a carpet-like configuration. On the other hand, fig. 3.1*b* shows the MWNTs-CN_x after their acidic open reflux treatment with an acidic solution of $Na_2[PtCl_6]$ in Ar atmosphere. Disordered tubes can be observed in this image and lighter particles spread over them. EDX analysis in fig. 3.1*d* confirmed that these particles were composed of Pt. A highly uniform distribution of Pt clusters can be observed in our product after the acidic treatment. A close up to 3.1*b* is shown in 3.1*c* where the particles are easily identified and can be seen to attach on the nanotubes surface. The average diameter of these particles was 49.66±9.83 nm, obtained by the geometrical mean of the measurements performed

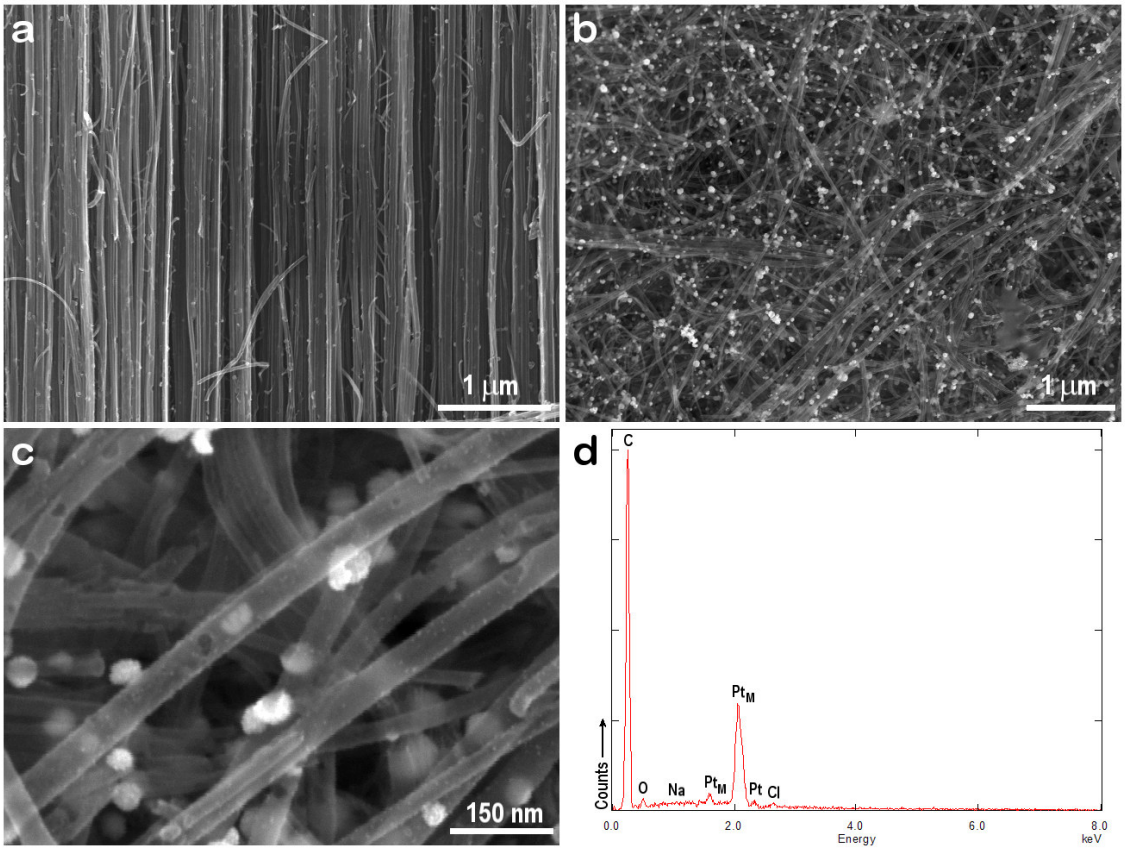

Figure 3.1: SEM images of MWNTs-CN_x before and after their treatment with $Na_2[PtCl_6]$. **a)** SEM image of as-produced MWNTs-CN_x. **b)** MWNTs-CN_x after their treatment with $Na_2[PtCl_6]$ in an aqueous CH_3COOH solution. Brighter spots are Pt nanoparticles. **c)** Close-up of (*b*). Two particle sizes can be observed, the larger are ∼50 nm in diameter meanwhile the smaller exhibit a diameter of 4.6 nm in average. **d)** EDX of the MWNTs-CN_x after treatment with $Na_2[PtCl_6]$. Transition M of platinum is detected. The atomic percentages measured are 92.99% C, 4.39% Pt, 1.89% O, 0.37% Na and 0.36% Cl.

in several SEM images taken from this sample.

When observing figure 3.1*c* carefully, bright dots and a rough surface can be observed on the MWNTs-CN_x. This rough surface exhibited small dots in bright contrast which are not observed in the MWNTs-CN_x before the treatment (see figs. 3.1*a* and 2.9*a*). Generally, this contrast difference indicates the presence of an element possessing a higher atomic number. Since the EDX analysis (fig. 3.1*d*) shows the presence of Pt as the only transition metal, we concluded that if the rugosity is done from metal particles, they were made of Pt. The average diameter found for these "dots" corresponded to 4.6±1.04 nm, also measured from the SEM

images. However, in order to verify the composition of the small particles, we also performed STEM and HRTEM imaging of this sample.

STEM imaging was performed on the sample in order to identify the nature of the particles and "dots" observed by SEM. The images taken can be seen in fig. 3.2. Figs. 3.2*a* and 3.2*b* show an uniform distribution of the small particles over the whole surface of the MWNTs-CN_x.

In order to clean up the residues of sodium, chlorine and cationic platinum within the sample, this product was washed with distilled hot water (T≤60 °C) followed by mechanical stirring by a vortex. The MWNTs-CN_x were recuperated by centrifugation at 3,500 rpm for 10 minutes. This complete process was repeated twice. Finally, the product was dried in an air convective oven at 60 °C overnight.

The washed Pt-MWNTs-CN_x were characterized by SEM and STEM imaging. Images of clean products are shown in figs. 3.2*c* to *e*. These images are very similar to that of the tubes before washing (fig. 3.1*c*). Bright field STEM images (figs. 3.2*d* and 3.2*e*), do not exhibit any difference in the distribution and size of the Pt particles deposited on MWNTs-CN_x when compared with the samples before washing. EDX performed in the washed sample (see fig. 3.2*f*) does not detect the signals of Na and Cl, which mean that the sample was efficiently cleaned. At the same time, the signals corresponding to platinum indicate that those particles remain in the sample. EDS measurements revealed a composition of 92.85 at. % C, 3.95 at. % Pt, 2.4 at. % O and 0.8 at. % Fe. The iron presence detected comes from the remainder catalyst used during the MWNTs-CN_x synthesis. Thus, from these studies we can conclude that the observed "bright dots" correspond to small Pt particles.

This indicates that our cleaning procedure to remove sodium and chlorine works efficiently, and that the observed particles are composed of platinum with oxidative state of zero. The absence of charge in the platinum clusters reduces their solubility in a polar solvent; this explains why the clusters remained deposited on the MWNTs-CN_x and were not wiped out from their surface. Therefore in our procedure, besides releasing the Pt from inside the coordination sphere, it is being reduced

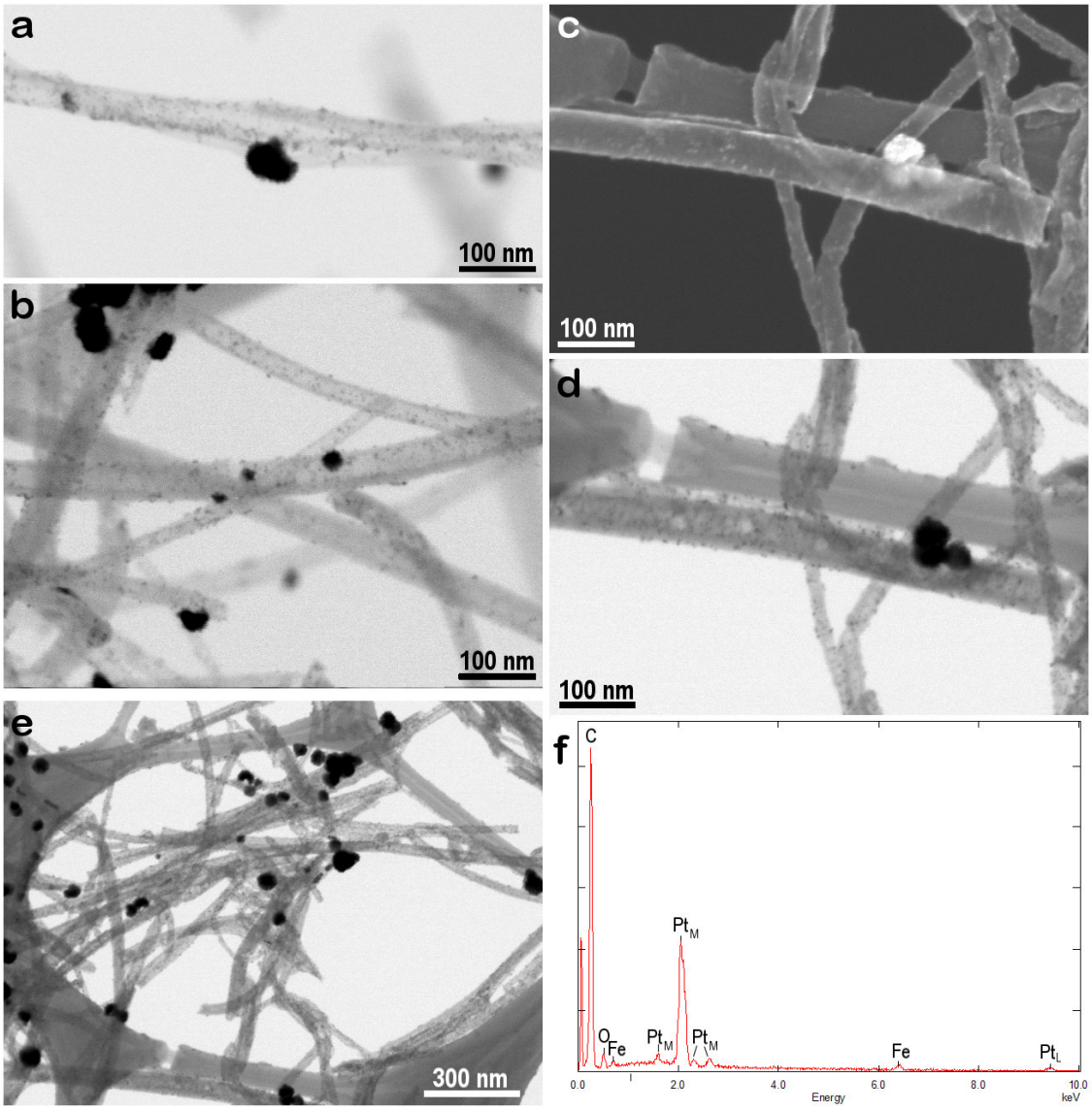

Figure 3.2: STEM images of MWNTs-CN_x after their treatment with $Na_2[PtCl_6]$. **a)** Bright field (BF) STEM image of MWNTs-CN_x after treatment with $Na_2[PtCl_6]$. **b)** BF STEM image of several MWNTs-CN_x after treatment with $Na_2[PtCl_6]$. **c)** SEM image of Pt-MWNTs-CN_x after washing in distilled water. The rough surface is due to Pt deposition. **d)** BF STEM image of *c*. **e)** BF STEM image of the product after washing. **f)** EDX performed on the Pt-MWNTs-CN_x after their distilled water washing. The atomic percentages measured with EDS correspond to 92.85% C, 3.95% Pt, 2.4% O and 0.8% Fe.

from the oxidation state of +4 to 0, which ensures the presence of a no removable deposit of these clusters by the action of water. This is remarkable, because the Pt clusters deposited on the MWNTs-CN_x can act as active catalysts that allows their implementation in diverse processes of interest.

Previous studies carried out by Gorišek, P. *et al.* in 2004, found that carboxylic acids act as reducing agents for the deposition of Pt particles on alumina substrates at temperatures between 100 and 200 °C. [2] Then, the presence of the acetic acid needed for the dispersion and protonation of MWNTs-CN_x in our system during the reflux treatment, could be responsible of the reduction of the deposited metallic Pt.

It is important to emphasize that the presence of oxygen detected in the sample is low and it is not associated to any kind of platinum oxide. This contrasts with the results observed for iron cluster deposition (fig. 2.12). This difference is easily explained by the fact that platinum does not oxidize in air at any temperature, [5] while the iron oxidizes easily at room temperature in the presence of air. [6]

HRTEM images of Pt-MWNTs-CN_x are shown in fig. 3.3. Figure 3.3*a* shows the bamboo-like structure of MWNTs-CN_x in addition to small particles deposited on the surfaces of the nanotubes. The average diameter of these particles, obtained from HRTEM was found to be 2.94±0.53 nm. This more accurate value is close to that obtained from SEM analysis (4.6 nm).

Fig. 3.3*b* shows Pt nanoclusters dispersed on MWNTs-CN_x. It can be observed that some of the particles tend to be deposited in the inter-compartment border of the bamboo-like structure of MWNTs-CN_x. This could probably be due to these linking regions are usually enriched in nitrogen. [7] Thus, we can state that it is reasonable to believe that an interaction between the N-sites and the Pt occurs.

A Pt-particle deposited on the external nanotube's surface, with easily visible atomic planes can be seen in fig. 3.3*c*. Particles laying on the internal surface are also observed. An agglomeration of Pt nanoclusters is observed in the exposed broken part of a MWNT-CN_x (fig. 3.3*d*), specifically in the neighborhood of the interlinking compartment section, just like in the image shown in figure 3.3*b*.

FFT were performed from the HRTEM of the Pt particles found along the MWNTs-CN_x. The FFT shown in the inset (*i*) belongs to the atomic planes of the Pt-particle enclosed in the dashed rectangle marked with the same character in fig. 3.3*c*. These planes were identified as the Pt (200) and its equivalent Pt ($\bar{2}00$)

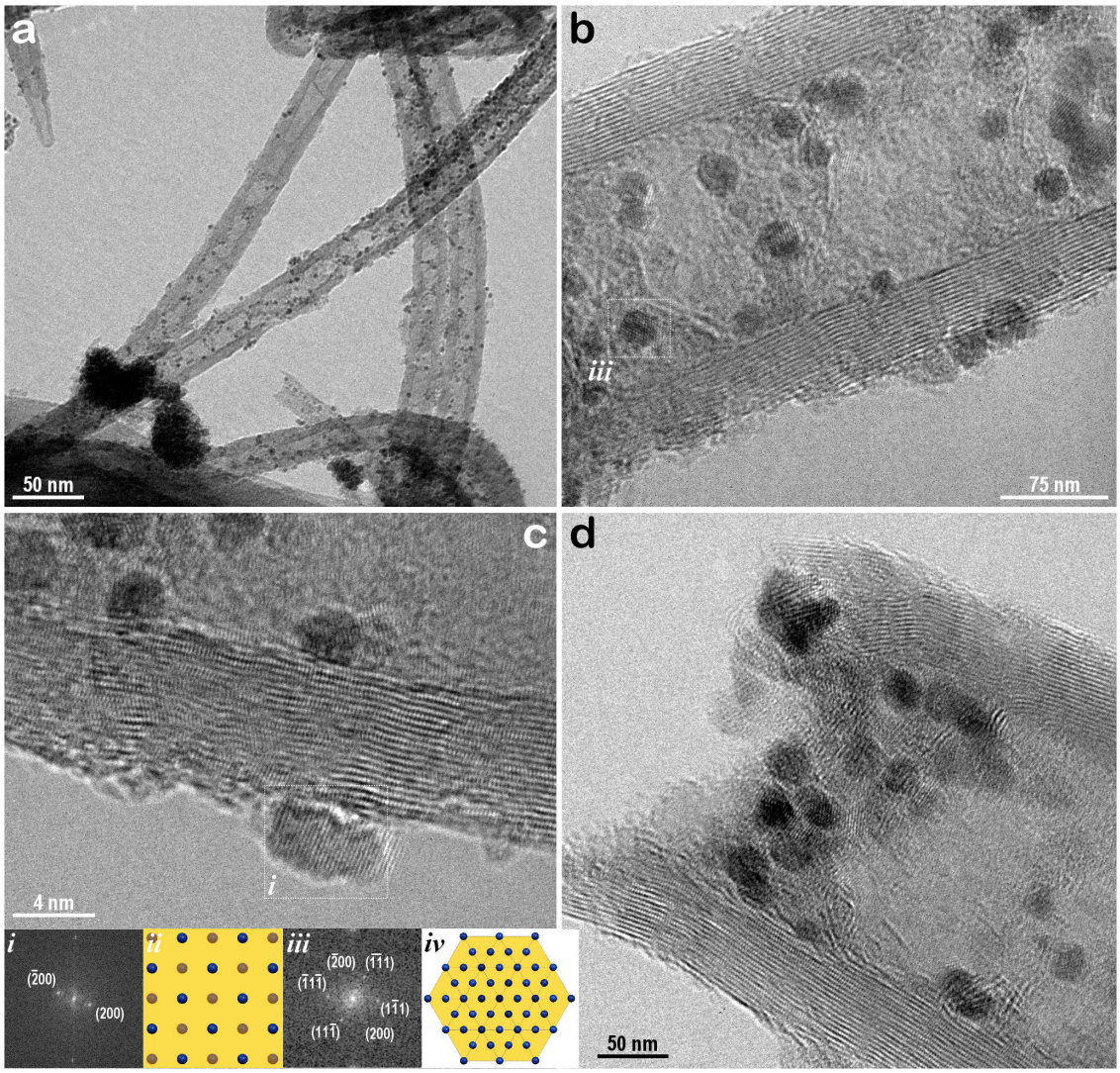

Figure 3.3: HRTEM images of washed Pt-MWNTs-CN_x . a) Low magnification HRTEM image showing the distribution of Pt particles on MWNTs-CN_x. **b)** High magnification HRTEM image where crystalline planes of the graphene layers and Pt particles can be observed. **c)** Close-up of a MWNT-CN_x where a Pt cluster can be seen deposited on the external surface. **d)** Broken MWNTs-CN_x showing several Pt particles at the end of a bamboo-like compartment. *Insets:* (*i*) FFT of the Pt cluster located on the surface of MWNT-CN_x; (*ii*) molecular representation of the normal view from the face (002) in a Pt *fcc* crystal; (*iii*) FFT of a Pt particle inside a MWNT-CN_x marked as *iii* in *b* and, (*iv*) molecular representation of the zone axis [011] in a Pt *fcc* crystal.

in a *fcc* structure exhibiting an interlayer spacing measuring 1.951 Å. A simulated Pt *fcc* ($Fm\bar{3}m$) crystal using a lattice parameter of $a = 3.923$ Å, [8] aided by the software *Cerius*^{2}, produced an interlayer space of 1.962 Å. Inset (*ii*) in fig. 3.3 is the molecular representation performed of the face that is readily observed on Pt

particle enclosed in (*i*). This corresponds to the direction [012] which is normal to the diffraction plane (200) that is observed in the FFT.

On the other hand, fig. 3.3, inset (*iii*) presents the indexed FFT corresponding to the Pt particle enclosed in the dashed rectangle marked as (*iii*) in fig. 3.3*b*. This FFT is equivalent to a single crystal diffraction pattern of a *fcc* structure taken from the direction [011] (see *iv* in fig. 3.3), which is normal to the planes (111) and (200) of Pt *fcc*. Interlayer spacing measured from the FFT for the planes of the {111} family shown in (*iii*) corresponds to 2.263 Å, which is similar to the value of 2.265 Å given by the simulation for these interplanar distances in *Cerius*^{2}.

XRD powder analysis were also performed on the Pt-MWNTs-CN_x before and after washing. The XRD pattern for MWNTs-CN_x after refluxing in aqueous acetic acidic medium with $Na_2[PtCl_6]$ is shown in fig. 3.4*a*. It indicates the presence of NaCl crystals and Pt, both belonging to the face-cubic centered structure. It is believed that the unidentified peaks correspond to other acetate and chloride salts of platinum and sodium.

After washing the sample (see fig. 3.4*b*), only the peaks corresponding to Pt *fcc* and the plane (002) of graphite are observed. A XRD pattern simulated for Pt *fcc* using the *Cerius*^{2} software is shown in fig. 3.4*c*. It is easily noted that all the signals corresponding to the distinctive structure of simulated Pt *fcc* and their relative intensities are in agreement with the experimental data.

We also performed an analysis of the size of the Pt crystallites using the Scherrer equation (see appendix B, a value of K=0.89 was used), by measuring the full width at half maximum (FWHM) for the diffraction peaks belonging to each plane in fig. 3.4*b*. The lengths obtained for the periodicity in the different planes are summarized in table 3.1.

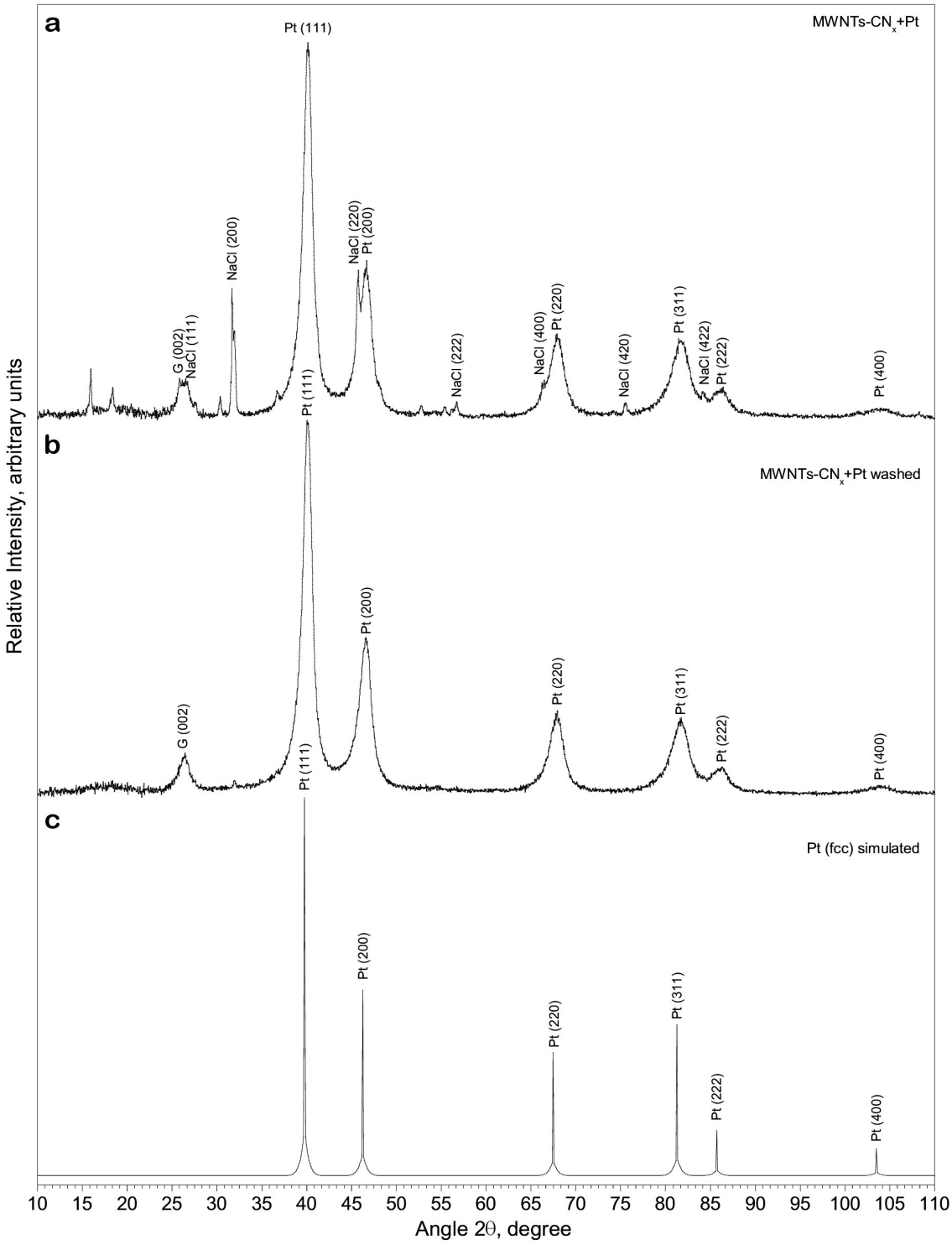

Figure 3.4: Comparative XRD patterns of Pt-MWNTs-CN_x. **a)** X-ray powder diffraction pattern of MWNTs-CN_x treated with $Na_2[PtCl_6]$. **b)** X-ray powder diffraction pattern of MWNTs-CN_x treated with $Na_2[PtCl_6]$ after washing with distilled hot water. **c)** Simulated powder XRD pattern using *Cerius*^{2}. Signals marked as G corresponds to graphite ($P6_3/mmc$, a = 2.4560 Å, c = 6.6960 Å); Pt nanoparticles exhibit a *fcc* structure ($Fm\bar{3}m$, a = 3.9231 Å) and NaCl to *halite* ($Fm\bar{3}m$, a = 5.620 Å).

Even though the values for the platinum crystallite sizes shown in table 3.1 do not exactly agree with those obtained by HRTEM, are close to them. This fact enables us to state that the Pt deposits on MWNTs-CN_x exhibit diameters smaller than 6 nm (being 3 nm the average size).

Table 3.1: Pt crystallite sizes in Pt-MWNTs-CN_x.

Plane	Crystallite size [nm]
111	6.43±0.64
200	5.06±0.51
220	5.16±0.52
311	4.10±0.41
222	4.25±0.42

The presence of two different sizes of Pt particles could be explained by the way in which the Pt atoms nucleate. Classically, two nucleation process are differentiated: homogeneous and heterogeneous. The homogeneous nucleation process is sometimes considered as an ideal process, but in practice some crystal growth process can be approximated to this approach. In order to grow a crystal, it is necessary that the nucleus acquire a critical size; but if the new nuclei are smaller than the critical size, they dissolve in the liquid phase again. Homogeneous nucleation is characterized, *grosso modo*, by exhibiting a higher nucleation volume than that expected for the heterogeneous mechanism for a particle with the same critical radius, r_c. [9] Since we observed that the larger Pt particles (50 nm in diameter) do not show interactions with the MWNTs-CN_x, we can suppose that they come from a nucleation mechanism close to the homogeneous one, possibly an heterogeneous one on very small impurities. On the other hand, the small particles (3 nm in diameter) probably grow by the adhesion of a few Pt atoms on MWNTs-CN_x sites, which exhibit affinity, and further addition of Pt atoms. These particles will exhibit smaller size because of the way they grew from the MWNTs-CN_x used as substrates.

Raman spectroscopy performed on the MWNTs-CN_x before and after their coverage with Pt shows no changes (fig. 3.5). The ratio I_D/I_G corresponds to 0.953 for the MWNTs-CN_x without any previous treatment (fig. 3.5*a*), and 0.909 after the

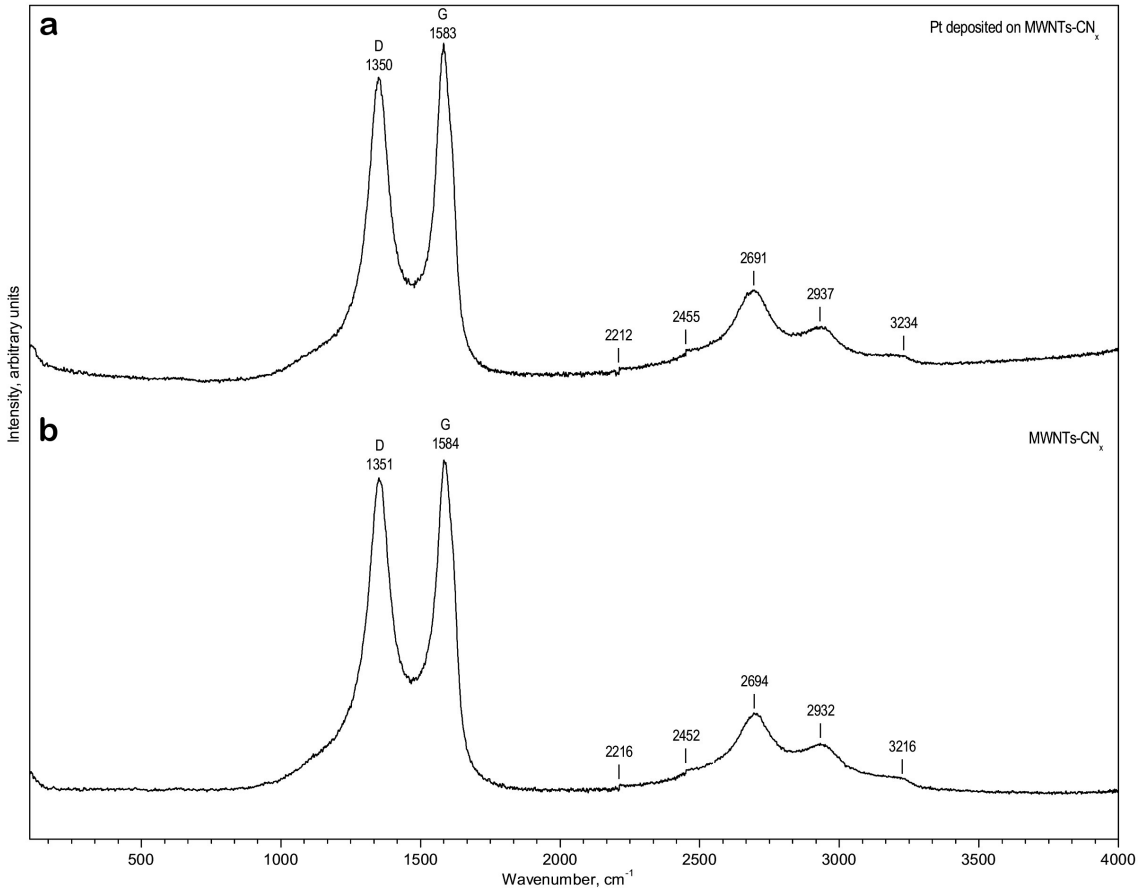

Figure 3.5: Raman spectrum for Pt-MWNTs-CN_x . a) Raman spectrum for Pt-MWNTs-CN_x after washing. **b)** Raman spectrum for MWNTs-CN_x before any treatment.

Pt deposition (fig. 3.5*b*). The average value of I_D/I_G for several Raman spectra of the Pt-MWNTs-CN_x samples is 0.932. This is similar to that previously reported in chapter 2 for MWNTs-CN_x just after their acidic treatment. As was stated in the same chapter, this decrement in the ratio I_D/I_G is indicative of a possible purification process performed on the MWNTs-CN_x.

This lack of changes in the intensities of the Raman and peaks position seems to indicate that the Pt particles are not covalently attached to the MWNTs-CN_x surface. Then, this behavior could lead to think that the Pt nanoparticles are deposited directly on the surface of the MWNTs-CN_x but not by any covalent bonding with oxygen or other element. This agrees with the proposed reaction mechanism that established that the nitrogen lone pair of electrons would aid to stabilize the metal particles without establishing any covalent bonding.

This would be desirable since we are depositing metallic particles on the MWNTs-CN_x without performing chemical modifications on their surface. Therefore, their mechanical properties would remain intact due to the absence of carboxyl groups on their sidewalls. However, the presence of metal particles on the nanotubes' surface would induce an enhancement on the electronic transport of MWNTs-CN_x.

3.3 Conclusions

In this chapter we demonstrated the feasibility of depositing Pt nanoclusters on MWNTs-CN_x using a relatively simple method that does not involve a further process for reducing the metallic particles using a coordination salt as precursor of Pt.

It was shown that these nanoclusters are composed only of Pt exhibiting the *fcc* structure. This observation ensured that the Pt was reduced, being it probably achieved by the presence of acetic acid. Diverse characterization techniques (SEM, STEM and HRTEM) showed that these metallic particles are homogeneously distributed on the outer surface of MWNTs-CN_x. Parameters such as temperature and inert gas flow were found to be important in the deposition process for controlling the size of the Pt particles deposited on the MWNTs-CN_x. Washing the sample with distilled water revealed that the Pt remained attached to the MWNTs-CN_x surface.

A bimodal distribution size of Pt particles was found. The larger particles ($\sim$50 nm in diameter) appear to be deposited mostly on the MWNTs-CN_x but it seems that they do not exhibit a large interaction with the nanotubes. The smallest clusters of 3 nm are practically covering all the surface of MWNTs-CN_x in a homogeneous way. However, agglomeration of such clusters was observed in the interlinker separators of the bamboo-like structures in the MWNTs-CN_x, containing higher nitrogen concentrations.

The presence of a bimodal distribution in the size of Pt particles found in the product, can be explained by the presence of two differentiated crystal growth mechanisms. This consideration appears to be in agreement with the apparent distinct interaction with the MWNTs-CN_x' surface exhibited by the Pt particles according to their size.

Other studies performed on the sample (HRTEM and XRD) allowed us to obtain the sizes of the small Pt particles, and it was concluded that they shown

the *fcc* phase. Some of their characteristic crystallographic planes were identified and confirmed by crystallographic simulations of Pt *fcc*.

Finally, aided by Raman spectroscopy of Pt-MWNTs-CN_x sample, we stated that the Pt was probably merely attached to the MWNTs-CN_x surface and not by covalent bonding. When the Raman spectrum of the Pt-MWNTs-CN_x system was compared with that of the MWNTs-CN_x before any treatment, only small differences were found. The decrease in the I_D/I_G ratio was similar to that found for MWNTs-CN_x refluxed in aqueous acetic acid, which suggests that these nanotubes and the Pt-MWNTs-CN_x are basically the same in their chemical structure.

Therefore, we can conclude that our method produced small Pt nanoclusters attached to the MWNTs-CN_x without producing any significant modification on their surface.

References

[1] Xiao, L. and Wang, L. *Structures of platinum clusters: Planar or spherical?* Journal of Physical Chemistry A **108**:8605–8614, 2004.

[2] Gorišeck, P.; Francetič, V.; Lengauer, C.L. and Maček, J. *The reduction of hexachloroplatinic(IV) acid on the surface of alumina.* Acta Chimica Slovenica **51**:203–211, 2004.

[3] Ramallo-López, J.; Requejo, F.; Craievich, A.; Wei, J.; Avalos-Borja, M. and Iglesia, E. *Complementary methods for cluster size distribution measurements: supported platinum nanoclusters in methane reforming catalysts.* Journal of Molecular Catalysis A: Chemistry **228**:299–307, 2005.

[4] Matsumoto, T.; T., K.; Nakano, H.; Arai, K.; Nagashima, Y.; Yoo, E.; Yamazaki, T.; Shimizu, H.; Takasawa, Y. and Nakamura, J. *Efficient usage of highly dispersed Pt on carbon nanotubes for electrode catalysts of polymer electrolyte fuel cells.* Catalysis Today **90**:277–281, 2004.

[5] Lide, D.R., ed. *CRC Handbook of Chemistry and Physics.* Taylor and Francis: Boca Raton, FL, 86th edition, 2005.

[6] Babor, J.A. and Ibarz Aznárez, J. *Química General Moderna.* Epoca: México, D.F., 1977.

[7] Lim, S.H.; Elim, H.I.; Gao, X.Y.; Wee, A.T.S.; Ji, W.; Lee, J.Y. and Lin, J. *Electronical and optical properties of nitrogen-doped multiwalled carbon nanotubes.* Physical Review B **73**:045402, 2006.

[8] Villars, P. and Calvert, L.D. *Pearson's Handbook of Crystallographic Data for Intermetallic Phases.* ASM International, 2nd edition, 1991.

[9] Mangonon, P.L. *Ciencia de Materiales: Selección y Diseño.* Prentice Hall: México, 2001.

Chapter 4

Titanium cluster deposits on MWNTs-CN_x

Two different approaches were used to obtain a Ti cluster deposit on MWNTs-CN_x. The first one consists on the use of MWNTs-CN_x as working electrodes. In this context, few electrochemical studies of this kind have been performed using MWNTs-CN_x as electrodes up to day, which contrasts with the considerable number [1–16] of investigations carried out for undoped carbon nanotubes. The electronic properties exhibited by MWNTs-CN_x, pointed out in section 1.2, suggest that they can show an efficient electrochemical behavior.

The second approach was the incorporation of Ti during the CVD synthesis of carbon nanotubes. An economical Ti precursor, compatible with the carbon sources employed was selected and tested. The experimental procedures and results of these approaches are described in this chapter.

4.1 Electrodeposition of Ti on MWNTs-CN_x

4.1.1 Introduction to electrochemical techniques

Electrochemical cells, in which faradaic currents are flowing, are classified as either *galvanic* or *electrolytic cells*. In *galvanic cells* reactions occur spontaneously on the electrodes when they are connected externally by a conductor, thus generating current flow. An *electrolytic cell*, in opposition, requires the imposition of an external voltage greater than the open-circuit potential of the cell in order to promote chemical reactions. Therefore, these cells are frequently employed to carry out desired chemical reactions by expending electrical energy. However, we are often concerned with reactions occurring on one of the electrodes. The term that defines broadly the chemical changes accompanying faradaic reactions[1] on the electrodes in contact with electrolytes is *electrolysis*. When discussing cells, the electrode in which reductions ($O + ne^- \rightarrow R$) occur is called the *cathode*, and the electrode at which oxidations occur ($R - ne^- \rightarrow O$), the *anode*. The current in which the electrons cross the interface from the electrode to the species in solution is named *cathodic current*; and when the electron flow goes from species in solution into the electrode it is known as *anodic current*. [17]

The electrochemical studies in a cell consist in observing changes in current, potential or concentration. In *potentiometric* experiments, the electrical potential remains constant during the reaction time. The chemical reactions to be promoted in the electrode, are frequently governed by the thermodynamic properties of the system. [17] One of the electrochemical techniques able to reduce chemical species found in solution on electrode surfaces' is *potentiometry*; because it promotes a chemical reaction by the application of potentials higher and lower than those exhibited by redox pairs in their thermodynamic equilibrium. An example of its

[1] A *faradaic reaction* is a heterogeneous charge-transfer reaction occurring at the surface of an electrode governed by Faraday's law: $i = F \cdot eq$, where i is the current, F the Faraday's constant (96,485.4 C/ eq) and eq are the chemical equivalent transfered in the reaction.

application is electrode metal plating.

Other electrochemical techniques that we will refer in this chapter is *cyclic voltammetry* (CV). In this technique a linear swept of potential *vs* time is applied to a working electrode (WE) in a cyclic way (reversal technique).

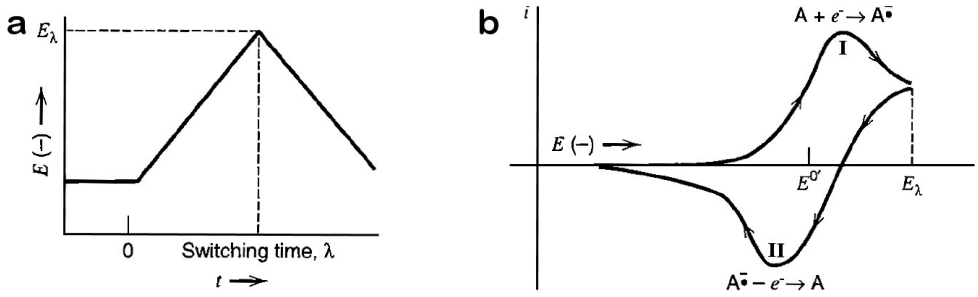

Figure 4.1: Cyclic voltammetry technique. a) Cyclic potential sweep. **b)** Resulting cyclic voltammogram. Image taken from [17].

Cyclic voltammetry has become a very popular technique for initial electrochemical studies of new systems, and has proven to be very useful to obtain information of fairly complicated electrodes. When the potential is lowered and is close to the equilibrium potential for the system, $E^{0'}$, the reduction begins and the current starts to flow. As the potential decreases towards more negative values, the surface concentration of the analyte, A, must drop, and hence the flux to the surface (and the current) increases. As the potential moves down to past $E^{0'}$, the surface concentration nearly drops to zero and mass transfer of the analyte to the surface reaches a maximum rate, and then it declines as the depletion effect sets in. This results in a current-potential curve with a peak-like feature, depicted in fig. 4.1 (labeled with I). [17] If we suddenly reverse the potential in a positive direction at this point, at first, will be a large concentration of the oxidizable analyte (A^-) in the electrode vicinity. As the potential increases to pass $E^{0'}$, the electrochemical balance at the surface grows more and becomes more favorable to the neutral analyte especies (A^0). Thus, the anion is reoxidized and an anodic current flows. This reversal current has a shape much like that of the forward peak for essentially the same reasons (see peak II in fig. 4.1). [17]

4.1.2 Carbon nanotubes as electrodes

Carbon has been widely used as an electrode material because of its many advantages, including good electrical conductivity, chemical inertness, and wide potential range. [5; 7] It was found that CNTs posess fascinating properties such as fast electron transfer rate and high electrocatalytic activity. [7] The referred electronic properties suggest that CNTs have the ability to promote electron-transfer reactions when used as electrodes in chemical reactions. [3] Recent applications of electrodes made of bundles of CNTs, CNTs membranes, polymer-CNTs composite and CNTs modified electrodes, indicate that carbon nanotubes can be used as effective electrochemical biosensors. [7]

Electrochemical phenomena of electrodes with critical dimensions (less than the scale of the diffusion layer) *i.e.* ultramicroelectrodes (UMEs) have been intensively studied since the 1980s due to their potential use as: ultrasensitive electrochemical sensors, analytical tools for measuring kinetics of fast-electron transfer reactions, and probes to detect species in microenvironments. Furthermore, by decreasing their size from microns to nanometers, the temporal and spatial resolution of the electrodes can be improved by orders of magnitude. [5]

The advantages of nanoelectrodes come from their high mass sensitivity, increased mass transport rate and decreased influence of the solution resistance. An array of nanoelectrodes can produce a much higher current than a single nanoelectrode, which can avoid the need for expensive electronic devices and improve the signal to noise ratio. In order to make such a device based on CNTs, it is important to ensure that the interspacing among CNTs must be higher than the radius of each nanotube in order to avoid an overlapping of the diffusion layers. Otherwise, arrays of nanoelectrodes will behave as macroelectrodes. [7]

Nanoelectrodes consisting of CNTs arrays show fast detection of analytes up to 2000 mV sweep voltages during voltammetric studies, [7] and high sensitivity in sensing trace species, of about 10^{-9} M, which is about 100 to 1000 times better than conventional electrodes (typically limited to concentrations $> 10^{-7}$ M). [5]. This

makes possible the construction of fast electronic sensors for detecting heavy metals or toxic species in water.

Recently, Jia *et al.* [18] have shown the immobilization of proteins on MWNTs-CN_x surface promoting redox reactions of their catalytic sites by electrochemical methods. Another study by Heng *et al.* [19] demonstrated that randomly dispersed MWNTs-CN_x are more electrochemically active than MWCNTs due to their bamboo-like structure, that comes from the existence of transverse walls in the MWNTs-CN_x at regular distances. These compartments act as the end caps of SWCNTs-MWCNTs, providing an ideal graphite edge-plane like electrode which is expected to have fast electron transfer rates. [5; 19] In this case, the electrons can pass from the open end of the CNT to the measuring circuit without hopping to different graphitic layers. The sidewalls of MWCNTs, in contrast, behave as the basal plane of highly oriented graphite and display a very slow transfer rate and low specific capacitances. [5] Therefore, MWNTs-CN_x enable us to build more efficient electrodes exhibiting higher response currents (about 5 times) [19] than glassy carbon or MWCNTs electrodes; without having to create a low density, highly ordered arrangement of them.

Furthermore, the existence of more active functional groups in CNTs such as hydroxyl and carboxyl species can enhance the electrochemical properties of the nanotubes as pointed out in the literature. [3; 8; 19] When compared to MWCNTs, the use of randomly carboxylated-MWNTs-CN_x as working electrodes, has shown a reduction of the potential difference in the peaks (ΔE_p) where the reduction and oxidation of the electroactive species occurs. This indicates a more rapid electron transfer rate in MWNTs-CN_x; an advantage conferred by the existence of more electroactive sites per unit area. [19]

It is then important to study the inherent properties of MWNTs-CN_x for electrochemical applications. In the first section of the chapter, their use as working electrodes for Ti deposition will be described.

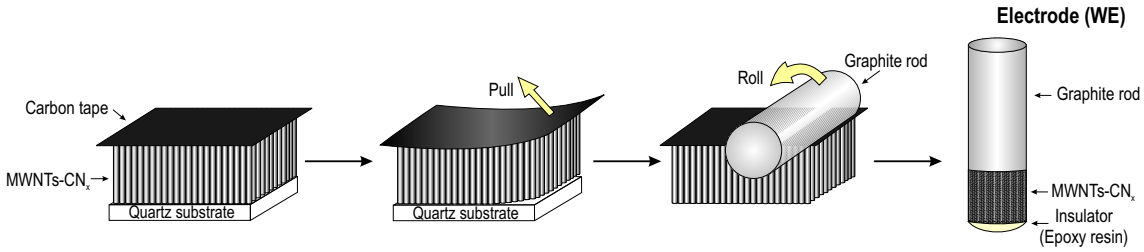

Figure 4.2: Schematic procedure for WE graphite-MWNTs-CN_x electrodes production. An aligned array of MWNTs-CN_x was used and fixed on the perimeter of a graphite rod using two sided carbon tape. Exposed graphite was isolated with expoxy resin. This procedure leaves the MWNTs-CN_x array recoverable for further possible analysis. Further details are explained in the main text (section 4.1.3.1).

4.1.3 Experimental

4.1.3.1 Elaboration of graphite-MWNTs-CN_x working electrodes

We started from aligned MWNTs-CN_x synthesized in a quartz plane substrate by a typical CVD process described elsewhere. [20–22]

1. Graphite rods of 3 mm and 5 mm in diameter, were cut to pieces of 1.5 to 2 cm and their ends were polished.

2. Two sided carbon tape was attached on the upper surface of aligned MWNTs-CN_x, which were growth in a flat quartz substrate (step 1, fig. 4.2).

3. Once this tape was fixed to the surface of the MWNTs-CN_x carpet, the graphite rod was rolled on the free side of the carbon tape (see fig. 4.2, steps 2 and 3) thus, obtaining MWNTs-CN_x radially aligned on the surface of the graphite rod.

4. Finally, the exposed end of the graphite rod was covered with a commercial epoxy resin, to prevent the graphite from acting as an electrode by itself.

These electrodes were used as working electrodes (WE) for performing different electrochemical reactions of interest.

The internationally accepted primary reference for measuring electrode potentials is the *normal hydrogen electrode* (NHE), but it is not very convenient from

an experimental standpoint. Along this chapter we used another common reference for electrochemical systems: the *saturated calomel electrode* (SCE), $Hg/Hg_2Cl_2/KCl$(sat in water) (E= 0.242 V *vs* NHE). [17] The voltages reported in this section would be referred to the SCE if otherwise is not indicated.

4.1.3.2 The electrochemical cell

Two Ti precursors were selected for the electrochemical tests: titanium(IV) oxide (TiO_2) and the titanium tetrachloride ($TiCl_4$). Due to the low solubility of TiO_2 in different usual inorganic solvents as aqueous solutions, some systems were tested in order to increase the solubility of Ti. The Pourbaix diagram for Ti was used (see fig. 4.3) in order to find the best solubility conditions of the oxide.

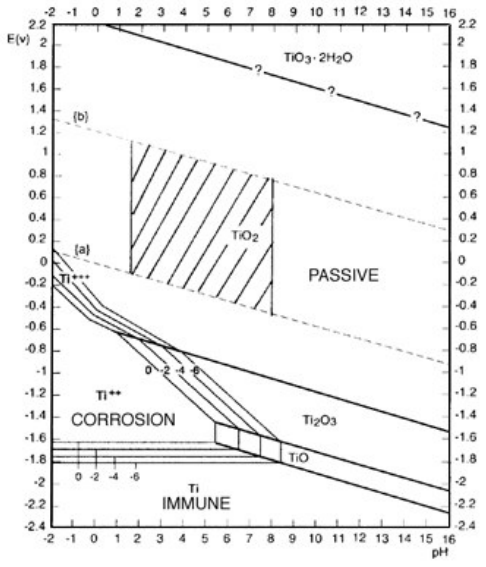

Figure 4.3: Pourbaix diagram (E vs pH) for titanium-H_2O system. For Ti in water there is only one corrosion region (availability to release metal ions into solution), and three different favored passive oxide phases. The *passive* region indicates that corrosion (though possible) is less likely than the formation of a protective oxide layer on the metal surface. The *immune* region implies that no corrosion will occur (this is the region sought for cathodic protection of the metal). [23] Image taken from [23].

For system using TiO_2, the following conditions were used: as electrolyte 0.0401 g TiO_2 ($\sim 5 \times 10^{-3}$ mol) were dispersed in an aqueous solution of HF, 2 v % and HNO_3, 4% v. The acidic solution along with the MWNTs-CN_x-WE and a Pt CE were placed in a plastic recipient since the hydrofluoric (HF) dissolves glass (SiO_2). This vessel was joined by an agar bridge of KNO_3 0.5 M to an aqueous solution 0.13 M of the same salt. This solution served as the reservoir of the SCE. The schematics of the experimental setup for this electrochemical cell is shown in

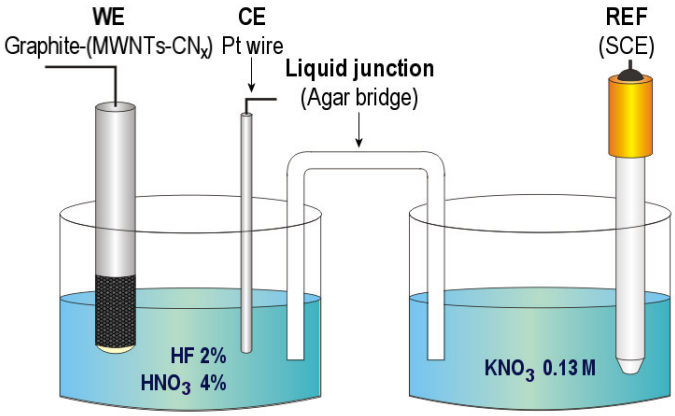

Figure 4.4: Cell used for electrochemical studies. Diagram of the experimental setup as an electrochemical cell for the cyclic voltammetric and potentiometric studies performed on the MWNTs-CN_x.

fig. 4.4.

For experiments with $TiCl_4$, solutions of concentrations $\leq$ 20 v % in ethanol, a Pt wire as counter electrode and HNO_3, KNO_3 as supporting electrolytes[2] were used. Water was also added to improve the solubility of the salts in some of the analyzed systems. This arrangement was joined to the SCE used as reference in the same way previously described.

A typical run of cyclic voltammetry was performed in a computer-controlled Pine AFCBP1 Bipotentiostat (located at the Corrosion and Electrochemistry Laboratory (LEC) in the University of Guadalajara, Mexico). The swept ratio was 50 mV/s in clockwise direction within -2 V and 2 V (vs SCE) range. Four-point average measurements were performed with the computer when recording the response signal. These measurements were monitored under continuous magnetic stirring of the dispersion in the reaction cell.

After several cycles of voltammetric response were recorded, a subsequent 10 min potentiometry was done in the system, using potentials between -1 and -1.85 V. These potential were chosen after observing the cyclic voltammetry given by the electrochemical system, indicating a possible deposit of TiO_2 from the electrolyte to the MWNTs-CN_x surface when using those values.

[2] A *supporting electrolyte* is the electrolyte added to the solution to decrease its resistance to ionic current transport and it is expected that they do not alter the electrochemical reaction of interest.

Finally, these samples were characterized by SEM and EDX in a FEI SFEG-XL30 operating at 10 keV.

4.1.4 Results and Discussion

4.1.4.1 Graphite-MWNTs-CN_x electrodes performance tests

One of the first tests performed on the electrodes for establishing its feasibility as functional WE, was the production of $H_2(g)$ from the electrochemical decomposition of water. Once the potential was adjusted below the required value for the semireaction $2H_2O + 2e^- \rightleftharpoons H_2 + HO^-$, ($E^0 = -0.8277$ V vs NHE) a potentiometry was performed. During this process, $H_2(g)$ bubble generation was identified on the immersed surface of MWNTs-CN_x, proving the feasibility of their use as WE.

The initial experiments were carried out in an electrochemical cell composed by the MWNTs-CN_x as WE, a graphite rod as counter electrode (CE) and a saturated calomel electrode (SCE) as reference (REF). The electrolytic system was TiO_2 suspended in an aqueous solution acidified with H_2SO_4. Further cyclic voltammetries (where the WE potential is swept from values lower to higher or vice versa from the equilibrium potential of the system, $E^{0'}$) were performed using this graphite-MWNTs-CN_x. These results can be observed on fig. 4.5. No stirring was induced while the voltammetric studies were carried out.

The objective of these voltammetric studies was to further test the use of MWNTs-CN_x as working electrodes. The voltammogram shown in figure 4.5*a* displays zones belonging to oxidation and reduction processes of the species in solution. The zones were numbered from I to VI, according to their order of appearance during the clockwise potential swept used. The presence of these zones indicates an efficient behavior of the MWNTs-CN_x-WE. However, these peaks are not well defined and the large background exhibited by the voltammogram is a signal of the electrode exhibiting large capacitance. This is undesirable for electroanalysis purposes, but might be advantageous for electrochemical double-layer capacitors,

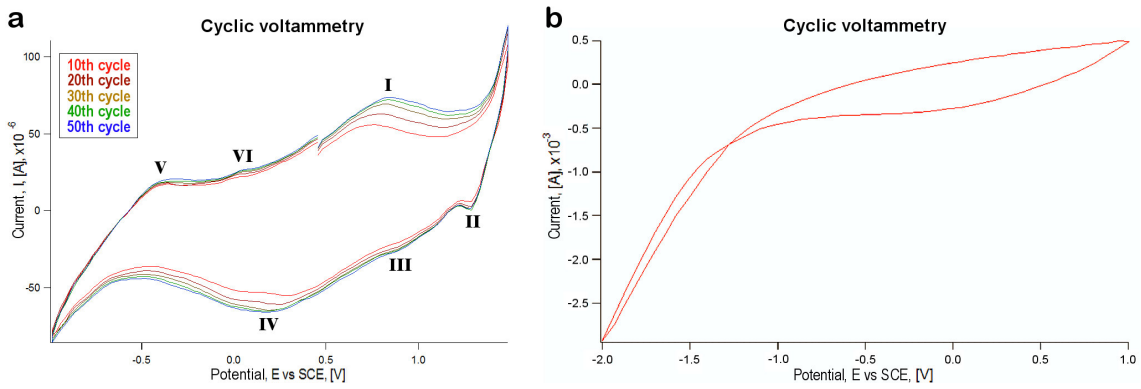

Figure 4.5: First Cyclic voltammetries for evaluating graphite-MWNTs-CN$_x$ WE performance. *Parameters for both voltammograms:* sweep potential rate, $v = 50$ mV/s, clockwise. Every plotted data is the average of 4 measurements. No stirring was used, $\omega_{WE} = 0$ rpm. *Electrochemical cell:* WE: Graphite-MWNTs-CN$_x$; CE: Graphite rod; REF: SCE. Electrolyte: TiO_2/H_2SO_4 (aq). **a)** Voltammogram of the 50 cycles performed in the system; only the cycles multiples of 10 were plotted for clarity. **b)** Voltammogram of the system, 3rd cycle. A crossover between the anodic and cathodic currents is observed.

which are devices that can be used for storing and releasing energy. [15]

It is important to note in fig. 4.5*a* that the current intensity of the peaks marked as I (ca. +0.8 V *vs* SCE) and IV (ca. +0.2 V vs SCE) enhances as the number of voltammetric cycles increases. This behavior is characteristic of the adsorption of chemical species on the electrode surface. With every cycle, the oxidized species do not have enough time to diffuse far away from the electrode. Because of that, a continuous accumulation of these species is observed in the voltammograms at the peaks I and IV, causing the saturation of the electrode. This process continues until a stationary state is achieved at around the 30th or 40th cycle. The fast increment in the current response at potentials higher than +1.0 V is related to the oxygen production from the water oxidation reaction ($2H_2O \rightleftharpoons O_2 + 4H^+ + 4e^-$). The cathodic peak II is characteristic of the reduction of some of the oxygen previously generated in the anodic cycle. The other peaks are most probably related to $SO_4^=$ reduction to $SO_3^=$ (peak VI), and other electrochemical reactions of the species in solution.

On the other hand, in the voltammogram shown in fig. 4.5*b* a crossover between the paths of the cathodic and anodic currents can be observed. This crossing,

is associated with an increase of the electroactive available surface, which is characteristic of a deposition process. [24] Even though this peak can be due to the Ti electrocrystallization on MWNTs-CN_x, it is not possible to discard the generation of hydrogen. Formation of H_2(g) from the reduction of the H^+ in solution, is also a nucleation and growing process or electrocrystallization, since it consists in a nucleus formation from an adsorbed intermediate (H_{ads}) followed by the formation of molecular hydrogen (H_2).

The graphite-MWNTs-CN_x electrodes built behaved satisfactorily in these initial performance tests for our purposes. Therefore, we decided to explore in more detail the possibilities of electrodepositing Ti using different electrolytes.

4.1.4.2 TiO_2 used as precursor for deposition of Ti nanoparticles

The voltammogram recorded for MWNTs-CN_x-WE in the TiO_2 suspension is shown in fig. 4.6. The crossover path between the current, observed below -0.81 V *vs* SCE (-0.86 V in the first cycle) in the voltammogram, indicates an increase in the electroactive area. This suggests electro-crystallization on the WE electrode surface. Because of the high negative value for the reduction of Ti, ($Ti^{+2} + 2e^- \rightleftharpoons Ti$ in standard conditions, -1.630 V *vs* NHE=-1.388 V *vs* SCE), the region in the voltammogram corresponding to an electrocrystallization can also be associated to the reduction of H^+ to H_2 (-0.2412 V). However, further characterization was required to identify this species.

Figure 4.6 shows how the number of cycles performed on the electrode increases the cathodic and anodic currents which become more negative or positive, at potentials lower than -0.8 V and higher +1.2 V respectively. The exhibited current is related to the evolution of hydrogen (using negative overpotentials) and oxygen (at positive overpotentials). This enhancement in the current could be related to several reasons. One explanation is that, in the initial voltammetric cycles, such as those shown in fig. 4.6, possible pollutants on the electrode surface are oxidized or reduced; process known as *electrode activation*. Therefore, it can be understood

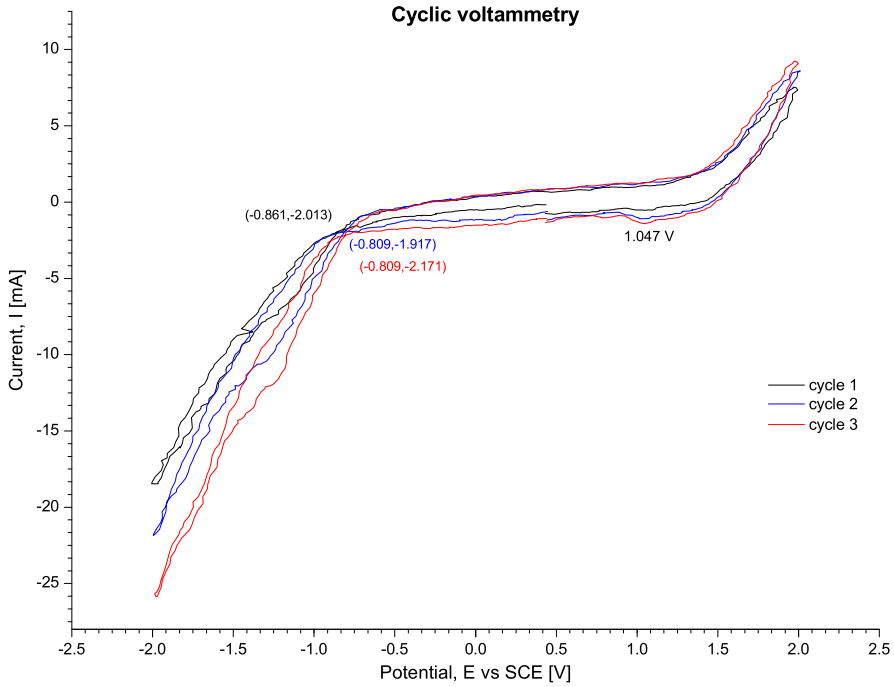

Figure 4.6: Cyclic voltammetry performed in the graphite–MWNTs-CN_x electrodes within the TiO_2 system. A dispersion of TiO_2 in an aqueous solution of HF (2 v %), HNO_3 (4 v %) was used as electrolite. SCE was placed in a 0.13 M KNO_3 solution jointed to the reaction system by an agar bridge 0.5 M in KNO_3.

as a cleaning process of the electrode surface that enhances its current response by increasing the available electroactive surface. Other possibility is the redissolution of adsorbed titanium on the WE surface in the electrolyte.

The reduction observed at around 1.05 V seems to be related to the reduction of O_2, previously generated when the potential was swept to positive potentials. This is possible since the sweep potential rate used was fast enough to avoid the diffusion of the electrogenerated O_2 far away of the electrode.

The electrode surface after one potentiometry step at -1.0 V (below to the intersection point of the currents remarked before) was observed with SEM. EDX measurements were preformed to evaluate if the indication of crystallization in fig. 4.6 corresponded to Ti.

Images of the MWNTs-CN_x-electrodes after the electrochemical treatment in

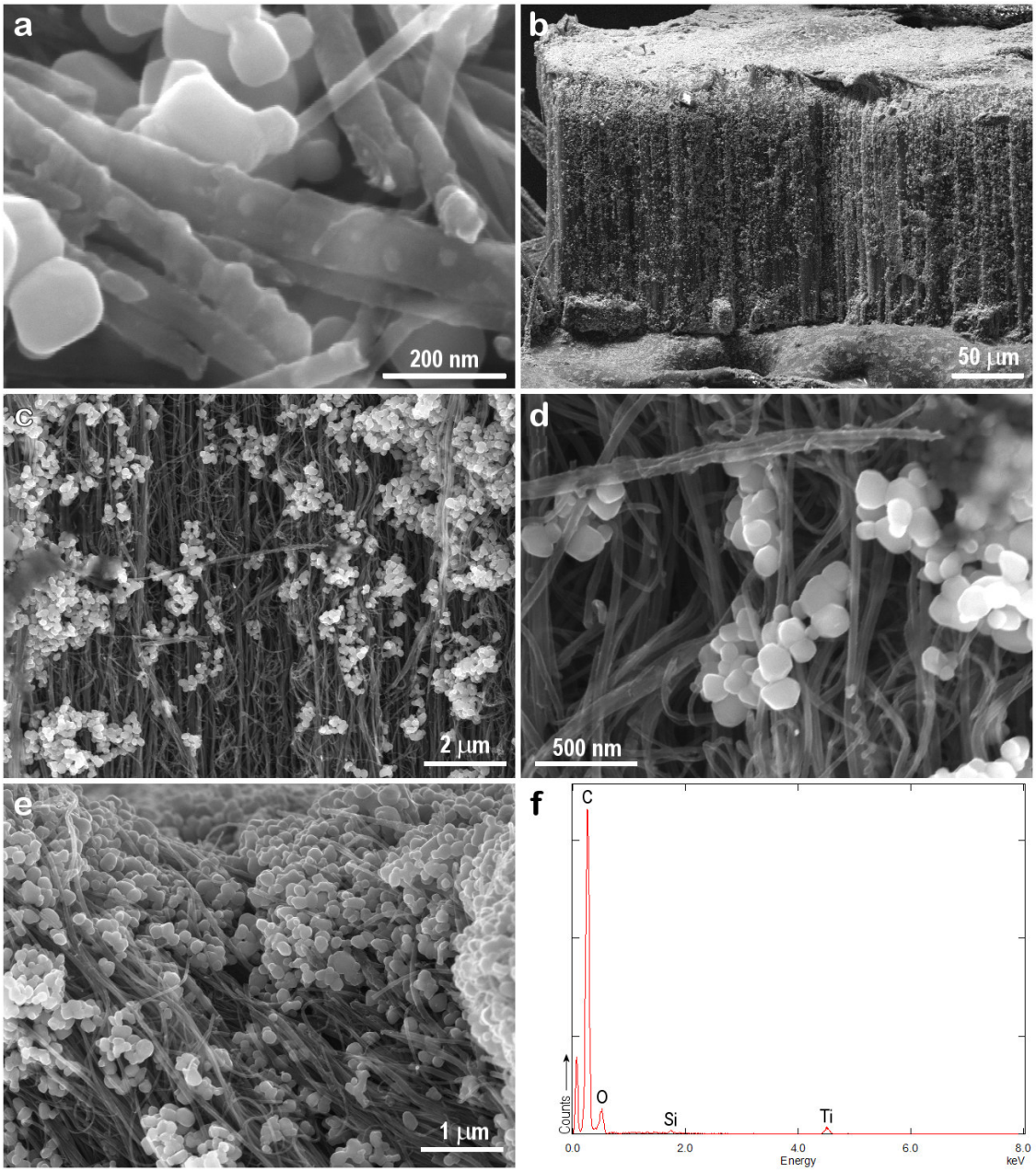

Figure 4.7: SEM images of the MWNTs-CN_x electrode after electrochemical treatment using TiO_2 as precursor for Ti deposition. Images taken after 10 min of potentiometry on the MWNTs-CN_x-WE at -1.0 V vs SCE. **a)** Close-up of rough MWNTs-CN_x showing round TiO_2 particles. **b)** A mat of MWNTs-CN_x covered externally by particles. **c)** Close-up of *b*. **d)** Close-up of *c*. **e)** Close-up to the end part of the MWNTs-CN_x , that is the top surface of the carpet shown in *a*. **f)** EDX of *d*. Atomic measurements: 89.87% C, 7.01% O, 2.84% Ti and 0.27% Si.

TiO_2 is shown in fig. 4.7. Fig. 4.7*a* shows some rough MWNTs-CN_x and round particles. The rugosity indicates a deposit on the surface of MWNTs-CN_xbut images

show that this was not homogeneous in all the sample. The round particles are composed of TiO_2 according to EDX analyses. Fig. 4.7*b* shows a carbon nanotube mat stuck on the carbon tape (inferior part of the image). It can be easily observed how the carpet, as a whole, supported the deposition of bright particles identified as TiO_2. Furthermore, these particles were also deposited on the surface of the carbon tape used for building the composite electrode.

At higher magnifications, it was possible to observe that the TiO_2 particles were deposited on the external part of the array (see fig. 4.7*c*), which is the part exposed to the reaction solution. As observed in fig. 4.7*d*, the particles are only deposited on the surface. Most of the MWNTs-CN_x seem clean while some TiO_2 particles are agglomerated. Smooth MWNTs-CN_x surfaces could also be seen within the sample, indicating a non-homogeneous coating of Ti on the surface of MWNTs-CN_x with this reaction system. EDX analysis of this image (fig. 4.7*f*) indicates the presence of Ti (2.84 at %) and O (7.01 at %) to state with high certainity that these particles are formed by TiO_2. The top surface of the MWNTs-CN_x mat, that is the roof of the carpet consisting of tubes caps, shows a higher density of TiO_2 particles. These results show that Ti tends to be deposited on the most available surface. Even though, the solution of reaction was under continuous stirring in order to increase the mass transfer with the electrode, the most inner MWNTs-CN_x did not have enough contact with the species in solution. Therefore, the tubes embedded inside the mat remain uncovered and the outer ones do not exhibit an homogeneous coating.

SEM imaging at the base of the MWNTs-CN_x mat (that is in the base of the nanotubes array observed in fig. 4.7*b*) showed similar results regarding TiO_2 particles deposition, but showed changes in the MWNTs-CN_x morphology at the contact point between the MWNTs-CN_x and the carbon tape (see fig. 4.8*a*).

This contact point is the closest to the cylindrical surface of the graphite rod which connects the MWNTs-CN_x to the variable potential source. Figure 4.8*b* shows the general morphology of the nanotubes located at that zone. They appear different

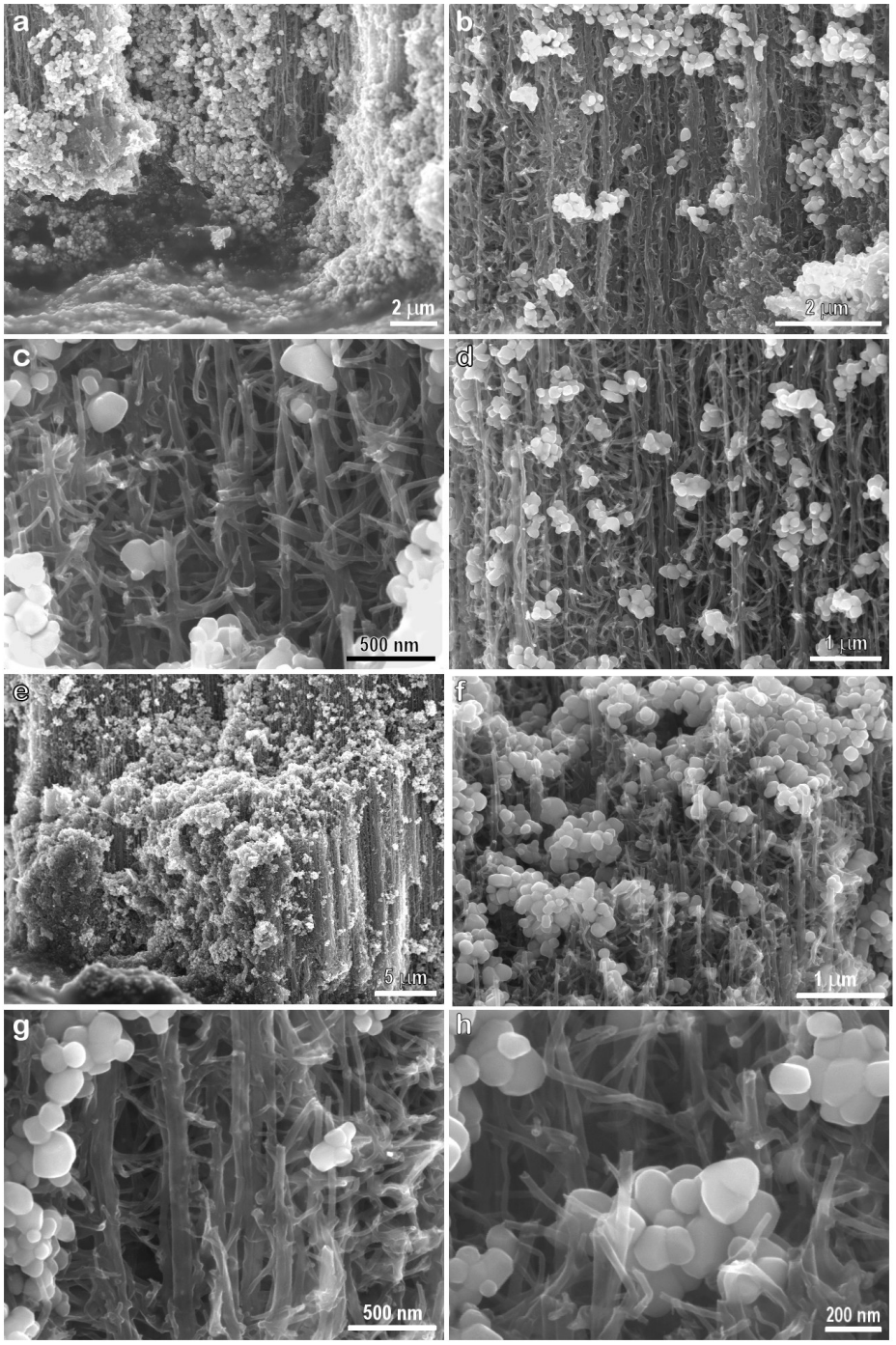

Figure 4.8: SEM images of MWNTs-CN_x on the electrode after electrochemical treatment on the zone close to the graphite rod using TiO_2 as precursor. a) Low magnification approach to the interface carbon tape-MWNTs-CN_x. **b)** A not aligned morphology of the MWNTs-CN_x was displayed. **c)** Close-up showing a branching-like morphology in the MWNTs-CN_x. **d)** Close-down of *d*. **e)** A small array of MWNTs-CN_x broken in their base part is shown in first plane. **f)** Close-up to the roof of the broken array in *f*. **g)** Branched structures found in the frontal view of the tubes in *g*. **h)** Branched structures found in the rupture point at of the tubes in array *g*.

from their straight well-aligned nature before the electrochemical treatment.

A close-up of the morphology exhibited by these MWNTs-CN_x (fig. 4.8*c*) shows a branch-like structure in the tubes. It is noteworthy that this branching disappears as we move away from the graphite rod surface (*i.e.* carbon tape). The pattern formed by the portion of the tubes showing a modified structure is displayed in fig. 4.8*d*, it appears that an interconnection network is being formed between the MWNTs-CN_x.

A carpet of MWNTs-CN_x, which broke at the point of the branching, allowed a better analysis of this morphology (fig. 4.8*e*). A close-up of their surface can be seen in fig. 4.8*f*, showing some of the broken branched MWNTs-CN_x besides the TiO_2 particles deposit. High magnifications of this zone (fig. 4.8*g*) allowed us to observe the branched structures in more detail, and to clearly see the top view of the branched carpet (fig. 4.8*h*). It can be seen that the branches are formed from the MWNTs-CN_x backbone and they exhibit a diameter a slightly lower than that of the original MWNTs-CN_x.

This phenomena could be due to the current density in the electrode. This density is higher at the base of the MWNTs-CN_x array because that part is the closest to the graphite rod surface. In cylindrical geometry, as we move along the radius of the electrode, we find lower current density because the surface area that the current crosses is higher.

4.1.4.3 $TiCl_4$ used as precursor for deposition of Ti nanoparticles

The analysis performed from the potentiometric process in graphite-MWNTs-CN_x electrodes at the $TiCl_4$/ethanol system, threw more encouraging results regarding Ti deposition. The results of the initial cyclic voltammetry studies performed on the MWNTs-CN_x electrodes are shown in fig. 4.9. A crossed path between the lines of current was not observed here.

In this voltammogram, we also see peaks around +0.8 V and +0.2 V previously observed in fig. 4.5*a* which are related to an accumulation of one specie on the

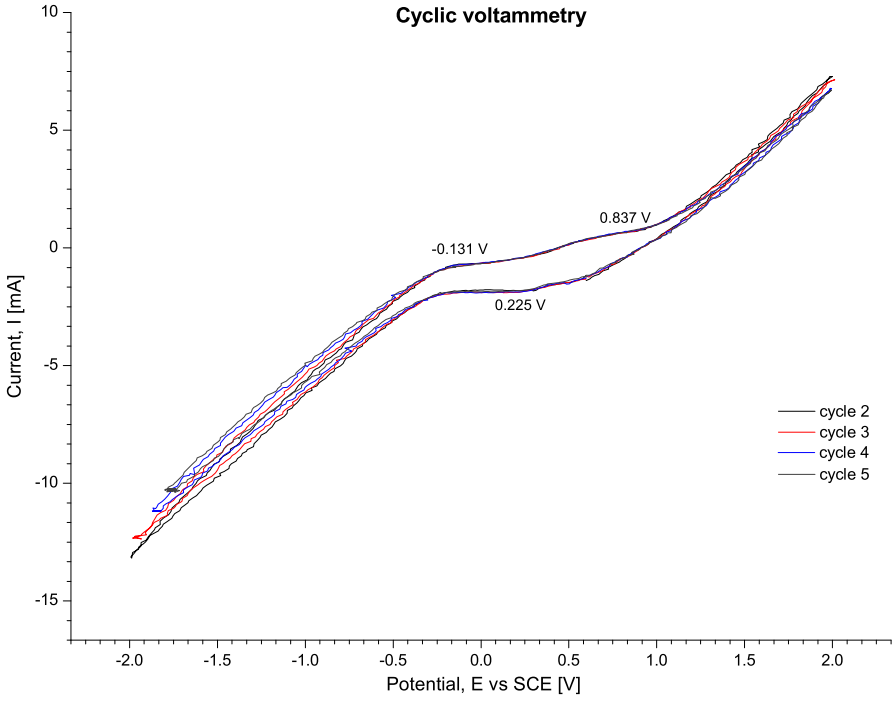

Figure 4.9: Cyclic voltammetry performed in the graphite–MWNTs-CN_x electrodes within the $TiCl_4$/ethanol system. A solution of $TiCl_4$ in ethanol with KNO_3 as support electrolyte was used. SCE was placed in a 0.13 M KNO_3 solution jointed to the reaction system by an agar bridge 0.5 M in KNO_3.

electrode's surface. At low and high potentials, it is observed the decomposition of the solvent with the corresponding enhancement in the current response when the number of cycles increases. This is in agreement with the previously observed voltammograms (see figs. 4.5 and 4.6).

After, a potentiometry treatment at -1.85 V for 10 min was performed on the electrode to promote the deposition of Ti on the surface of the MWNTs-CN_x. This value was selected because it is lower than the value required for the titanium reduction semireaction (-1.388 V).

SEM images performed on the sample after its potentiostatic treatment are shown in fig. 4.10. The general appearance of the electrode is different from those treated with TiO_2 in acidic medium.

From fig. 4.10*a* it can be seen that the structure of MWNTs-CN_x resembles

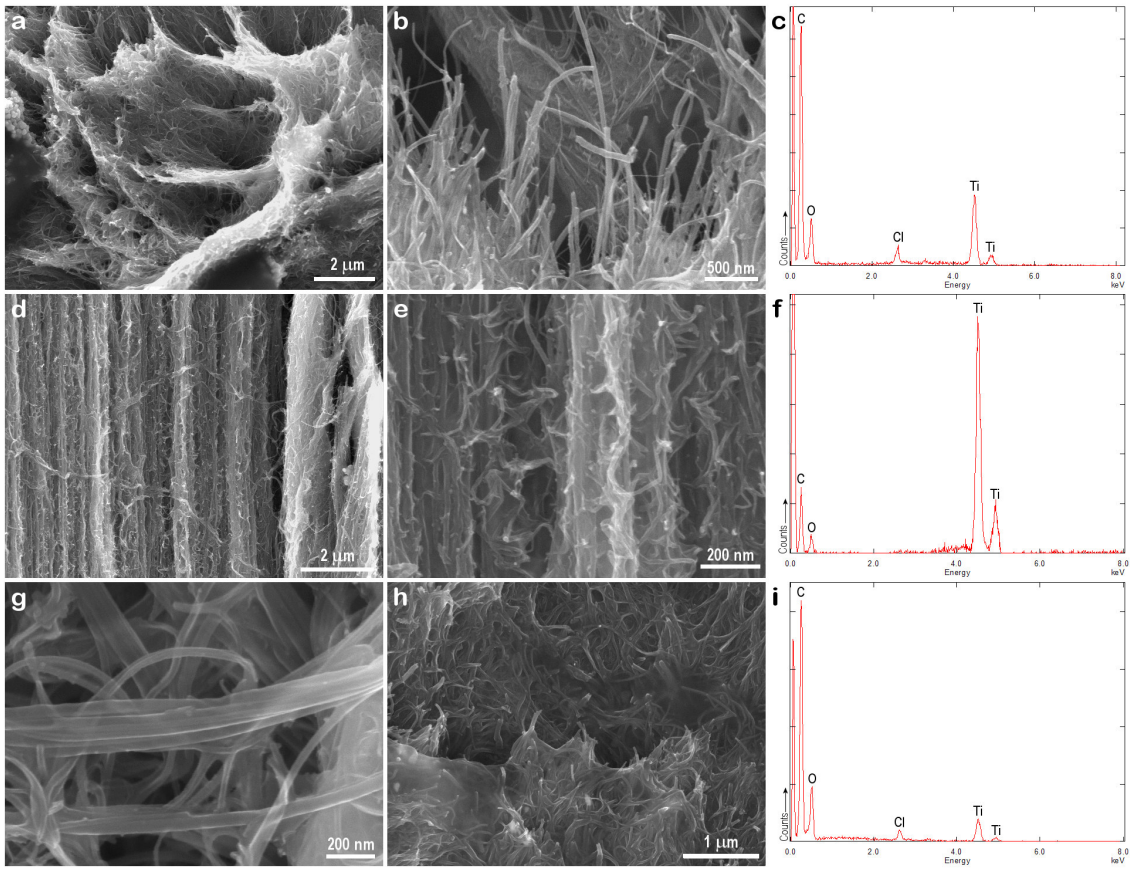

Figure 4.10: SEM images of MWNTs-CN_x on the graphite electrode after its electrochemical treatment with $TiCl_4$, ethanol system. **a)** Low magnification image of MWNTs-CN_x-electrode surface. **b)** Close-up of the tubes forming the WE. **c)** EDX of *b*: 66.96% C, 19.71% Ti, 11.62% O and 1.71% Cl. **d)** Wet-like fistful of MWNTs-CN_x on the electrode. **e)** Close-up of *d*. **f)** EDX of *e*: 74.59% Ti, 18.36% C and 7.06% O. **g)** General morphology observed on the MWNTs-CN_x on the sample. **h)** MWNTs-CN_x embedded in a wet-like way. **i)** EDX of *h*: 75.34% C, 14.68% O, 8.65% Ti and 1.33% Cl. All percentages reported are atomic ones.

a wet bundle pressed together. Neither rugosity nor rounded particles at higher magnifications (fig. 4.10*b*) were observed. Nevertheless, the EDX of this image (shown in fig. 4.10*c*), clearly exhibits a signal of Ti, with 19.71 at % (Ti) which is higher than the amount of chlorine (1.71 at %) and oxygen (11.62 at %). This is important because the molar ratio Cl/Ti is about 46 times lower than the expected if this wetting were due to $TiCl_4$. Also the O/Ti ratio is below the expected for the inert TiO_2.

Fig. 4.10*d* shows a section of aligned wavy MWNTs-CN_x exhibiting also a "wet" appearance. A close-up of the central part of this zone is shown fig. 4.10*e*. It reveals

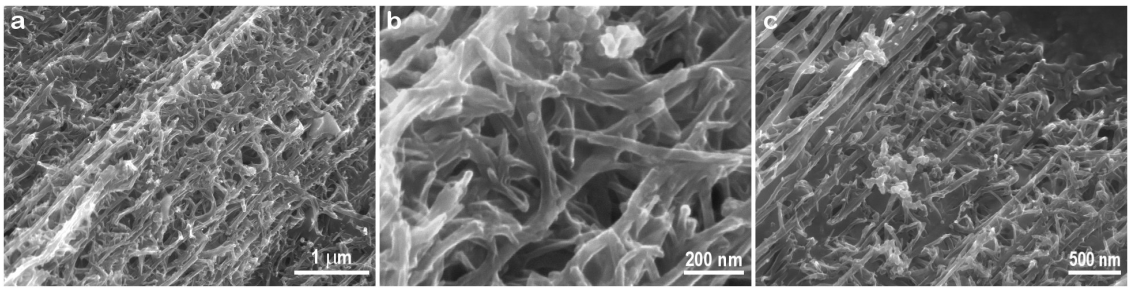

Figure 4.11: SEM images of MWNTs-CN_x on the electrode after the electrochemical treatment on the zone close to the graphite rod in a $TiCl_4$, ethanol system.

a wavy arrangement of the tubes, which is different from the nanotube morphologies resulting from any prior treatment. As in the previous EDS analysis, this sample presents a very high percentage of Ti (about 74.59 at %) (fig. 4.10*f*). Even if the percentage could be overestimated in this last analysis, it is important to note that the presence of Ti is noticeably higher than in the sample processed with TiO_2.

A further observation of MWNTs-CN_x on the electrode is shown in fig. 4.10*g*. This zone exhibits also a smooth surface. MWNTs-CN_x from the inner part of the electrode are displayed in fig. 4.10*h*. Its corresponding EDX spectrum (fig. 4.10*i*) indicates that this zone of the sample contains 73.34 at %C, 14.68 at %O, 8.65 at %Ti and 1.33 at %Cl.

The high percentage of Ti detected on the unembedded surface of MWNTs-CN_x, without a particle coating, suggests a continuous Ti deposit on the surface of the nanotubes. This supposition is supported by the theoretical findings of Zhang *et al.* [25] indicating that titanium atoms deposited on the surface of SWCNTs can form continuous wires, whereas other metals such as gold, palladium, iron, aluminum, and lead can only form incontinuous and amorphous wires outside the tube wall. This behavior results because deposition of Ti is energetically much more favored over Au and Al to form a continuous chain on the SWCNTs.

The bottom part of the MWNTs-CN_x array was also analyzed by SEM in order to look for branched structures in this system. Representative images are shown in fig. 4.11. They exhibit similar branching to that shown in fig. 4.8. This indicates that

branched morphologies could be caused by radial variations in the current density during the electrochemical treatment.

4.1.4.4 Si deposition on MWNTs-CN_x

During an experiment working with TiO_2 in an aqueous HF/HNO_3 solution, a SiO_2 contamination occurred in the sample due to glass accidentally dissolved by the HF. This soluble form is the $SiF_6^{=}$ anion. The observations carried out on the MWNTs-CN_x after their electrochemical treatment in the presence of Si in solution, showed important findings worth discussing, even that this element was not aimed to be studied in the preset work.

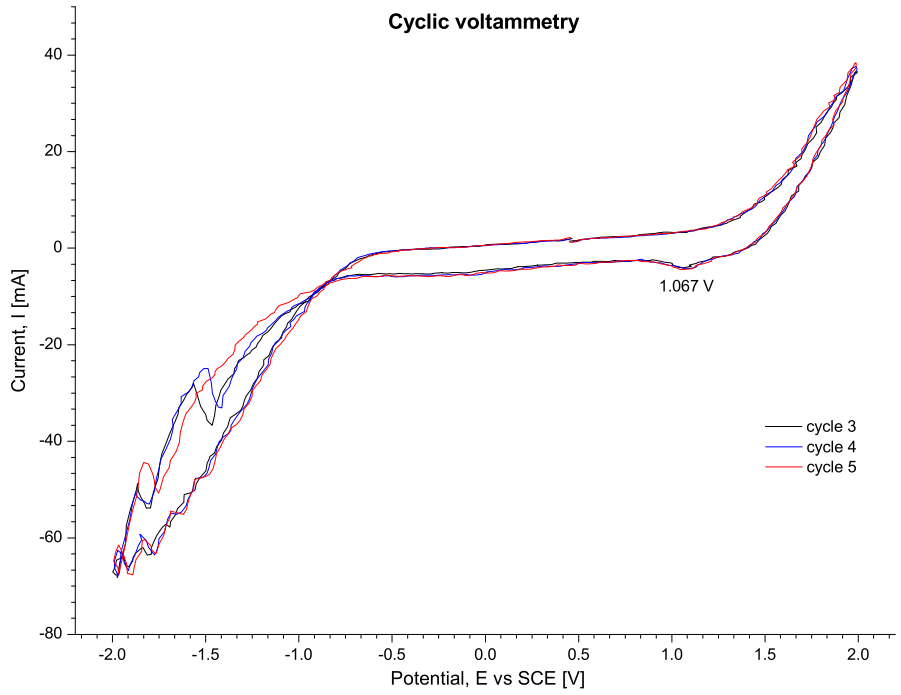

Figure 4.12: Cyclic voltammetry performed in the graphite–MWNTs-CN_x electrodes within the TiO_2 system contaminated with Si.

Fig. 4.12 shows the cyclic voltammetry performed on the reaction system containing dissolved Si. Even that the current lines get close around -0.82 V, in this case they do not cross. The reduction of $SiF_6^{=} + 4e^- \rightleftharpoons Si + 6F^-$ occurs at -0.999 V

at standard conditions. This behavior, then suggested a possible electrochemical deposition of Si on the tubes.

The humps observed in the current below -1.5 V, could be due to the generation of H_2, forming bubbles on the surface of the electrode, which changed drastically the current response. The anodic signal found at ca. +1.1 V seems to correspond to the known reduction of dissolved electrogenerated oxygen observed in previous voltammograms.

From the voltammograms, it can be deduced that the incorporation of Ti on the MWNTs-CN_x is not only a simple redox reaction in solution but an adsorption process as well. These voltammograms do not exhibit the shape of a typical redox system in solution; instead, the capacitance is high, the peaks are too wide and not well defined. In addition, the two possible couple of redox peaks are separated by a ΔE_p higher than the value of reversibility (59 mV/n, where n is the number of chemical equivalent transfered in the redox reaction).

When the species are adsorbed on the WE, the potentials at which the voltammetric peaks appear do not correspond to the values reported in tables of semireaction potentials, because these values are for species in solution interacting with an inert electrode. The difference between the hydrogen and oxygen evolution potentials observed in the graphite-MWNTs-CN_x electrode when compared with those involving noble metals, indicate that both reactions involve adsorption phenomena. In these non-reversible processes, the adsorption forces can be high enough to displace the thermodynamical equilibrium towards a monolayer assembly of the adsorbate. This process continues until the activity of the deposited metal equals the unitary value, and is called *underpotential deposition*.

After undergoing the cyclic voltammetry, this electrode, as the others, was subjected to a potential of -1.2 V for 10 min, to deposit Ti. However, since this potential is below the needed for $SiF_6^{=}$ reduction, Si was also reduced on the surface of the MWNTs-CN_x. After its potentiostatic treatment, the electrode exhibited a blue coloration, not seen for the electrodes treated in a Si free medium.

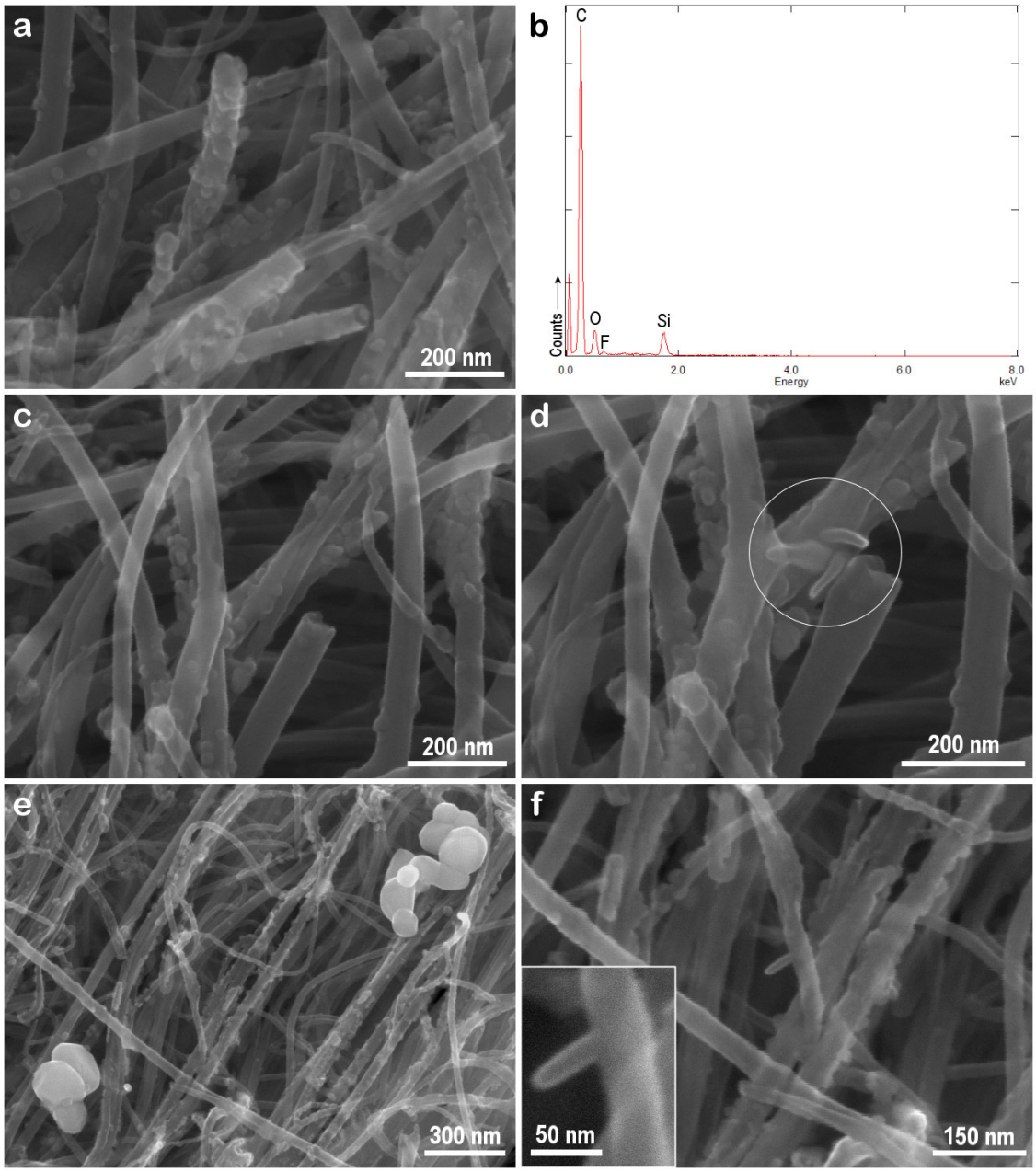

Figure 4.13: SEM images of the MWNTs-CN_x electrodes treated in the TiO_2 system contaminated with Si. a) MWNTs-CN_x exhibiting small particles deposited on their surface. **b)** EDX of *a*: 90.23 at % C, 5.88 at % O, 2.79 at % Si, 0.74 at % F, 0.23 at % K and 0.13 at % Ti. **c)** MWNTs-CN_x coated by Si particles before an EDX spot analysis. **d)** The MWNTs-CN_x in *c* after the electron beam incidence on Si particle: *Circled:* new carbonaceous structure growth. **e)** MWNTs-CN_x coated by Si particles before an EDX spot analysis. **f)** Close-up of the center zone of *e* after the electron beam incidence for 100 s on a Si particle. *Inset:* New carbonaceous structure growth from the Si deposited particle on MWNTs-CN_x.

The SEM analysis of this electrode after electro-deposition is shown in fig. 4.13. Fig. 4.13*a* shows particles smaller than those previously shown for TiO_2 which tend to be more dispersed on the surface of MWNTs-CN_x. An EDX analysis (fig. 4.13*b*) indicates that these particles are made of Si. Quantification in this zone was 2.79 at % Si and 0.13 at %Ti. However, in other zones of the sample, amounts as high as 8.3 at % of Si were detected.

Fig. 4.13*c* shows Si particles deposited on the MWNTs-CN_x surface. After this image was taken, a close-up was performed on several of the Si particles in one of the tubes near the center. The electron beam of the microscope was focused for 100 s on the particles to record an EDX spectrum of deposited Si, and afterwards image 4.13*d* was obtained. This resulted in the growth of new rod-like nanocarbon structures from the Si particle (marked with a circle).

We believe that these rod-like structures grew because of the heating propitiated by the electron beam focused on the Si particle. The source of carbon could be the sample itself or any hydrocarbon vapor remaining in the SEM chamber. This effect was never observed with the other transition metals observed on MWNTs-CN_x.

Figure 4.13*e* shows another section of the sample where large TiO_2 particles lay on some tubes (upper right and lower left corner). Small Si particles can be also seen dispersed over the nanotubes surface. It is noteworthy the location and affinity for the nanotubes surface exhibited by both type of particles.

When the electron beam was directed to a Si particle at 10 keV, the growth of a carbon nanostructure was observed in real time. This new carbon nanostructure can be seen in 4.13*f*. A higher magnification of this growth is shown in the inset.

Although, the growth of carbonaceous structures by the electron beam is not new and has been reported previously, to our knowledge a siliceous nanoparticle has not been shown to be a catalyst for this process. Further characterization of these new carbonaceous structures by STEM and HRTEM is required to identify if they are carbon nanotubes or amorphous carbon rods. The possibility of depositing Si electrochemically on MWNTs-CN_x has not been explored completely, but this work

strongly suggest that it will give good results. The deposit of this semiconductor on the surface of the MWNTs-CN_x, besides opening the possibility of growing branches in the carbon nanotubes, would offer alternative applications.

4.1.5 Summary

Two electrochemical systems for Ti particle deposition were tested giving different results. The dispersion of titanium(IV) oxide in an acidic medium produced an apparent deposit of TiO_2 particles on the surface of the electrode. These nanoparticles cover the arrays of MWNTs-CN_x as it was a unique structure, but most of the surface of the individual MWNTs-CN_x appeared to be clean. These particles tended to agglomerate and are not well dispersed on the MWNTs-CN_x surface.

In the second electrolytic solution tested, titanium(IV) chloride in ethanol was used as the Ti source. After potentiometry, a "wet" morphology was observed on the MWNTs-CN_x electrodes. Neither a rugosity or particles where found on the MWNTs-CN_x surface that could indicate the presence of Ti. But Ti was detected by EDX, in higher amounts than in the prior approach. Percentages of about 20 at % were easily found in the sample. This suggests a continuous coverage of this metal over the surface of the MWNTs-CN_x. However, further analysis by STEM and HRTEM of the MWNTs-CN_x scraped from the surface electrode would be needed to corroborate this fact.

In the electrodes used in both electrochemical systems, a branching was found on the part where the MWNTs-CN_x are closer to the graphite rod (the base of the electrode). This branching is considered to be a consequence of the high current density exhibited in that zone of the electrode. This result opens the possibility of further studies on electrochemical modifications on the morphology of the MWNTs-CN_x to build hierarchical networks.

Finally, a deposit of Si particles on the surface of MWNTs-CN_x resulted from an accidental presence of Si dissolved in the electrolyte. These particles appear to have more affinity for anchoring on the MWNTs-CN_x surface when compared to

TiO_2. Also, a better dispersion of Si particles on the MWNTs-CN_x was obtained, when compared with titanium(IV) oxide. During their characterization by scanning electron microscopy, it was found that these particles can promote the growth of new carbon structures when the electron beam was focused directly to them.

In the following section, we will describe the results obtained when Ti was added during the synthesis of carbon nanotubes.

4.2 Incorporation of Ti precursor from the MWNTs-CN_x synthesis

The basic idea of this procedure was to include a Ti precursor in the reagent mixture used to synthesize carbon nanotubes. This mixture, generally is composed of benzylamine or toluene (for MWNTs-CN_x or MWCNTs according with the case) and ferrocene ($FeCp_2$) as catalyst.

$TiCl_4$ was selected for its low price and its solubility with toluene. However, titanium(IV) chloride reacts with amines, chemically active metals and water among others. During various tests performed, it was observed that $TiCl_4$ readily reacts with the catalyst, $Fe(C_{10}H_{10})$, and forms a dark brown precipitate. Besides, $TiCl_4$ also reacted with benzylamine, the precursor used for producing MWNTs-CN_x, producing an orange precipitate. This does not allow to make a reagent mixture containing Ti for the CVD production of carbon nanotubes. Some modifications in the CVD procedure, were necessary to overcome these limitations. They are described in the following section.

4.2.1 Experimental

The experimental CVD setup used was the differential pressure system, shown in fig. 4.14 due to the low quantity of solution needed for the test experiments (around

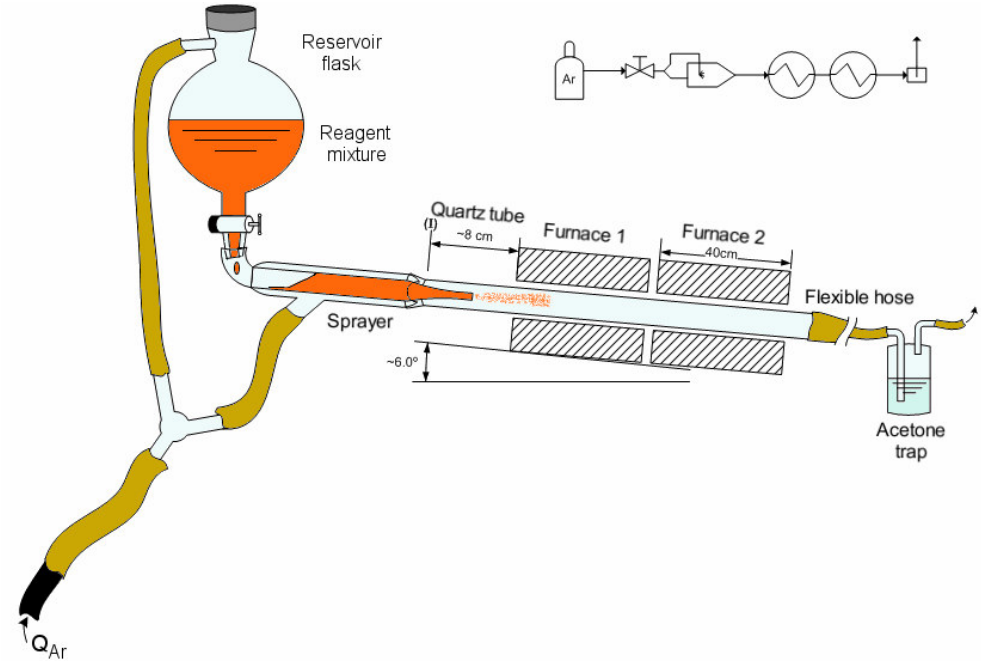

Figure 4.14: Experimental setup for Ti incorporation during CNTs growth by CVD. The process consisted in a consecutive spray of three different reagents mixtures at 825°C and 2.5 L Ar/min flow: *1)* A 7.5 wt % of $FeCp_2$ in benzylamine solution; *2)* Pristine tolune for pipeline cleaning; *3)* Solution of $TiCl_4$ in toluene (15.4 v %).

10-15 mL in total).

A three step CVD process was used to avoid contact between the $TiCl_4$ solution and the ferrocene or the benzylamine.

This procedure is described as follows:

1. 5 mL of a solution of ferrocene, $Fe(\eta^5 - C_5H_5)_2$ (Aldrich 98%), 7.5 wt % in benzylamine, $C_6H_6CH_2NH_2$ (Aldrich 99%) were prepared. The dispersion of ferrocene in the continous phase was aided by sonication. This solution was labeled as *1-CNx*.

2. A second solution (ca. 5 mL) of titanium tetrachloride, $TiCl_4$ (Fluka 98%), 15.4 v % in toluene, C_7H_8 (Fermont 99.9%) was also prepared. This volume percentage corresponds to an atomic ratio of 2.5% between Ti and the C provided by the toluene. This solution was labeled as *2-C,Ti*.

3. The experimental system was mounted as shown in fig. 4.14, the flow of Ar

adjusted to 2.5 L/min and the temperature was set to 825°C. The solution *1-CNx* was poured in the reservoir flask.

4. Once the desired temperature was reached, the reservoir valve was opened to begin the spraying process. Is in this step when MWNTs-CN_x start to grow.

5. Before solution *1-CNx* was finished, a small quantity of pure toluene was added to the reservoir flask to remove most of the ferrocene and benzylamine residues from the pipelines, while the system was spraying.

6. Before the last of the toluene diluted solution *1-CNx* was sprayed, the solution *2-C,Ti* was added into the system in the same way that was done before with pure toluene. Some precipitate appeared in the sprayer line but not enough to block the tip of the sprayer. This ensured that some catalyst was been sprayed into the system at the same time as the $TiCl_4$ solution began to flow, which was desired to avoid the closing of the growing nanotubes caps.

7. Finally, the solution of *2-C,Ti* was sprayed until it almost finished for avoiding the entrance of oxygen into the CVD chamber. After that, the system was allowed to cool down to room temperature. Then the product was recovered by scraping.

These products were characterized by SEM and STEM in a Philips SFEG-XL30, operating at 10 keV and equipped with an EDAX detector; powder XRD performed in a Brucker D8, equipped with a Cu anode operated at 35 kV, 25 mA and 293 K from 10 to 110° in 2θ angle, and by TGA in a Thermo Haake, Cahn VersaTherm HS.

4.2.2 Results and Discussion

SEM imaging proved that carbon nanotubes had grown in our experiment, this is shown in fig. 4.15.

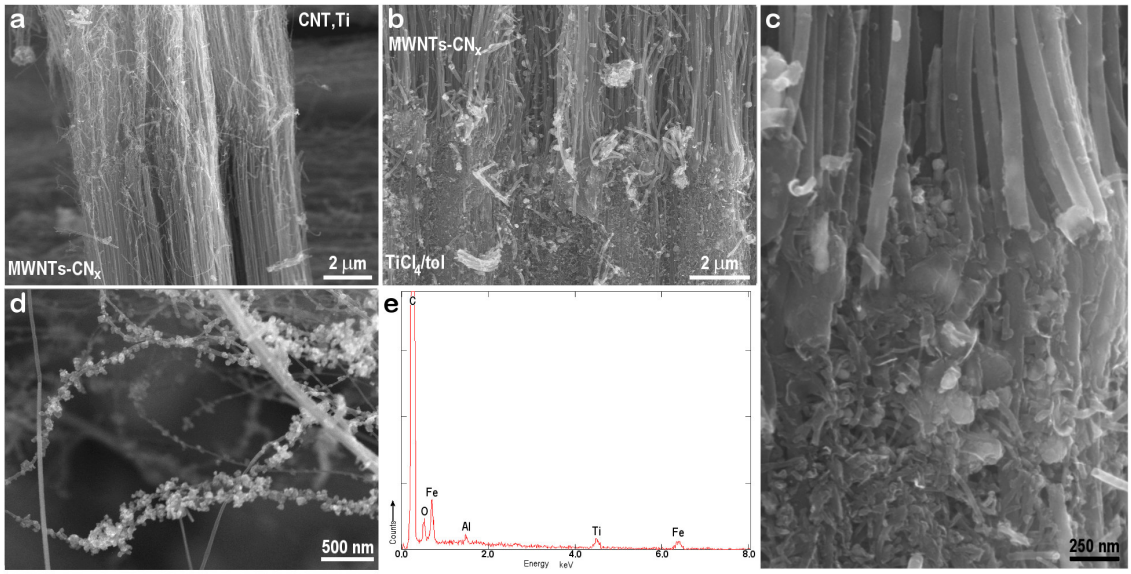

Figure 4.15: SEM images of MWCNTs/MWNTs-CN_x synthesized with a Ti precursor. a) Low magnification at the interface in the growing of a bundle of CNTs. **b)** Close up to one similar interface shown in *a*. **c)** Close up of *b*. **d)** Particles composed by Ti and O deposited on the surface of CNTs. **e)** EDX analysis of the particles shown in *d* and *e*. The atomic content corresponded to 94.53 % C, 2.88% Fe, 1.76% O and 0.82% Ti.

It is worth noting that the two growth stages are easily identified (figs. 4.15*a* to *c*). In the first step (see fig. 4.15*a*, lower part), MWNTs-CN_x grew in a well aligned array. Once the carbon source was changed to toluene with $TiCl_4$, the CNTs continued growing from the open ends of MWNTs-CN_x, but in a disordered fashion (see fig. 4.15*a*, upper part). This observation allows us to state that CNTs keep growing after the carbon source was changed and probably exhibit a part doped with nitrogen while the other section is not doped. Then, it seems that titanium incorporation induce disorder in the growing array, and at first glance, an apparently tapering effect is noted at the tips.

In some cases (figs. 4.15*b* and *c*) amorphous carbon (see low part of image) at the end of well aligned carbon nanotubes promote the formation of irregular structures such as narrow tubes. This could be happening because the ends of

MWNTs-CN_x could serve as active supports for further growth of carbon structures that eventually close.

Since ferrocene was not added to the solution of $TiCl_4$ with toluene, and it is known that Ti *per se* can not catalyze the growth of CNTs; then the transition step in the change of reactive solutions into the thermolysis system needs to be carefully controlled. Otherwise, the carbon nanotube ends can close and therefore they will not allow further carbon aggregation. Therefore, the steps 5 and 6 in the experimental procedure described in section 4.2.1 should be followed with special care. If it is allowed to conclude the $FeCp_2$/benzylamine solution spraying before the solution of the titanium and carbon precursors gets sprayed into the system, the yield of the product extremely decreases, and practically no carbon nanotubes are produced. This could be probably due to the occurrence of the nanotubes capping. In addition, when the reservoir is being filled with the reactive solution, it is possible that oxygen had been able to enter to the reservoir, and in consequence, it is necessary to avoid its entrance to the CVD chamber because it can degrade the nanotubes during synthesis.

Deposited particles were found on MWNTs-CN_x in a part of the sample (fig. 4.15*d*). These particles are dispersed over the whole surface of a few nanotubes but a high interaction between them can not be determined here. EDX analysis performed on the sample (fig. 4.15*e*) confirmed the presence of Ti (0.82 at %) and other signals corresponding to C (94.53 at %), O (1.76 at %), and Fe (2.88 at %) were detected. The morphology of the particles and the O/Ti molar ratio of 2.15 obtained make us conclude that they are composed by TiO_2.

More examples of the particle distribution are shown in fig. 4.16*a*; which also shows, at the center, an unusual termination of carbon nanotubes. A close-up of these endings can be seen in fig. 4.16*b*. It is clearly observed that the CNTs are tapering at one end. To the best of our knowledge, this termination has not been observed before in the CVD production of MWNTs-CN_x and MWCNTs.

Image 4.16*c* illustrate more of these sharp tips. At the center, a noticeable

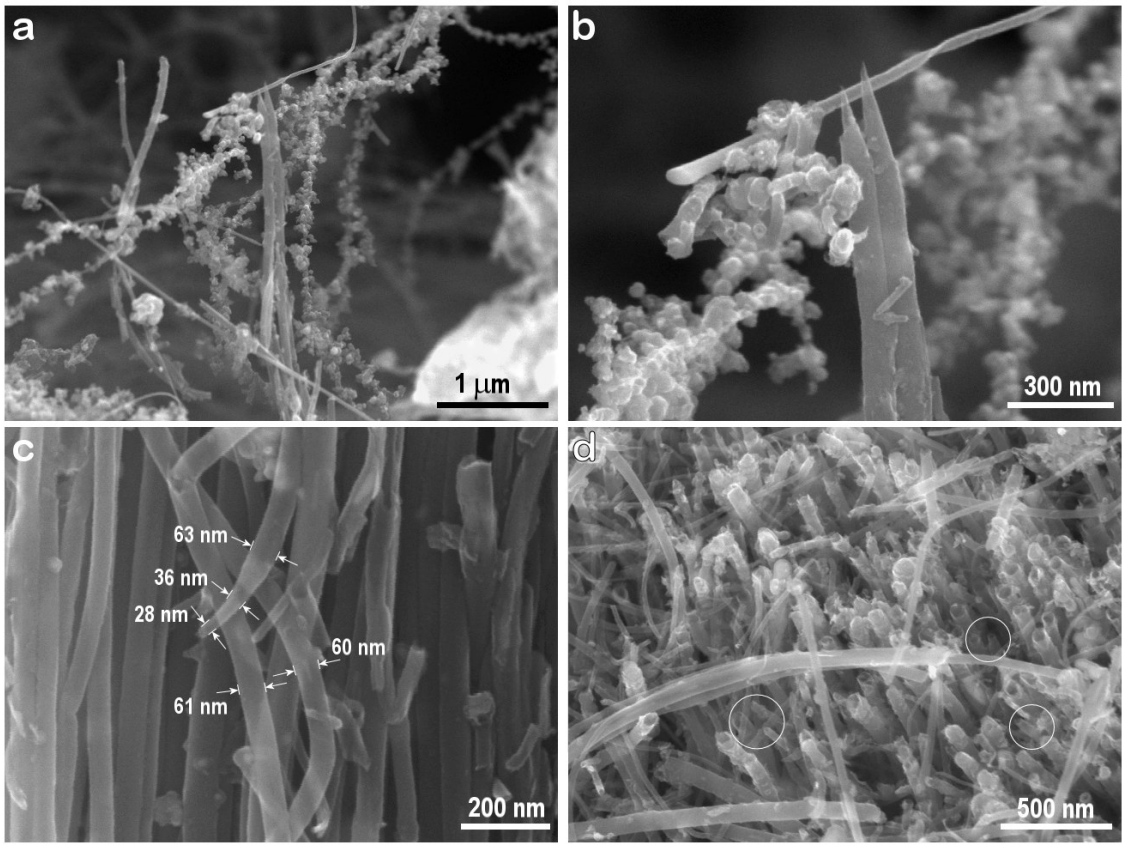

Figure 4.16: SEM images of MWCNTs/MWNTs-CN_x synthesized with a Ti precursor. a) Dispersion of the particles in some zones of the sample. **b)** Narrow-end observed in the CNTs obtained. **c)** Drastic narrowing observed in the end of CNTs. **d)** End open-tips of the CNTs obtained. *Circled:* some sharp tips observed.

decrease in diameter can be observed, going from ∼63 nm to ∼28 nm in ca. 190 nm. Other tubes exhibit a diameter within the same range (∼60 nm).

Open ends of CNTs are observed from an aerial perspective in fig. 4.16*d*. A sharpening at the ends also seen in some of these tubes. A few of them were enclosed in circles to facilitate their identification. An EDX performed on this zone (not shown here) indicates Ti presence (0.42 at %) besides C (96.32 at %), O (2.29 at %) and Fe (0.97 at %). It is noticeable that small clusters of TiO_2 cannot be observed on this region. Because of this, the presence of Ti is intriguing, even though is not discarded that the signal could come from particles hidden inside the CNTs mat.

These sharper tips within CNTs were further investigated by STEM imaging in

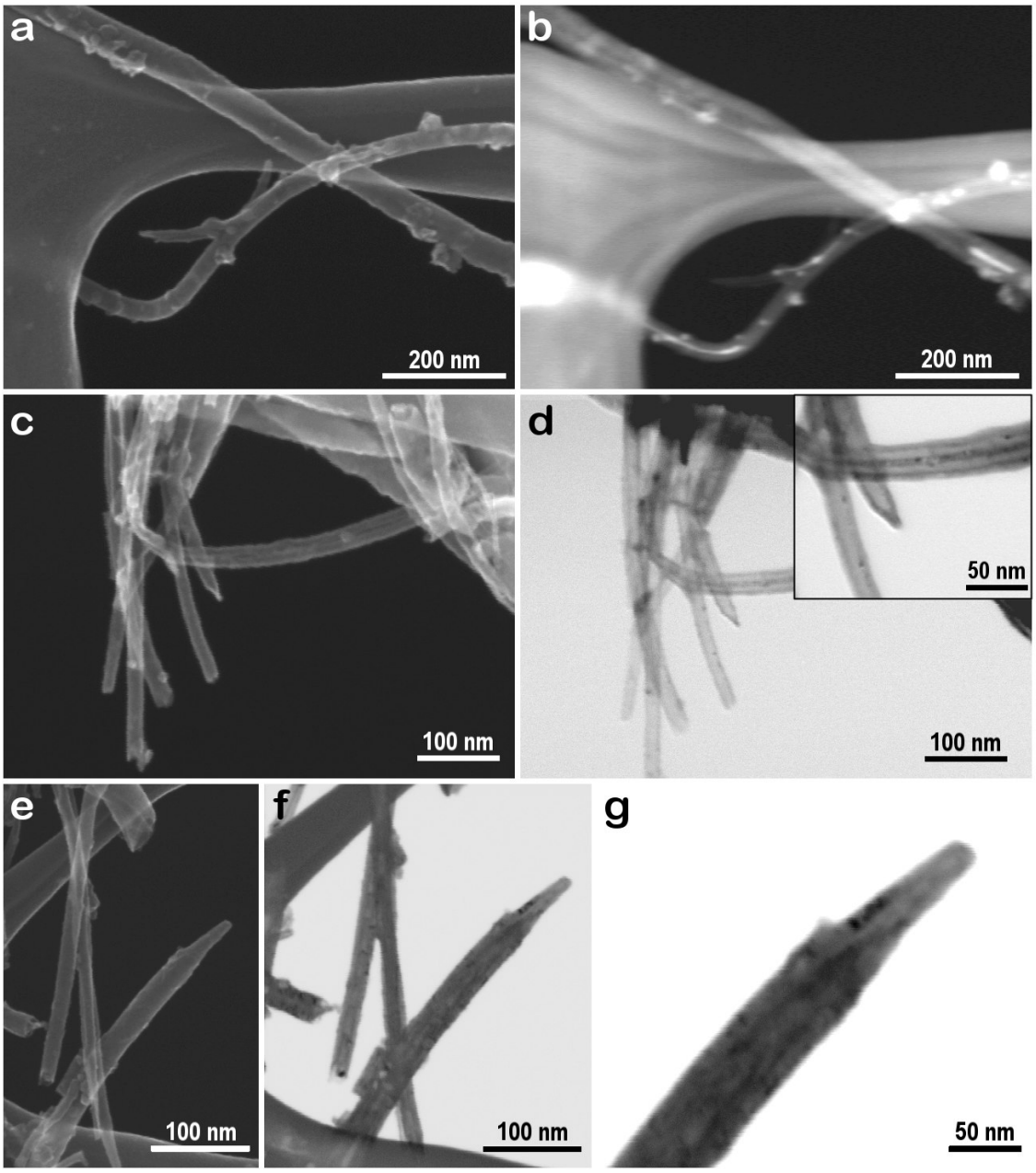

Figure 4.17: STEM images of the tips obtained in MWCNTs and MWNTs-CN_x. a) SEM image of the product obtained. **b)** Dark field STEM image of *b*. **c)** SEM image of some tips observed in the product. **d)** Bright field STEM image of *d*. *Inset:* a close-up to narrow-end in the CNT. **e)** SEM image of other narrow-end found. **f)** Bright field STEM image of *e*. **g)** Close-up of *f*.

an attempt to clarify how they form. Fig. 4.17 shows a slightly corrugated tubes which, in dark field STEM imaging, exhibit partial metallic filling and particles of high atomic number on their surface.

By contrast, fig. 4.17*c* shows several CNTs ends. Bright field (BF) STEM image of them (fig. 4.17*d*) shows a closed narrow-end, which must also be the case for the structures observed in fig. 4.15*h*. Small metallic particles can be also observed on the surface of other nanotubes.

A pronounced sharpening effect within a nanotube is shown in fig. 4.17*e*, and its corresponding BF STEM image in fig. 4.17*f*. In this figure a bamboo-like structure can be distinguished, usually related to MWNTs-CN_x morphology. This tube does not appear to end in a complete peak but in a smaller diameter as shown in fig. 4.17*g* where also their compartment like morphology can be identified.

It could be of interest to point out that the tube exhibiting a closed narrow-end, does not exhibit the internal bamboo-like structure while the one that ends in an small final diameter does. Another possibility is that the compartment like-structure of fig. 4.17*d* is outside the field of view. However, HRTEM imaging must be performed in order to have more experimental evidence before any possible inference can be done.

In order to examine possible structural differences of these nanotubes with respect to as-produced MWNTs-CN_x and MWCNTs synthesized using similar temperatures (800°C), powder XRD measurements were performed on the MWNTs-CN_x–MWCNTs with Ti (produced at 825°C). The corresponding XRD patterns for the three nanotube types are depicted in fig. 4.18.

The presence of an of iron oxide ($Fe_{21.34}O_{32}$) in the MWNTs-CN_x (fig. 4.18*b*) and Fe *fcc* in MWCNTs (fig. 4.18*c*), is the only major difference. The three patterns look similar in the planes belonging to the bulk graphite layers arrangement. However, the presence of two low intensity peaks in the pattern of 4.18*a*, which is not observed in the others, is remarkable. These signals, marked as (•), have positions that correspond to the two more intense diffraction planes for TiC *fcc* (the (200) and (220)). According to the Ti-C phase diagram, [26] this phase is stable in the range of temperature and concentrations used. The presence of these diffraction signals in our product suggests a possible interaction between the C in the graphitic network

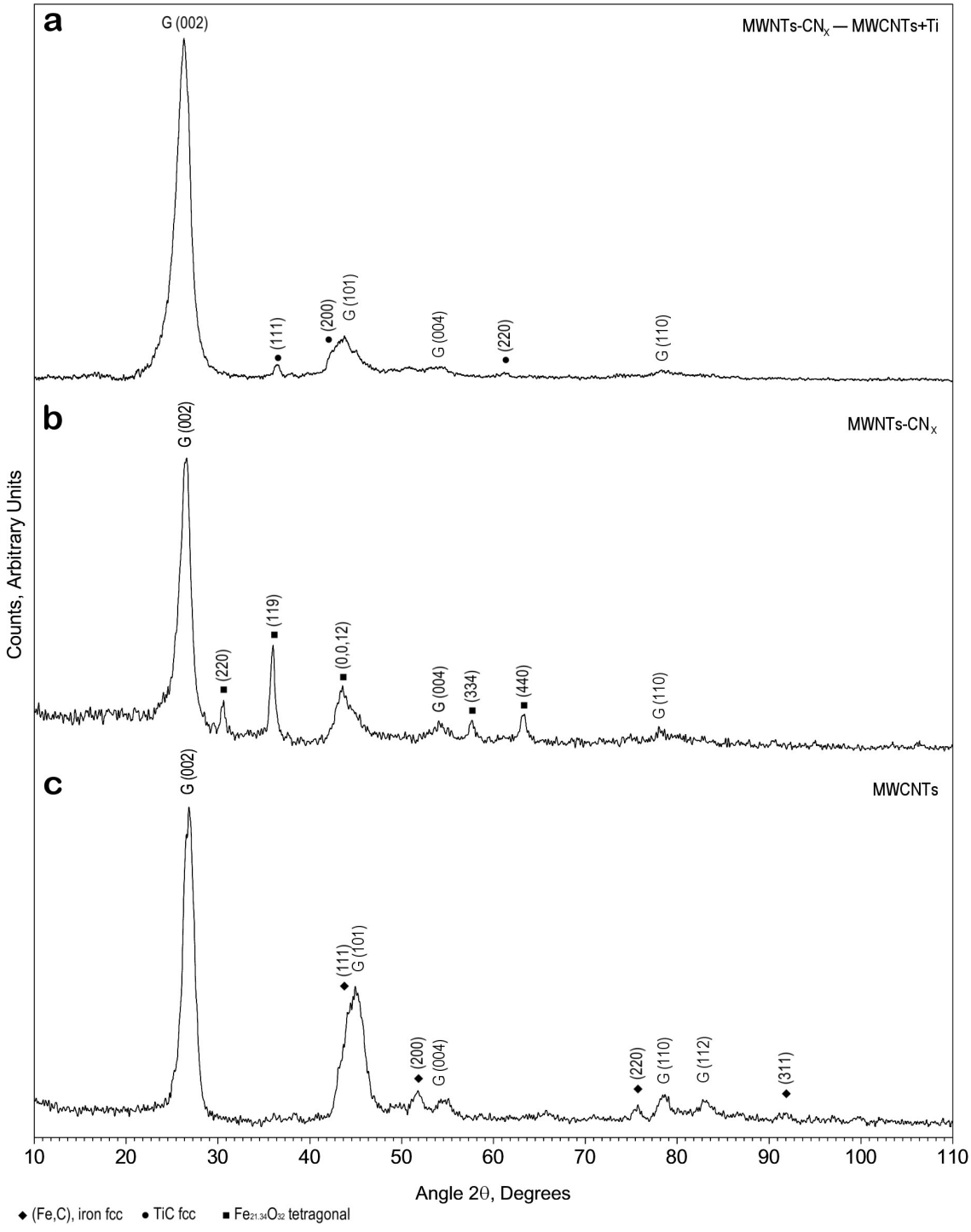

Figure 4.18: XRD pattern of CNTs synthesized in presence of Ti. a) Powder XRD pattern for the CNTs synthesized in presence of $TiCl_4$ at 825°C. **b)** MWCNTs growth at 800°C. **c)** MWNTs-CN_x growth at 800°C. Signals marked as G correspond to graphite ($P6_3/mmc$, $a = 2.4560$ Å, $c = 6.6960$ Å); ♦ to Fe *fcc*, ($Fm\bar{3}m$, $a = 3.600$ Å); ■ to and iron oxide, $Fe_{21.34}O_{32}$ (P41212, $a = 8.3474$ Å, $c = 25.0422$ Å); and ● to TiC *fcc*, ($Fm\bar{3}m$, $a = 4.3178$ Å).

or in the by product when Ti was added in the form of $TiCl_4$ during the thermolysis process. This would play a role in the abrupt diameter decrease at the tips of the CNT as they were forming in the presence of Ti.

One of the possibilities is that the Ti works as a promoter for the cone shape end. In the case of the MWNTs-CN_x part, this element would probably tend to be localized at the sites rich in nitrogen, like the interlinker compartments. [27] We suggest that their presence then could extend the interlayer spacing of the outer shells in those points and, making them more fragile. Consequently it would allow an easier sliding among the polymerized "nanobells" forming the MWNTs-CN_x structure. This could explain why the caps exhibit a tapering end, very similar to that of the minor diameter extreme of the "nanobells" forming each bamboo-like compartment.

TGA of the obtained products is shown in fig. 4.19 as the derivative of the weight loss *vs* temperature. The experiments were performed in air, in similar conditions to those described in section 2.5.1. The N-doped and undoped carbon nanotubes used as reference were the synthesized at 800 °C.

The upper and middle graph in fig. 4.19 show the thermal degradation temperature for MWNTs-CN_x (378 °C) and MWCNTs (476 °C) respectively. The lower plot shows that the thermal degradation of the MWNTs-CN_x–MWCNTs, Ti in air is 422 °C, above the temperature for MWNTs-CN_x and below of MWCNTs. In fact, the temperature for thermal decomposition of MWNTs-CN_x–MWCNTs, Ti is near to the geometric average of these last two values, $\bar{T}_{geom} = 423.8$ °C.

Even this temperature would be more probably a coincidence, it is interesting to see how this new structure shows only one intermediate decomposition temperature and not two.

However, the high temperature tail of its corresponding decomposition temperature curve (for MWNTs-CN_x–MWCNTs, Ti) does not decreases in an exponential way like the others, but it exhibits a lineal behavior. If we consider the plot in fig. 4.19 as a representative of the rate of decomposition, we find in the

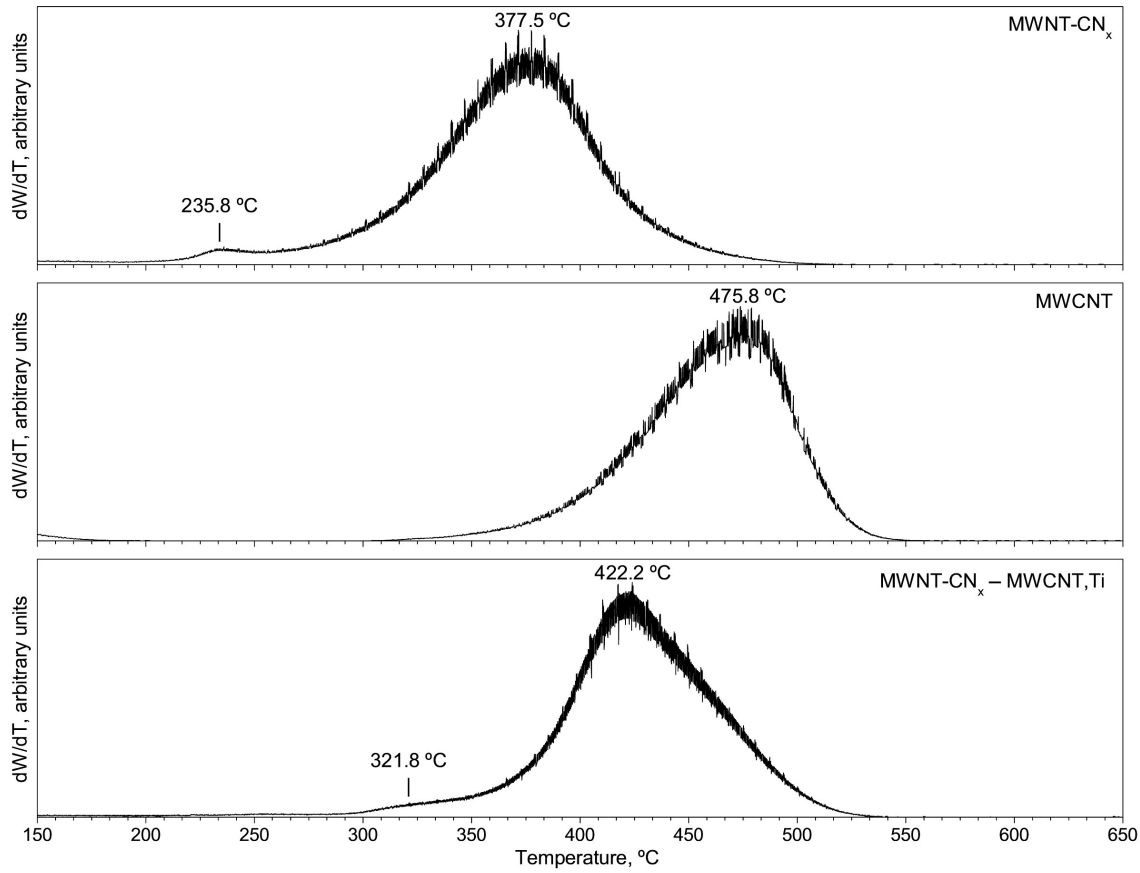

Figure 4.19: Comparative TGA analysis of CNTs synthesized in presence of Ti. First derivative of the weight respect to temperature of *(top to bottom)* MWNTs-CN_x, MWCNTs (both synthesized at 800°C) and MWNTs-CN_x–MWCNTs, Ti synthesized at 825°C.

final tail of the curve an analog to an uniform decomposition rate. Which means that the product is being decomposed at the same relative low ratio (about $\frac{1}{91\ °C}$) until ∼492 °C is reached. Above that temperature, the decomposition rate increases in an exponential way.

This thermal analysis could be a confirmation that hybrid structures have been created. Noticeably, the decomposition temperature for these structures is different from those their formers by about ±50 °C respectively.

4.2.3 Summary

In this section we showed the effect of adding $TiCl_4$ during the production of nanotubes (N-doped in its first section and undoped in the rest). Narrow-close cap end and abrupt reductions in the diameter size near their tips have been obtained by a continuous two step CVD growth process.

Besides obtaining TiO_2 particles deposition on the surface of the low part of the product, named MWNTs-CN_x–MWCNTs, Ti, the addition of Ti also induced unexpected effects in the carbon nanotube morphologies.

Characterization allowed us to suggest that two kinds of tip-endings were produced. However, further HRTEM analysis on the sample will be of great utility to confirm or deny this hypothesis. XRD analysis revealed that the graphene planes obtained in the sample were almost the same that the exhibited by control samples (MWNTs-CN_x and MWCNTs); evidence of C–Ti bonding in a *fcc* structure was found from two of the most intense crystallographic planes of the TiC.

TGA analysis showed, that the obtained product, exhibit one well identified thermal degradation temperature. The linear decay in the thermal degradation rate after passing the decomposition temperature indicates that the compound slowly degradates and not spontaneously with the temperature increment. This tendency is different to the observed in MWNTs-CN_x and MWCNTs where the decomposition rate decelerates in a faster way.

Therefore, the difference in thermal properties between the MWNTs-CN_x and MWCNTs could be an indication that a new structure that exhibits simultaneously the properties of doped- and undoped- carbon nanotubes was obtained. On the other hand, other of the more attractive features in the product is that we were able to abruptly diminish the diameter size of the carbon nanotubes in a very narrow longitudinal length. It could lead to a more efficient manipulation of the carbon nanotubes for promising new carbon based structures.

Improvements to the process presented here could aid to produce arrays ended

in tips that could be valuable in electronic applications.

4.3 Conclusions

In this chapter we have explored two different approaches to obtain a deposit of Ti on MWNTs-CN_x.

For one of the methods developed, we had achieved working electrodes using MWNTs-CN_x arrays and the deposition of possibly continuous layers of Ti on MWNTs-CN_x. On the other hand, we also showed the modification of the morphology on the nanotubes arrays by two different methods: electrochemical treatment and incorporation of a Ti precursor since the CNTs CVD synthesis. The modifications observed by these methods were the branching of MWNTs-CN_x arrays and the abrupt change in the diameter end of the MWNTs-CN_x respectively, which will be very promising for new applications and industrial production of these structures. We consider that these three are important contributions in the field of carbon nanotube science.

In addition to these results; we also showed the feasibility of depositing Si nanoparticles by electrochemical methods and its ability to promote a further growth of carbonaceous structures.

References

[1] Campbell, J.K.; Sun, L. and Crooks, R.M. *Electrochemistry using single carbon nanotubes.* Journal of American Chemical Society **121**:3779–3780, 1999.

[2] Diao, P.; Liu, Z.; Wu, B.; Nan, X.; Zhang, J. and Wei, Z. *Chemically assembled single-wall carbon nanotubes and their electrochemistry.* ChemPhysChem **10**:898–901, 2002.

[3] Hu, C.G.; Wang, W.L.; Wang, S.X.; Zhu, W. and Li, Y. *Investigation of electrochemical properties of carbon nanotubes.* Diamond and Related Materials **12**:1295–1299, 2003.

[4] Valentini, F.; Amine, A.; Orlanducci, S.; Terranova, M.L. and Palleschi, G. *Carbon nanotube purification: Preparation and characterization of carbon nanotube paste electrodes.* Analytical Chemistry **75**:5413–5421, 2003.

[5] Koehne, J.; Li, J.; Cassell, A.M.; Chen, H.; Ye, Q.; Tee Ng, H.; Han, J. and Meyyappan, M. *The fabrication and electrochemical characterization of carbon nanotube nanoelectrode arrays.* Journal of Materials Chemistry **14**:676–684, 2004.

[6] Gupta, S.; Hughes, M.; Windle, A.H. and Robertson, J. *In situ Raman spectro-electrochemistry study of single-wall carbon nanotube mat.* Diamond and Related Materials **13**:1314–1321, 2004.

[7] Tu, Y.; Lin, Y.; Yantasee, W. and Ren, Z. *Carbon nanotubes based nanoelectrode arrays: Fabrication, evaluation, and application in voltammetric analysis.* Electroanalysis **17**(1):79–84, 2005.

[8] Googind, J.J. *Nanostructuring electrodes with carbon nanotubes: A review on electrochemistry and applications for sensing.* Electrochimica Acta **50**:3049–3060, 2005.

[9] Heller, I.; Kong, J.; Hendrik, A.; Williams, K.A.; Lemay, S.G. and Dekker, C. *Individual single-walled carbon nanotubes as nanoelectrodes for electrochemistry.* Nano Letters **5**(1):137–142, 2005.

[10] Gong, K.; Yan, Y.; Zhang, M.; Su, L.; Xiong, S. and Mao, L. *Electrochemistry and electroanalytical applications of carbon nanotubes: A review.* Analytical Sciences **21**:1383–1393, 2005.

[11] Diao, P. and Liu, Z. *Electrochemistry at chemically assembled single-wall carbon nanotube arrays.* Journal of Physical Chemistry B **109**:20906–20913, 2005.

[12] Kaempgen, M. and Roth, S. *Transparent and flexible carbon nanotube/polyaniline pH sensors.* Journal of Electroanalytical Chemistry **586**:72–76, 2006.

[13] Hu, C.; Chen, X. and Hu, S. *Water-soluble single-walled carbon nanotube films: Preparation, characterization and applications as electrochemical sensing films.* Journal of Electroanalytical Chemistry **586**:77–85, 2006.

[14] Heller, I.; Kong, J.; Williams, K.A.; Dekker, C. and Lemay, S.G. *Electrochemistry at single-walled carbon nanotubes: The role of the band structure and quantum capacitance.* Journal of American Chemical Society **128**:7353–7359, 2006.

[15] Niessen, R.A.H.; de Jonge, J. and Notten, P. *The electrochemistry of carbon nanotubes.* Journal of The Electrochemical Society **153**(8):A1484–A1491, 2006.

[16] Zheng, B.; Wei, S.; Xiao, F. and Zhao, F. *Voltammetric behavior and determination of rutin at a single-walled carbon nanotubes modified gold electrode.* Sensors and Actuators B **115**:240–246, 2006.

[17] Bard, A.J. and Faulker, L.R., eds. *Electrochemical methods: Fundamentals and Applications.* John Wiley and Sons: Danvers, MA, 2nd edition, 2000.

[18] Jia, N.; Wang, L.; Liu, L. and Zhou, Q. *Bamboo-like CN_x nanotubes for the inmobilization of hemoglobin and its bioelectrochemistry.* Electrochemistry Communications **7**:349–354, 2005.

[19] Heng, Y.L.; Chou, A.; Yu, J.; Chen, Y. and Gooding, J.J. *Demonstration of the advantages of using bamboo-like nanotubes for electrochemical biosensor applications compared with single walled carbon nanotubes.* Electrochemistry Communications **7**:1457–1462, 2005.

[20] Kamalakaran, R.; Terrones, M.; Seeger, T.; Kohler-Redlich, P.; Rühle, M.; Kim, Y.A.; Hayashi, T. and Endo, M. *Synthesis of thick and crystalline nanotube arrays by spray pyrolysis.* Applied Physics Letters **77**(21):3385–3387, 2000.

[21] Mayne, M.; Grobert, N.; Terrones, M.; Kamalakaran, R.; Rühle, M.; Kroto, H.W. and Walton, D.R.M. *Pyrolytic production of aligned carbon nanotubes from homogeneously dispersed benzene-based aerosols.* Chemical Physics Letters **338**:101–107, 2001.

[22] Terrones, M. *Science and technology of the twenty-first century: Synthesis, properties, and applications of carbon nanotubes.* Annual Review Material Research **33**:419–501, 2003.

[23] Gleixner, S. *The characterization of particulate debris obtained from failed orthopedic implants: Chapter 5.* website of San José State University, `http://www.engr.sjsu.edu/WofMatE/projects/srproject/srproj5.html`, 2005.

[24] Barin, C.S.; Correia, A.N.; Machado, S.A.S. and Avaca, L.A. *The effect of concentration on the electrocrystallization mechanism for cooper on platinum ultramicroelectrodes.* Journal of the Brazilian Chemical Society **11**(2):175–181, 2000.

[25] Xie, R.H.; Zhao, J. and Rao, Q. *Encyclopedia of Nanoscience and Nanotechnology*, volume 10, chapter Doped Carbon Nanotubes, pages 1–31. Nalwa, H. S.: www.aspbs.com/enn, 2004.

[26] Massalski, T.B., ed. *Binary Alloy Phase Diagrams.* ASM International: Materials Park, OH, 2nd edition, 2001.

[27] Lim, S.H.; Elim, H.I.; Gao, X.Y.; Wee, A.T.S.; Ji, W.; Lee, J.Y. and Lin, J. *Electronical and optical properties of nitrogen-doped multiwalled carbon nanotubes.* Physical Review B **73**:045402, 2006.

Chapter 5

Conclusions and Future Work

5.1 Conclusions

The main purpose of this thesis work, was to achieve an efficient method for obtaining metallic nanoparticle deposition directly on nitrogen doped multiwalled carbon nanotubes (MWNTs-CN_x) throughout a procedure which did not involve prior chemical modification of the nanotube surface, in order to avoid alterations of the characteristic electronic and mechanical properties of CNTs. It was proposed that the chemical interaction of the nitrogen atoms in these nanotubes, an advantage they have over undoped MWCNTs, could be used for this purpose. The objective was achieved by producing MWNTs-CN_x with iron, platinum or titanium nanoparticles over their surface, using different species as precursors for the metals.

Two different methods were developed for iron deposition. The first approach used potassium hexacyanoferrate(III), $K_3[Fe(CN)_6]$; in the second one, an acidic solution of Fe^{+3} was used as iron source. Both methods produced iron nanoparticules distributed over the nanotube surface.

The iron nanoparticles deposited on the MWNTs-CN_x allowed us to generate new carbon nanotube structures, under a secondary CVD treatment with pure toluene, without any additional catalyst. This procedure produced several kinds of junctions between carbon nanotubes, producing heteroatomic nanotube networks, where the

core is made up of MWNTs-CN_x and the exterior of nanotubular undoped carbon layers. We call these structures CNx@CNT. One of these structures, reported for the first time, consists of coaxially arranged nanocables composed of these two types of nanotubes, with different electronic properties, which could be of interest for the fabrication of novel nanoelectronic devices. However, more studies must be performed in order to explore their potential applications.

For platinum deposition, sodium hexachloroplatinate(IV), $Na_2[PtCl_6]$ was used. Particles of about 50 nm in diameter were found between the tubes, and Pt nanoparticles of ∼3 nm in diameter were homogeneously dispersed on the MWNTs-CN_x's surface. These small Pt nanoparticles were usually more abundant on the N-enriched sites of the interlinker compartments that make up the bamboo-like structure of the tubes. This would indicate that there is an interaction between the nitrogenated sites and the metal precursors.

XRD analysis of the products reveled that the nanoparticles are made of metallic Pt exhibiting a *fcc* structure. No reduction step was performed, and we believe that platinum was reduced by the acetic acid used as disperser for the MWNTs-CN_x. We also found that the size of Pt nanoclusters strongly depends on the temperature. Since it is know that diminishing particle size enhances the catalytic properties of transition metals, these Pt-deposits over MWNTs-CN_x could be used as catalysts for heterogeneous systems.

For titanium deposition two different approaches were followed. The first one was based on electrochemical methods, where MWNTs-CN_x were used as working electrodes (WE) in two different systems. The first system was the $TiO_2/H_2O, HF, HNO_3$ electrolyte; in this case the surface of the MWNTs-CN_x mats was covered with TiO_2 randomly and no special affinity of TiO_2 for the MWNTs-CN_x was found. However, when the products were analyzed by SEM, a branching of carbon-based material was observed at the base of mat, originally consisting of straight aligned MWNTs-CN_x. We suggest that the current density injected during the electrochemical treatment onto the MWNTs-CN_x was responsible of

this branching. The production of nanostructured carbon networks of carpet-like arranged MWNTs-CN_x by electrochemical methods, could be a promising alternative for the massive production of these structures at low cost.

The second electrochemical system studied was $TiCl_4$/ethanol solution. EDX analysis performed on these tubes revealed the existence of Ti in relatively high percentages (up to 20 at %) but clusters on the surface of MWNTs-CN_x were not observed. Therefore, we believe that the MWNTs-CN_x are probably covered by a continuous layer of Ti.

Additionally, during these experiments we found that Si can be deposited by electrochemical methods. Si nanoparticles seem to have a higher affinity with the MWNTs-CN_x than the TiO_2 particles. Si nanoparticles also promoted the growth of carbon nanostructures when exposed to the electron beam energy. Since this element was not one of the study subjects of this thesis work, we leave for a future study the Si deposition by electrochemical methods.

MWNTs-CN_x have not been studied extensively in electrochemical systems and this research opens a wide range of possibilities for the electrochemical modifications of their morphology.

The second approach for the deposition of Ti tested its incorporation in the CVD synthesis of CNTs. The presence of Ti did not lead to deposition of nanoparticles but it produced a notorious narrowing at the tips of CNTs. Optimizing this procedure for the massive production of MWNTs-CN_x could lead to an enhancement in their field emission properties, which would make them more attractive to the semiconductor and electronic industry.

In this work we developed methods to exploit the chemical properties of MWNTs-CN_x for deposition of transition metal nanoparticles, showing that the nitrogen doping makes CNTs more reactive, facilitating their manipulation without needing aggressive chemical modifications. The procedures developed in this work also resulted in the production of new nanotube structures, which could be the bases

of new research lines for MWNTs-CN_x applications. In conclusion, we have shown experimental methods that effectively deposit metal nanoparticles on nitrogen doped carbon nanotubes and methods that could lead to the production of new nanotube structures. In both cases, this work can lead to the development of new applications for CNTs.

5.2 Future work

The methods developed in this work, can be applied to the production of MWNTs-CN_x coated with other kind of metallic particles. For example, we obtained preliminary results (not shown in this thesis) for the deposition of palladium nanoparticles using coordination salts, where further optimization studies need to be performed.

In the case of the Pt deposited-MWNTs-CN_x, it would be necessary to scale-up the procedure (which uses milligrams) to prepare gram amounts to be able to perform catalytic essays to test their use as catalysts in hydrogenation reactions for instance.

The new coaxial carbon structures reported in our work promise interesting applications, theoretical and experimental studies are necessary in order to understand and exploit their capabilities. It would be also very helpful to carry out optimization studies for the controlled production of these heteroatomic networks. One of the approaches that can be useful to achieve this objective, is to change the current CVD reaction horizontal system described in section 2.5.1 a fluidized bed vertical reactor. In that case, the Fe coated-MWNTs-CN_x will act as the suspended substrates for the reaction. An optimization to the procedure so that iron was deposited in a controlled manner on the MWNTs-CN_x, is one of the possibilities envisioned for the improvement of the networks production.

Diverse chemical reactions in the N-doped sites of MWNTs-CN_x can be tested to explore in detail their chemical properties. For example, the reaction of these sites with organic compounds could lead to the production of polymer precursors for the *in situ* preparation of hybrid nanocomposites. Very promising results regarding this resulted from reacting MWNTs-CN_x with nylon 6,6 monomers, producing MWNTs-CN_x covered with polymer. For details, refer to appendix A.

The improvement of network junctions production and their subsequent incorporation in polymeric systems, or in the production of nanosized catalysts,

as well as their use in electrodes of high capacity are also new fields of applications. The range of possibilities for the new structures described in this thesis is too wide, and new possibilities for their further use are expected to appear in the near future.

Appendix A

Characterization studies of the in-situ polymerization of Nylon-6,6 in presence of MWNTs-CN_x

One of the additional chemical reactions we derivated for using the N-doping sites in the MWNTs-CN_x, is in the production of new MWNTs-CN_x-composite materials using a modification of a known polymeric procedure for the nylon-6,6 production. Our approach was to utilize the N-sites on the MWNTs-CN_x as starting points in the polymerization beginning process.

A.1 Experimental

The expected reaction between the MWNTs-CN_x and the adipoyl chloride, $ClCO(CH_2)COCl$, a precursor for nylon-6,6 is schematically depicted in fig. A.1.

If the monomer reacts first with the N-sites in the MWNTs-CN_x, the following step is to add the second monomer, the hexamethylenediamine, $C_6H_{16}N_2$. This species reacts with adipoyl chloride to form a polymer chain of nylon-6,6. The first proposed procedure used to perform this reaction is written below.

1. Dispersion of MWNTs-CN_x in dried toluene in an ultrasonic bath.

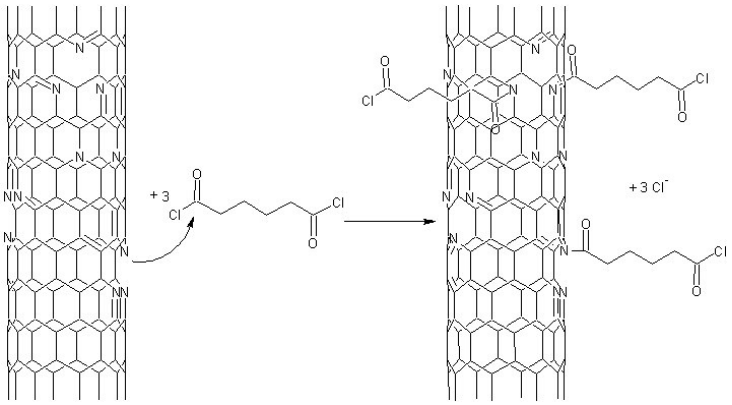

Figure A.1: Proposed reaction of adipoyl chloride with MWNTs-CN_x.

2. Addition of adipoyl chloride to the dispersed MWNTs-CN_x at a temperature range of 60–80 °C in continuous stirring. The reaction is allowed to proceed by 3 h.

3. The hexamethylenediamene is then added by fast dropping under continuous stirring. This reaction is also allowed proceed by 2 h at the conditions described above.

4. The product is washed three times with ethanol and separated by centrifugation (4,000 rpm/10 min).

The products obtained by this methodology have been characterized by SEM using a FEI FEG-XL30 (at acceleration voltages below 10 keV) equipped with an EDS detector; by *Attenuated Total Reflection Infrared Spectroscopy* (IR-ATR) using a Bruker Vector 22 ATR with a diamond window of Pike technologies; Raman spectroscopy performed in a Kraiser Holo Lab 5000 system (2.33 eV at $\lambda = 533$ nm; located at Shinshu University, Japan); and by TGA using a Thermo Haake, Cahn VersaTherm HS in N_2 atmosphere (with a thermal rate of 5 °C/min).

A.2 Results and discussion

A first indirect indication of a change in the tubes can be seen in fig. A.2.

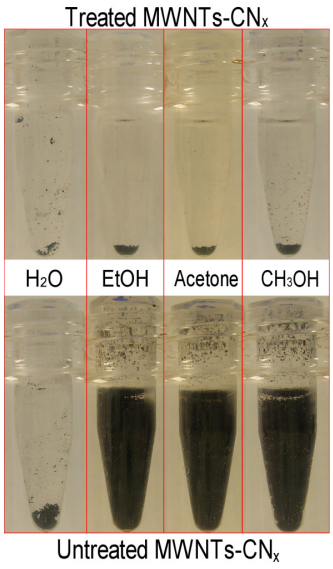

Figure A.2: Comparative dispersion of treated and untreated MWNTs-CN_x in diverse mediums. *From left to right:* Proofs of the MWNTs-CN_x dispersion in water, ethanol, acetone and methanol. The upper row corresponds to MWNTs-CN_x treated as specified in the experimental process proposed in page 161. The lower row shows the as synthesized MWNTs-CN_x used.

It can be observed in this image how the untreated MWNTs-CN_x disperse in acetone, ethanol and methanol, and how they tend to agglomerate when water is used as solvent. On the other hand, it is noteworthy how after undergoing to the treatment with the polymer precursors, the MWNTs-CN_x were not dispersed as well as untreated MWNTs-CN_x. The treated MWNTs-CN_x, instead, remain at the bottom of the vial for all the mediums.

This change in the dispersability of the MWNTs-CN_x after treatment is an indication that the tubes experimented modifications on their surface. However; it is not an evidence of covalent bonding between the MWNTs-CN_x and the polymer chains.

STEM and SEM characterizations (fig. A.3) were performed on the product. Images A.3*a* and *b* show different magnifications of the MWNTs-CN_x after their treatment with adipoyl chloride.

In fig. A.3*b* can be noted a contrast difference along the axis of the tubes which is delineated in the inset for clarity. This, together with a different surface morphology from the usual exhibited by the MWNTs-CN_x, suggest that a layer of

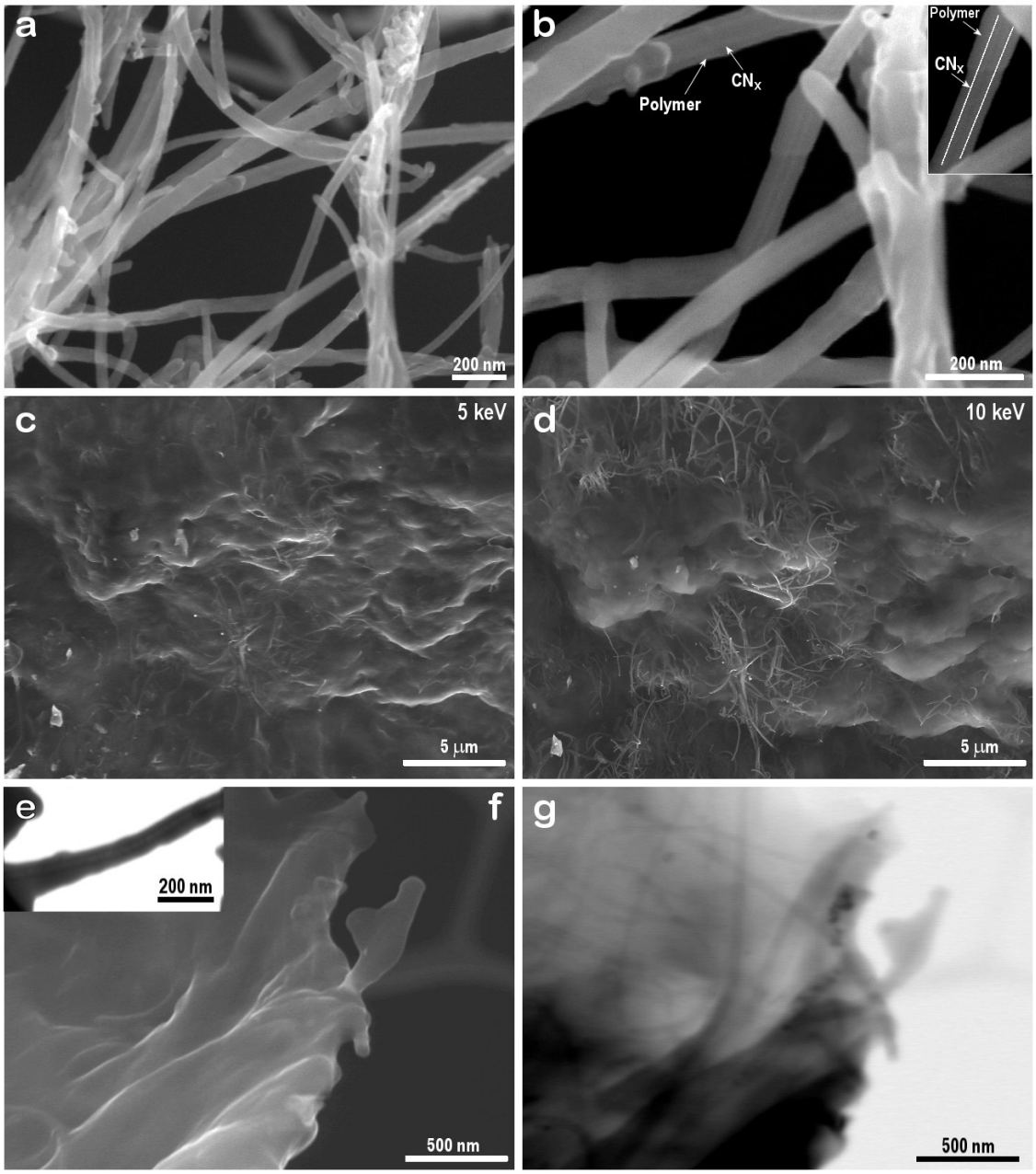

Figure A.3: SEM and STEM images of MWNTs-CN_x reacted with Nylon-6,6 precursors. a) MWNTs-CN_x reacted only with adipoyl chloride. **b)** Close-up of *a*. **c)** Polymer surface of MWNTs-CN_x treated with adipoyl chloride and hexamethylenediamene. **d)** Image *c* taken with a higher acceleration voltage (10 keV). **e)** Bright field (BF) STEM image of MWNTs-CN_x covered by a polymer layer. **f)** SEM image of the polymeric composite obtained. **g)** BF STEM image of *f*.

the polymer precursor wrapped the nanotubes. Figs. A.3*c* and *d* shows SEM images of the polymer obtained after reacting the MWNTs-CN_x with both adipoyl chloride and hexamethylenediamene. The image taken at an accelerating voltage of 5 keV

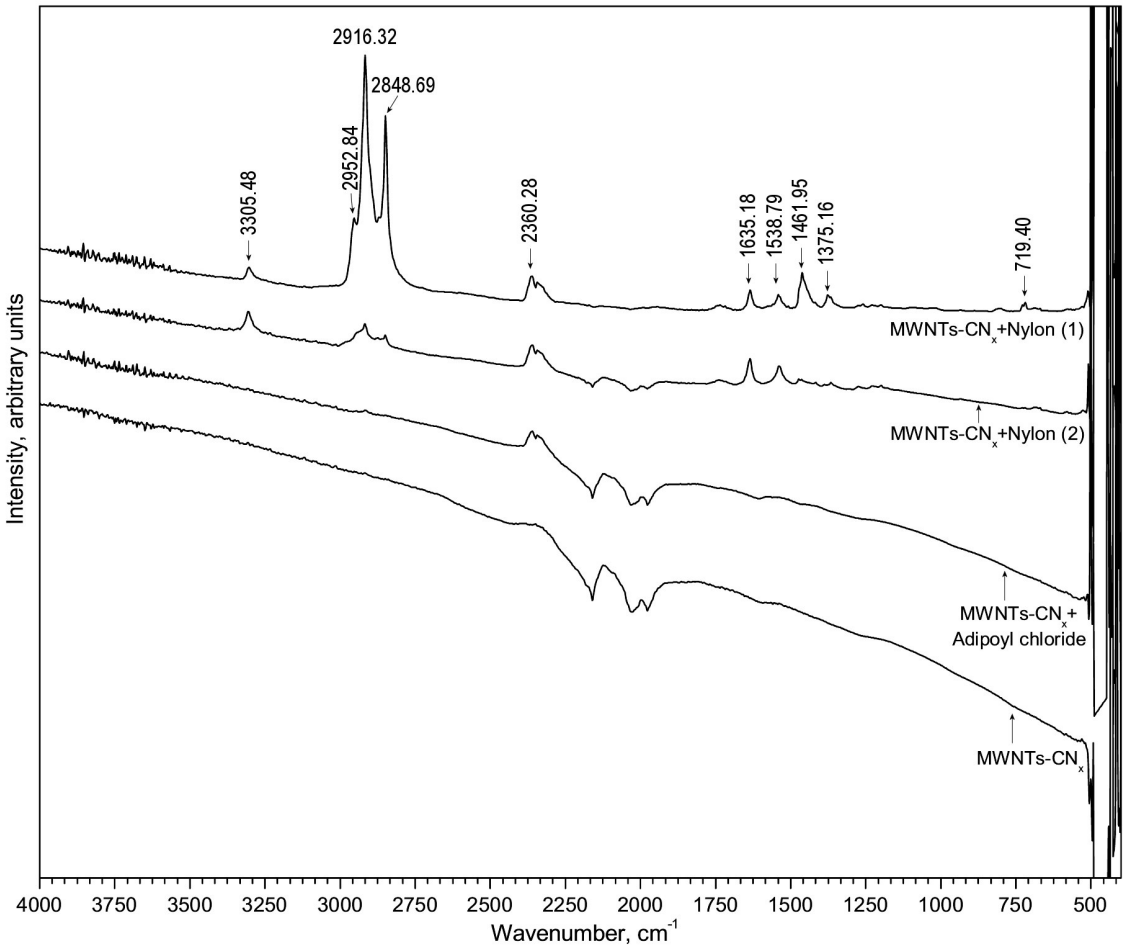

Figure A.4: IR-ATR spectra of MWNTs-CN_x reacted with Nylon-6,6 precursors. *Top to bottom:* MWNTs-CN_x reacted with adipoyl chloride and hexamethylenediamene with a high amount of polymer precursors in (1) and a low amount in (2); MWNTs-CN_x reacted only with adipoyl chloride and, as-produced MWNTs-CN_x.

(fig. A.3*c*) allow us to observe MWNTs-CN_x completely covered with nylon. On the other hand, an image taken at the same zone at 10 keV (fig. A.3*d*) evidence the embedding of MWNTs-CN_x in the nylon matrix.

This polymer cover can be easily observed in subsequently STEM imaging of the sample (fig. A.3*e*), where the bamboo-like structure of the MWNTs-CN_x is identified in the core of a polymeric structure. An edge of a thin composite-polymer sheet observed by SEM is depicted in fig. A.3*f* and its corresponding bright field STEM image (fig. A.3*g*) reveals a dispersion of MWNTs-CN_x immersed in the polymeric matrix.

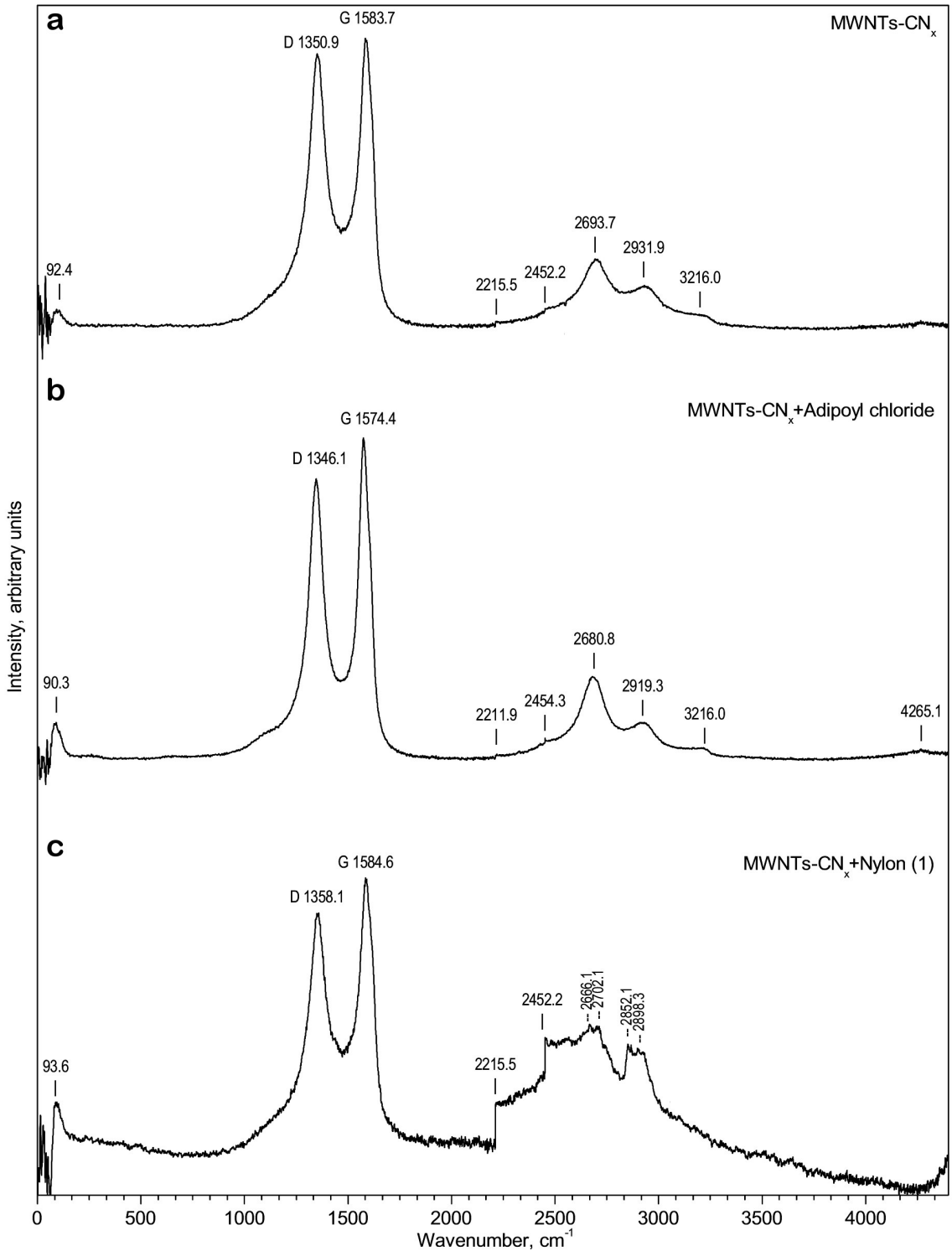

Figure A.5: Raman spectra of MWNTs-CN_x reacted with Nylon-6,6 precursors. **a)** as-produced MWNTs-CN_x. **b)** MWNTs-CN_x reacted with adipoyl chloride only. **c)** MWNTs-CN_x reacted with adipoyl chloride and hexamethylenediamene.

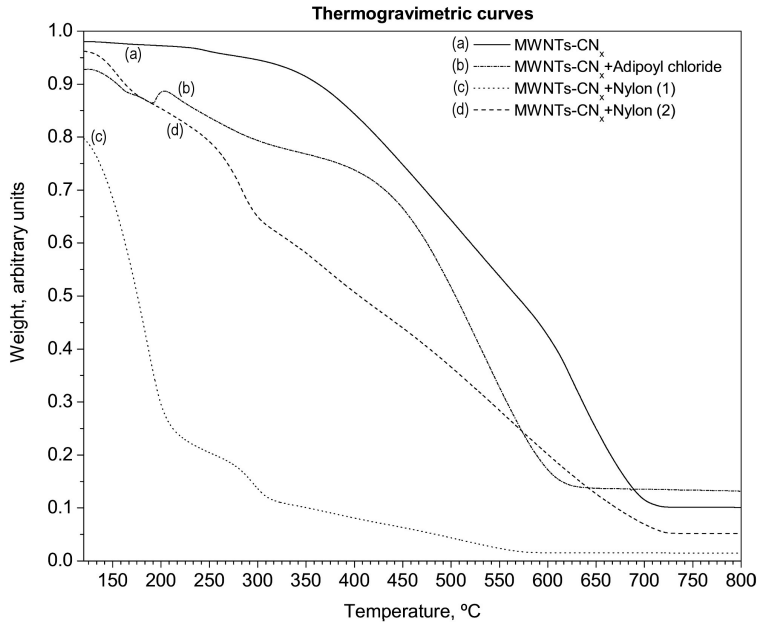

Figure A.6: TGA curves obtained for MWNTs-CN_x reacted with Nylon-6,6 precursors. N_2 atmosphere was used during the analysis. Curves belonging to as-produced MWNTs-CN_x, MWNTs-CN_x reacted only with adipoyl chloride and its subsequent reaction with hexamethylenediamene.

Further analysis performed on the sample, such as IR-ATR (fig. A.4) and Raman spectroscopy (fig. A.5) show evidence of polymer presence; but they do not give conclusive information about formation of covalent bonding between nylon chains and MWNTs-CN_x.

The IR-ATR spectra (fig. A.4) of MWNTs-CN_x reacted with nylon precursors is similar to the reported in the literature for nylon-6,6. [1] In this spectrum, the peak at 3305 cm^{-1} corresponds to the N–H stretching and the following three signals (2953, 2916 and 2849 cm^{-1}) to the C–H stretching. The signal located at 2360 cm^{-1} is characteristic of the CO_2(g) present in the air during the measurement. The further signals, located at 1635 cm^{-1} (probably due to N–H bending), 1539 cm^{-1}, 1462 cm^{-1} and 1375 cm^{-1} are in the *fingerprint* zone for nylon-6,6. Meanwhile; the IR of MWNTs-CN_x+Adipoyl chloride exhibits the signal of atmospheric CO_2, but, in general is not very different from that of as-produced MWNTs-CN_x (fig. A.4 in the bottom).

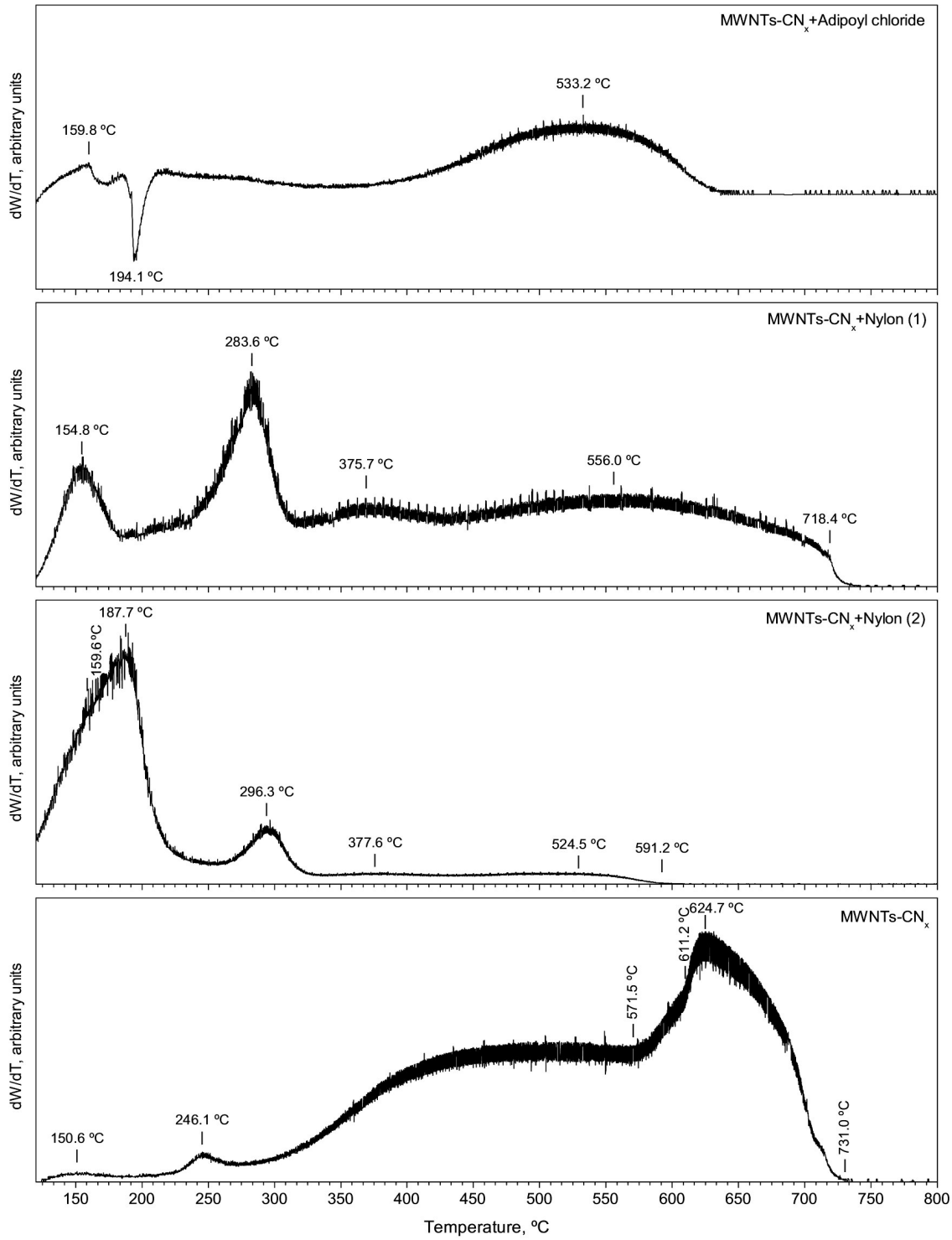

Figure A.7: Comparative TGA analysis of MWNTs-CN_x reacted with Nylon-6,6 precursors. N_2 atmosphere was used during the analysis. First derivative of the weight respect to temperature of (*top to bottom*) MWNTs-CN_x reacted with adipoyl chloride only; MWNTs-CN_x reacted with adipoyl chloride and hexamethylenediamene with a higher amount of polymer precursors in (1) and a lower in (2) and, as-produced MWNTs-CN_x.

A slightly displacement in the MWNTs-CN_x G signal of about 10 cm^{-1} to lower wavenumbers (*i.e.* from 1584 to 1574 cm^{-1}) was found in the Raman spectrum of MWNTs-CN_x treated with adipoyl chloride (fig. A.5*b*). The I_D/I_G ratio also decreased from 0.953 to a mean value of 0.872 which corresponds to a reduction in amount of defects in the MWNTs-CN_x. On the other hand, the MWNTs-CN_x G band in the first nylon production experiments (fig. A.5*c*) exhibit a very similar value to the as-produced MWNTs-CN_x (fig. A.5*a*), but also a decreasing in the I_D/I_G value (to 0.907) was found. The noisy modification of the peaks at the region between 2200 and 4000 cm^{-1} could be related to the presence of nylon.

The TGA analysis curves obtained of the sample in inert atmosphere (N_2) are plotted in fig. A.6. In these curves is easily noted the first mass loss of volatile compounds in the MWNTs-CN_x+nylon, believed to correspond to a mixture of water and ethanol because of the synthesis conditions. The high mass loss rate exhibited until ∼188 °C in fig. A.6*c* suggests the loss of polymer forming the matrix, not linked directly with MWNTs-CN_x. First derivatives of these curves are depicted in fig. A.7. They suggest two kinds of polymer presence, one of probably covalently bonded and other that does not.

Further analysis by *X-Ray photoelectron spectroscopy* (XPS) could help to confirm a covalent bonding between the MWNTs-CN_x and the polymeric chain. Also, *atomic force microscopy* (AFM) could help with indirect proofs, by for instance, synthesizing a polymer-brush MWNTs-CN_x and visualizing them and their interaction with the nanotube.

Direct participation of MWNTs-CN_x in polymeric reactions would be of greatest importance in achieving a higher interaction between carbon nanotubes and polymeric matrices. This will help to obtain more efficiently polymer reinforcement without the necessity of previous chemical treatments of MWNTs-CN_x; since the formation of functional groups could lead to a decrement in their mechanical properties.

References

[1] *IR Spectra Database.* Aldrich website, 429171 Nylon 6/6, `http://www.sigmaaldrich.com/catalog/search/ProductDetail/ALDRICH/429171#RelatedCategories`, 2006.

Appendix B

The Scherrer Equation

The peaks obtained in XRD patterns of ideal infinite crystals are expected to be as narrow as Dirac delta functions. But, due to their limited size, there are no perfect crystals in nature. Such deviation from the perfect crystallinity will lead to the broadening of the diffraction signal, which is negligible when the crystallite size is larger than 200 nm. This crystallite size is a measure of the size of a coherently diffracting domain. [1] When individual crystallite domains are in phase, they reinforce the diffraction of the X-ray beam, resulting in a tall narrow peak. [2] Therefore, the broadening β due to crystallite size t arises from the limited number of diffracting planes within a diffracting object. This diffracting domain size can be assumed to be equal to the average crystallite size given by the Scherrer (1918) equation: [3]

$$t = \frac{K\lambda}{\beta \cos\theta} \tag{B.0.1}$$

where K is a *shape factor*, named also *Scherrer constant*, with a somewhat arbitrary value that falls in the range of 0.87-1.0 (and it is usually assumed to be 0.9); β is measured in radians at the full width at half maximum (FWHM) true peak breadth and it is valid if the broadening arises entirely as a result of the size effects; λ is the wavelength of the X-ray used; finally, θ is the Bragg angle of the peak position. The β value is corrected for broadening due to the instrument by analyzing a reference solid (with crystallite size >500 nm) at the same conditions that the sample of

interest. The observed width is then corrected from the instrumental broadening as follows: $\beta^2 = \beta^2_{observed} - \beta^2_{reference}$.

The error obtained by applying the Scherrer equation to XRD patterns of known substances is of the order of 10%, meaning that it is difficult to measure small changes in the grain size with great certainty. [1; 3]

References

[1] *"CHEM 484, Lecture notes, weeks 3 and 4"*. University of Washington, Chemistry Department, `http://depts.washington.edu/chemcrs/bulkdisk/chem484A_spr06/notes_Notes_3&4_CHEM484Aspr06.pdf`, 2006.

[2] *"Crystallite size and microstrain analysis of thin films"*. AMIA Laboratories, `http://www.rigakumsc.com/contract/amia_res_TN-C01.htm-20k`, 2006.

[3] Kelsall, R.; Hamley, I. and Geoghega, M. *Nanoscale: Science and Technology*. John Wiley: Hoboken, NJ, 2005.